

# The nanofluidics of graphene oxide

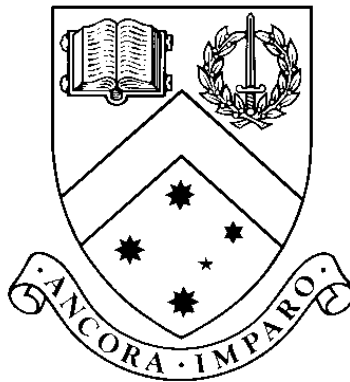
by

**Samuel T. Martin**

**Bachelor of Mechatronic Engineering (Hons.), Bachelor of  
Science**

*Thesis submitted in fulfilment  
of the requirements for the degree of*

**Doctor of Philosophy**



Supervisors: Prof. Adrian Neild and Assoc. Prof. Mainak Majumder

**Nanoscale Science and Engineering Laboratory (NSEL)**

**Laboratory for Micro Systems (LMS)**

**Department of Mechanical and Aerospace Engineering**

**Faculty of Engineering**

**Monash University**

**Australia**

**February 2017**

© Copyright

by

Samuel T. Martin

2017

# The nanofluidics of graphene oxide

## Copyright Notices

### Notice 1

Under the Copyright Act 1968, this thesis must be used only under the normal conditions of scholarly fair dealing. In particular no results or conclusions should be extracted from it, nor should it be copied or closely paraphrased in whole or in part without written consent of the author. Proper written acknowledgement should be made for any assistance obtained from this thesis.

### Notice 2

I certify that I have made all reasonable efforts to secure copyright permissions for third-party content included in this thesis and have not knowingly added copyright content to my work without the owner's permission.



---

Samuel T. Martin  
6th February 2017

# Abstract

This thesis is comprised of four projects which firstly use then examine the nanofluidic properties of graphene oxide.

The first project examined the transport of ions parallel to the plane of the graphene oxide sheets for film samples of different geometries. It was found that when the film had a trapezoidal shape between the two measurement reservoirs an ionic rectifier was made. This rectification phenomenon is suggested to be due to the asymmetry in the two reservoir-film junctions.

Planar nanofluidic designs like the rectifier discovered above can be combined with others to form nanofluidic circuits. A xurographic method was developed for patterning nematic liquid crystals of graphene oxide on a substrate which then had its shape, fidelity and molecular ordering charactered. Patterning techniques such as this are also useful for energy storage and sensing. To demonstrate the efficacy of the technique nanofluidic devices were produced which demonstrated surface charge governed conduction. Interestingly the surface conduction regime showed a power-law dependence of the surface charge density on the concentration.

Reduced graphene oxide samples exhibited a strange hysteresis when their ion transport was examined. This was attributed to polarization of the conductive reduced graphene oxide in the applied electric field. This hypothesis was developed into a device used for storing energy in an electrolyte, an ionic supercapacitor, which is the first of its kind. This ionic supercapacitor can be implemented directly in ionic/nanofluidic circuits in an equivalent manner to a capacitor in an electrical circuit. Studies showed the dependence of this capacitance and power on the conductivity of the reduced graphene oxide. The ionic supercapacitor demonstrates the ability to filter signals in an electrolyte by smoothing the output of a bridge rectifier circuit.

Electrokinetic investigations of shear aligned membranes of graphene oxide found that samples in low pH exhibited unusually high conductance which was attributed to proton conduction. Due to the small interstitial height and surface charge density the streaming currents measured through these membranes were very low. Further investigation of the surface charge density found that nanofluidic estimates of the charge did not match colloidal measurements. A charge regulation model attempted to examine the effect of confinement on the surface charge density and whilst some effect was observed, it could not explain the difference between the two techniques. The model did succeed in explaining the power-law dependence of the surface charge density on the concentration for a range of pH values.

Investigation of a possible high interfacial permittivity lead to close examination of the ion transport data which was exhibiting an unexpected hysteresis. It was concluded that at least part of the hysteresis was due to transient shifts in the conductance of the diffuse boundary layers of the membrane due to concentration polarization. When comparing the membrane geometry to the planar case it was found that this polarization effect was significantly more pronounced in the membrane geometry. The planar geometry was found to be significantly more conductive ( $\sim 6.87 \times 10^7$  times more conductive) than the membrane geometry for the experimental parameters used.

# Thesis declaration and publications

I hereby declare that this thesis contains no material which has been accepted for the award of any other degree or diploma at any university or equivalent institution and that, to the best of my knowledge and belief, this thesis contains no material previously published or written by another person, except where due reference is made in the text of the thesis.

This thesis includes 2 original papers published in peer reviewed journals and 0 submitted publications. The core theme of the thesis is the nanofluidics of graphene oxide. The ideas, development and writing up of all the papers in the thesis were the principal responsibility of myself, the student, working within the mechanical engineering department under the supervision of professor Adrian Neild.

(The inclusion of co-authors reflects the fact that the work came from active collaboration between researchers and acknowledges input into team-based research.)

In the case of chapters 4 & 6 my contribution to the work involved the following:

Thesis chapter	Publication title	Status	Nature and % of student contribution	Co-author name and Nature and % of Co-author's contribution	Co-author(s), Monash student Y/N*
4	Graphene-based ion rectifier using macroscale geometric asymmetry	Published	70% Experimental design, performed experiments, wrote first draft and edited	<ol style="list-style-type: none"> <li>1. Adrian Neild, input into manuscript 15%</li> <li>2. Mainak Majumder, input into manuscript 15%</li> </ol>	<ol style="list-style-type: none"> <li>1. No</li> <li>2. No</li> </ol>
6	The inside-out supercapacitor: induced charge storage in reduced graphene oxide	Published	75% concept, performed experiments, wrote first draft and edited	<ol style="list-style-type: none"> <li>1. Abozar Akbari, chemical synthesis 5%</li> <li>2. Parama Chakraborty Banerjee, performed experiments, input into manuscript 10%</li> <li>3. Adrian Neild, input into manuscript 5%</li> <li>4. Mainak Majumder, input into manuscript 5%</li> </ol>	<ol style="list-style-type: none"> <li>1. Yes</li> <li>2. No</li> <li>3. No</li> <li>4. No</li> </ol>

I have not renumbered sections of submitted or published papers in order to generate a consistent presentation within the thesis.

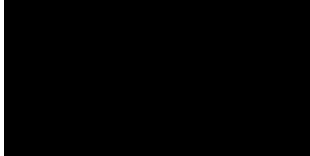
Student signature:



Date: 6/2/2017

The undersigned hereby certify that the above declaration correctly reflects the nature and extent of the student's and co-authors' contributions to this work. In instances where I am not the responsible author I have consulted with the responsible author to agree on the respective contributions of the authors.

Main Supervisor signature:



Date: 6/2/2017

*"Geb' nicht so leicht auf!"*

-Prof. Helmut Jex, on elliptical coordinate transformations

*"With me Sam, you work with me, not for me."*

-Dr. Matt Dimmock

*"Excellent!"*

-Prof. David Paganin

This thesis is dedicated to-  
my family, for their support;  
my friends, for their loyalty;  
and my colleagues, for their wisdom.

# Acknowledgements

Firstly I would like to thank my supervisors, Associate Professor Mainak Majumder and Professor Adrian Neild, for helping through this project and allowing me to have the freedom to explore it. Your encouragement, support and wisdom were always of great assistance.

I have had the benefit of financial support from the Australian Postgraduate Award scheme also from the Monash Centre for Atomically Thin Materials (MCATM) and the Endeavour Scholarship program. It almost goes without saying but without financial support I would have not been able to perform this research.

To my colleagues and friends from Mechanical Engineering and New Horizons over the years, you were always there to help, support me and sometimes indulge my mad ideas- Dave C. (for the culinary experience), Jue Ni, Bulut, Emin, Nin, Muhsincan, Saab, Jason, Jia Wei, An, Armaghan, Ganaka, Dave G., Zhi, Sepideh, Lucy, Tash, Caitlin, Tom, Yan, Delia, Cindy, Billy, Paco, Tori, Mazyar, Ms. Professor (Abozar) Akbari, Phil, Derrek, Rachel, Dhanraj, Parama, Tanesh, Prasoon, Mahdokht and Kath. I would like to especially thank Abozar for the extraordinary effort he gave to make sure the lab always had GO- my project would have been impossible without you, to Parama for always being able help out and to Mahdokht- even though you killed our basil and coriander.

To my colleagues and friends from ENS- Anthony, Hiroaki, Benoit, Luca, Jean, Elenora, Elisa, Voytech, Adrien, Sophie, Antoine, Alessandro and my supervisor in France, Lydéric, it was a truly inspiring experience working with you all.

To the two mentors that inspired me to pursue research all those years ago- Dr. Matt Dimmock and Professor David Paganin, thank you so much.

To my friends for their ongoing support and kindness. Every moment I get to spend with you is always time well spent. I would like to especially thank Vince for his comradery and being bad at heroes. I would also like to thank Fairy and Daniel for always wanting to go adventuring with me.

To my brothers Nick and Elliot and my sister Nat, thanks for being there and always having a spot on the couch for me! To my uncle Ian for keeping me up to date with all the green news. To my grandparents Gwenda, Terry and Diane for their love. Finally I would like to thank my parents for supporting me throughout this time. My mum for her unending supply of delicious meals, my dad for entertaining my whimsical scientific thoughts. Words just don't seem like enough. Thank you. Thank you so very much.

# Contents

<b>Abstract</b> . . . . .	<b>iv</b>
<b>Thesis declaration and publications</b> . . . . .	<b>vi</b>
<b>Acknowledgements</b> . . . . .	<b>x</b>
<b>List of Figures</b> . . . . .	<b>xiv</b>
<b>List of Tables</b> . . . . .	<b>xix</b>
<b>1 Introduction</b> . . . . .	<b>1</b>
1.1 Overview of chapters . . . . .	1
1.1.1 Literature and theory . . . . .	1
1.1.2 Experimental methodologies . . . . .	1
1.1.3 Graphene based ion rectifier using macroscale geometric asymmetry . . . . .	2
1.1.4 The patterning of graphene oxide liquid crystals . . . . .	2
1.1.5 The inside-out supercapacitor: induced charge storage on reduced graphene oxide . . . . .	2
1.1.6 The nanofluidics of shear aligned graphene oxide membranes . . . . .	2
<b>2 Literature and theory</b> . . . . .	<b>4</b>
2.1 Nanofluidics . . . . .	4
2.1.1 The theory of nanofluidics . . . . .	4
2.1.2 Important phenomena in nanofluidics . . . . .	15
2.1.3 Carbon in nanofluidics . . . . .	20
2.1.4 Nanofluidics in this thesis . . . . .	21
2.2 Graphene, graphene oxide and reduced graphene oxide . . . . .	22
2.2.1 Graphene oxide films . . . . .	23
2.2.2 Graphene oxide liquid crystals . . . . .	25
2.2.3 Graphene oxide in nanofluidics . . . . .	26
2.2.4 Graphene oxide in this thesis . . . . .	26
<b>3 Experimental Methodologies</b> . . . . .	<b>27</b>
3.1 Graphene oxide synthesis and concentration . . . . .	27
3.2 Film formation and characterization . . . . .	29

3.2.1	Xurography patterning . . . . .	30
3.2.2	Electron microscopy . . . . .	30
3.2.3	Profilometry . . . . .	31
3.2.4	Four point probe . . . . .	32
3.2.5	Polarized light studies . . . . .	32
3.3	Ion transport studies . . . . .	34
3.4	Electrochemical techniques . . . . .	36
3.5	State of the art nanofluidic fabrication . . . . .	38
3.6	Use of the experimental techniques in this thesis . . . . .	39
<b>4</b>	<b>Graphene based ion rectifier using macroscale geometric asymmetry . . . . .</b>	<b>40</b>
4.1	Introduction . . . . .	40
4.2	Publication: Graphene based ion rectifier using macroscale geometric asymmetry . . . . .	40
<b>5</b>	<b>The patterning of graphene oxide liquid crystals . . . . .</b>	<b>49</b>
5.1	Introduction . . . . .	49
5.2	Experimental methods . . . . .	51
5.2.1	Fabrication of patterns . . . . .	51
5.2.2	Film characterization techniques . . . . .	52
5.2.3	Nanofluidic demonstration . . . . .	53
5.3	Results . . . . .	56
5.3.1	Shape and fidelity of resultant patterns . . . . .	56
5.3.2	Surface roughness and film order . . . . .	59
5.3.3	Nanofluidic results . . . . .	62
5.4	Discussion . . . . .	64
5.5	Conclusion . . . . .	68
<b>6</b>	<b>The inside out supercapacitor: induced charge storage in reduced graphene oxide . . . . .</b>	<b>69</b>
6.1	Introduction . . . . .	69
6.2	Publication: The inside-out supercapacitor: induced charge storage in reduced graphene oxide . . . . .	69
<b>7</b>	<b>The nanofluidics of shear aligned graphene oxide membranes . . . . .</b>	<b>77</b>
7.1	Introduction . . . . .	77
7.2	Experimental methods . . . . .	80
7.2.1	Experimental setup for membrane studies at ENS . . . . .	80
7.2.2	COMSOL modelling of GO at equilibrium . . . . .	81
7.3	Results . . . . .	84
7.3.1	Experimental results . . . . .	84
7.3.2	Simulation results . . . . .	88
7.4	Discussion . . . . .	93
7.5	Conclusion . . . . .	102

<b>8 Conclusion</b> . . . . .	<b>103</b>
8.1 Outcomes from this work . . . . .	103
8.2 Future outlook . . . . .	105
<b>Bibliography</b> . . . . .	<b>107</b>
<b>MicroTAS 2015 Conference paper</b> . . . . .	<b>124</b>
<b>Electronic supporting information for PCCP publication the inside out supercapacitor: induced charge storage on reduced graphene oxide</b> . . .	<b>128</b>

# List of Figures

2.1	The concentration profiles of monovalent cations and anions with a bulk concentration of $10\text{ mM}$ as a function of the distance from an interface with a surface potential of $50\text{ mV}$ . The Debye length in this case is $3\text{ nm}$ . . . . .	12
2.2	The molecular dilution is the average molecular separation normalized by the Bjerrum length. Here a monovalent solution of ions was considered at $25^\circ\text{C}$ . . . . .	14
2.3	An idealized graph of the three regions of concentration polarization effects on a membrane or nanochannel. Region 1 is ohmic and linear which after a certain potential gives way to region 2 where the current roughly plateaus to the limiting current due to concentration polarization. Region 3 is the overlimiting current region where linear behaviour is somewhat restored due to a variety of effects. . . . .	19
2.4	The interaction energy densities of the two dominant interparticular forces; double layer repulsion and the attractive van der Waals force, of which the van der Waals has the longer range. This was calculated for a pair of graphite sheets (Hamaker constant was $\sim 10^{-19}$ [1]) with a monovalent aqueous electrolyte concentration of $0.1\text{ M}$ at room temperature. . . . .	24
2.5	A scanning electron micrograph of a cross section of an RGO film made via vacuum filtration . . . . .	25
3.1	a) A film being formed by vacuum filtration is prepared by using negative pressure to pull solvent through a support membrane, on which the graphene oxide flakes collect, b) a shear-aligned film of graphene oxide prepared by sweeping a doctor blade across a substrate. . . . .	29
3.2	At the top of this image a vinyl pattern has been prepared by the cutter. The offcuts have been removed using a weeding tool and the vinyl is still on its backing. In the middle the pattern is being transferred using adhesive tape to hold the pattern in shape. At the bottom the vinyl has been adhered to a glass microscope slide ready for being used as a mould for a shear-aligned graphene oxide pattern. . . . .	30
3.3	This cross sectional image of a GO film has the typical layered microstructure observed in this material. As GO is not very conductive charging is also evident on the surface on the bottom. . . . .	31

3.4	A slow axis alignment image of a shear-cast graphene oxide film. The edge of the film is visible on the right. The slow axis scale is the angle of the azimuth from the x-axis. . . . .	33
3.5	The basic setup for conducting ion current measurements in a sensitive system	34
3.6	With the addition of a relay switch more samples could be handled simultaneously. While the relay switch does increase the impedance of the circuit the relative difference is negligible as the sample impedance is simply so high.	34
3.7	Two distinct gradients are observable here which was first incorrectly interpreted as some sort of potential dependent gating or switching present in the GO. However it was in fact found to be an artefact of the measuring equipment when current measurement ranges were swapped. Following this further study of the measuring equipment and development of our own Labview program to control the SMU was necessary. . . . .	35
3.8	a) The Randles circuit is an equivalent circuit model of an electrochemical interface such as where the electrolyte meets the electrode. $W$ on the schematic refers to the Warburg impedance. b) The Nyquist plot of a Randles circuit plots the real impedance ( $Z_{re}$ ) against the imaginary impedance ( $Z_{im}$ ) which gives a visualization of how the impedance changes with frequency. At high frequencies the impedance of the system approaches $R_{sol}$ , the lower frequencies are dominated by the Warburg element indicated by the $45^\circ$ slope of the line at high values of $Z_{re}$ . . . . .	37
5.1	Fabrication procedure for making a patterned film and then a PDMS based device. 1) A vinyl mould is cut using a plotter cutter, 2) The vinyl is adhered to a glass substrate, 3) GO is spread over the vacancy in the mould and is sheared using a doctor blade, 4) PDMS is cast over the device and quickly set at $150^\circ\text{C}$ , 5) The ends of the film are opened with a mechanical blade, 6) Reservoirs are bonded on top of exposed ends and are filled with electrolyte.	51
5.2	Binary image analysis conversion of a) an 0.8 mm square, b) 1.5 mm square, c) a 10 mm circle with a tearing defect and d) a pristine 10 mm circle, please note that analysis considered only continuous bodies over a certain area threshold so that blotches such as those present in c) and d) were not analyzed by the software. . . . .	52
5.3	The conductance of a series of devices, sealed using vinyl (labelled) or PDMS (curing temperature listed) was monitored for 20 hours in 1 mM NaCl electrolyte. The $25^\circ\text{C}$ sample had an average conductance of 9 nS. . . . .	54
5.4	a) A PDMS based device which measures 14 mm long, b) a typical rectifier sealed in vinyl with a fine $200\ \mu\text{m}$ tip, $\sim 2\ \text{mm}$ of tip are what remains of a longer sacrificial thin film that is washed off after the relevant parts of the rectifier are protected by the vinyl. . . . .	55

5.5	a) Profile of interdigitated fingers which have burring present on their edges, the inset shows a photograph of the interdigitated structure. Micrographs of film extremities in two cases; low in-mould drying time, (b)) and high in-mould drying time (c)) which lead to different defects at the film edges. Optical profilometry indicates that whilst the centre of the films doesn't seem to change as a function of the mould removal time the edges do- the two samples had their moulds removed at 2 (d) and 5 (e) minutes respectively.	56
5.6	a) Photograph of a vinyl mould and an example of a resultant GO patterned film (the squares and circles that were tested and studied had critical dimensions (diameters or lengths) of 0.8 mm, 1.5 mm, 3 mm, 5 mm and 10 mm), b) a comparison of area difference between that of the cast object and that of the mould (normalized by the mould area for all data in these figures) for 10 mm features, c) the same comparison plotted for 0.8 mm features and d) normalized area difference for various sized features. . . . .	58
5.7	a) A sample still in its mould is placed in a shallow water bath, b) after a while the water infiltrates the film and causes it to expand and debond from the substrate and float free in the water. . . . .	59
5.8	a) Rq, the RMS surface roughness for 3 mm circular GO film plotted against a) in-mould drying time, b) blade height of the doctor blade, c) casting speed.	60
5.9	a) A profile of a sample with low in-mould drying time, b) a falsely coloured slow axis image of the edge of a low in-mould drying time sample, c) an SEM of a low in-mould drying time sample illustrates the spreading of the edge and the absence of any wall structure, d) a profile of a high in-mould drying time sample shows the characteristic spike of a tall thin structure at the film's edge, e) a falsely coloured slow axis image of the edge of a high in-mould drying time sample shows a uniquely aligned thin structure at the films edge and significant in-plane order in the film structure nearby, f) an SEM of a high in-mould drying time sample with the wall structure in view.	61
5.10	a) Heights of samples plotted against the number of castings performed, b) a schematic of the GO film in its mould and the regions of molecular order c) a tilted image of a single casting sample's wall structure d) the wall of an eight casting thick sample illustrating how multiple layers combine to thicken the wall structure, which in this particular case is around 5 μm thick	61
5.11	a) A slow axis image of a 100 μm wide digit, b) a slow axis image of a 200 μm wide digit (edge opposing edge just out of view), c) a slow axis image of a 600 μm wide digit and d) a slow axis image of a 1 mm wide digit . . . . .	62
5.12	The conductance of the two sets of devices of different thickness. The electrolyte in both cases was KCl. Error bars here are one S.D. . . . .	63

5.13	Fabrication procedure for producing a patterned film and then incorporation into a lab-on-a-chip style device. 1. A vinyl mould is cut using a plotter cutter, 2. The vinyl is adhered to a glass substrate, 3. GO is spread over the vacancy in the mould and is sheared using a doctor blade, 4. A double adhesive sided vinyl is then cut to make the microchannels that interface with the sample, 5. The vinyl is adhered to a plasma exposed polydimethylsiloxane lid, 6. The sealed channels and their lid are aligned and placed onto the film sample sealing the system, which can then have ports cut and tubing inserted in the usual manner. . . . .	65
5.14	The conductance of the two sets of devices of different thickness. The electrolyte in both cases was KCl. Error bars here are one S.D. . . . .	66
7.1	Two different experimental setups for investigating 2D nanochannels. a) The 'planar' case typically has the ion transport parallel to the substrate supporting the 2D film structure. b) The transverse/u-tube type experiment has the disadvantage of having the 2D sheets perpendicular to the direction of transport. . . . .	78
7.2	The ion current measurement cell design used in these experiments. The Ag/AgCl electrodes are depicted in red, one was a mesh electrode placed in close contact with the membrane's porous support, the other was placed near the GO surface in the electrolyte. . . . .	80
7.3	A data sample from a typical experiment. The current data is depicted in black and relaxes from an initially high value to a more stable one over the course of 10s of seconds. The applied voltage is depicted in red with the two important parameters; the wait time $t_{wait}$ and the voltage step size $V_{step}$ depicted. . . . .	81
7.4	A schematic of the COMSOL model with parameters and boundaries marked.	83
7.5	The conductance is plotted against the concentration for the two pHs considered. . . . .	84
7.6	Streaming current densities at various applied pressures and concentrations for a) pH 10 and b) pH 4. . . . .	85
7.7	I/V curves for GO generally have an unusual hysteresis. The data is for pH 4 with a concentration of 10 mM of KCl. . . . .	86
7.8	Increasing the wait time did cause the hysteresis to reduce however the conductance of the membrane also decreased. . . . .	87
7.9	The conductance (a) and the capacitance (b) of the GO membrane at various scan rates for an aqueous electrolyte and a 5% ethanol electrolyte. . . . .	88
7.10	It was found for both cases that the conductance of the GO membrane was proportional to its calculated capacitance. . . . .	89
7.11	An oscillating pressure signal applied to the membrane results in an oscillating streaming current. . . . .	90

7.12	Concentration gradient driven currents for pH 10 and 4 under a concentration ratio of 1000. A small I/V is applied to help measure the conductance of the GO nanochannels. . . . .	90
7.13	a) The potentials for 3 different surface charges on GO at $pH_i = pKa_i$ , b) the surface potentials calculated using the model match the expected surface potentials calculated from the Grahame equation. . . . .	91
7.14	The pH as a function of the distance from the centreline between the two GO sheets. The GO sheets are separated by 200 nm in a 15 mM background electrolyte. . . . .	91
7.15	The surface charge density for GO is plotted here against pH. Equilibrium data are calculated using the equilibrium equations with no coupling to any model/geometry, Gudarzi's data are calculated from zeta potential measurements in 15 mM KCl background electrolyte, Konkana's data are calculated using charge titration results and by assuming a GO surface area of 1800 m <sup>2</sup> /g, the full PNP model was also solved for two interstitial distances; 1.4 nm and 200 nm. . . . .	92
7.16	The ionic conductivities of the pH 10 data and Guo's [2] are compared. The graphene hydrogel membrane is significantly more conductive than the GO. . . . .	94
7.17	The bulk concentration of KCl was modified showing the effect of H <sup>+</sup> on the surface charge density for a range of pHs. . . . .	96
7.18	The motivating picture for the hysteresis observed in GO. There are two mechanism - resistive like ionic conduction and capacitive behaviour due to an expected large dielectric constant of water. . . . .	97
7.19	A comparison of SPICE simulation data with experimentally collected data from a GO membrane for a) conductance and b) capacitance as a function of the wait time. The value of $R$ is 50 k $\Omega$ and the value of $C$ is 5 mF. The potential applied in all cases was the same. . . . .	98
7.20	This figure is a recreation of figure 1 in [3], it describes a membrane with infinitely thin electric double layers and diffuse boundary layers of thickness $\delta^I$ and $\delta^{II}$ . . . . .	99
7.21	This data is a snippet of data collected from a GO membrane at a concentration of 10 mM at pH 4. At this point in the experiment the membrane is already perturbed from equilibrium. . . . .	100
7.22	A comparison of the I/V data of the two different geometries illustrated in figure 7.1. a) The current-time and voltage-time data for a GO SAM membrane with a concentration of 1 mM KCl with a pH of 10, b) The current-time and voltage-time data for a planar device described in chapter 5 at a concentration of 1 mM with a pH of $\sim 6$ . . . . .	101

# List of Tables

2.1	The nanofluidic parameters and their equivalent condensed matter terms show the similarity between the two sets of physics. . . . .	20
7.1	The 3 equilibrium reactions proposed by Konkena [4] which form the basis for GO's surface charge. The * denotes carboxyl groups stabilized by near by hydroxyl groups near the edge of the GO sheet. . . . .	82
7.2	The boundary conditions for the PNP equations solved using the COMSOL model described in this section. . . . .	83
7.3	The values of various parameters used in the COMSOL modelling performed here. . . . .	83
7.4	A comparison of power law exponents measured experimentally and those calculated using the charge regulated COMSOL model described here. The * is a result extrapolated from the simulation data. . . . .	96

# Chapter 1

## Introduction

### 1.1 Overview of chapters

This thesis has two literature based chapters, which summarize the literature and existing research to give the reader a background into nanofluidics and GO (graphene oxide), as well as the experimental techniques used to perform the work in this thesis. The four research projects that follow (chapters 4-7) were performed over the course of this thesis and develop a picture of how GO can be understood and used for various applications in nanofluidics and other soft matter sciences.

#### 1.1.1 Literature and theory

In the first chapter the theory of PNP (Poisson, Nernst Planck) based nanofluidics is outlined. The notions of the electric double layer, Donnan equilibrium and various length scales are derived and explained. Literature based on nanofluidic phenomena such as rectification, concentration polarization and surface charge governed conduction is discussed. The role carbon plays in nanofluidics is highlighted and then graphene as a material is introduced. The difference between graphene and its derivatives - GO and reduced GO is clarified and finally the limited literature on GO in the field of nanofluidics is examined, which lays out the background to the investigations that follow.

#### 1.1.2 Experimental methodologies

Here the various methodologies and experimental techniques are examined. A description of the synthesis and concentration of GO is given. The methods for how films of GO were produced for this work are then described. Techniques used for characterization are then discussed including electron microscopy, profilometry, 4-point probe and polarized light microscopy. Finally the details behind the ion transport studies and the electrochemical techniques used are explained.

### **1.1.3 Graphene based ion rectifier using macroscale geometric asymmetry**

In the first research chapter investigations of ion transport in GO films lead to a study of how the film geometry might affect the ion transport. By embedding films of GO in an impermeable polymer and opening access points to the film, one can then hydrate the GO and study ion transport between the two openings. Our findings demonstrate that for trapezoidal films an ionic rectifier is made and is a consequence of the film's geometric asymmetry. A model motivating its existence is also proposed. This work was published in APL Materials in 2014 and shows the ease at which one can use GO to access nanofluidic effects.

### **1.1.4 The patterning of graphene oxide liquid crystals**

Being able to pattern and control the shape of GO films became increasingly important after the initial rectification findings. Controllably patterning a film sample over a substrate has potential application as a form of iontronic circuit or as electrodes for sensing. Here a mould made using a vinyl cutter masks a glass substrate and nematic phase GO is cast on top. Once the vinyl is removed the negative of the vinyl mask is patterned in GO. The resultant pattern fidelities, thicknesses and roughnesses are characterized and edge phenomena are examined using polarized light microscopy. Ion transport studies were performed on sample devices demonstrating surface charge governed conduction. This technique enabled rapid fabrication of planar style nanofluidic devices without the need for cleanroom fabrication tools.

### **1.1.5 The inside-out supercapacitor: induced charge storage on reduced graphene oxide**

Observations made in the initial rectifier work lead to the development of an ionic supercapacitor, which is the focus of this chapter. This concept is yet to be discussed in the paradigm of iontronic components and this work opens this discussion, which will allow future iontronic circuit designs to incorporate it. The inside-out supercapacitor has its method of fabrication outlined and undergoes an extensive study to demonstrate and understand how this system stores charge and how it is equivalent to the electrical supercapacitor. Finally a demonstration of this capacitor filtering various signals in an electrolyte illustrates its potential in iontronics. This work was published in Physical Chemistry Chemical Physics in 2016 and highlights an intriguing connection between conventional capacitors, ion transport and iontronics.

### **1.1.6 The nanofluidics of shear aligned graphene oxide membranes**

By way of collaboration with a leading research group in France, a study on shear aligned GO membranes was performed. While so far studies in this thesis have centred on a planar device being used for nanofluidic/electrochemical experiments a thin shear aligned graphene layer on a highly porous membrane support is investigated. This membrane

has proven to be an excellent for nanofiltration but the underlying mechanisms of how it works remains unclear. This transverse system underwent a comprehensive electrokinetic investigation which yielded a number of interesting conclusions- such as the role proton conduction in these films, the anomalously low surface charge of this structure and, again, an unusual hysteresis which is related to concentration polarization in ionically selective membranes.

## Chapter 2

# Literature and theory

### 2.1 Nanofluidics

At the beginning of previous decade, just before the rise of graphene as research topic, the concept of nanofluidics entered the literature [5]. In this particular form nanofluidics began its roots as a extension of microfluidics and like most nanosciences succeeded due to improvements in and availabilities of electron microscopy, scanning probe technologies like atomic force microscopy (AFM) and improvements in lithographic techniques however experts [5, 6] in the field are quick to highlight the fact that some of the breakthrough discoveries [7, 8] are in fact well known colloidal phenomena long since described. Particular examples include Donnan equilibrium [9] and semi-permeability. Furthermore while this word 'nanofluidics' is new to the literature, many scientists have been studying 'nanofluidics' for decades without calling it by this particular title. An explicit example of this is the development of what would now be termed a nanofluidic transistor developed in 1992 by Gajar et al. [10]. The first experimentally reported [11] slip of a fluid against an interface [12] was in 1952 and the topic of slip is now of intense interest in the nanofluidic community.

So what is this curious science that has been studied without a name for such a long time? Nanofluidics is probably best described as the 'study of fluidic transport at nanometer scales' [6] and is as an amalgam of existing areas of research which include hydrodynamics, thermodynamics, statistical physics, surface sciences, colloidal sciences, microbiology, separation science and micro/nano-fabrication. In this thesis the nanoscopic interlayer distance between sheets of graphene oxide is used to confine fluids for further study.

#### 2.1.1 The theory of nanofluidics

The phenomena observed in nanofluidics are frequently of an apparent electrostatic nature. The presence and actions of charged particles within a solvent dominate its behaviour at these small length scales. While the fluid itself can be acted upon in a conventional sense (with for instance a pressure gradient) the electrical body force term in the Navier-Stokes equations plays an important role in nanofluidics. In this picture there is a confined solvent

and solute, typically some charged ions. The ions are moved by three 'forces' - the force of the electric field, convection due to the movement of the solvent and diffusion. The electric field itself is defined by where the charged particles are located, so it is coupled to the motion of the ions. With the introduction of the electric body force term to the Navier-Stokes equation the movement of the solvent is also strongly coupled to the motion of the ions. In the continuum picture of nanofluidics the transport of ions and fluids is described by three equations- the Poisson equation, the Nernst-Planck equation and the Navier-Stokes equation. As nanofluidics describes almost without exception flows with very low velocities (and low Reynolds numbers) the Stokes equation is typically used rather than Navier-Stokes. This set of equations is used in other fields- such as electrochemistry, electrokinetics, colloidal sciences and electrophysiology as they all concern themselves with the motion of ions in a fluid.

These equations will be detailed in the following sections and their relevant terms discussed. For the moment however, the applicability of these equations to nanofluidics will be considered. There are some important limitations to the application of these equations. For instance, is the solvent considered continuous or is it so discrete that Navier-Stokes isn't valid for extreme confinements (for example inside the interior of a 2 nm carbon nanotube)? Remarkably Navier-Stokes is still valid for confinement on the order of  $\sim 1nm$  [6,13]. This is particularly striking as on the order of this confinement in graphene water is expected to be found in discrete layers [14]. While the Navier-Stokes equation describes the flow and pressure of the fluid well enough at the nanoscale, the description of the electric field is more problematic. In its standard treatment the Poisson equation which describes the electric field is combined with elements of Boltzmann statistics to give the Poisson-Boltzmann equation. This equation rests on some assumptions (such as the mean field approximation of the interaction between ions, the lack of other forms of interaction etc) that limit the applicability of the equation to modest applied potentials and concentrations. These limitations are frequently ignored in the literature as the description given by these equations remains relatively well behaved if handled carefully [15]. Luckily when we begin to include additional effects, they often tend to counteract each other and roughly cancel out. For instance these equations assume that the permittivity is constant throughout the fluid which isn't correct close to an interface where the ion concentration can be very high but if we also include the fact that the ions aren't point charges this limits the concentration at the interface due to steric effects and ion-ion repulsion and the two effects approximately counteract each other [16]. So the description that follows is by no means perfect and is only an approximation, however these equations have proven to be highly capable of explaining most of the observed phenomena in the literature.

### Electrostatics

The classical description of how electric and magnetic fields behave is given by Maxwell's equations-

$$\nabla \cdot \mathbf{E} = \frac{1}{\epsilon_0} \rho, \quad (2.1)$$

$$\nabla \cdot \mathbf{B} = 0, \quad (2.2)$$

$$\nabla \times \mathbf{E} = -\frac{\partial \mathbf{B}}{\partial t}, \quad (2.3)$$

and

$$\nabla \times \mathbf{B} = \mu_0 \mathbf{J} + \vartheta_0 \epsilon_0 \frac{\partial \mathbf{E}}{\partial t} \quad (2.4)$$

where  $\mathbf{E}$  is the electric field,  $\epsilon_0$  is the permittivity of free space,  $\rho$  is the spatial charge density,  $\mathbf{B}$  is the magnetic field,  $\vartheta_0$  is the permeability of free space and  $\mathbf{J}$  is the current density. Here the use of  $\mu$  for the permittivity has been avoided as it will cause some confusion later on when it is used for mobility. Together with the Lorentz force law

$$\mathbf{F} = q(\mathbf{E} + v \times \mathbf{B}), \quad (2.5)$$

which describes how these fields act on a particle travelling with velocity  $v$ , these equations give a comprehensive picture of how, classically, electrodynamics works. When working with ions travelling in fluids their velocity is always quite small (at most mm/s). So the contribution to the Lorentz force from the magnetic field is considered negligible. Typically these research areas concern themselves with electrostatics where the equations above simplify greatly into just equation 2.1 known as Gauss' law. Knowing that  $-\nabla\phi = \mathbf{E}$  (where  $\phi$  is the field's potential) and combining it with equation 2.1 we arrive what is referred to as the Poisson equation

$$\nabla^2 \phi = -\frac{1}{\epsilon} \rho. \quad (2.6)$$

Note here that  $\epsilon_0$  has change to simply  $\epsilon$  as these equations will be used in a dielectric medium other than a vacuum. With this equation we are able to relate the potential (and thus the electric field) at any point to the arrangement of charge (the ions & surface charges) within the space we're examining. The Poisson equation describes electrostatics in general, when a description for the volumetric charge density as a function of the concentration is developed, the two equations can be combined to give the Poisson-Boltzmann equation.

### Ion motion

There are three basic processes by which ions move around inside a solvent. Firstly there is diffusion which can be described by Fick's law

$$\mathbf{J}_{Diff,i} = -D_i \nabla C_i, \quad (2.7)$$

where  $J_{Diff}$  is the molar flux of ions,  $D$  is the coefficient of diffusivity and  $C$  is the concentration of the ions. This flux is due to the Brownian motion of the ions due to thermal excitation or a difference in chemical potential. Increasing the temperature will result in an increase in the coefficient of diffusivity and as a result a larger flux.

When an electric field is applied to the solution the ions move via a process referred to as electrophoresis.

$$\mathbf{u}_{E,i} = \mu_i \mathbf{E} \quad (2.8)$$

where  $\mathbf{u}_{E,i}$  is the velocity of the ion and  $\mu_i$  is a quantity known as the electrophoretic mobility. Electrophoresis is often used interchangeably with the terms electromigration or drift for ions [16]. Some authors [17] create a distinction between the motion of a charged microparticle moving due to the presence of an electric field, calling it electrophoresis and the motion of a much smaller charged object, such as an ion, calling it electromigration. Nevertheless when reporting a mobility of an ion in the literature, it is invariably referred to as an electrophoretic mobility. This thesis doesn't really concern itself with the motion of microparticles so it will refer to these processes using one general term; electrophoresis.

Ions can additionally be convected by solvent flow. The resultant ion velocity being simply the sum of the electrophoretic contribution and the velocity of the solvent-

$$\mathbf{u}_i = \mathbf{u}_{E,i} + \mathbf{u}_{solvent}. \quad (2.9)$$

The molar flux due to these contributions is given by

$$\mathbf{J}_i = \mathbf{u}_i C_i. \quad (2.10)$$

Combining our fluxes and inserting them into the continuity equation gives us the Nernst-Planck equation-

$$\frac{\partial C_i}{\partial t} = -\nabla \cdot (\mathbf{J}_{Diff,i} + \mathbf{J}_i), \quad (2.11)$$

$$\frac{\partial C_i}{\partial t} = -\nabla \cdot (-D_i \nabla C_i + \mu_i C_i \mathbf{E} + C_i \mathbf{u}_{solvent}). \quad (2.12)$$

For cases in this thesis however this equation can be simplified by assuming that there is no solvent flow. Thus the total flux is given by

$$\mathbf{J}_i = -D_i \nabla C_i + \mu_i C_i \mathbf{E}. \quad (2.13)$$

Replacing the electric field with its potential  $\phi$  the equation takes the form

$$\mathbf{J}_i = -(D_i \nabla C_i + \mu_i C_i \nabla \phi). \quad (2.14)$$

So ignoring motion of the solvent, we have a description of how the electric field is defined by the ions (the Poisson equation (2.6)) and coupled to it how the electric field and diffusion move the ions (the Nernst-Planck equation (2.14)).

It is worth drawing attention to the fact that using some simple assumptions we can show that these equations lead to electrical circuit like behaviour when looking at ion transport through a membrane. Entrance and exit effects of the membrane aren't considered in this derivation. Firstly we simplify equation 2.14 to a 1-D equation, ie

$$J_i = -(D_i \frac{dC_i}{dx} + \mu_i C_i \frac{d\phi}{dx}). \quad (2.15)$$

The Nernst-Einstein equation describes the relationship between how ions behave in concentration (chemical potential) gradients and how they behave in electrostatic gradients

$$\frac{D_i}{RT} = \frac{\mu_i}{z_i F} \quad (2.16)$$

where  $R$  is the ideal gas constant,  $T$  is the temperature,  $z_i$  is the valence of the ion and  $F$  is Faraday's constant. Substituting this in we find

$$J_i = -\frac{\mu_i C_i}{z_i F} \left( RT \frac{d(\ln(C_i))}{dx} + z_i F \frac{d\phi}{dx} \right). \quad (2.17)$$

Since we are looking for electrical circuit like behaviour we'll convert the ion flux to electrical current by multiplying by  $z_i F A$ , where  $A$  is the cross sectional area of the membrane pore.

$$I_i = -\mu_i C_i A \left( RT \frac{d(\ln(C_i))}{dx} + z_i F \frac{d\phi}{dx} \right) \quad (2.18)$$

Now if we assume this transport is in steady state and that the reservoirs either side of the membrane are large then  $\frac{\partial C_i}{\partial t} = 0$ . It follows from the continuity equation that if  $\frac{\partial C_i}{\partial t} = 0$  then  $-\nabla J_i = 0$ . Which means that our current density is constant regardless of our position in  $x$ . We can now integrate across the thickness of our membrane (assigning the membrane a thickness of  $d$ )

$$I_i \int_0^d \frac{dx}{-\mu_i z_i F A C_i} = \frac{RT}{z_i F} \int_0^d \frac{d(\ln(C_i))}{dx} dx + \int_0^d \frac{d\phi}{dx} dx \quad (2.19)$$

which gives us

$$I_i \int_0^d \frac{dx}{-\mu_i z_i F A C_i} = \frac{RT}{z_i F} \ln\left(\frac{C_i(d)}{C_i(0)}\right) + \phi(d) - \phi(0). \quad (2.20)$$

So we have a current, the remaining integral has the units of resistance, the equilibrium potential across the membrane given by the Nernst equation and the applied potential, ie

$$I_i R = E_i + \Delta V_i \quad (2.21)$$

which is essentially Ohm's law for a membrane. While simplistic this clearly illustrates the electric-circuit like nature of this hypothetical membrane pore. However this result is true for this arbitrary membrane with these particular properties and doesn't really describe a system that is in fact nanofluidic. What is also perhaps surprising is the appearance of the Nernst equation term in equation 2.20, within the context of membrane equilibrium this term is referred to as the membrane potential, which will be addressed in further detail later (see section 2.1.1), additionally Schoch [18] provides an excellent description of the equilibrium potentials of nanochannels. This mean field, continuum approach describes nanofluidics rather well, which is surprising as confinement in these systems can get to fundamental levels. The space occupied by water between sheets of graphene oxide is only a couple of layers of water molecules thick and yet a continuum approach still describes some of the phenomena observed [14, 19].

### Solvent flow in nanofluidics

Work in nanofluidics is almost exclusively conducted in aqueous media so more often than not the solvent is water. The flow of water is typically described by the incompressible Navier Stokes equations-

$$\frac{\partial \mathbf{u}}{\partial t} + (\mathbf{u} \cdot \nabla) \mathbf{u} - \nu \nabla^2 \mathbf{u} = \frac{-1}{\rho_f} \nabla p + \mathbf{f} \quad (2.22)$$

where  $\nu$  is the kinematic viscosity,  $\rho_f$  is the density of the fluid and  $\mathbf{f}$  is an additional body force term.  $\mathbf{f}$  in the field of nanofluidics invariably takes the form  $\frac{\rho}{\rho_f} \nabla \phi$ , where  $\rho$  is the charge density of the fluid as before. In these highly confined environments the Reynolds number is almost without exception very small so the Stokes equations are used to describe the behaviour of the fluid

$$\frac{1}{\rho_f} \nabla p = \nu \nabla^2 \mathbf{u} + \frac{\rho}{\rho_f} \nabla \phi. \quad (2.23)$$

There are two distinct areas of interest in the literature when it comes to solvent flow in highly confined systems. The first is enhanced flux due to hydrodynamic slip of the solvent against the walls of the channel [20]. This is particularly of interest in the study of carbon nanotubes [21–24] where large flux enhancements have been reported. Within the context of the Navier-Stokes equations this is treated as the ‘slip boundary condition’

$$\mathbf{u} = \beta \frac{\partial \mathbf{u}}{\partial n} \quad (2.24)$$

where  $n$  is the coordinate normal to the wall and  $\beta$  is the slip length. Typical slip lengths for hydrophobic systems are on the order of nanometers [25, 26].

The second area is due to the coupling of the solvent transport equations with the ion-interface behaviour. While not as pronounced as the slip in carbon nanotubes this coupling gives rise to a series of interesting behaviours where solvent flow can be created in response to a gradient of electric potential (electroosmosis), concentration (diffusioosmosis) and even temperature (thermoosmosis) [27–30]. In order to tackle these phenomena, particularly electroosmosis, it is necessary to first discuss the electric double layer.

### The electric double layer

Now that the foundations of how ions move with respect to fields has been discussed the effect of confinement needs to be attended to. It is quite common for the wall of a nanochannel to have some non-zero charge. This is often due to the presence of functional groups or adsorbed molecules [31]. Ions of opposing charge migrate towards the wall whilst co-ions are repelled. This leads to the establishment of what is referred to as the electric double layer (or here it will just be referred to as the double layer). The double layer has two parts- the ions that are specifically adsorbed to the surface and the surface itself, which is called the Stern layer and the diffuse ions that cloud the area around this charged surface, which is referred to as the diffuse layer. The double layer cannot arise from purely Coloumbic attraction and repulsion, in the double layer’s simplest form this force is

balanced by the Brownian motion of the ions which gives the diffuse layer of the double layer its distinctive exponential like decay [16]. In more complex and realistic models factors like ion-ion repulsion and steric hindrance are also considered but the overall important qualitative behaviour is well described by the model that is to be presented here.

This derivation is based off Kirby's book [16] and is a simple mathematical description of the double layer, as it will prove instructive to the phenomena described in later sections and all research chapters. From arguments in Boltzmann statistics and by making the following assumptions- that the ions are treated using the point-charge approximation, that they don't interact with each other and are located in a solvent which has a mean field which governs the interactions of the ions, the concentration  $C_i$  is given by

$$C_i = C_{i,\infty} \exp\left(-\frac{z_i F \phi}{RT}\right). \quad (2.25)$$

where the  $\infty$  subscript refers to the state far from the interface and in the bulk of the solution, we also assume that in the bulk of the solution, the potential is 0. This equation can be summed over and multiplied by  $z_i F$  to give us an equation for the charge density

$$\rho = \sum_i z_i F C_{i,\infty} \exp\left(-\frac{z_i F \phi}{RT}\right), \quad (2.26)$$

This equation we can simply substitute into Poisson's equation (equation 2.6) to derive the Poisson-Boltzmann equation:

$$\nabla^2 \phi = -\frac{1}{\epsilon_0} \sum_i z_i F C_{i,\infty} \exp\left(-\frac{z_i F \phi}{RT}\right). \quad (2.27)$$

To solve this equation for a binary electrolyte Kirby [16] normalizes the potential with respect to what is referred to as the thermal voltage

$$\hat{\phi} = \frac{F \phi}{RT} \quad (2.28)$$

and the lengths by the Debye length

$$\lambda_d = \sqrt{\frac{\epsilon RT}{2F^2 I_c}} \quad (2.29)$$

where  $I_c$  is the ionic strength of the electrolyte which is given by

$$I_c = \frac{1}{2} \sum_i C_i z_i^2. \quad (2.30)$$

The Debye length is the first length scale given here and describes the length over which an electrostatic force decays by  $\frac{1}{e}$  due to charge screening. It's used ubiquitously (and sometimes incorrectly, as mentioned in [6]) throughout the literature to describe the range of nanofluidic effects. The Debye length is often used to provide a length scale of a double layer, which is due to the Debye-Hückel approximation of the double layer.

For a symmetric, monovalent electrolyte (such as KCl) the nondimensionalized 1D form of the Poisson-Boltzmann equation looks like

$$\frac{\partial^2 \hat{\phi}}{\partial \hat{x}^2} = \frac{1}{z} \sinh(z\hat{\phi}). \quad (2.31)$$

For small values of  $\hat{\phi}$  this equation can be approximated by the linear Poisson-Boltzmann equation, which is known as the Debye-Hückel approximation

$$\frac{\partial^2 \hat{\phi}}{\partial \hat{x}^2} = \hat{\phi}, \quad (2.32)$$

which for the boundary conditions  $\hat{\phi} = \hat{\phi}_0$  for  $\hat{x} = 0$  and  $\hat{\phi} = 0$  for  $\hat{x} = \infty$  has the following solution

$$\hat{\phi}(\hat{x}) = \hat{\phi}_0 \exp(-\hat{x}) \quad (2.33)$$

or in dimensionalized form

$$\phi(x) = \phi_0 \exp\left(-\frac{x}{\lambda_D}\right) \quad (2.34)$$

Now that the potential is known, the concentration distribution can be found-

$$C_i = C_{i,\infty} \exp\left(\frac{-z_i F \phi_0}{RT} \exp\left(-\frac{x}{\lambda_D}\right)\right). \quad (2.35)$$

Despite the simplifications it is important to draw the following key concept from equation 2.35, there is a depletion of ions (of the same charge as the surface) near this boundary. These are referred to as the co-ions. To balance this surface potential there is an enrichment of ions of the opposing charge. These are referred to as the counter-ions. So within a few Debye lengths of this boundary the solution is not electroneutral (an example is plotted in figure 2.1) which leads to a host of effects that have been used in membrane and colloidal sciences and more recently in nanofluidics. This charged layer is sometimes referred to as the Debye layer (which is on the order of a Debye length). For boundaries that are close together, such as in the confines of a parallel pair of graphene oxide sheets or a nanopore in a polymer membrane, the solution looks a little different (and in fact this treatment isn't valid for the extreme confinement of graphene oxide), however importantly the Debye layers from the two GO sheet-electrolyte interfaces are said to overlap. This overlap means that the entire interior of the material is charged (and neutralized by the charge at the interfaces).

The double layer has an effect on the conductivity of the channel which is termed surface conductivity (other appropriate terms follow accordingly - surface conductance, surface current etc.). This contribution is due to the concentration enrichment near the double layer. Additional more complex effects, like electroosmotic flow, contribute to the surface current in various manners.

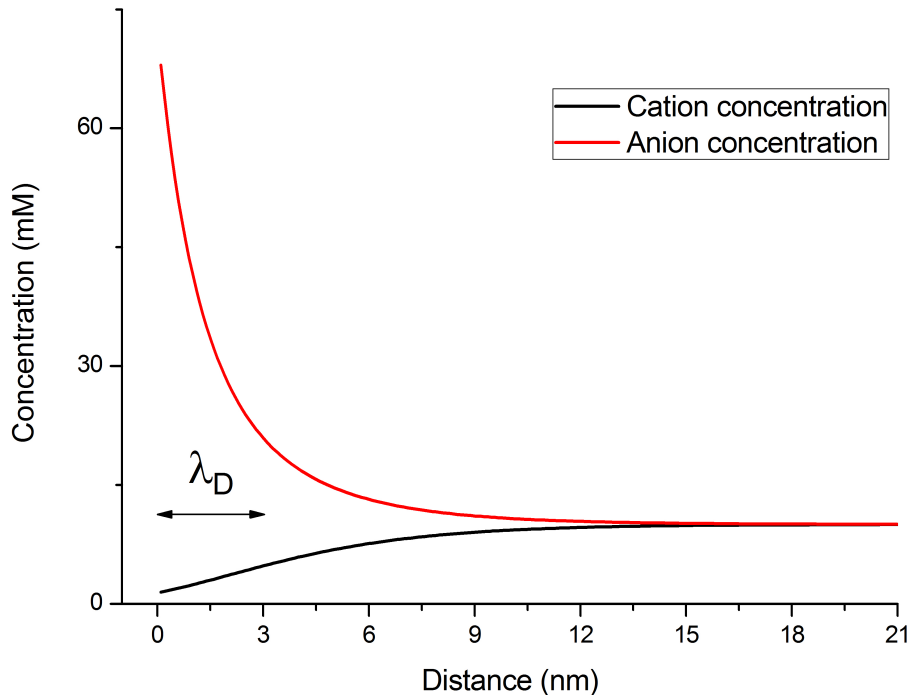


Figure 2.1: The concentration profiles of monovalent cations and anions with a bulk concentration of  $10\text{ mM}$  as a function of the distance from an interface with a surface potential of  $50\text{ mV}$ . The Debye length in this case is  $3\text{ nm}$ .

### Donnan equilibrium

The double layer described above is an equilibrium double layer. There do exist other examples of non-equilibrium double layers which can exhibit different phenomena [32,33]. The equilibrium described is called the Donnan equilibrium [9, 18] which balances the concentration difference of the ions with an electric potential. The Donnan equilibrium is very useful in describing how the concentration and potential differs from the bulk solution (say in a microchannel) and the solution within a nanochannel. The balance is expressed as [18, 34]

$$RT \ln \hat{C}_{i,\infty} + z_i F \phi_\infty = RT \ln \hat{C}_{i,n} + z_i F \phi_n, \quad (2.36)$$

where  $\hat{C}$  is the concentration normalized by  $1\text{ mol/m}^3$  and the  $n$  subscript refers to the solution within a nanochannel. The potential difference between the bulk and the nanochannel interior is known as the Donnan potential ( $\phi_D = \phi_n - \phi_\infty$ ). The Donnan equation can easily be derived from the Nernst Planck equation (equation 2.14) by assuming that equilibrium has been reached. This is the same electrochemical balance found in the Nernst equation, hence their identical nature. By setting the bulk potential to zero one can quickly arrive at equation 2.25. The Donnan equilibrium can give a clear picture of the enriched/depleted concentration present in nanochannels by introduction of the Donnan ratio  $r_D$  [18]. For a symmetric electrolyte of valence 1, the expression is

$$r_D = \left( \frac{C_{i,\infty}}{C_{i,n}} \right)^{\frac{1}{z_i}} = \frac{C_{cat,\infty}}{C_{cat,n}} = \frac{C_{an,n}}{C_{an,\infty}} \quad (2.37)$$

here clearly the sign of the charge is included in  $z_1$  so the expression has the right form. For generality this description will be given in terms of co-ions and counter-ions denoted  $co$  and  $counter$  respectively. From equation 2.37 it is clear that

$$C_{co,\infty}C_{counter,\infty} = C_{co,n}C_{counter,n} \quad (2.38)$$

and with the knowledge that

$$C_{counter,n} = C_\sigma + C_{co,n} \quad (2.39)$$

where  $C_\sigma$  represents the surface charge of the channel averaged over it's volume. The following two equations are formed

$$C_{co,n} = \frac{1}{2}\sqrt{4C_{co,\infty}^2 + C_\sigma^2} - C_\sigma \quad (2.40)$$

and

$$C_{counter,n} = \frac{1}{2}\sqrt{4C_{counter,\infty}^2 + C_\sigma^2} + C_\sigma. \quad (2.41)$$

These two equations show how the surface charge contribution affects the concentration in a nanochannel. This description gives an accurate picture of how concentration differs at the junction of a nanochannel and the bulk but doesn't describe, for instance, the behaviour in the nanochannel when it is exposed to two different solutions at two different electrochemical potentials, like in the case of a nanoporous membrane which spans two reservoirs containing different solutions. In this case the potential across the membrane is the sum of the two Donnan potentials at each junction and what is referred to as the diffusion potential which depends on the permselectivity of the membrane. While the Donnan potential is usually calculated, the membrane potential (the sum of these potentials) is an experimentally measureable quantity.

### Important length scales

In order to look at some other length scales that play important roles in the theory it is necessary to take a step back and define a more basic length scale than the Debye length which is the Bjerrum length. The Bjerrum length is the length where the energy of an electrostatic interaction between two ions is approximately equal to the thermal energy, this is given by

$$l_B = \frac{z^2 e^2}{4\pi\epsilon k_B T}, \quad (2.42)$$

where  $e$  is the elementary unit of charge and  $k_B$  is Boltzmann's constant. Below the Bjerrum length electrostatic interactions dominate thermal effects, however the Bjerrum length is quite small. For  $z = 1$  at  $25^\circ C$  the Bjerrum length in water is a miniscule  $0.7\text{ nm}$ . So when we refer to a dilute limit one measure of this is to compare the mean distance between ions and the Bjerrum length. By this scaling we can see (figure 2.2) that in fact the solution remains 'dilute' until considerable concentrations. Even at 1 M concentrations the average separation is greater than the Bjerrum length, suggesting that ion-ion interactions

remain limited, which supports the assumptions behind the Poisson-Boltzmann description of the electric field.

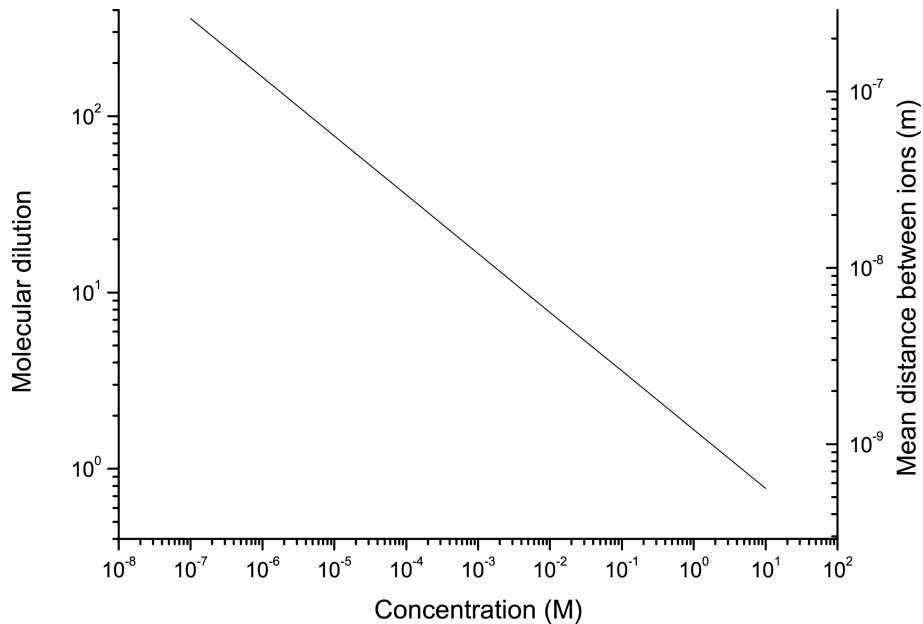


Figure 2.2: The molecular dilution is the average molecular separation normalized by the Bjerrum length. Here a monovalent solution of ions was considered at 25 °C.

We can re-express the Debye length in terms of the Bjerrum length (making comparisons between length scales easier)

$$\lambda_D = \sqrt{\frac{1}{8\pi l_B C_\infty}}, \quad (2.43)$$

in this case as the Bjerrum length is considering ions of the same valency this follows for this definition of the Debye length. Interestingly although the Debye length gives us the length scale of the double layer it itself does not depend on any property of that boundary (neither the surface charge, nor the surface potential). Indeed, although it may seem surprising, it isn't even necessary to have a nonzero surface charge on the surface to give a Debye layer. Other effects like dipoles on the boundary can also result in a double layer being formed in the fluid at equilibrium. In general the Debye length describes the screening length or the distance where the electrostatic free energy of the ion surrounded by counterions is  $k_B T$  [6]. The Gouy-Chapman length, however, describes the length where an ion's electrostatic interaction with the boundary is equal to the thermal energy

$$l_{GC} = \frac{e}{2\pi\sigma l_B} \quad (2.44)$$

where  $\sigma$  is the surface charge density of the boundary. Typical surface charge densities of  $\sim 50 \text{ mC/m}^2$  (as given in [6]) give  $l_{GC} \sim 0.7 \text{ nm}$ , however the surface charge of graphene oxide has been reported to be much lower than that, merely  $0.77 \text{ mC/m}^2$  [35] which gives a much larger value of  $l_{GC} = 47.3 \text{ nm}$ . In dilute solutions, where the Debye length is large, the size of the diffuse layer is described by the Guoy-Chapman length. Much like

the Debye length, as more charge is added to the system, perhaps unexpectedly, the Guoy-Chapman length decreases, in the case of the Debye length this is attributed to an increased screening of the charge by oppositely charged ions. In contrast to the Debye length, the Gouy-Chapman length depends on the surface charge of the boundary and not on the concentration of the solution contacting it.

The reason for the low surface charge density of graphene oxide has not been reported or discussed in the literature. Bocquet [6] suggests that as this is on the order of the hydration shell of an ion, ions may have to go through the energetically unfavourable process of shedding some of their hydration shell in order to fit in this confined space. This would lead to fewer adsorbed ions on the surface of the material and a lower surface charge value.

The final length of importance describes the length over which surface conduction dominates bulk conduction and is known as the Dukhin length, which is given by

$$l_{Du} = \frac{\sigma}{zFC_{\infty}} \quad (2.45)$$

This equation is significant in surface charge governed conduction and concentration polarization in nanofluidic systems.

### 2.1.2 Important phenomena in nanofluidics

Ion transport in nanofluidics is dominated by a couple of phenomena where most papers in the field touch or draw inspiration from. These are, in no particular order, surface charge governed conduction, electroosmosis, rectification and concentration polarization. All stem from phenomena that reside in the double layer described in the previous section.

#### Surface charge governed conduction

Surface charge governed conduction was first observed for nanochannels in 2004 [36] and is a consequence of the non-electroneutrality of the double layer. While studying ion transport in electrolyte filled fused silica nanochannels of varying height (70 nm to 1015 nm) it was found that as the concentration of the electrolyte decreased the corresponding conductance began to plateau. This result is unexpected when one considers the conductivity of such a channel of length  $L$ , width  $w$  and height  $h$  to be given by

$$G = \frac{I_i}{\Delta\phi} = \sum_i \frac{-e\mu_i z_i w h C_i}{L}, \quad (2.46)$$

which is the Nernst-Planck equation (equation 2.14) expressed in terms of the current for a system with no concentration gradient. This equation suggests that the current and thus the conductance will scale linearly with the concentration. This surprising experimental result is explained by demanding electroneutrality for the entire channel system including the charge on the boundary. When the bulk concentration  $C_{bulk}$  becomes increasingly small, then  $h < l_{Du}$  and at this point the conduction in the channel is dominated by surface conduction and as long as this condition is true, the contribution from bulk conduction

is negligible. The dominance of the surface at low values of concentration is significant as it has led to the development of field effect nanofluidic transistors [37] and field effect nanofluidic diodes [38]. A basic description for the conductance in these systems is given by Schoch [39] for a KCl electrolyte

$$G = (\mu_{K^+} + \mu_{Cl^-})C_\infty F \frac{wh}{L} + 2\mu_{K^+}\sigma_s \frac{w}{L}. \quad (2.47)$$

The first term in the equation can be arrived at from equation 2.46 (with the assumption that  $\nabla\phi = \frac{\Delta\phi}{L}$ ). The second term can be arrived at by simply demanding electroneutrality for the boundaries of the channel (in this case a pair of parallel walls) and the solution within it, ie.

$$\rho_n = \frac{2\sigma_s}{h}. \quad (2.48)$$

This effect is not just observed with ion current measurements, the presence and dominance of surface charge and the resulting enrichment of counter-ions and depletion of co-ions affects the permeability of the channel under passive transport as well. Plecis [40] demonstrated that the diffusive permeability of negative charged molecules through a negatively charged nanochannel decreased with decreasing concentration. This is due to the dominance of the surface charge in the channel rejecting the negatively charged molecules and forms the basis for permselectivity in nanoporous membranes [41].

### Electroosmosis and streaming potential

The equation for electrophoresis (equation 2.8) appears in an essentially phenomenological manner here, however this equation is used to describe ions as well as large ( $\sim 1 - 10\mu m$ ) charged colloidal particles and particularly for large colloidal particles there do exist analytical solutions for the mobility. In the case of small particles that can be treated like point charges, such as ions, the Nernst-Einstein equation (equation 2.16) is applicable.

If one were to stand on the surface of one of these large colloidal particles and observe the solvent in the presence of an electric field, it would be difficult to tell whether the particle is moving or the solvent. In the case where the particle is held in place the solvent actually flows along its surface.

The effect of solvent motion due to the presence of a charged interface and an applied field is known as electroosmosis. Naturally, colloidal particles have their own double layers as they too have an interface with the electrolyte. Channels made of the same material as the colloidal particles thus also have flow occurring along them when an electric field is applied. As a result of the charged diffuse layer of the double layer the application of a potential along the channel results in net motion of the boundary layer and a Couette-like surface driven flow (for thin double layers relative to the channel dimensions). The resultant velocity in the channel is a result of viscous forces accelerating the bulk of the fluid and is given by

$$\mathbf{u} = \frac{\epsilon\phi_0}{\eta} \mathbf{E}_{applied} \quad (2.49)$$

where  $\epsilon$  is the dielectric constant of the medium,  $\phi_0$  is again the surface potential of the interface and  $\eta$  is the fluid's viscosity and much like electrophoresis we can then define a so called electroosmotic mobility given by

$$\mu_{EO} = \frac{\epsilon\phi_0}{\eta}. \quad (2.50)$$

Anytime a potential is applied to a system with surface charge there is a contribution to the resultant measured current due to the convection of ions due to electroosmotic flow. For instance Stein [36] describes a more complete solution to the Poisson Nernst-Planck equations to find the surface conductance of a nanochannel. In the dilute limit the conductance is given by-

$$G = |\sigma|\mu\frac{w}{L}\left(1 + \frac{4\epsilon k_B T}{e\mu\eta}\right). \quad (2.51)$$

where the term  $\frac{4\epsilon k_B T}{e\mu\eta}$  describes the electroosmotic contribution to the overall conductance. At standard values for these variables this term is  $\sim 1.8$  which puts the equation in reasonable agreement with the more approximate equation provided by Schoch [39].

There are authors who state that the contribution of electroosmosis to the total current measured is relatively limited [8, 15, 42] which seems to contradict the findings of Stein [36] shown above where clearly the osmotic contribution to the conductance is greater than the electrophoretic. It is known that for highly charged surfaces [30] and for surfaces exhibiting hydrodynamic slip [25, 27] electroosmosis can play a dominate role in the system's behaviour.

Electroosmosis is of great importance in microfluidics where the effect is used to pump fluids with an applied voltage. This has some important advantages over pressure driven systems as the resultant velocity profile is quite uniform, the velocity doesn't depend on the dimensions of the channel, applying an electric field on a chip is relatively easy and doesn't required additional bulky equipment like a pressure driven system [33, 43]. There are drawbacks however, as this flow is driven by the physics of the channel's surface and small changes to this affect the flow greatly. Surface potential can change due to adsorbed molecules, changes in concentration and changes in pH, all of which affect the resultant electroosmotic velocity.

Streaming potential is almost exactly the reversed scenario, a pressure gradient is applied in the channel and the result is that a potential is created due to the build up of charge in one end of the channel relative to the other. Streaming potential is of interest to the community as a measurement tool but has interesting implications in nanofluidic's potential in energy conversion. The ability to harvest energy in this manner has been of great interest to many authors [30, 44–47] and while experimental results were initially unimpressive (around 12% efficiency was achieved) [45], predictions [27] that hydrodynamic slip would radically increase the overall efficiency of a system create opportunity for further study.

### Concentration polarization

Concentration polarization is a long studied effect in membrane science [9, 48]. It arises in permselective membranes due to the differences in permeability of different ions. When driving flow through a membrane with a pressure gradient the ions that are rejected build up at the entrance of the membrane. Electroneutrality requires that this charge be negated, so on the input side of the membrane there is a build up of ions of both charges, resulting in an increase in the concentration. This high concentration region then has a number of different interpretations as to how it reduces the flux [49, 50]. Essentially the layer is interpreted to create additional flow resistance which results in declining flux or the layer creates an osmotic pressure opposing the applied pressure, which again, then reduces the flux. Concentration polarization is an inconvenience in filtration sciences as it reduces the permselectivity of the membrane by creating this region of high concentration. There are however methods to combat this effect including introducing changing hydrodynamic conditions and applying ultrasound or electric fields to the membrane [50].

In the context of applying an electric field to a membrane or nanochannel the effect of concentration polarization occurs in an equivalent manner due to the permselectivity of the membrane. In these experiments the side of the membrane that has the concentration enrichment depends on the charge of the membrane as the electric field moves ions of opposite charge in opposing directions [7]. This phenomenon has long been studied by researchers interested in electrodialysis [51, 52] and manifests itself in electrical studies as three distinct regions on a standard current-voltage plot as described in figure 2.3. Initially there is an Ohmic region where the current response is linearly proportional to the applied voltage, then there is a limiting region where the concentration polarization is strong and changes in applied potential have little or no affect on the measured current. While the Ohmic and limiting current regions are predicted in classical literature [51] the overlimiting region is not, despite knowledge of its existence at the time. Rubenstein [53] showed that the low concentration on the depleted side of the membrane caused by the concentration polarization leads a series of electrokinetically driven vortices which overcome the diffusion limitation of this region.

While this concentration polarization layer is thin, it isn't as thin as nanofluidic structures and channels. Pu [7] was able to image the enrichment and depletion regions using fluorescence at the junction of a micro- and a nanochannel. If one were to take a symmetric electrolyte at relatively low concentration then the conductance in the microchannel would be dominated by the first term in equation 2.47 as the microchannel's height is significantly larger than the double layer and the conductance in the nanochannel would be dominated by the second term, the ratio of the conductances is then found to be the Duhkin number

$$\frac{G_{nano}}{G_{micro}} = \frac{\sigma}{zFC_{\infty}h}. \quad (2.52)$$

The Duhkin number, the associated length has been already described in equation 2.45, is an important scaling number for concentration polarization in a number of known geometries [31, 54, 55].

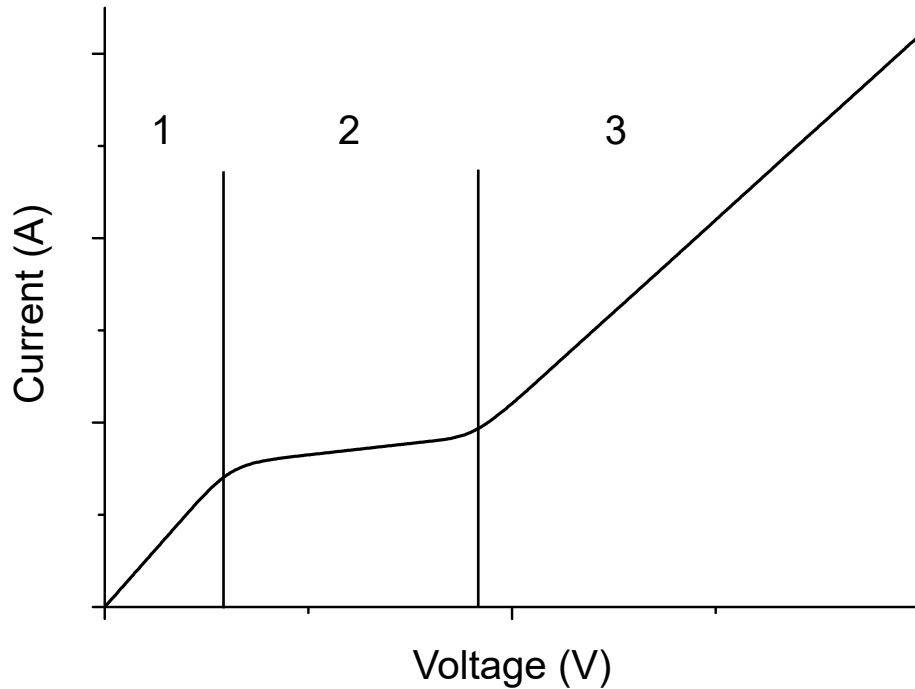


Figure 2.3: An idealized graph of the three regions of concentration polarization effects on a membrane or nanochannel. Region 1 is ohmic and linear which after a certain potential gives way to region 2 where the current roughly plateaus to the limiting current due to concentration polarization. Region 3 is the overlimiting current region where linear behaviour is somewhat restored due to a variety of effects.

Being able to enrich or deplete ions from a nanochannel using an applied voltage has been used to great effect in the literature [54–57] to preconcentrate samples before further analysis. This is in contrast to the procedures performed in pressure driven membrane experiments where the electric field is applied to reduce the effect of concentration polarization allowing enhanced flux through the membrane [58]. Concentration enhancement values as high as  $10^6 - 10^8$  [57] have been claimed which allow dilute protein samples to be concentrated for further on-chip study. The effect has also been used to desalinate water by flowing salty water into a junction where one branch is covered in a depletion zone which deflects away any charged particles [59]. This technique, while difficult to scale, is very attractive as the system is very efficient for its size and the particles and ions do not come into contact with the membrane which completely removes the problem of the membrane fouling, a common and serious issue.

### Rectification

Rectification describes an asymmetry in conductance, dependent on the direction of the applied potential. An example of this would be an electrical diode where current flows in one direction and is blocked in the other. The hydraulic analogue would be a one-way valve. Rectification has been a vast area of interest in the field [6,8,15,18,60–69]. Rectification is the result of one of a number of relatively equivalent asymmetries that can be introduced to a nanofluidic system. The simplest analogue to the electrical diode exists for systems with areas of different surface charge resulting in a junction within the nanochannel where

Nanofluidics	Semiconductors
$\rho_-$ negative ion concentration	$\rho_n$ electron density in the conduction band
$\rho_+$ positive ion concentration	$\rho_p$ hole density in the conduction band
$\rho_s$ electrolyte concentration	$n_i$ carrier density in the intrinsic semiconductor
Surface charge $2\Sigma/h$	Doping concentration in the semiconductor
Donnan potential	Shift of the Fermi level

Table 2.1: The nanofluidic parameters and their equivalent condensed matter terms show the similarity between the two sets of physics.

the two zones meet [62,65,66]. The point where the two distinct regions of surface charge meet behaves like the junction between two differently doped semiconductors resulting in diode-like behaviour. Generally speaking the creation of a junction between two areas of different surface charge results in diode like behaviour, however there are many ways to change the effective surface charge of a material. As has already been stated nanofluidics has strong links to semiconductor systems, in fact the complete analogy is laid out in Bocquet's work [6] and the corresponding table from that work is reproduced here in table 2.1.

Other ways of introducing asymmetry include channels which have regions with Debye layer overlap (even partial overlap is enough) and regions that do not, this includes concentration based rectifiers [64] and conical nanopores [61,70]. Highly confined systems like carbon nanotubes can even use the physical size of the charge carriers to hinder each others' motion leading to rectification [71].

Rectifying systems have been popular to develop sensors out of as their signals can then be incorporated into logic circuits [68,72]. By attaching species that specifically absorb target molecules like antibody-antigen coupling [73] or by changing the pH [74] and thus modifying the surface charge the performance of these systems changes radically. Sensors and demonstrations of logic gates are now beginning to give way to more complex circuits such as this full-wave rectifier [75] and this voltage multiplier circuit [76]. The development of systems like these is sometimes called ionic circuits or iontronics [77]. Chun's review [77] suggests that there could be considerable benefits in using these electrolyte based semiconductor like systems for computational purposes. In more complex and selective designs circuit components would have different effects on each different species of ion, leading to carrier dependent signals which could allow massive increases in computational speed and reuse of components (as some carriers may see the component as a resistor, others might see it as a diode etc). While there is a massive difference in the mobility of an electron and an ion (some  $\sim 7$  orders of magnitude between an ion moving in water and an electron moving in silicon) biology clearly demonstrates to us that this difference is capable of being overcome by clever design.

### 2.1.3 Carbon in nanofluidics

While carbon based systems have been investigated in colloidal environments before [78,79], there has been significant attention drawn to the interfacial properties of carbon with

the advent of carbon nanotubes [80–83] then around a decade later [84] the surprising simulation result that water could enter the hydrophobic channel of a carbon nanotube and that the water molecules were moving at a rate on the order of aquaporin-1, the transmembrane water channel protein. As this nanotube was quite small the water entered in a single file and went through a phase transition to an ice-like state. This exciting result was followed by mass transport studies through carbon nanotube membranes [21–23]. These initial experiments [21, 22] reported large hydrodynamic slip lengths for carbon nanotubes and as a result massive flow enhancement through these membranes which conceptually agreed with the simulated confined flow studies. These results have ignited extensive debate [6, 85–92] as to the exact value of this intriguing interfacial property. Experimental values range from  $1\text{ nm}$  to  $485\ \mu\text{m}$  while simulations give values ranging from  $1\text{ nm}$  to  $1100\text{ nm}$ . Most recently unprecedented experiments have allowed researchers to examine the flow field created by a jet of water exiting a single carbon nanotube [24]. The results of the study agree with trends from simulations [88, 92] that the curvature of the nanotube plays a significant role in defining the friction of the water-carbon interface. Secchi [24] found slip values of up to  $300\text{ nm}$  in the smallest size tube investigated, which exceeded expected values from simulation. An overview of this debate which examines the results of many different experiments and simulations is given in [92] but lacks the most recent developments of Secchi’s findings.

As the slip length depends on the nanotube curvature the slip length for fluid flow in graphene systems is found to be lower, however the confinement is still very strong and mass transport in graphene-based membranes has aroused significant interest in the literature as the permeability of these membranes is significantly higher and the complexity of making a graphene-based membrane is significantly easier than a carbon nanotube one. New experiments performed by Radha [93] found that the slip length of graphene nanocapillaries was around  $\sim 60\text{ nm}$  and that the capillary pressure in this system is enormous- around  $1000\text{ bar}$ . Understanding of this slip value has dominated carbon’s presence in nanofluidics.

#### 2.1.4 Nanofluidics in this thesis

The theory given here provides grounding and context for the research that follows. The rectification observed in chapter 4 is thought to be due to asymmetry in the concentration polarization occurring at the junctions between a film of graphene oxide and the bulk electrolyte solution. Surface charge governed conduction is experimentally observed in chapters 5 and 7, from which, using the Dukhin length, the surface charge density of graphene oxide is calculated. The electric double layer is important to the charge storage mechanism in supercapacitors and in chapter 6 a new kind of ionic supercapacitor is designed and characterized, the electric double layer is essential in explaining its behaviour. In chapter 7 three different forcings (electric, pressure and concentration difference) are applied to a membrane of graphene oxide along with PNP simulations to understand more completely how the material is behaving. Findings here show a connection between surface charge and concentration and suggest a connection between concentration polarization and geometry and between the material’s surface charge density and the confinement.

## 2.2 Graphene, graphene oxide and reduced graphene oxide

Since 2005 there has been an explosion of interest in 2D materials [94] centering on the material known as graphene. Graphene is a one atom thick hexagonal lattice of carbon atoms with extraordinary properties [95]. The material is the strongest ever measured [96], has an enormous specific surface area of  $2630\text{ m}^2/\text{g}$  [97], is an excellent thermal conductor [98], a fantastic electrical conductor [95] and exhibits a host of interesting quantum mechanical effects [95,99]. While this material promises much, bulk techniques required for processing and synthesizing it are necessary if the science is going to leave the days of scotch tape [100] and rubbing graphite [101] behind it.

The world of chemistry has been processing graphite for a very long time into a material known as graphite oxide which is well known to form aqueous dispersions in water [102]. After the findings of Novoselov and Geim there was significant interest in making graphene and graphene-like materials more accessible via this route [103,104]. From this effort the material known as graphene oxide (GO) came into the literature. This material is simply monolayer sheets of graphite oxide which are produced typically by exfoliating graphite oxide. Soon after, via the use of various deoxygenating or reducing treatments, reduced graphene oxide (RGO), which is often referred to as chemically converted graphene, also came into being. The success of these materials in capturing the world of science's minds is irrefutable, they have been used to enhance material strength [105–107], develop new transparent conductive films for touch screens [108–110] and they also demonstrate fantastic potential as an energy storage material in supercapacitors [111–113].

So what are the differences between graphene, GO and RGO? Graphene, as described before, is purely carbon, it is a monolayer of graphite which can be produced by a wide variety of exfoliation and chemical vapour deposition (CVD) techniques [94,114–117]. GO is (ideally) a monolayer of oxidized graphite. While graphene very specifically refers to a purely carbon-based hexagonal lattice, GO is far more poorly defined. As described in [117] due to variances in the methods and variability in sample size there is no stoichiometric description of this material. There are many models that have tried to describe this material over the years but the Lerf-Klinowski model [118] of the material tends to appear the most in visual descriptions. This model suggests that the structure is that of a defective graphitic plane which is covered in defects and a variety of functional groups - epoxies, hydroxyls and whose edge is functionalized with carboxyl functionalities.

GO is synthesized through exfoliation (typically using ultrasound) of graphite oxide. There are a number of routes to synthesizing graphite oxide, the most common being Hummers' method [102], however this method is quite dangerous due to its use of high concentration sulfuric acid and the use of large amounts of potent oxidizing agents such as potassium permanganate. Once synthesized and exfoliated a dispersion of GO is brown in colour (lighter brown to yellow if more heavily oxidized) [119,120].

Chemical, thermal, electrochemical even photochemical reduction of GO is possible [117]. By removing the oxygen functionalities and partially restoring the graphitic molecular structure of GO the material becomes a graphene-like substance known as reduced graphene oxide (RGO). This may seem like a roundabout manner to get essentially what

we had at the beginning but GO is considerably easier to process into films than pure graphene as it can be so easily handled in aqueous dispersions. RGO is perhaps the most poorly defined of all the materials described here. For instance most reducing chemicals don't remove all the oxygen present on GO and there is presently no clear, well-defined distinction for when a material transitions from GO to RGO. Generally speaking however, RGO is black, conductive and far less stable than GO in aqueous solutions. Typically a significant fraction of the basal plane oxygen-bearing functionalities have been removed by some reducing process but the carboxyl groups on the edges of the sheets could remain.

It should be mentioned however that significant work has gone into finding a solvent capable of dissolving graphene, chlorosulfonic acid [121] is a super acid capable of protonating pure graphene and rendering it soluble. This has allowed researchers to process graphene in the same manner to GO, however this solution is significantly more dangerous and difficult to handle than an aqueous dispersion of GO.

### 2.2.1 Graphene oxide films

In plainest terms, the fabrication of GO films is incredibly important to this work, as all the research performed in this thesis starts at this point. As will be seen in the following chapters the films produced link the material properties of GO and RGO to the fluid-interface physics of nanofluidics described earlier. While there are a number of different methods to form films like drop casting [122], dip coating [123], vacuum filtration [104,124], shear-alignment of GO liquid crystals [125], capillary-force assisted self-assembly [126], spraying [127], etc. films produced are often thin [122,123,127] (only a few layers of RGO or GO sheets) and transparent with the ultimate objective of replacing conductive metal oxide thin films [123].

The films have a stacked structure where the GO/RGO sheets lie in planes parallel to the substrate. Numerous X-ray diffraction studies [35,124,128] give relatively similar values for the distance between GO sheets in these structures, around  $\sim 0.85\text{ nm}$ . Once hydrated the interlayer spacing increases to  $\sim 1.4\text{ nm}$  [35]. Reducing agents decrease the interlayer spacing as the resultant system (while still water permeable) becomes increasingly graphitic, interlayer spacings as low as  $0.36\text{ nm}$  have been achieved using hydriodic acid treatments [128].

It is somewhat surprising how stable the GO films are when immersed in water. Whilst mechanically weak the film will happily remain there and not visibly begin to disperse into the water. On the other hand GO suspensions exhibit long term stability in water. Yeh [129] suggests that this is due to the introduction of contaminant multivalent ions during the membrane formation process. This report [129] even demonstrates  $\text{Al}^{3+}$  contamination in their membranes when porous  $\text{Al}_2\text{O}_3$  membranes are used and the relative instability of the films when prepared on a different membrane. Yeh suggests that this is due to a 'cross linking effect' however DVLO theory [31,34] would suggest that the role of the multivalent ions is to reduce the effect of the double layer repulsion, allowing the van der Waals attraction to dominate and stabilize the film structure. In figure 2.4 the interaction energy per unit area for two parallel sheets of graphite is plotted showing the effect of

the two forces- double layer repulsion and van der Waals attraction. The exact reasoning seems to be still incomplete, for instance Yeh suggests that this is the mechanism by which the films are stabilized ie. the introduction of multivalent ions (like  $\text{Mn}^{2+}$ ) in the synthesis step and then the  $\text{Al}^{3+}$  ions in the film formation step. Whilst contamination is likely, GO suspensions prepared before the film formation step still exhibit excellent stability and if they were contaminated, one might expect some coagulation of the suspension.

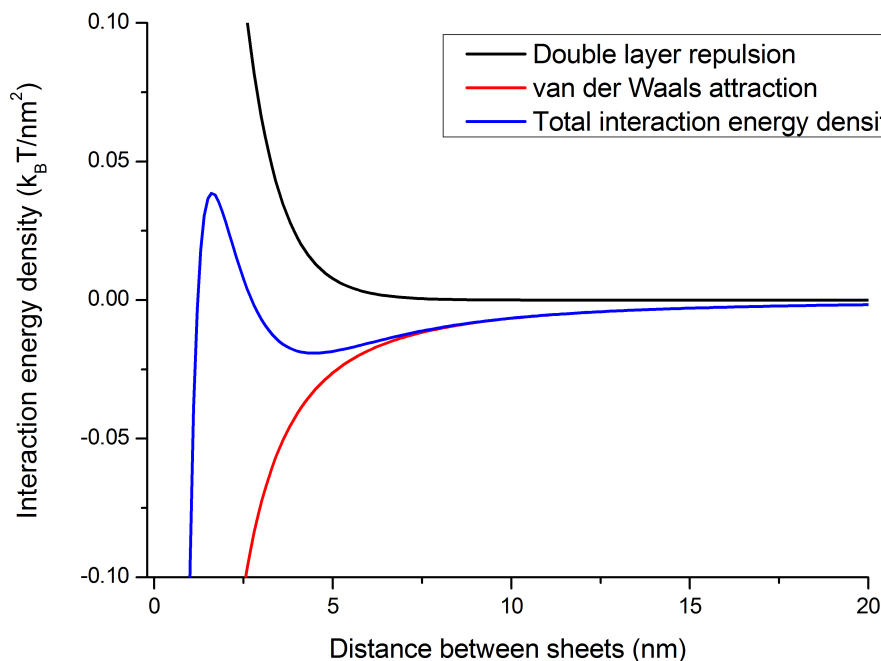


Figure 2.4: The interaction energy densities of the two dominant interparticular forces; double layer repulsion and the attractive van der Waals force, of which the van der Waals has the longer range. This was calculated for a pair of graphite sheets (Hamaker constant was  $\sim 10^{-19}$  [1]) with a monovalent aqueous electrolyte concentration of  $0.1 M$  at room temperature.

When examining transport in GO the typical method is vacuum filtration [35, 130–132]. There has been a great interest developed around membranes using GO which are shown to be helium-leak-tight, whilst being permeable to water vapour [131], they have large water flux which makes them attractive for applications in nanofiltration [125] and due to their layered structure they are a rapid way of fabricating systems of ordered nanochannels [35]. Vacuum filtration refers to a method by which a dispersion is pulled through a filter membrane (using negative pressure) leaving the once-dispersed particles deposited on the filter. This works quite well with GO as the sheets are often around  $1 \mu\text{m}$  in size so many commonly available membranes are capable of separating the sheets from their solvent (typically water). Dikin [124] suggests that in the initial stages when the water flux through the filter membrane is at its highest the GO sheets form a disordered and crumpled structure on its surface. The filter is then quickly clogged and the flux decreases significantly. At lower flow rates the film forms in a far more ordered manner giving rise to the layered structure one observes in cross sectional studies of these films (see figure 2.5).

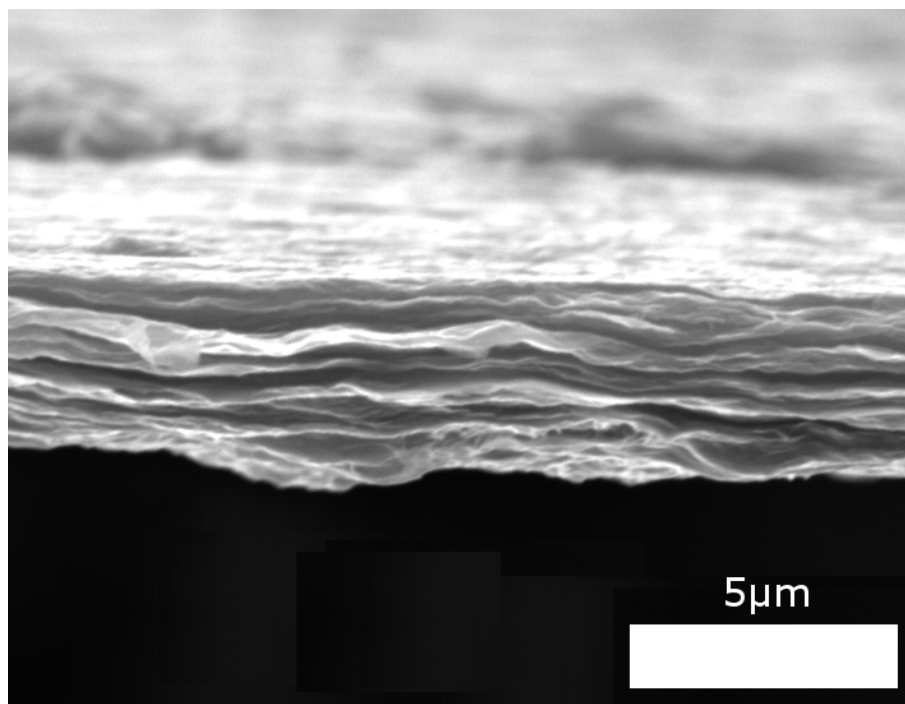


Figure 2.5: A scanning electron micrograph of a cross section of an RGO film made via vacuum filtration

These thicker films have a variety of relevant applications, most notably as supercapacitor electrodes [97, 111, 112, 133, 134]. In typical sandwich style capacitors RGO is combined with a binder and cast onto a stainless steel current collector from which Stoller [97] measured a specific capacitance of 135 F/g in 5.5 M KOH. This was the earliest report of graphene being used as the porous carbon electrodes of a supercapacitor, since then the field has flourished and given rise to a host of different electrode structures and fabrication methods [111–113, 135, 136].

### 2.2.2 Graphene oxide liquid crystals

Of particular importance to later works in this thesis is GO's ability to form lyotropic nematic liquid crystals [137–139]. A liquid crystal is an ordered state of anisotropic particles which have both liquid like fluidity but also crystal like long-range ordering [140]. A lyotropic liquid crystal exists only in mixtures (ie. a solute and a solvent are required) and requires a strong interaction between the solute (GO) and the solvent (water). At low solute concentration the solution is isotropic and no ordering can be observed but as the solute concentration is increased the ordering in the solution increases.

Liquid crystals go through a variety of long-range orderings. Beginning in the low concentration limit as solute is added groups of solute (often in the case of liquid crystals these are micelles) gather and allow a certain preferred axis to be the time average description of the ensemble's alignment. This phase is known as the nematic phase. In the case of GO as it is disk-like the GO sheets roughly align parallel to one another. The other two axes, however, don't exhibit long-range ordering. It is possible for this to occur and this phase is known as biaxial nematic but this hasn't been observed in GO. After orientational

ordering there is an additional phase expected to be observed in GO called the columnar phase where GO sheets form pillar like structures (like a tower of coins) which then form fibrous bundles, however this has not yet been reported in the literature, possibly due to the variance in GO sheet size.

From studies performed by Tkacz [141] it is evident that GO nematic phase can be manipulated to form ordered films which is brought to great use in her work and by those that follow it [125]. What is gained from Tkacz's work [126] on suspensions of RGO is that there are significant benefits to increasing the order of RGO films from virtually purely disordered vacuum filtration based films to highly ordered capillary-force assisted self-assembly (CAS) films. In the report it is shown that CAS films are 8 times more conductive than an equivalent film formed via vacuum filtration. Similar findings are reported by Akbari [125] where highly ordered membranes formed using a similar technique were found to have almost 7 times higher water flux than vacuum filtration films reported in the same work.

### 2.2.3 Graphene oxide in nanofluidics

Only very recently have the two fields considered here been combined and examined in a quantitative fashion [35]. GO is quite attractive to the field of nanofluidics as the hydrated films have exceptionally confined interlayer spacings [35,132]. Transport of ions (and indeed solvent) within GO continues to be an ongoing question which many authors are attempting to come to grips with [19,132,142]. However the tantalizing accessibility to this relatively well-structured system allows experimenters to quickly access nanofluidic confinement without the need to perform clean room based fabrication. Greater understanding of nanofluidics can be quickly translated into large area membrane applications through the use of this material. Ion transport in both conventional membrane form [130,132] and planar form [35,143] have been examined. There are hints of large anisotropy in properties due to the shape of GO sheets [113]. However since the system is so confined the equations that one uses to conventionally describe nanofluidics are potentially even less valid in this case, studies up until this point have largely used molecular dynamics [19]. It is unclear how the differences in concentration, pressure and electric potential might couple and behave on this length scale where the channel size is typically smaller than the Debye length and commensurate with the Bjerrum and Gouy-Chapman lengths.

### 2.2.4 Graphene oxide in this thesis

Initially GO is used in this work as a means to fabricate nanochannels for nanofluidic investigations in chapters 4 and 5. From observations made in both those works GO was then reduced and these investigations formed chapter 6. Finally the investigations turned to the material itself, chapter 7 attempts to examine GO using nanofluidics to try to understand some of its properties that have been overlooked in the literature.

## Chapter 3

# Experimental Methodologies

### 3.1 Graphene oxide synthesis and concentration

The graphene oxide (GO) in this thesis was synthesized using Hummers' method and concentrated into the nematic phase using SAP (super absorbent polymers). The technique used in our laboratory is based off work performed by Kovtyukhova [144] and utilizes an additional pre-oxidation step to ensure completeness of the graphite oxidation. The graphite used in the work performed for this thesis was Bay Carbon SP-1 grade 325 mesh graphite powder.

The following procedure was performed; 5 g of potassium persulfate (Merck) and 5 g of phosphorus pentoxide (Sigma Aldrich) were dissolved in 15 mL of sulfuric acid heated to 90 °C, once dissolved 10 g of graphite were added to the mixture and this was allowed to stir at 80 °C for 4 hours. This pre-oxidized material was removed, washed until neutral and then dried. 230 mL of sulfuric acid (Univar 98%) was then placed in an ice bath along with the dried pre-oxidized graphite. 30 g of potassium permanganate (Sigma Aldrich) was slowly added to the mixture (ensuring that the reaction didn't warm more than a few degrees above 0 °C), after which the reaction was held at 35 °C for 2 hours. Afterwards the solution was diluted to a volume of 2 L with deionized water and 25 mL of hydrogen peroxide solution (Merck 30%) was added to quench the reaction. The graphite oxide was then washed with 1.7 L of 10% hydrochloric acid solution (Univar 32%), to remove the salts from the reaction and then a solution of sodium bicarbonate (Sigma Aldrich) was added to neutralize the graphite oxide suspension. Here our methodology deviates from Kovtyukhova's. The neutralization using sodium bicarbonate is novel and while this introduces more undesirable ions into the graphite oxide at this point, in order to form a high quality nematic phase GO an intensive washing step is required. No peaks for sodium bicarbonate could be found in our resultant GO using Fourier transformed infrared spectroscopy. The product was then washed three more times with deionized water to remove the sodium bicarbonate. At this point the graphite oxide has a clay like consistency and is brown in colour. Samples from this suspension were diluted again 1 : 2 with deionized water, sonicated for half an hour and centrifuged. This process is repeated a number of times to produce a sufficient quantity of graphene oxide suspension. Concentration was performed using SAP to remove water from the suspension leaving the

GO in place. This procedure needed to be repeated a few times in order to concentrate the suspension to the concentration used in these experiments, which was  $\sim 30\text{ mg/mL}$ . Concentration of the resultant liquid crystal was measured by controlled dilution and measurement of the characteristic peak at 230 nm using UV-Vis spectroscopy (Ocean Optics USB4000).

It was possible that the nematic phase GO had agglomerations of even more concentrated GO within it, possibly due to a GO concentration gradient forming around the SAP particles. In this event the GO was dispersed in a large volume of water and centrifuged again. Any particulate matter was then removed before the concentration procedure was repeated.

### 3.2 Film formation and characterization

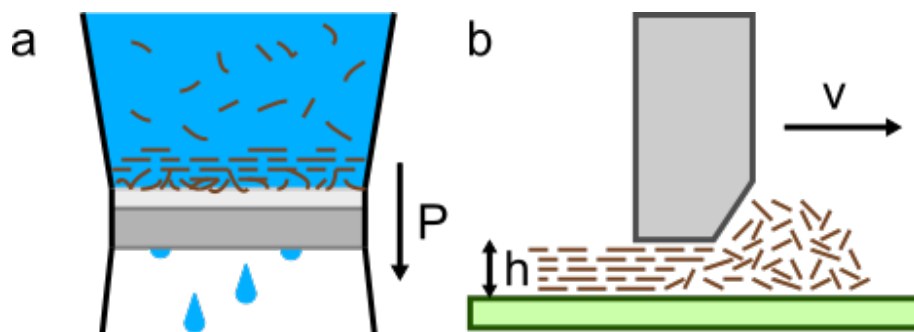


Figure 3.1: a) A film being formed by vacuum filtration is prepared by using negative pressure to pull solvent through a support membrane, on which the graphene oxide flakes collect, b) a shear-aligned film of graphene oxide prepared by sweeping a doctor blade across a substrate.

Two techniques are used to form GO films in the works in this thesis. Initially vacuum filtration was used, which is quite common in the literature [104, 124, 128, 130, 131]. Briefly a dispersion of graphene oxide is prepared and pulled through a porous membrane by negative pressure by applying a vacuum to the other side of the membrane (figure 3.1a). The initial film formed is relatively disordered as the flux through the membrane is high [124], however as more sheets are deposited the flux decreases and the individual GO sheets deposit on the membrane in a more ordered manner. This method was used to produce both free standing GO membranes from aqueous GO dispersions and free standing RGO membranes from RGO dimethylformamide (DMF) dispersions. Obtaining a large ( $r > 20\text{ mm}$ ) free standing membrane using either of these materials required the deposition of a thick (around  $50\ \mu\text{m}$ ) layer so that the film had sufficient structural strength. The process is limited by the size of filter and also by the lengthy filtration process. This is particularly pronounced with GO which has a strong interaction with its solvent, a single GO membrane can potentially take 48 hours of continuous filtration to produce.

Following the work of Akbari et al. [125] an alternate method was used to form films in the later works. By concentrating GO using superabsorbent polymer (SAP) to remove water from the solution, very high concentrations of GO can be reached with relative ease. Once concentrated into the nematic phase and sheared the GO sheets align and form an ordered dense film as illustrated in figure 3.1b. The blade of the doctor blade is rigid, relatively thick and set such that the edge of the blade is  $\sim 30\ \mu\text{m}$  above the surface of the substrate. As the height of the blade ( $h$ ) is small compared to its velocity ( $v$ ) the resultant shear rate ( $\dot{\gamma}$ ) on the fluid is very high-

$$\dot{\gamma} = \frac{v}{h}. \quad (3.1)$$

The applied shear on the liquid crystal results in the director field of the liquid crystal being aligned perpendicular to the substrate. This creates long range molecular order in the film which cannot be achieved using vacuum filtration [125].

### 3.2.1 Xurography patterning

Xurography comes from the graphic art world. Using a computer controlled cutter patterns can be cut into thin polymeric films. The technique is rapid and allows cutting of structures on the range of  $\sim 10 - 100 \mu\text{m}$  [145]. It first appeared in the literature as a method for rapidly preparing micro-channels through the use of adhesive thin polymeric films [145–147]. In the laboratory a Roland SV-8 Stika cutter was used to cut samples of Metamark series 7 vinyl. This film has a thickness of approximately  $\sim 100 \mu\text{m}$  and a solvent based acrylic adhesive. The lateral precision of the cutter was limited to approximately  $\sim 200 \mu\text{m}$  due to differences in the step size of the motors and the friction between the rollers and the substrate. An example of how an arbitrary pattern is prepared and transferred to a glass slide is depicted in figure 3.2.

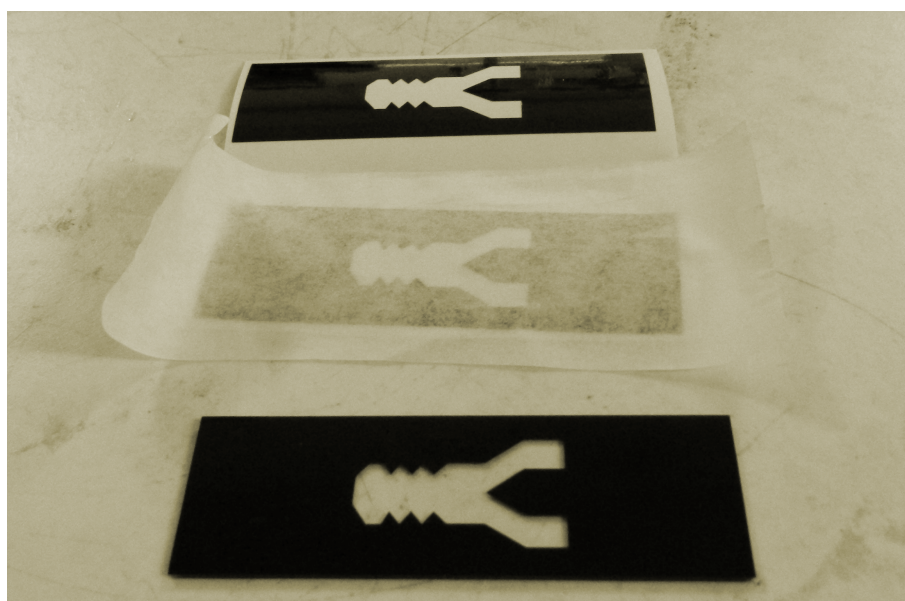


Figure 3.2: At the top of this image a vinyl pattern has been prepared by the cutter. The offcuts have been removed using a weeding tool and the vinyl is still on its backing. In the middle the pattern is being transferred using adhesive tape to hold the pattern in shape. At the bottom the vinyl has been adhered to a glass microscope slide ready for being used as a mould for a shear-aligned graphene oxide pattern.

### 3.2.2 Electron microscopy

Scanning electron microscopy (SEM) is an invaluable tool to almost any experimentalist working in the nanotechnology domain [148, 149]. The technique provides surface information with incredibly high resolution for samples which are relatively conductive (typically GO, as it is quite insulating, requires a conductive coating) and can be performed relatively swiftly with minimal preparation. Most SEM imaging in this thesis was performed on an FEI Nova NanoSEM 450 FEGSEM. A typical image is depicted in figure 3.3. Cross sections in this work were performed by freezing a sample in liquid nitrogen and then shattering it. The shards were adhered to an SEM stub using carbon tape and coated with a thin layer of sputtered gold before imaging.

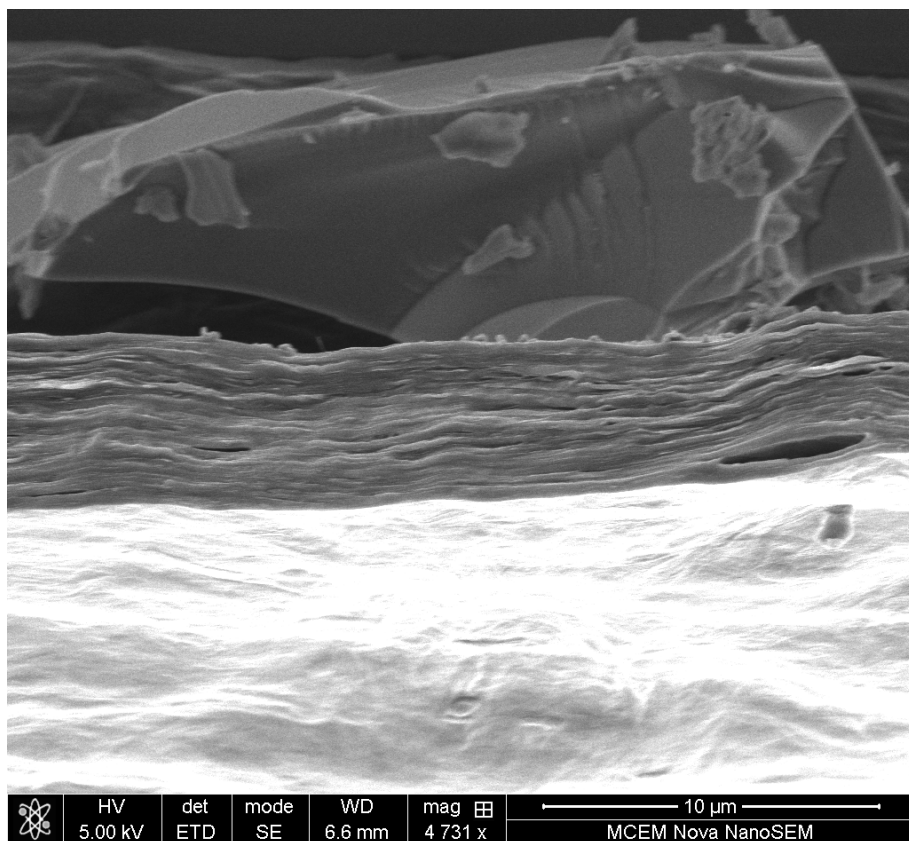


Figure 3.3: This cross sectional image of a GO film has the typical layered microstructure observed in this material. As GO is not very conductive charging is also evident on the surface on the bottom.

### 3.2.3 Profilometry

Profilometry is a very popular technique used to examine substrates and surfaces [150,151]. The two varieties of profilometer used in this work are the standard stylus profilometer (Ambios XP 200) which uses a small stylus to contact the material and the optical profilometer (Bruker Contour GT-I) which uses a microscope and lasers to gather surface height information. Standard profilometry moves a small, relatively sharp stylus across the surface of the substrate. As the stylus strikes objects it deflects and this deflection is detected by a laser. By moving the stylus at a constant speed simple 1D profiles of the surface can be made with a resolution around  $\sim 10\text{ nm}$ . Optical profilometry uses interference from a laser rastered over the substrate to collect height information. The optical profilometer is a more sophisticated instrument allowing 2D height maps to be collected and doesn't risk damaging the sample as the method is contactless. Typically both profilometry techniques have some difficulties with samples with particularly steep gradients and sudden changes in feature height on the order of  $\sim 10\ \mu\text{m}$ . The stylus can jam quite easily on such a "large" feature and the laser based optical system's signal quality is quite poor. These features can occur at film edges if the samples are prepared in a certain manner, however the bulk of the film is well handled by these techniques which can swiftly provide an abundance thickness and surface information. Profilometry was used extensively in this thesis to examine patterns of GO.

### 3.2.4 Four point probe

In the interest of being able to rapidly characterize film samples, a four point probe was constructed to measure the sheet resistance of film samples. The four point probe is a common technique used to study thin films where a set of four contacts in a line are lowered onto the sample. The outer contacts apply a current ( $I$ ) permitting the inner two to measure the voltage drop ( $V$ ) between each other. As no current is flowing in these inner contacts (approximately), the potential difference measured is purely the resistance of the substrate and the contact resistance (which can be quite troublesome) is circumvented. The relation which gives the sheet resistance ( $\rho_{\square}$ ) of the material is remarkably simple

$$\rho_{\square} = \frac{\pi V}{\ln 2 I}. \quad (3.2)$$

An issue encountered in this work was that the probe size was relatively large compared to the film dimensions. The equation above is formulated assuming that the film is an infinitely large sheet [152] relative to the probe, however in this case the sheet has a definite finite size which reduces its conductance leading to the sheet resistance being overestimated. It is necessary to then apply an adjustment factor to allow for its finite geometry [153].

While measuring the sheet resistance doesn't provide chemical information in the way infrared spectroscopy or X-ray photoelectron spectroscopy could, it does provide an idea of the level of reduction in the film and allows rapid comparison between samples, since in some of the studies performed here conductivity was a more useful metric than exact chemical composition. The first probe constructed was a rigid probe using circuit board pin contacts. For thicker samples ( $> 10 \mu m$ ) this probe performed admirably connected to a Agilent (B2900) source measurement unit. For thinner samples a Jandal 4-point probe station was used.

### 3.2.5 Polarized light studies

GO exhibits two optical properties which are leveraged here to provide information on the molecular ordering of a suspension or film. These properties are inherited from its parent material graphite due to the fact that the two have very similar molecular ordering [141]. The first is birefringence which means the materials have two refractive indices. The second is di-attenuation which is the differential transmission of light through a material. This is to say that light of differing polarities will be transmitted in different amounts through the material. This anisotropic optical structure is due to the lack of symmetry between the wide sheets of graphite and the layered out of plane stacked structure. These properties enable GO samples to be investigated on an LC-Polscope [126,154], whose (rather complex) mechanism is described here [155,156]. The benefit is that one can very swiftly gather images of the in-plane ordering of the GO sheets.

Measurements of the film's slow axis (as shown in figure 3.4) are used in this thesis to give a measure of the ordering of GO sheets in the film's structure. The slow axis is the (apparent) azimuth, which is also the angle of the sheet's normal vector when projected

into the image plane. Critically when a sheet lies flat in the plane (and perpendicular to the light beam) no measurement can be made as the system has no optical anisotropy in this state. It is necessary to assume that this is the only anisotropy present in the sample, despite individual sheets exhibiting additional anisotropies [126]. The system is very sensitive so only small angles of inclination away from the flat plane are needed to show some anisotropy. Thus darker regions in figure 3.4 are indicative of two things- the sheets are lying perpendicular to the light beam in that region and/or the film is significantly thinner at that point, thus producing a far smaller signal. Given the uniformity of the film the former seems more likely than the latter. Thus we can begin to get an idea of the structure of the GO sheets. As the hue is almost the same everywhere we can conclude that the GO sheets are all tilted in roughly the same direction. Variances in the hue are likely to be due to changes in the inclination angle, so the sheets' orientation at a molecular level is slightly wavy. This indicates a very high level of molecular order. This is measurable by an order parameter  $S$  which is given by

$$S = \langle 2 \cos^2 \phi - 1 \rangle \quad (3.3)$$

where  $\phi$  is the angle between the azimuth at a particular measured point and the average azimuth. Films produced using shear aligned methods can have incredibly high order parameters  $S \sim 1$  [125].

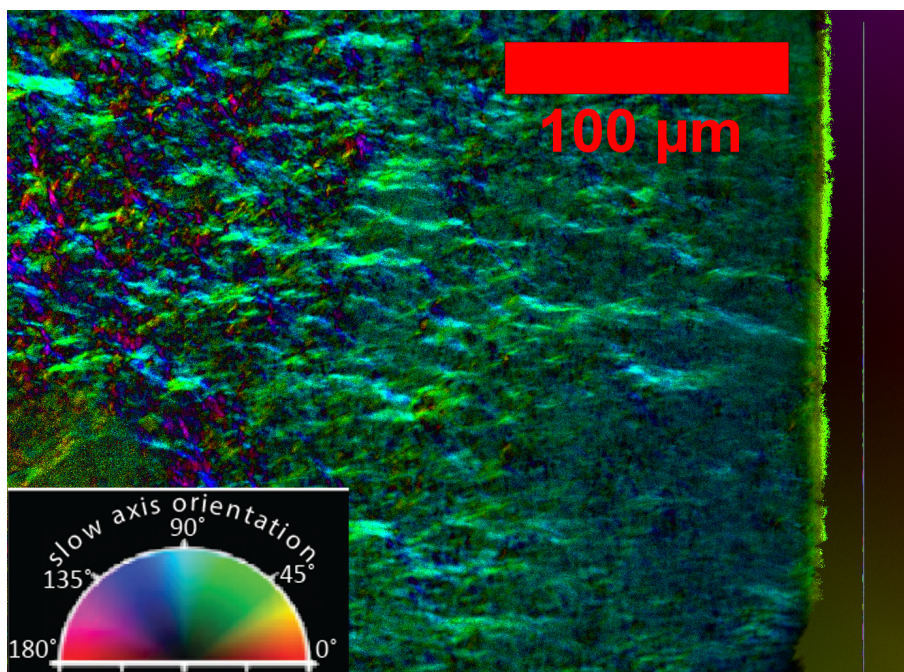


Figure 3.4: A slow axis alignment image of a shear-cast graphene oxide film. The edge of the film is visible on the right. The slow axis scale is the angle of the azimuth from the x-axis.

### 3.3 Ion transport studies

Ion transport is probably the easiest and thus the first experiment one can do with a nanofluidic system. It can provide fundamental nanofluidic characteristics about the system under investigation, particularly the region of concentration which is surface charge governed. This gives an experimenter an idea whether their experiment will show non-bulk behaviour at a particular concentration. Other studies, such as applying a pressure or concentration gradient can often prove to be difficult to interpret as while electronics excel at sensitive detection, equivalent techniques for detecting these miniscule flow rates or subtle changes in concentration can often require bulky equipment and specialist expertise. By placing a pair of electrodes in reservoirs either side of the nanofluidic system and applying a potential, the flux of ions is easily measured as the current passing through the electrodes. Currents greater than picoamps are detectable with relatively common laboratory equipment. This experimental setup also allows access to a host of electrochemical techniques, such as impedance spectroscopy, which provide even more information about the system.

Regardless of the device design ion transport was studied on a Keithley 6403 sub-femto amp source measurement unit (SMU) in a Faraday cage with a custom purpose written Labview program, the setup is described in figure 3.5. At a later point in the research in order to increase sample throughput this was combined with a 4 channel relay switch which enabled 4 samples to be measured in a time sharing manner without the need to unplug anything or open the faraday cage, this modified setup is laid out in figure 3.6. This improved setup radically eased the task of reproducibility and control in experiments as multiple samples could be tested simultaneously.



Figure 3.5: The basic setup for conducting ion current measurements in a sensitive system

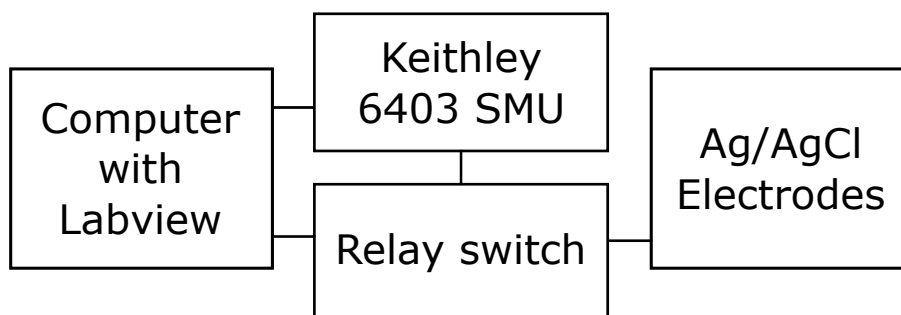


Figure 3.6: With the addition of a relay switch more samples could be handled simultaneously. While the relay switch does increase the impedance of the circuit the relative difference is negligible as the sample impedance is simply so high.

The need arose for the custom Labview program after the provided program showed some anomalous results (see figure 3.7) which turned out to be due to the SMU changing measurement ranges during an experiment. The original software offered very limited control of the SMU's measuring parameters (delay between application of a signal and measurement of the system's response, etc.) so to investigate this anomaly new software was written.

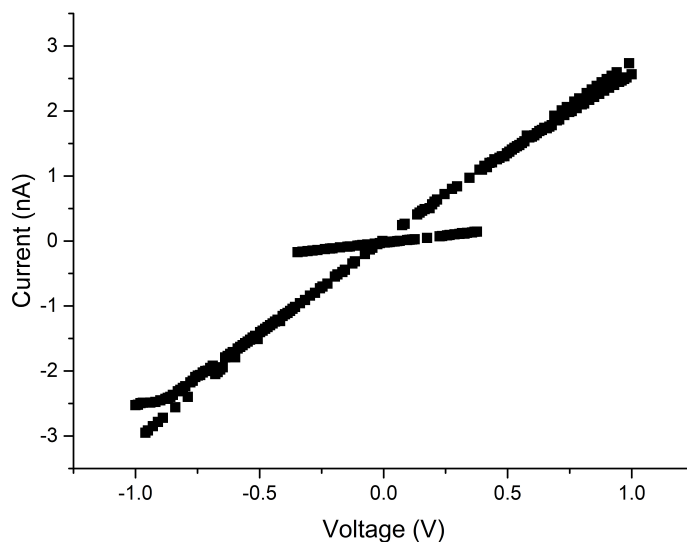


Figure 3.7: Two distinct gradients are observable here which was first incorrectly interpreted as some sort of potential dependent gating or switching present in the GO. However it was in fact found to be an artefact of the measuring equipment when current measurement ranges were swapped. Following this further study of the measuring equipment and development of our own Labview program to control the SMU was necessary.

### 3.4 Electrochemical techniques

Electrochemical techniques such as cyclic voltammetry, galvanostatic charge/discharge and impedance spectroscopy were performed on a Biologic VSP using Ag/AgCl electrodes from BASi.

Cyclic voltammetry is typically used to investigate electrochemical systems such as batteries [157], supercapacitors [112,158] and functionalized electrodes acting as sensors or functional coatings [159]. In cyclic voltammetry the voltage is swept at a certain rate from an initial potential to another and then returned to the initial state. This procedure is performed multiple times and it provides, in the case of supercapacitors which is relevant to chapter 6, information about the amount of charge stored, some information about the kinetics of the process and provides evidence of the mechanism of charge storage (whether there are faradaic reactions present or that most of the charge is stored in the electric double layer).

Galvanostatic charge/discharge experiments provide matching information to cyclic voltammetry experiments. In this case a constant current is applied (often this is stated in terms of a current density) until the system has reached a certain potential. Then the reverse current is applied returning the system to its original state. Galvanostatic charge/discharge experiments show, in well behaved supercapacitors, the resistive loss of the capacitor during discharge and are frequently used to demonstrate the long term stability of a supercapacitor [111,112].

Finally electrochemical impedance spectroscopy provides a host of information open for analysis about the impedance of the system as a function of an applied AC perturbation's frequency. By examining how a system's impedance behaves at different frequencies models can be developed and matched to the data to try to describe and understand the various interfaces and resistances in a system. A classic example for an electrode, such as the Ag/AgCl electrodes used in these experiments is a Randles circuit [160]. This is modelled using two resistances  $R_{sol}$  and  $R_{ct}$ , a capacitance  $C_{edl}$  and a Warburg impedance modelling the diffusion limitation of a system  $W$ .  $R_{sol}$  is the resistance of the electrolyte,  $R_{ct}$  is the resistance required to transfer charge across the interface, the capacitance  $C_{edl}$  describes the dynamic behaviour of the electric double layer under this perturbation (which is quite well approximated with just a capacitor). The Randles circuit is depicted in figure 3.8a and its plot of its impedance spectrum given as a Nyquist plot is in figure 3.8b.

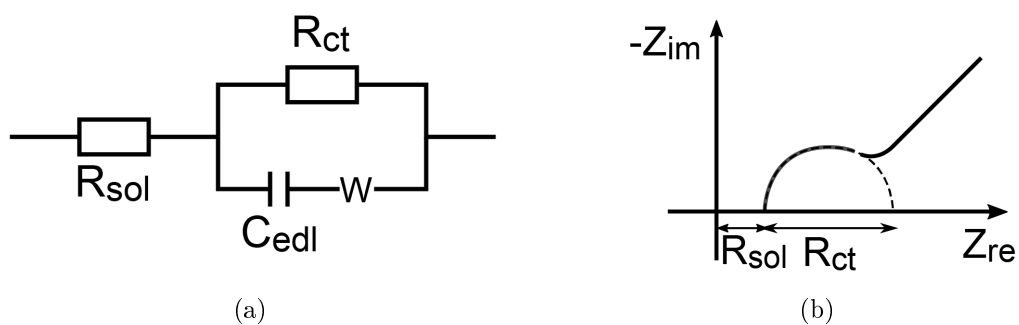


Figure 3.8: a) The Randles circuit is an equivalent circuit model of an electrochemical interface such as where the electrolyte meets the electrode.  $W$  on the schematic refers to the Warburg impedance. b) The Nyquist plot of a Randles circuit plots the real impedance ( $Z_{re}$ ) against the imaginary impedance ( $Z_{im}$ ) which gives a visualization of how the impedance changes with frequency. At high frequencies the impedance of the system approaches  $R_{sol}$ , the lower frequencies are dominated by the Warburg element indicated by the 45° slope of the line at high values of  $Z_{re}$ .

### 3.5 State of the art nanofluidic fabrication

It merits discussion at this point to consider the current state of the art techniques researchers are using to probe nanofluidic systems. Traditional silicon/photolithography based systems [36,37,44] have been extended down to channel heights of  $2\text{ nm}$  [161]. These have been used to perform fundamental demonstrations of nanofluidic properties [36,44] and also to produce devices for various applications [37]. Nafion is another popular [59,162] choice for researchers as the pore size is small  $\sim 5\text{ nm}$  and Nafion is known to have large number of ionizable functional groups at its surface. Typically Nafion is injected into micrometer scale features and allowed set leaving a nanoscopically porous structure behind, as it cannot be as accurately handled Nafion has remained on the application side of nanofluidics. Extensive work performed by Tybrandt and Gabrielson [67,68,72,75] in patterning polymeric bipolar membranes has enabled iontronic style applications of nanofluidic-like planar devices. These techniques describe planar systems which could see application in lab-on-a-chip style devices such as protein concentration [55] and other applications.

Membrane-like systems are more troublesome [85] to integrate into compact devices but allow scalable of applications of nanofluidics (such as desalination and osmotic power generation). Initial works on single conical nanopores [70,163] have lead to interesting applications of the pores as sensors [73] and using arrays of pores as a demonstration of energy extraction from thermal noise [164]. Since these findings nanopores have been drilled into substrates using various techniques- heavy ions [70], focussed ion beam [165], eletrochemical etching [166], to name a few. Studies on isolated single nanotubes have recently emerged as a highly successful method for demonstrating fantastic nanofluidic properties [24,30]. While studies like this and others [166] demonstrate promising results these platforms are not easily scaled, furthermore there is some evidence that these effects may not extrapolate linearly to larger scales [165].

GO with its numerous functional groups may prove to be a new nanofluidic element for on chip sample pre-concentration and other applications if methods can be found to incorporate the material into the standard fabrication process. On the other hand thanks to the scalability offered by GO shear aligned membranes studies performed here can be brought to much larger scales as well.

### **3.6 Use of the experimental techniques in this thesis**

Ion transport studies are a common theme throughout this thesis and used extensively in each of the coming chapters. Chapter 4 is the only chapter that makes use of GO films produced using vacuum filtration, all other chapters take advantage of the superior molecular ordering of shear-aligned nematic phase GO films. Chapter 5 examines patterns of GO films and characterizes them using profilometry, polarized light microscopy and electron microscopy. Chapter 6 uses a four point probe and electrochemical techniques to characterize the studies performed on RGO film samples. Chapter 7 uses ion transport measurements extensively and cross sectioning on a scanning electron microscope to estimate the thickness of a shear aligned GO layer on its porous support.

## Chapter 4

# Graphene based ion rectifier using macroscale geometric asymmetry

### 4.1 Introduction

In this initial work we found an interesting rectification phenomenon in geometrically asymmetric film samples of graphene oxide. Our investigations began as an extension of work performed by Raidongia [35] and the fabrication technique used in this work is based upon Raidongia's. Development of a switch-like element would be quite important if circuit-like implementations of nanofluidics were to be developed. This rectifier is an attractive combination of planar design and uses of PDMS, which is ubiquitous in microfluidics research. It could be useful future projects where microfluidic interconnections might be used to connect different planar elements together. Biosensors based on rectifiers have been demonstrated [73] and remain a driving force in applications of nanofluidic research. In the end this project served to highlight the complexity of the field, as even now, the exact nature of the rectification mechanism observed here remains elusive. From the  $\sim 1\text{ nm}$  pores to film samples on the scale of centimetres, the device, while deceptively simple, has important interactions occurring on vastly different length scales. Self assembled structures such as graphene oxide enable researchers to easily and rapidly study highly confined systems.

In terms of this thesis this work served as its first iontronic component and was to lead, after improved fabrication techniques were developed in chapter 5, to the inside-out super capacitor in chapter 6 which serves as the only iontronic capacitor in the literature. The following work was published in APL Materials in 2014.



## Graphene-based ion rectifier using macroscale geometric asymmetry

S. T. Martin, A. Neild, and M. Majumder

Citation: *APL Materials* **2**, 092803 (2014); doi: 10.1063/1.4894499

View online: <http://dx.doi.org/10.1063/1.4894499>

View Table of Contents: <http://scitation.aip.org/content/aip/journal/aplmater/2/9?ver=pdfcov>

Published by the *AIP Publishing*

---

### Articles you may be interested in

[Realistic-contact-induced enhancement of rectifying in carbon-nanotube/graphene-nanoribbon junctions](#)

*Appl. Phys. Lett.* **104**, 103107 (2014); 10.1063/1.4868410

[Graphene as anode electrode for colloidal quantum dots based light emitting diodes](#)

*Appl. Phys. Lett.* **103**, 043124 (2013); 10.1063/1.4816745

[Near-ultraviolet light-emitting diodes with transparent conducting layer of gold-doped multi-layer graphene](#)

*J. Appl. Phys.* **113**, 113102 (2013); 10.1063/1.4795502

[Rectifying and perfect spin filtering behavior realized by tailoring graphene nanoribbons](#)

*J. Appl. Phys.* **112**, 114319 (2012); 10.1063/1.4768727

[Electrical characteristics and carrier transport mechanisms of write-once-read-many-times memory elements based on graphene oxide diodes](#)

*J. Appl. Phys.* **110**, 063709 (2011); 10.1063/1.3639287

---

**AIP** | Applied Physics  
Letters

Meet The New Deputy Editors



Alexander A.  
Balandin



Qing Hu



David L.  
Price

## Graphene-based ion rectifier using macroscale geometric asymmetry

S. T. Martin,<sup>1,2</sup> A. Neild,<sup>2</sup> and M. Majumder<sup>1,a</sup>

<sup>1</sup>*Nanoscale Science and Engineering Laboratory (NSEL), Department of Mechanical and Aerospace Engineering, Monash University, Clayton, Victoria 3800, Australia*

<sup>2</sup>*Laboratory for Microsystems (LMS), Department of Mechanical and Aerospace Engineering, Monash University, Clayton, Victoria 3800, Australia*

(Received 30 June 2014; accepted 19 August 2014; published online 3 September 2014)

Ion rectification is the asymmetrical conduction of ions through a system under different polarities of applied potentials. In this article we report the finding of a novel form of ion rectification in graphene oxide (GO) and reduced graphene oxide (RGO) films which act as an ensemble array of nanochannels. Rectification is imparted by introducing geometric asymmetry in fluidic inlets to the counter-ion selective nanochannels of GO/RGO which creates asymmetry in the enrichment/depletion effects at the macro-/nano-interface. The devices are made simply by cutting a GO or RGO film into a trapezoid and sealing the film within a Polydimethylsiloxane block so that fluid may only enter through one of two inlets. These devices exhibit rectification ratios larger than 20 (in 1 mM NaCl) while operating at modest voltages [−1 V, +1 V]. © 2014 Author(s). All article content, except where otherwise noted, is licensed under a Creative Commons Attribution 3.0 Unported License. [<http://dx.doi.org/10.1063/1.4894499>]

Microfluidic technologies have the potential to revolutionize analytical sciences by reducing the volume requirement for fluids, providing faster response time-scales, and simplifying large scale parallelization.<sup>1,2</sup> Several technologies are very mature and some are commercially available, however fluidic systems combining micro- and nano-structures are still in their infancy<sup>3,4</sup> underlining that several scientific phenomena that traverse these scales are yet to be fully understood. Nanoscale fluidic systems<sup>5</sup> involving fluid flow across or through structures with one of the dimensions less than 100 nm can exhibit interesting surface charge governed properties.<sup>6</sup> In these circumstances the Debye length

$$\lambda_D = \sqrt{\frac{\epsilon k_B T}{e^2 \sum_i z_i^2 c_i}} \quad (1)$$

(where  $\epsilon$  is the permittivity of the material,  $k_B$  is the Boltzmann constant,  $T$  is the temperature,  $e$  is the charge of an electron,  $z_i$  is the valency of ion  $i$ , and  $c_i$  is the bulk concentration of ion  $i$ ) begins to encroach upon or exceed the characteristic dimension of the nanofluidic device. In such an environment the fluidic properties of ionic solutions deviate from that of the bulk, exhibiting surface charge dependent ionic conduction and in more complex systems rectification of ion currents.<sup>7-9</sup>

Ion rectifiers are artificial analogues of biological ion-channels, which are intracellular pores in cell membranes that aid communication and signaling by being permeable to ionic species; they are intimately involved in the complex machinery of our thought, movement, heartbeat, response, and well-being.<sup>10</sup> Among numerous functions, ion-channels have the ability to respond to electric fields leading to changes in ion current flowing through the channel. A very typical example is rectification

<sup>a</sup>Electronic mail: [REDACTED]



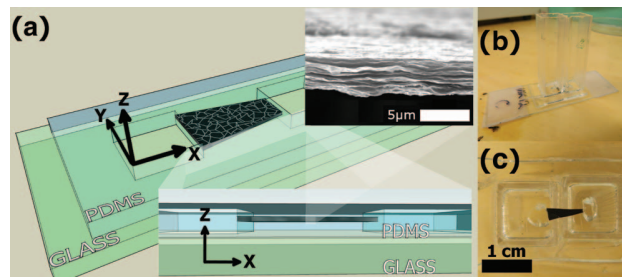


FIG. 1. **GO/RGO-based nanofluidic devices:** (a) Schematic of the device illustrating the continuous sheet structure of the GO/RGO films made from smaller microplates which are embedded in PDMS. The electrolyte reservoirs have not been included for clarity. The inset shows a scanning electron microscope image of the cross-section of a typical RGO film highlighting the layered 2D structure. (b) An image of a completed device used in our experiments. (c) An image of the bottom of a device with the asymmetric (trapezoidal) RGO film in view.

where a change in the polarity of the electric field can produce drastic change in the amount of ion current being supported by the pores.<sup>11</sup>

Developing structurally more robust, synthetic analogues to these complex biological systems is an area of growing interest. We draw attention to three types of artificial systems which describe rectification of ions.<sup>12</sup> The conical nanopore is a system where a conical pore provides the path through a membrane, at the narrow end the length scale is usually less than 20 nm,<sup>8</sup> at the wider end the length scale is often on the order of micrometers. The cause of rectification in nanopores has been the subject of much debate,<sup>12–14</sup> however the asymmetry of the pore is important to how the rectification is achieved. The track etching method<sup>14</sup> using accelerated heavy ions, laser pulling of quartz nanopipettes,<sup>15</sup> or the electron beam stimulated decomposition of silicon nitride membranes<sup>16</sup> illustrates the difficulty in fabricating these nanopores.

Systems that have asymmetrical distributions of surface charge density are the closest analogue to a diode in the nanofluidic domain.<sup>9</sup> Defining regions within the nanochannel with different surface charges has, however, proven to be experimentally challenging but has been realized.<sup>17</sup> These systems rely on an asymmetrical potential field inside the nanochannel, which produces asymmetry in their ion transport behavior.

More recently<sup>7</sup> it has been found that geometrically and electrically symmetrical systems with asymmetric concentrations in electrolyte will also rectify ionic current. Regarding these rectifying properties the ion enrichment/depletion phenomenon<sup>4</sup> is of direct relevance. This occurs due to an imbalance in the ion currents inside the nanochannel and just outside the nanochannel (in the bulk fluid). As a result of these effects counter-ions and co-ions will enrich at one end of the nanochannel (together) and deplete at the opposing end. When the electrolyte in each reservoir is of different concentrations an asymmetry occurs in the enrichment/depletion effects which can cause large sections of the nanochannel to deplete or enrich with ions and the nanochannel to rectify. The asymmetry in this scenario is suggested to be equivalent to an asymmetry in a nanochannel's potential and both effects lead to rectifying transport of ions.<sup>7</sup> In addition to these examples, more exotic systems such as rectification using electromechanical macromolecular tethers attached to the entrances of carbon nanotubes<sup>18</sup> or the use of steric hinderance of large ions in the confines of a carbon nanotube<sup>19</sup> have also been reported.

In a recent publication<sup>3</sup> researchers have demonstrated that surface charge governed conduction is exhibited in a layered film of graphene oxide (GO). GO and reduced GO (RGO) in their film forms are layered structures of many individual GO/RGO flakes, see Figure 1(a), and offer ion transport pathways between these flakes. The flakes themselves are a few layers of graphitic crystals decorated in oxygen bearing functional groups (carboxyls, alcohols, and carbonyls).<sup>20</sup> Although the material is by no means a precision fabricated nanochannel it offers significant advantages over nanofabrication methods such as the enormous ensemble of nanochannels, their characteristic height  $\sim 1$  nm<sup>3,21,22</sup> and the ease (and cost) at which such a device can be produced. Here we report that a structural

asymmetry in the ensemble nanochannels of GO or mildly reduced GO can rectify ion current with rectification ratios exceeding 20.

A schematic of the device in Figure 1(a) along with an image of a working device in Figure 1(b) are provided to give the general form of the device. The asymmetry is created by cutting the GO or RGO film into a trapezoidal shape which is shown in Figure 1(c) and connecting the ends of the film to large fluidic reservoirs. The length of the films used in our experiments had dimensions on the order of mm with the large inlet  $\sim 2\text{--}10$  mm and a small inlet  $\sim 0.5\text{--}4$  mm whilst the thickness was  $\sim 30\text{--}50$   $\mu\text{m}$ . The fabrication method is similar to a previous report;<sup>3</sup> however rectification behavior was not observed in those structurally symmetric devices. The ion transport is measured across the length of the film where the ions move in parallel to the GO/RGO sheets.

GO was produced using modified Hummer's method. For producing mildly reduced GO (RGO), 0.3 g of GO were dissolved in 50 ml of water and reduced in solution with 0.5 g of sodium borohydride at 100 °C for  $\sim 2$  h. The resultant solution was then washed with deionized (DI) water, filtered, and dried. Samples of RGO were then weighed, dispersed in 90 mL Dimethylformamide (DMF) and 10 mL DI water and ultrasonicated until well dispersed. The dispersions were then vacuum filtered onto nylon membranes, dried, and removed. To make the devices a base layer of Polydimethylsiloxane (PDMS) was cured first for the GO/RGO samples to be placed on. The film samples were then cut using a scalpel and carefully placed on the PDMS base and then additional PDMS was poured on top, to embed the sample in a PDMS block. Once cured the embedded films were plasma bonded to glass slides which act as the base of the device, ends of the film were cut open, small holes were cut into the PDMS, wells for the electrolyte were placed on top of the holes and glued into place with more PDMS. The devices then had their wells filled with electrolyte and allowed to wet for at least 24 h. All I/V measurements were conducted on Keithley 6430 sub femptoamp SMU using Ag/AgCl electrodes (BASi, IN, USA) and inside a Faraday cage. Before each test, devices had their open circuit potential checked to ensure that the potential within the devices did not fluctuate at a rate greater than 10 mV/h. For preliminary testing of the GO devices, we used DI water as the electrolyte, which has a conductivity of 0.067–0.1  $\mu\text{S}/\text{cm}$  according to the manufacturer of the system (equivalent concentration of  $\sim 0.6$   $\mu\text{M}$  NaCl). Experiments on RGO devices used 1mM NaCl unless otherwise stated.

Initially experiments were carried out on GO devices and the I-V characteristics have an apparent trend between the inlet ratio of the device and its corresponding rectification ratio as shown in Figure 2(a). Although these experiments demonstrate the proof-of-concept, we must note that the GO devices were structurally unstable because of the solubility of GO. Further investigations were conducted using RGO because of its higher stability in aqueous solutions. Mild reduction was selected because it was hypothesized that extreme reducing treatments would drastically reduce the material's surface charge, restack the exfoliated sheets by strong van der Waals interactions, and render it difficult to wet. It is expected that the mildly reduced GO inter-layer distance is smaller than observed for GO and would be  $\sim 4\text{--}8$   $\text{\AA}$ <sup>21,22</sup> when dry.

Figure 2(b) demonstrates the key rectifying behavior (using an RGO film) and shows the dramatic difference in I-V behavior of a symmetrical (rectangular, inlets size 3.0 mm, length 5.0 mm, thickness 40  $\mu\text{m}$ ) and asymmetric (trapezoidal, inlets sizes were 2.6 mm and 0.6mm, length 7 mm, thickness 40  $\mu\text{m}$ ) fluidic devices. The inlet ratio of the trapezoidal system was 4.3 in this experiment. The rectification ratios for the trapezoidal and rectangular devices were  $20.4 \pm 0.2$  and  $0.847 \pm 0.002$ , respectively. In its conventional definition,<sup>23</sup> the rectification ratio of the trapezoidal system varies widely from 53.3 at 1 V to 16.4 at 0.5 V. Here we calculated the rectification ratio by the ratio of the gradients of lines of best fit fitted to the data at positive and negative applied potentials, this gradient based definition should make comparisons between different systems in our experiments more consistent. Below we will discuss the transient effects of I-V characteristics which are dominant at negative potentials but because of these effects the negative range was truncated to  $[-0.8$  V, 0 V] to determine the rectification ratio. The offset from 0 A at 0 V applied potential and the deviation of the rectangular system's rectification ratio from 1 is attributed to capacitive-like hysteresis in the I-V characteristics. This is confirmed by conducting cyclic voltammetry tests on the rectangular system at multiple scan rates which shows hysteresis curves which shrink as the scan rate is decreased (Figure 2(c)). Although more prominent in the case of the rectangular systems because of the larger

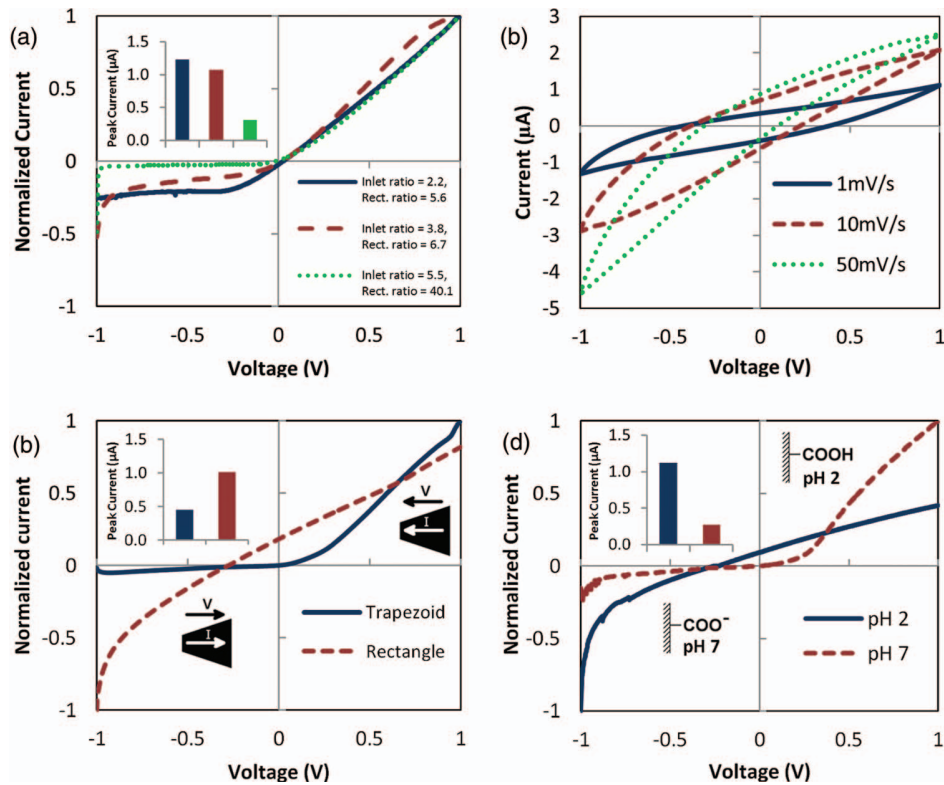


FIG. 2. **Transport properties of GO/RGO-based nanofluidic devices:** (a) The I/V characteristics of GO-based devices. (b) The I/V characteristics of trapezoidal and rectangular RGO-based devices. (c) Cyclic voltammograms of a rectangular device illustrating the system's capacitive-like hysteresis. (d) The pH behavior of a typical trapezoidal system. The increase in conductivity at low pH is attributed to the addition of the  $H^+$  ions and the comparatively low concentration of the electrolyte.<sup>19</sup>

current it supports, both kinds of systems (rectangular and trapezoidal) displayed some transient, scan rate dependent behavior that causes the systems to move away from ideal operation. As these systems were scanned typically from  $-1$  V to  $+1$  V the initial behavior (i.e., the behavior around  $-1$  V) is attributed to transient effects, hence our choice of the potential window  $[-0.8$  V,  $0$  V] for calculating the rectification ratio.

To investigate whether the rectification effect was related to the surface charge of the nanochannels, the effect of pH on the rectification behavior was studied at two pHs, one above the  $pK_a$  ( $\sim 4$ ) of carboxylic acid groups (pH 7) and one below that (pH 2). The results in Figure 2(d) confirm that the rectification behavior is related to the surface charge however the change in conduction due to the presence of  $H^+$  ions also contributes to this effect. In this typical experiment, the rectification ratio changed from  $13.1 \pm 0.1$  at pH 7, when the carboxylic acids groups are deprotonated to  $0.754 \pm 0.004$  at pH 2, when they are protonated. Based on this evidence, we can conclude that rectification is due to a combination of nanoscale surface charge effects (Figure 2(d)) and macroscale geometric asymmetry (Figure 2(b)), both are necessary for these devices to function.

The mechanism of rectification observed here differs from those reported in the following ways: the surface charge on GO/RGO is uniformly distributed throughout the film so ignoring the edge effects, one can say that the surface potential is uniform throughout the film, the electrolyte is symmetrical at either end and the nanochannel's characteristic dimension is reasonably uniform throughout the films. A model describing our proposed mechanism of rectification is shown in Figure 3.

It is known that the concentration of counter ions will exceed the concentration of co-ions in the surface charge dominated nanochannel region, for a symmetrical monovalent electrolyte of  $A^+$

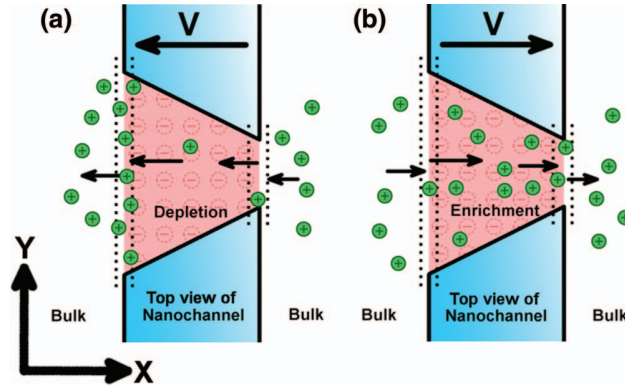


FIG. 3. **The states of the nanofluidic devices due to applied potentials:** Here only counter-ions are illustrated as they dominate this effect. The fields of red negative charges represent the surface charge on the film. The arrows at the interfaces give an indication of the relative magnitudes of the counter-ion currents at the end regions of the nanochannel. In (a) the nanochannel is in depletion, whereas in (b) the nanochannel is enriched with counter ions.

and  $B^-$  they are related by

$$[A^+]_{nano} = \alpha[B^-]_{nano}, \quad \alpha > 1. \quad (2)$$

The following relations are found between the ion currents of the “macro” (bulk) and “nano” (within the nanochannel) interfaces at each end region of a negatively charged nanochannel (marked by dotted lines in Figure 3):<sup>4</sup>

$$i_{macro}^{A^+} = \left( \frac{\mu_{A^+} + \mu_{B^-}/\alpha}{\mu_{A^+} + \mu_{B^-}} \right) \cdot i_{nano}^{A^+} \quad (3)$$

and

$$i_{macro}^{B^-} = \left( \frac{\mu_{B^-} + \alpha \cdot \mu_{A^+}}{\mu_{A^+} + \mu_{B^-}} \right) \cdot i_{nano}^{B^-}, \quad (4)$$

where  $i_{macro}^{A^+}$  is the counter-ion current outside of the nanochannel,  $i_{nano}^{A^+}$  is the counter-ion current inside of the nanochannel,  $\mu_{A^+}$  is the electrophoretic mobility of the counter-ion and the co-ion,  $B^-$ , symbols follow analogously. Since  $\alpha > 1$  it follows that:  $i_{nano}^{A^+} > i_{macro}^{A^+}$ . Depending on the direction of the applied potential relative to the interface at either end of the channel this will result in enrichment or depletion of ion  $A^+$  in the nanochannel’s end regions. For example, for a negatively charged nanochannel, the enrichment will occur at the cathode (–ve electrode).

If it is assumed that the electric field within the nanochannel is relatively constant then it follows that the counter-ion currents in the nanochannel can be described by

$$i_{nano, large}^{A^+} = zFE_{nano}S_{large}\mu_{A^+}[A^+]_{nano}, \quad (5)$$

and

$$i_{nano, small}^{A^+} = zFE_{nano}S_{small}\mu_{A^+}[A^+]_{nano}, \quad (6)$$

where  $z$  is the valency,  $F$  is the Faraday constant,  $E_{nano}$  is the electric field within the nanochannel,  $S_{large}$  is the cross-sectional area of the large end of the trapezoid, and  $S_{small}$  the smaller. Then it follows simply that

$$\frac{i_{nano, large}^{A^+}}{S_{nano, large}} = \frac{i_{nano, small}^{A^+}}{S_{nano, small}}, \quad (7)$$

which gives most importantly  $i_{nano, large}^{A^+} > i_{nano, small}^{A^+}$ . This effectively results in the entire nanochannel behaving like the small end region. When the large end goes into ion enrichment, more counter-ions are being removed from the nanochannel than are able to enter it at the small end, and the

entire channel becomes counter-ion depleted (Figure 3(a)). In the opposing case (Figure 3(b)) the depletion of the larger end results in the enrichment of counter-ions within the nanochannel due to the difference between the two inlet ion currents. When the channel is enriched the device is in forward mode and the nanochannel conducts a greater number of ions, when it is depleted the device is in reverse mode and the nanochannel's current shrinks to current values as small as  $\sim 10$  nA (Figure 2(b)).

It is important to note that there is an additional assumption here: the counter-ion concentration is large compared to the co-ion concentration ( $\alpha$  is large). This is quite important to establish rectification because the exact opposite occurs with the  $B^-$  ions. If the co-ion current could be considered much smaller than the counter-ion current then clearly the hypothesis stated seems to correctly describe and give an understanding of this effect. This assumption is in agreement with findings<sup>24</sup> where co-ions were shown to have very small permeability in nanochannels compared to counter-ions, particularly where the electric double layer is predicted to have a large overlap (in this case the characteristic height is  $\sim 1$  nm and the Debye length for 1 mM NaCl is  $\sim 10$  nm).

In the pH data (Figure 2(c)) it is observed that reduction in surface charge disabled the device's rectifying capability. Since protonating the functional groups on the RGO effectively reduces  $\alpha$ , the results in Figure 2(c) agree with our proposed model. A decrease in pH would effectively increase the co-ion permeability of the nanochannel. Additionally it does not stop the pH 2 system exhibiting the enrichment/depletion phenomena, only that there is insufficient difference in co-/counter-ion current to cause rectification.

The device in its functionality is most similar to an asymmetric concentration rectifier, in which depletion or enrichment zones are created at the inlets of the nanochannel. Depending on the applied bias, the device will allow the enrichment/depletion state of the smaller end of the nanochannel to affect the entire nanochannel structure, enriching or depleting it. The mechanism appears to simply depend on the fact that the device has asymmetry in the ion currents through the two inlets, when they are sufficiently different the rectification can occur. Such a physical re-arrangement of ions over millimeters of material also would take some appreciable time (given the modest values of ion mobilities in water) which agrees with the scan-rate anomalies observed in these systems. Whilst this is by no means a conclusive understanding of the scan-rate dependence it does suggest reasons as to why it may be occurring.

In conclusion a new cause of ion rectification has been demonstrated and a basic model motivating its existence has been proposed. The effect depends on the surface charge and the dimensions of the nanochannels of a layered GO/RGO structure which makes the nanochannels counter-ion selective, while the relative difference in size of the device inlets causes the depletion/enrichment effects to affect the entire nanochannel which causes large asymmetry in the ion-transport behavior. This work shows the ease at which devices can be made which exhibit complex nanofluidic phenomena. By additional chemical modification additional functionality like biochemical sensing could be achieved and even larger rectification ratios could also be realized.

The authors acknowledge funding from Australian Research Council (LP 110100612 and DP 110100082). The authors acknowledge use of facilities within the Monash Centre for Electron Microscopy.

<sup>1</sup>G. M. Whitesides, *Nature (London)* **442**, 368 (2006).

<sup>2</sup>T. M. Squires and S. R. Quake, *Rev. Mod. Phys.* **77**, 977 (2005).

<sup>3</sup>K. Raidongia and J. Huang, *J. Am. Chem. Soc.* **134**, 16528 (2012).

<sup>4</sup>Q. Pu, J. Yun, H. Temkin, and S. Liu, *Nano Lett.* **4**, 1099 (2004).

<sup>5</sup>R. B. Schoch, J. Han, and P. Renaud, *Rev. Mod. Phys.* **80**, 839 (2008).

<sup>6</sup>D. Stein, M. Kruithof, and C. Dekker, *Phys. Rev. Lett.* **93**, 035901 (2004).

<sup>7</sup>L. Cheng and L. J. Guo, *Nano Lett.* **7**, 3165 (2007).

<sup>8</sup>Z. S. Siwy, *Adv. Funct. Mater.* **16**, 735 (2006).

<sup>9</sup>H. Daiguji, *Nano Lett.* **5**, 2274 (2005).

<sup>10</sup>B. Hille, C. M. Armstrong, and R. MacKinnon, *Nat. Med.* **5**, 1105 (1999).

<sup>11</sup>Y. Jiang, A. Lee, J. Chen, M. Cadene, B. T. Chait, and R. MacKinnon, *Nature (London)* **417**, 515 (2002).

<sup>12</sup>L. Cheng and L. J. Guo, *Chem. Soc. Rev.* **39**, 923 (2010).

<sup>13</sup>H. S. White and A. Bund, *Langmuir* **24**, 2212 (2008).

<sup>14</sup>Z. Siwy, Y. Gu, H. A. Spohr, D. Baur, A. Wolf-Reber, R. Spohr, P. Apel, and Y. E. Korchev, *EPL* **60**, 349 (2002).

- <sup>15</sup> C. Wei, A. J. Bard, and S. W. Feldberg, *Anal. Chem.* **69**, 4627 (1997).
- <sup>16</sup> C. Ho, R. Qiao, J. B. Heng, A. Chatterjee, R. J. Timp, N. R. Aluru, and G. Timp, *Proc. Natl. Acad. Sci. U.S.A.* **102**, 10445 (2005).
- <sup>17</sup> R. Karnik, C. Duan, K. Castelino, H. Daiguji, and A. Majumdar, *Nano Lett.* **7**, 547 (2007).
- <sup>18</sup> J. Wu, X. Zhan, and B. J. Hinds, *Chem. Commun.* **48**, 7979 (2012).
- <sup>19</sup> J. Wu, K. Gerstandt, H. Zhang, J. Liu, and B. J. Hinds, *Nature Nanotechnol.* **7**, 133 (2012).
- <sup>20</sup> D. R. Dreyer, S. Park, C. W. Bielawski, and R. S. Ruoff, *Chem. Soc. Rev.* **39**, 228 (2010).
- <sup>21</sup> S. Park, J. An, I. Jung, R. D. Piner, S. J. An, X. Li, A. Velamakanni, and R. S. Ruoff, *Nano Lett.* **9**, 1593 (2009).
- <sup>22</sup> I. K. Moon, J. Lee, R. S. Ruoff, and H. Lee, *Nat. Commun.* **1**, 73 (2010).
- <sup>23</sup> I. Vlasiouk and Z. S. Siwy, *Nano Lett.* **7**(3), 552 (2007).
- <sup>24</sup> A. Plecis, R. B. Schoch, and P. Renaud, *Nano Lett.* **5**(6), 1147 (2005).

## Chapter 5

# The patterning of graphene oxide liquid crystals

### 5.1 Introduction

While materials and simple structures, such as membranes [125] and fibres [167,168] have been prepared from graphene oxide (GO) liquid crystals there are many potential applications in being able to pattern the liquid crystals on a substrate. Works such as El-Kady's [111] have attracted significant attention and could potentially be further improved with the more ordered microstructure of GO liquid crystals. Within the fields of micro- and nanofluidics one of the more difficult task in fabrication is incorporating membrane structures into conventional lab-on-a-chip like devices [85]. While there are many techniques suggested in the literature [162,169–171], the problem remains open to significant improvement.

Controllably patterning nanofluidic components on large scale could enable the microscopic phenomena of this regime, such as rectification, to be used in more complex circuit-based systems. Being able to scale nanofluidic systems such as Siria's boron nitride nanotube experiment [30] or the more recent studies on molybdenum disulfide nanopores [166] would have enormous implications for the until now relatively inaccessible energy associated with salination. Access to nanofluidic phenomena typically requires photolithographic approaches [36,37] such as etching shallow silicon trenches [40,161]. One of the issues with this is that even at trench depths of  $\sim 100\text{ nm}$  many of the effects of nanofluidics remain weak and perform well only at very low concentrations. This is a direct consequence of the scaling of the Debye and Dukhin lengths discussed in chapter 2.

There are methods that take advantage of molecular tube-like structures such as carbon nanotubes [172] and boron nitride nanotubes [30]. Commonly these techniques grow the tubes in place and then fabricate structures onto them to isolate the inlets and outlets. This has allowed some intriguing fundamental studies of nanofluidic transport in these systems which due to the simple geometry can be approximated or partially analytically solved using the Poisson Nernst-Planck equations [24,30,173]. Whilst insightful the results found in these systems are difficult to scale to larger membrane like systems. Even carbon

nanotube membranes have not been able to completely follow in the success of studies on individual tubes.

The conical nanopore is a highly successful geometry in nanofluidic studies. They are commonly made by either track-etching a defect in a membrane (created by a linear particle accelerator) or more accessably by studying glass or quartz nanopipettes [174,175]. The production of membranes with multiple defects has allowed this geometry to scale to a variety of applications [76] but isolated nanopores have proven to be highly interesting for detection of nanoparticles, particularly DNA [176–179].

The final method, which is most closely associated with this work here is to take an existing structure whose pore size falls into the required size range for nanofluidics, such as Nafion [162,180]. Two dimensional materials are quite interesting for this field of study, as they self-assemble into a disordered stack of 2D channels. Patterning membrane-like structures is an attractive approach as it takes advantage of the self-assembly of the membrane, is scalable and doesn't require photolithography or complex fabrication techniques. Recently it was demonstrated [35] that one can use the layered structure of GO as a rapid and easy way to self-assemble a large network of nanochannels. Other two dimensional materials however remain relatively un-explored (vermiculite [181] being the only other material studied in this manner that the author has come across) but there's great promise in these materials in bringing nanofluidics to larger scales.

There's been significant interest within separation science in graphene and graphene-like materials such as GO [130,131]. Other studies demonstrating energy harvesting via streaming currents [2], curious permeation of ions [130] and brand new electrokinetic phenomena [182] suggest that further investigation is warranted. Whilst numerous patterning techniques in the literature work directly with graphene itself [183–185] for a variety of purposes there are advantages in using these derivatives like GO to pattern [186], such as the ability to process the nanosheets in solution [104] and as found more recently the ability of GO to form aqueous lyotropic nematic liquid crystals [137,187].

In this chapter the patterning is produced using moulds, fabricated using a vinyl cutter, into which a nematic phase GO liquid crystal was placed and then sheared. The patterned cutting of vinyl and other polymer films or xurography [145] has been commonly used in the literature to design microfluidic platforms [146,147] made from polymer films and is attractive because it allows rapid fabrication without the need for photolithography - it has not previously been used in conjunction with nanofluidic systems.

Once the desired film shape is produced the GO can be hydrated and its interesting nanofluidic transport properties [130,131,188] can be studied. In addition to ion transport studies these films have potential applications such as planar electrodes (when suitably reduced) for energy storage [189] and chemical and biological sensing [190], integration as membranes on lab-on-a-chip devices [59], strain sensors [191] and in capillary electrochromatography. This work demonstrates the promise GO offers for rapid, simple and industrially scalable nanofluidics that could be integrated on to lab-on-a-chip type applications.

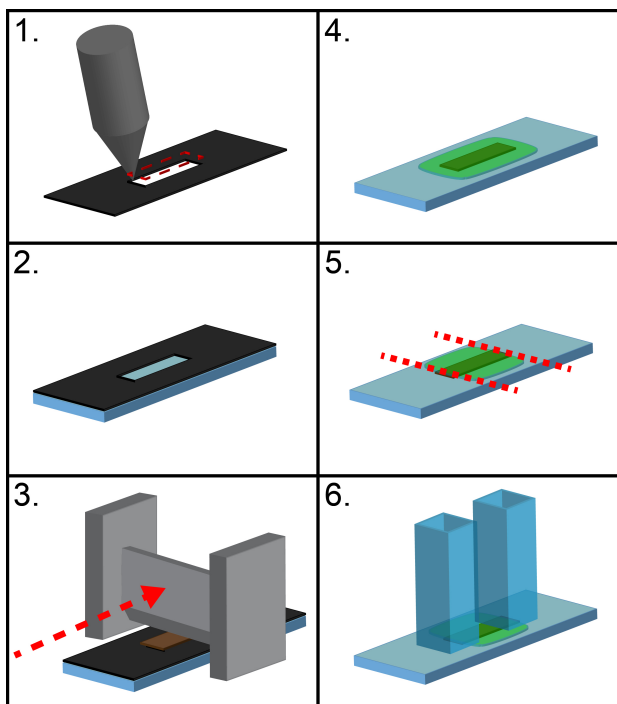


Figure 5.1: Fabrication procedure for making a patterned film and then a PDMS based device. 1) A vinyl mould is cut using a plotter cutter, 2) The vinyl is adhered to a glass substrate, 3) GO is spread over the vacancy in the mould and is sheared using a doctor blade, 4) PDMS is cast over the device and quickly set at  $150^{\circ}\text{C}$ , 5) The ends of the film are opened with a mechanical blade, 6) Reservoirs are bonded on top of exposed ends and are filled with electrolyte.

## 5.2 Experimental methods

This section examines the fabrication of GO patterns using xurographic techniques. The techniques used to characterize the patterns in terms of their microstructure, resolution and fidelity are discussed. Finally the GO patterns are fabricated into planar nanofluidic devices to demonstrate surface charge governed conduction. The conditions of these experiments are detailed.

### 5.2.1 Fabrication of patterns

Patterns were created using software and cut into an adhesive vinyl film using a Roland SV-8 Stika cutter. The vinyl used was Metamark series 7 vinyl with a solvent based acrylic adhesive. The pattern was then adhered to a glass microscope slide. From there GO is cast into the mould and once dry the mould is removed leaving the GO pattern in place. A schematic of this process is given in figure 5.1. The shear casting procedure using GO was pioneered in Akbari et al. [125] but using a doctor blade to shear mixtures has been experimentally explored extensively for slurries [192–194] and theoretically [195, 196]. The GO is placed on a smooth substrate and the doctor blade is swept over the liquid crystal shearing it. The height of the doctor blade is set to be  $\sim 30\ \mu\text{m}$  above the vinyl substrate, which has a thickness of  $\sim 100\ \mu\text{m}$ . Speed analysis of the blade was performed by filming

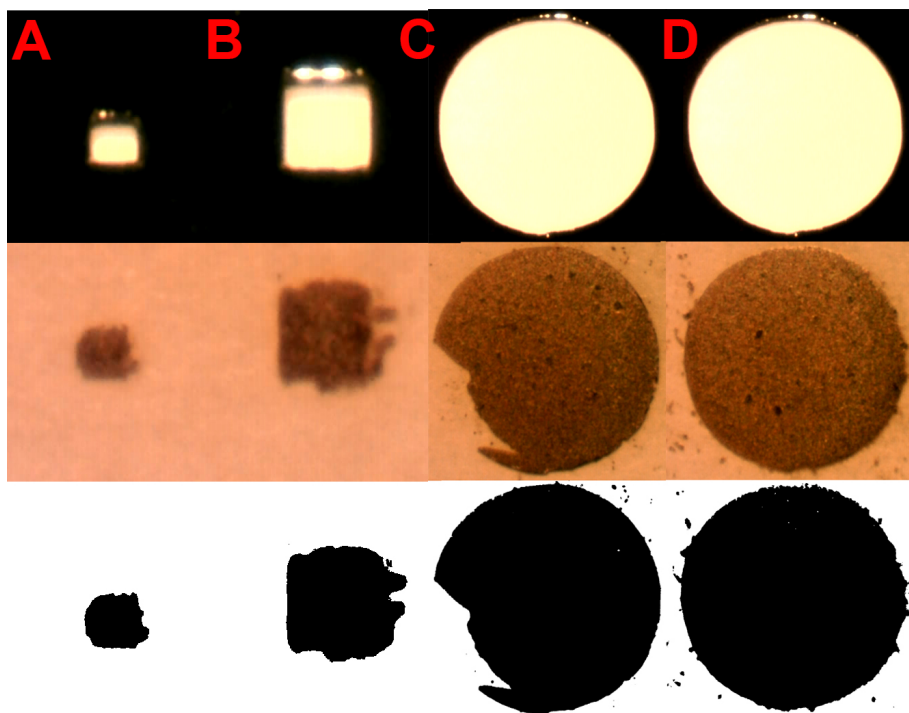


Figure 5.2: Binary image analysis conversion of a) an 0.8 mm square, b) 1.5 mm square, c) a 10 mm circle with a tearing defect and d) a pristine 10 mm circle, please note that analysis considered only continuous bodies over a certain area threshold so that blotches such as those present in c) and d) were not analyzed by the software.

the user when performing the casting action. The films taken were then analysed to yield a rough speed at which the blade moves at when it is over the sample. From 5 tests the average velocity was found to be  $1.7 \pm 0.1 \text{ m.s}^{-1}$ . Given a height of  $\sim 130 \mu\text{m}$  from the bottom of the blade to the glass substrate the shear rate experienced by the GO at the glass interface is about  $\sim 13000 \text{ s}^{-1}$ .

### 5.2.2 Film characterization techniques

#### Film thickness and roughness

To characterize the shape, height and roughness of the films, profilometry of the GO films was performed on an Ambios XP 200 (stylus profilometer) and a Bruker Contour GT-I (optical profilometer). A typical measurement of considerable importance to a large number of fields is the thickness of a GO film. Most researchers opt for a cross section of the film prepared either by focussed ion beam or liquid nitrogen shattering of the membrane and its support (as done in [125]). As the films in this work have been typically deposited on glass substrates which are relatively clean and smooth optical profilometry and stylus profilometry can gather significantly more data than SEM imaging of a cross section. Molecular ordering was also examined using an LC-Polscope, which is described in chapter 3.

### Shape and fidelity characterization

Binary image analysis (BIA) was used to examine the patterns and how they differed from the mould that made them. BIA can be performed using simply a photograph. In this particular case images of samples were taken through a microscope in order to examine the shape of the sample relative to the mould which formed it. BIA converts the image into something that is simply black or white (1 or 0), as depicted in figure 5.2 which then allows object area, perimeter and a host of other geometric metrics to be calculated. Selection of the correct threshold is critical as it will set the intensity at which the boundary around the film will be calculated. Fortunately GO at the particular thickness examined is dark brown which contrast nicely against a white background which makes selecting a particular threshold value relatively easy. By keeping the lighting and sample position constant the threshold value could then be held constant for all samples which is essential so that images of the samples have equitable standing.

Once collected the metrics calculated based on the binary images provide a large amount of statistical information based on the shape of these images. BIA doesn't provide a complete picture of the sample's structure (in fact it provides no information on the structure other than some partial information of the sample's perimeter) thus needs to be combined with other techniques to give a complete picture.

Binary images of both the resultant films and the moulds themselves were used in these experiments as the plotter cutter doesn't faithfully reproduce the dimensions programmed into it at low length scales. This is due to the accuracy of the stepper motors, simplicity of the blade design, the cutting technique and deformation of the vinyl under the applied blade pressure.

#### 5.2.3 Nanofluidic demonstration

Previous nanofluidic device designs based on GO [35,60,197] have used polydimethylsiloxane (PDMS), however there is a problem here. The PDMS is able to invade into the film and partially (or completely) block the array of channels, as illustrated in figure 5.3. PDMS sealed samples were cured at different temperatures allowing the PDMS to penetrate different depths into the sample, this resulted in changes in the device's conductance. It is not clear whether a device produced with a vinyl seal completely prevents ion transport other than through the GO so PDMS was preferred for these tests.

In demonstrating the nanofluidic potential of patterned films of GO, 8 devices were produced of two thicknesses (4 devices for each thickness). The two thicknesses fabricated were  $2.1 \pm 0.3 \mu m$  and  $7.1 \pm 0.3 \mu m$ . The thickness data were collected using the optical profilometer. The devices then had PDMS cast on them and were cured at  $150^\circ C$ , so as to reduce the effect of PDMS infiltration. While exposing the GO to this temperature reduces it, the exposure time was 5 minutes and thus only slight reduction occurred. It was supposed that one might be able to estimate the PDMS penetration depth  $\delta$  by comparing the conductance data to the thickness data.

A distinct difference between this work and those previous is that the shape of the film is defined by the mould whereas works prior to this relied on manual cutting to define

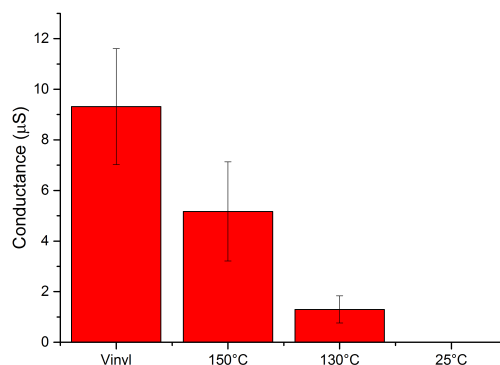


Figure 5.3: The conductance of a series of devices, sealed using vinyl (labelled) or PDMS (curing temperature listed) was monitored for 20 hours in 1 mM NaCl electrolyte. The 25°C sample had an average conductance of 9 nS.

the shape of the film. It should be noted that manual cutting is still used to remove excess GO but the shape of the resultant film is defined first by the mould. Sacrificial lengths of film are included in the designs so that the seal covers the desired structure (figure 5.4). Figure 5.4 also has an image of an alternate seal design using the vinyl adhesive used to form the GO patterns. This seal’s adhesive was found to weaken in high salt concentrations and couldn’t provide the same robust experimental design as a PDMS seal.

The devices were produced to demonstrate surface charge governed conduction as described in chapter 2, which has already been demonstrated in hand cut vacuum filtration films of GO [35]. This experiment is performed by hydrating the GO devices with the lowest concentration of electrolyte considered (here 0.1 mM KCl) and giving sufficient equilibration time (around 12 hours) and then measuring the conductance of the device using ion current measurements. Each time the concentration is increased care was given to provide plenty of equilibration time and replacement of electrolyte that had sat in the cell for more than 12 hours. In this way the pH of the electrolyte could be maintained at around 5.5 – 7, the change here being due to absorption of carbon dioxide from the air. While the pH could be more accurately maintained using a buffer it is quite impossible to achieve the low ionic strengths required due to the buffer’s conductivity.

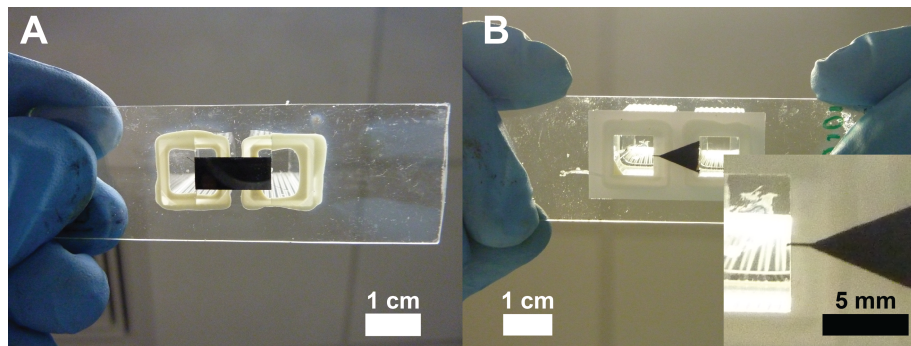


Figure 5.4: a) A PDMS based device which measures 14 mm long, b) a typical rectifier sealed in vinyl with a fine  $200\ \mu\text{m}$  tip,  $\sim 2\ \text{mm}$  of tip are what remains of a longer sacrificial thin film that is washed off after the relevant parts of the rectifier are protected by the vinyl.

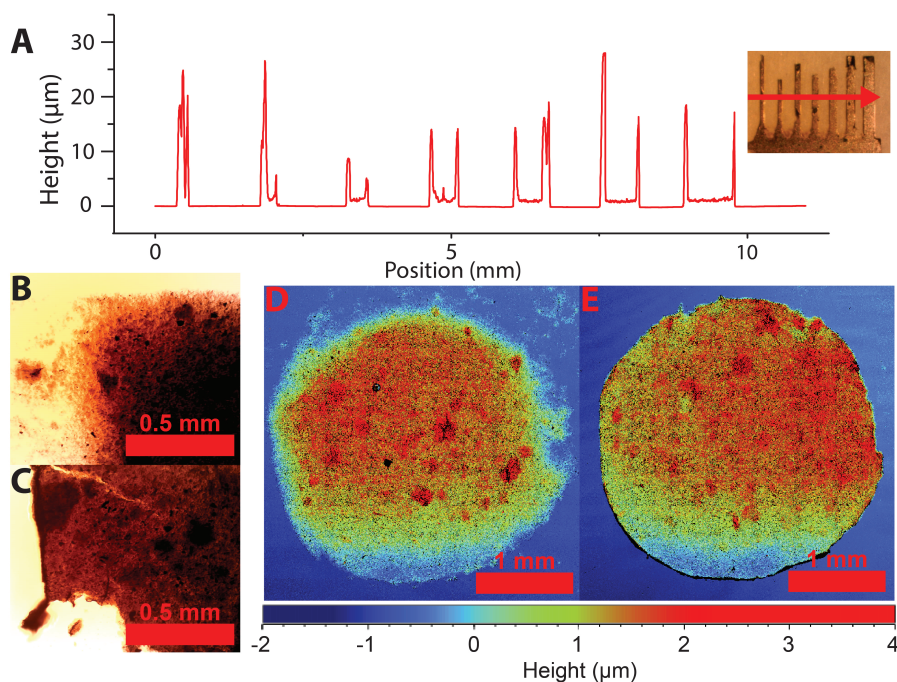


Figure 5.5: a) Profile of interdigitated fingers which have burring present on their edges, the inset shows a photograph of the interdigitated structure. Micrographs of film extremities in two cases; low in-mould drying time, (b)) and high in-mould drying time (c)) which lead to different defects at the film edges. Optical profilometry indicates that whilst the centre of the films doesn't seem to change as a function of the mould removal time the edges do- the two samples had their moulds removed at 2 (d) and 5 (e) minutes respectively.

## 5.3 Results

Once dry the resultant films form layered structures with nanometric interlayer spacings between each GO sheet, which form the pores of the structure. While the thickness of the film is dominated by the rheology of the GO and surface properties of the substrate, it is easily controlled by simply casting the GO multiple times. This method was used to produce the two different sample thicknesses in the nanofluidic demonstration. Shear casting processes like this offer good thickness control [125], so here we concentrate on the degree of lateral dimension definition that can be obtained by using vinyl moulds, this is of crucial importance for the rectifiers in the previous chapter (the performance of which is dependent on the geometry), repeatability in experimentation and in applications such as interdigitated electrodes [111].

### 5.3.1 Shape and fidelity of resultant patterns

The most immediate differences can be observed when one compares samples that had their vinyl mould removed whilst the GO was still 'wet' and those that were given sufficient time to dry in their mould (which can be seen in figure 5.5). In this wet case there is a sudden step created between the prism of cast GO liquid crystal and the unoccupied substrate where the vinyl is removed. This causes the GO to flow and lose definition at its edges. The wet film thickness is smaller than the capillary length (which is  $\sim 2.2\text{ mm}$ )

$$l = \sqrt{\frac{\gamma}{\rho g}}, \quad (5.1)$$

where  $\gamma$  is the surface tension ( $\gamma \sim 49 \text{ mN.m}^{-1}$  for a GO concentration of  $40 \text{ mg.mL}^{-1}$  [125]),  $\rho$  is the density of the GO (as the volume fraction is low, this is close to that of water) and  $g$  is the acceleration due to gravity. For distances shorter than the capillary length the surface tension forces dominate the dynamics. What results is a surface tension driven hydrodynamic levelling of the fluid much like what is observed in rod coating [198]. However the distinct difference here is that the levelling time is greater than the drying time

$$t_{dry} = \frac{\Delta h}{J}, \quad (5.2)$$

where  $h$  is the thickness of solvent required to evaporate to cause solidification of the film and  $J$  is the evaporation current. The outcome of this is smearing of the edge of film samples prepared in this manner as shown in figures 5.5b and 5.5d.

If the GO is allowed more time in the mould at around the 5 minute mark there is a visible change observable at the extremities of the sample - they have solidified. Exact elucidation of this point is difficult due to the swiftness of the process and the limited rate at which the vinyl can be removed however from experimental observation it occurs around the 5 minute mark for a temperature of  $23^\circ\text{C}$ , wet film thickness of  $\sim 100 \mu\text{m}$  and lateral feature size on the order of  $1 \text{ mm}$ . Mould removal after this time requires the fracturing of the GO overlapping from the mould recess to the vinyl mould and is discussed later on in the context of shrinking the feature size limit. This fracturing is evident in film defects from films with high in-mould drying times (figure 5.5c). Film drying in itself is a complex topic and the two extreme examples (dry and wet) chosen here are used to ease the discussion and don't provide a comprehensive overview of the host of phenomena found in this topic.

Images taken using a microscope were converted to binary images and then analysis was performed on the processed data. Images of the test mould are shown in figure 5.6a. To compare samples to one another the area of each sample was calculated using binary image analysis and the difference between this and the mould area was then normalized by the mould area to give the figure of merit for each film shape. Samples which have their vinyl moulds removed at later times tend to have higher degrees of fidelity to their mould, this is particularly evident with larger features (figure 5.6b), this is logical as the later removal times mean that the films are relatively dry when the supporting mould is removed. Negative values of normalized area indicate tearing of the film (such as figure 5.2c) which was more common with the circular test shape. This is thought to be because the connection to the vinyl mould is stronger due to the lack of sharp edges in the shape so there is a longer continuous overlapping film layer between the GO on the mould and the GO in the mould's recess. The smallest features ( $0.8 \text{ mm}$  diameter circles and  $0.8 \text{ mm}$  length squares) are largely delaminated at higher in-mould drying times figure (5.6c) which results in fewer data points at these higher times. Here the bond between the film and the

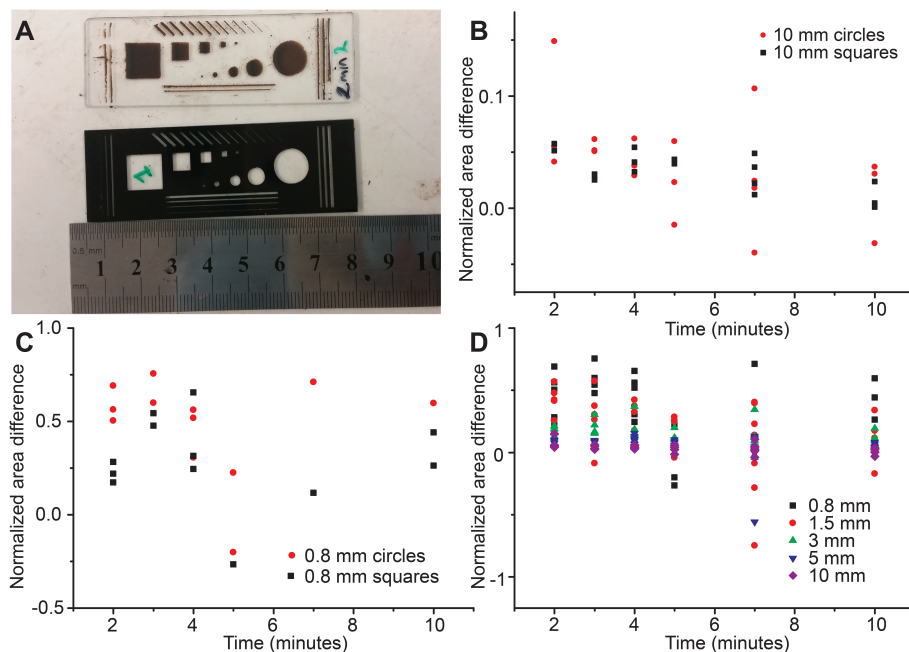


Figure 5.6: a) Photograph of a vinyl mould and an example of a resultant GO patterned film (the squares and circles that were tested and studied had critical dimensions (diameters or lengths) of  $0.8\text{ mm}$ ,  $1.5\text{ mm}$ ,  $3\text{ mm}$ ,  $5\text{ mm}$  and  $10\text{ mm}$ ), b) a comparison of area difference between that of the cast object and that of the mould (normalized by the mould area for all data in these figures) for  $10\text{ mm}$  features, c) the same comparison plotted for  $0.8\text{ mm}$  features and d) normalized area difference for various sized features.

excess GO on the mould is so strongly developed that it overcomes the adhesion to the glass substrate. Features produced at low in-mould drying times don't accurately hold their shape due to the edge of the film flowing before drying as illustrated in figure 5.6c. This spreading however, is not captured well in the binary image analysis and is better observed and described using optical profilometry (figure 5.5d). Spreading could be controlled by changing the surface properties of the substrate or by increasing the concentration and thus the viscosity of the GO. As this spreading is largely driven by surface wetting to the glass changing to a more hydrophobic surface could reduce or eliminate this effect however a change of substrate introduces new issues such as dewetting and defects in the resultant thin film [125].

Fine features of  $200 \pm 20\ \mu\text{m}$  (figure 5.4a) can be resolved better with high in-mould drying times but as the area of these features is small on the glass they tend to tear and be delaminated when the mould is removed. Thus consideration of the mould removal and careful design are required. It was found that long thin structures work best relative to the removal direction which is reflected in studies performed on the tearing of adhesive films [199]. As the force due to adhesion at the crack tip is proportional to the width of the GO film and the fracture energy doesn't depend on this width (rather the film thickness), a greater portion of the work done on narrower films is used to fracture the GO-vinyl interface than on wider films. There is a general trend across all drying times that larger features are more accurately replicated which isn't surprising given that all films have

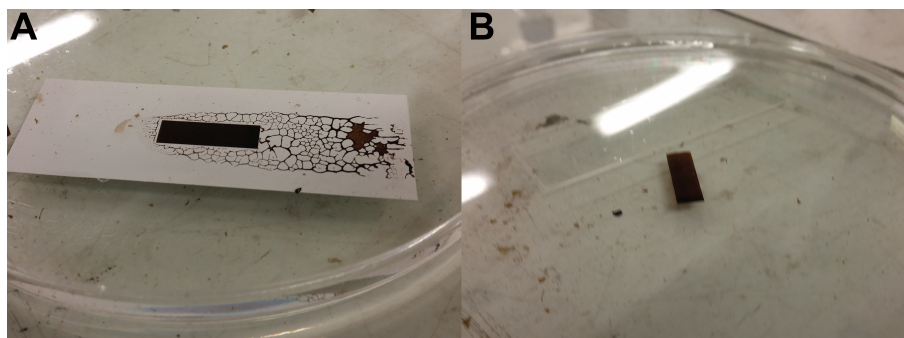


Figure 5.7: a) A sample still in its mould is placed in a shallow water bath, b) after a while the water infiltrates the film and causes it to expand and debond from the substrate and float free in the water.

similar thickness so edge spreading effects are minimized in larger patterns and the effect of delamination and edge defects are also minimized for larger areas (figure 5.6d).

Delamination for this particular application is not desired however it is possible also to controllably delaminate the film patterns by simply immersing the substrate in water before the vinyl mould is removed. The hydrated GO films expand and debond from the glass substrate as can be seen in figure 5.7. With some gentle teasing patterns can be floated onto an arbitrary substrate. To remove a pattern from the glass is a surprisingly facile task. The pattern is taken whilst still in the mould and immersed in water. After approximately 10 minutes the sample expands sufficiently that it typically pops out of the mould. Once free in the water the pattern can then be located onto an arbitrary substrate and dried.

### 5.3.2 Surface roughness and film order

The 3 mm diameter circle from each sample produced was then examined for its roughness. As the optical profilometer had difficulty measuring the edge artefacts on some of the samples (those with high in-mould drying times, see the black regions in figure 5.5e), the area considered for surface roughness was a 2 mm diameter circle placed in the centre of the circular film. It was found that drying times don't have a strong effect on surface roughness, suggesting that their effect is limited to the morphology of the edge of the film which can't be reliably probed with this technique (figure 5.8a). For the samples considered in this test the root mean square surface roughness was  $515 \pm 160 \text{ nm}$ , averaged over 19 samples.

Roughness has a modest trend with increasing blade height (figure 5.8b) which agrees with the fact that at higher blade heights the shear applied to the fluid would be decreased, leading to poor molecular order and increased roughness of the resultant film. Initial studies of the effect of speed (comparing hand casting to a doctor blade pushed by a syringe pump at  $18 \text{ cm.min}^{-1}$ ) don't clearly show a trend with roughness despite the very large difference in applied shear.

As can be seen in figure 5.5a, the interdigitated finger pairs have a 'spike' at the film edges. This is understood to be due to the GO drying on the walls of the vinyl mould

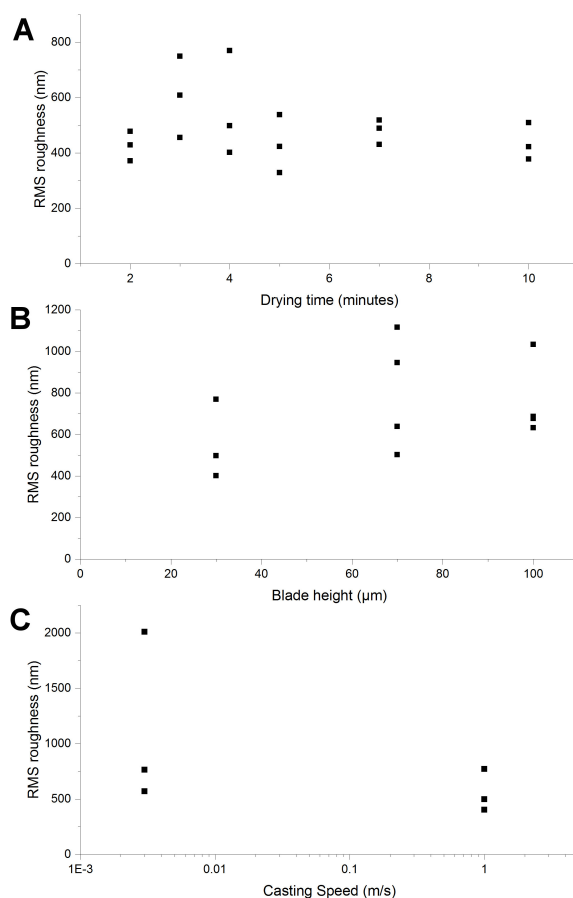


Figure 5.8: a)  $R_q$ , the RMS surface roughness for 3 mm circular GO film plotted against a) in-mould drying time, b) blade height of the doctor blade, c) casting speed.

and leaving a vertical thin film upon the mould's removal. Investigation of this wall under polarized light microscopy and SEM imaging (figure 5.9) revealed the wall's structure. The wall is highly aligned which due to the high shear experienced at the mould walls during the casting process and then a swift drying process as these samples dry from their extremities inwards. As can be seen in figure 5.9a and c this feature is not observed in samples with low in-mould drying times. Examination of the edge under a microscope whilst drying confirmed that the wall structure is formed during casting and not during the drying process.

This structure is relatively unique in the literature and can in fact be thickened by casting on top of the existing structure whilst it is still in its mould (5.10). After 8 castings the wall structure could be thickened to  $\sim 5 \mu\text{m}$ . It can also be observed that the area near the wall structure exhibits relatively good in-plane alignment compared to the low in-mould drying time case (figure 5.9b and e). Further investigation of this effect by casting digits of varying thickness found that samples which were relatively long in the casting direction and thin perpendicular to it were highly aligned (figure 5.11). This is not related to any increase in the shear applied to the GO but rather that wider digits take longer to dry and can disorder during this period as is observed from the images taken that the extremities of these films retain a high degree of in-plane order regardless of their thickness. This is

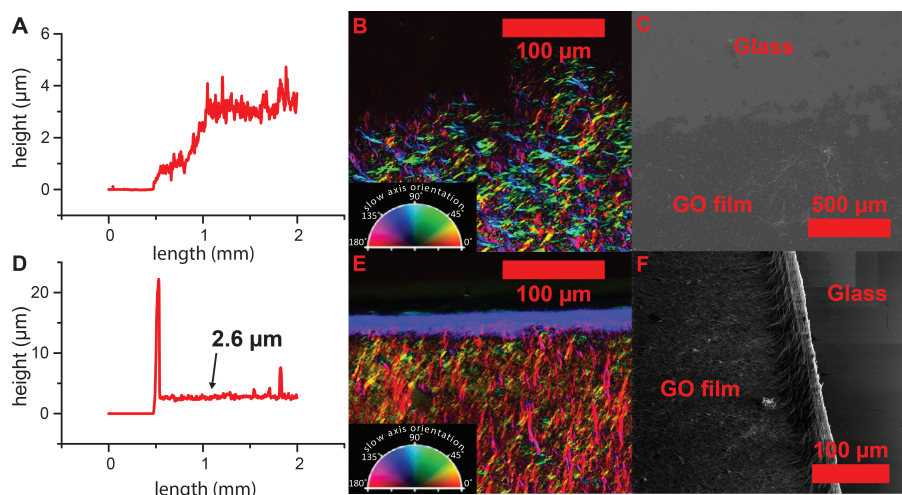


Figure 5.9: a) A profile of a sample with low in-mould drying time, b) a falsely coloured slow axis image of the edge of a low in-mould drying time sample, c) an SEM of a low in-mould drying time sample illustrates the spreading of the edge and the absence of any wall structure, d) a profile of a high in-mould drying time sample shows the characteristic spike of a tall thin structure at the film's edge, e) a falsely coloured slow axis image of the edge of a high in-mould drying time sample shows a uniquely aligned thin structure at the films edge and significant in-plane order in the film structure nearby, f) an SEM of a high in-mould drying time sample with the wall structure in view.

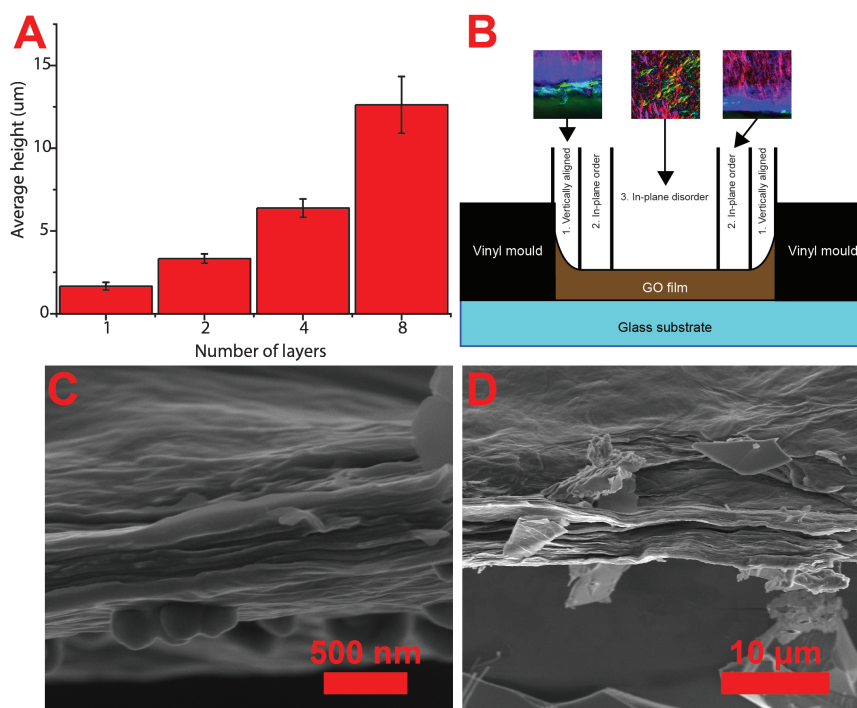


Figure 5.10: a) Heights of samples plotted against the number of castings performed, b) a schematic of the GO film in its mould and the regions of molecular order c) a tilted image of a single casting sample's wall structure d) the wall of an eight casting thick sample illustrating how multiple layers combine to thicken the wall structure, which in this particular case is around  $5 \mu\text{m}$  thick

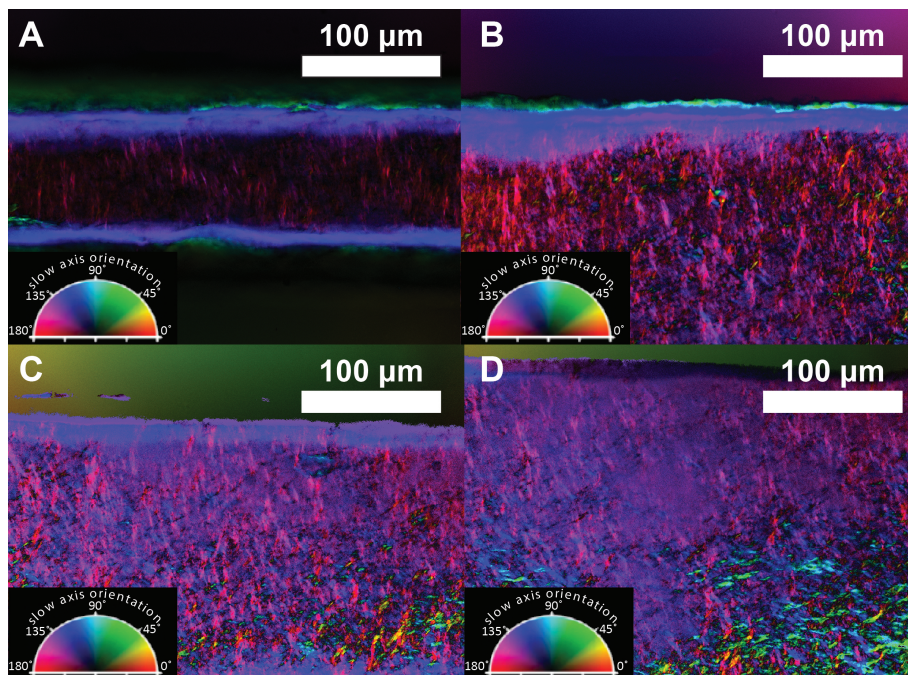


Figure 5.11: a) A slow axis image of a  $100\ \mu\text{m}$  wide digit, b) a slow axis image of a  $200\ \mu\text{m}$  wide digit (edge opposing edge just out of view), c) a slow axis image of a  $600\ \mu\text{m}$  wide digit and d) a slow axis image of a  $1\ \text{mm}$  wide digit

attributed to initial shear alignment, then surface tension based flattening and swift drying time. When the digits widen the structure becomes increasingly disordered in the centre suggesting that longer drying times allow for increasing amounts of disorder to occur. A schematic of this proposed structure is given in figure 5.10b.

### 5.3.3 Nanofluidic results

Conductances were measured for concentrations varying from  $0.1\ \text{mM}$  to  $1\ \text{M}$  KCl. The results of the concentration sweep are shown in figure 5.12. Two features are immediately apparent- the conductance doesn't plateau at low concentrations and there is some strange variation occurring in the  $7.1\ \mu\text{m}$  samples. Regardless one can still use the Dukhin length to estimate the surface charge density at the transition between the surface conduction and the bulk, in this case assuming  $l_{\text{interstitial}} \sim 1.4\ \text{nm}$  and  $C_{\text{transition}} \sim 30\ \text{mM}$  the surface charge is approximately  $4.05\ \text{mC}/\text{m}^2$ . This is somewhat in contrast to the value given by Raidongia of  $0.77\ \text{mC}/\text{m}^2$  [35] which will be discussed in the next section.

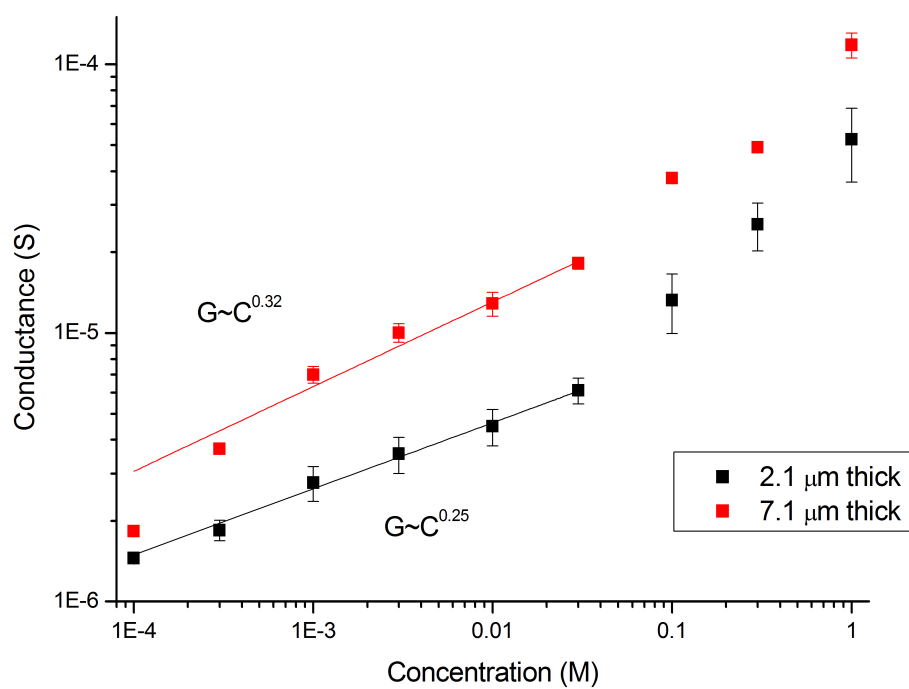


Figure 5.12: The conductance of the two sets of devices of different thickness. The electrolyte in both cases was KCl. Error bars here are one S.D.

## 5.4 Discussion

As a rule of thumb, well defined patterns should be prepared by allowing the GO to dry in its mould rather than removing it early and potentially losing edge definition. The resultant patterns are smooth (roughness  $515 \pm 160 \text{ nm}$ ) and can have features down to  $200 \pm 20 \mu\text{m}$ . Additionally as this technique can not only pattern an arbitrary structure but also control the location of the produced film samples (figure 5.6a) more complex devices, circuits and applications can be conceived.

In order to improve the resolution a further and more close examination of the forces determining the behaviour of the liquid would be necessary. A careful selection of materials should allow greater resolution. Using a more hydrophobic mould may prevent the GO from drying on it and reduce low limit delamination. Partially hydrophobic substrates may encourage pattern stability by making it energetically costly to spread. Excessive hydrophobicity will of course force the samples to bead. At these resolutions the system is comparable to jet based printing systems [200,201]. The advantage of this system over printing systems would be the superior molecular ordering due to the shear casting step. It is also likely (given the results in figure 5.11) that small features will have excellent alignment if the edge effect can be removed by a careful selection of surfaces.

On the other hand creating a method to radically worsen the edge effect is also of interest. Vertically aligned GO, if it could be made in large areas, would have an enormous increase in porosity over planar films. This anisotropy is not lost amongst those working in the energy storage fields where indications that not only porosity but ion conductivity [113], capacitance and electrode kinetics [134] all improve when one works with large numbers of exposed graphitic edges. The success of graphene based planar micro supercapacitors [111,112] is indeed partially due to the fact that the graphene sheets are parallel to the motion of ions. Methods that enable the growth of this edge merit further investigation as presently there exists no large scale method for producing a densely packed, vertically aligned GO based film (regardless of the resultant thickness).

The mould design here is essentially a stepping stone to better technologies. The shear-aligned GO membranes used in Akbari's work [125] are produced using a commercial gravure printer with a blank image plate allowing rapid fabrication of large area membranes. With improvements in the technology patterned plates would print the patterns and allow more accurate, thinner designs. The GO would be applied in an analogous manner to what is described here to the patterned plate and then it would be transferred to the final substrate. Printing on to an impermeable, flexible polymer film would allow integration of the patterns in to lab-on-a-chip type systems.

There are, however, issues with greater application in compact lab-on-a-chip (LOC) like systems. Conventional research based LOC systems use PDMS in their construction which is cured over a patterned mould. This patterned mould creates the microchannels in the PDMS. How exactly one incorporates the patterned GO substrated into this remains an open question. Conventional plasma bonding treatments used to bond PDMS to a glass substrate only damage the GO. During the course of this work we examined the possibility of using double-sided adhesive vinyl, which has a fabrication method outlined

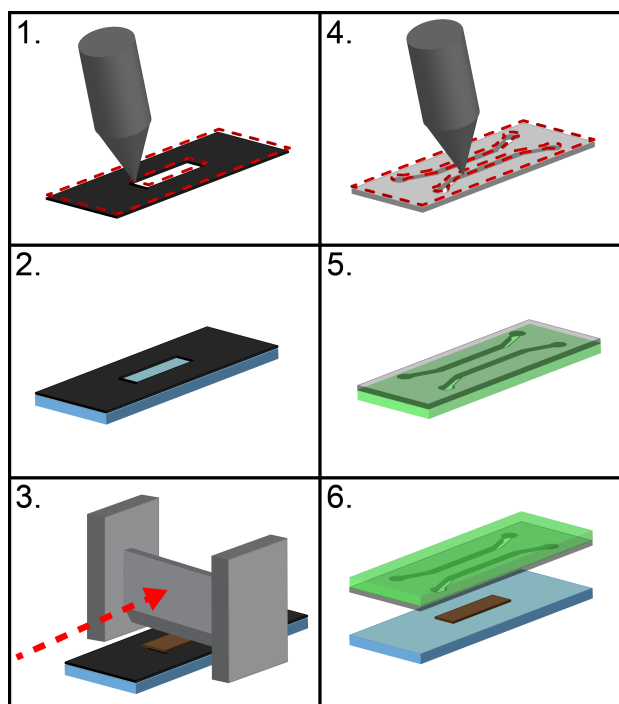


Figure 5.13: Fabrication procedure for producing a patterned film and then incorporation into a lab-on-a-chip style device. 1. A vinyl mould is cut using a plotter cutter, 2. The vinyl is adhered to a glass substrate, 3. GO is spread over the vacancy in the mould and is sheared using a doctor blade, 4. A double adhesive sided vinyl is then cut to make the microchannels that interface with the sample, 5. The vinyl is adhered to a plasma exposed polydimethylsiloxane lid, 6. The sealed channels and their lid are aligned and placed onto the film sample sealing the system, which can then have ports cut and tubing inserted in the usual manner.

in figure 5.13. While fabrication was simple and fluid could flow in the microchannels of the device there were some issues with this technique. The key problem was the stability of the vinyl adhesive. In various concentrations of electrolyte the adhesive weakens and eventually debonds which destroys the device. This problem could be solved by using a film which cures in place irreversibly and renders this bonding region impermeable. If such an adhesive film can be found then the device would allow incredibly easy incorporation of nanometric components into a milli- / microfluidic systems.

The results of the nanofluidic findings merit further examination. Perhaps a preliminary question may be- are they correct if a conductance plateau and therefore constant surface charge as a function of concentration is not observed? Trends like this are not unprecedented- for instance Secchi [173] reports a 1/3 power law for the concentration-conduction plots measured for carbon nanotubes. This is explained using a charge regulation model describing the adsorption of hydroxyl ions onto the surface of the nanotube. While a 1/3 power law isn't the best fit to the low concentration data in figure 5.12, 1/4 being preferable for the well-behaved  $2.1 \mu\text{m}$  data, it does suggest that an equivalent yet different mechanism may be occurring. What is so interesting about the surface conduction regime is that  $G \propto \sigma$  so the relationship proposed in figure 5.12 also means  $\sigma \propto C^{0.25}$  or  $\sigma \propto C^{0.32}$ . So the concentration conductance plot is revealing interesting interfacial

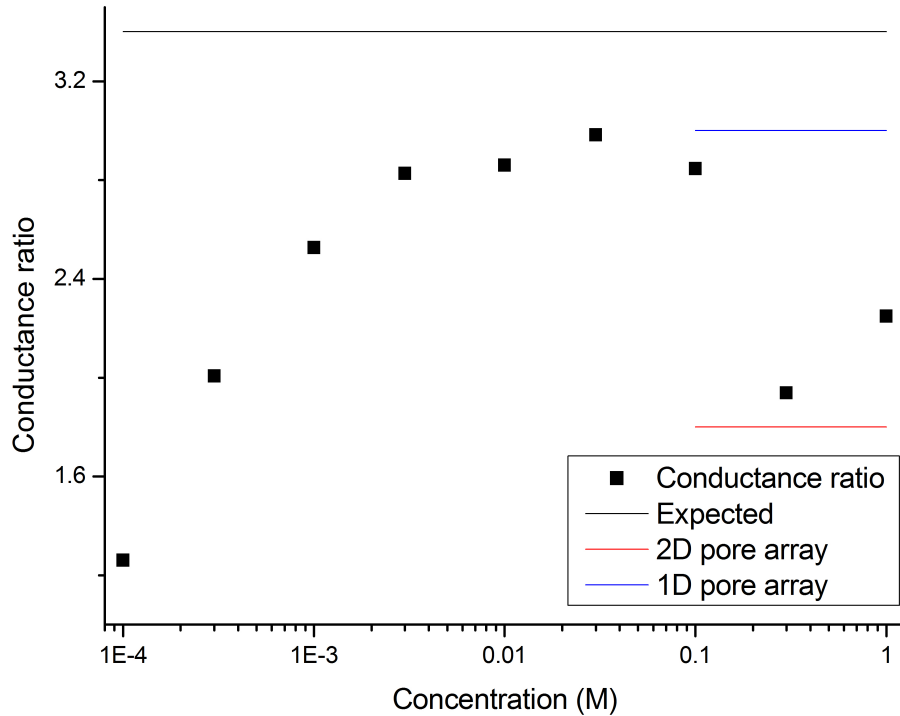


Figure 5.14: The conductance of the two sets of devices of different thickness. The electrolyte in both cases was KCl. Error bars here are one S.D.

behaviour. Re-examining Raidongia’s data and taking the first deviation from bulk concentration as the transition from bulk conduction to surface conduction gives  $4.05 \text{ mC}/\text{m}^2$  for both HCl and KCl measurements and  $2.70 \text{ mC}/\text{m}^2$  for the  $\text{CaCl}_2$  measurements, which is in good agreement with the studies performed here. Implicit in those calculations is the suggestion that results below around  $0.1 \text{ mM}$  aren’t showing the ‘expected’ power law, variable surface charge behaviour. Given how difficult it can be to prepare solutions of very low concentration without contamination (and unduly absorption of  $\text{CO}_2$  from the air) and that both data sets show the same deviation at the same concentration, it is likely that GO is truly showing this power law behaviour. The exact nature of the surface charge of GO is the one of the main subjects in chapter 7 and modelling suggests that charge regulation [16, 173] can explain a significant portion of these measurements.

The difference between the  $2.1 \mu\text{m}$  and  $7.1 \mu\text{m}$  data in figure 5.12 has a couple of interesting features. Firstly the  $7.1 \mu\text{m}$  data are not 3.4 times more conductive. The conductance ratios between the two data sets are plotted as a function of concentration in figure 5.14. Studies on large diameter nanopores in the high concentration regime have shown that the conductance through arrays of pores scales sub-additively with 2D arrays of pores scaling with  $G \sim \sqrt{N}$  and 1D arrays of pores scaling with  $G \sim N/\log(N)$  [165]. This phenomenon is due to entrance effects at the junction between the nanopore and the bulk solution. The lines for 2D and 1D on figure 5.12 are drawn assuming that the approximate number of layers is equal to  $N$  (the number of layers is approximately given by sample thickness divided by  $1.4 \text{ nm}$ ). These calculations were performed based on an array of cylindrical nanopores fabricated using a focussed ion beam, however the principal that the pores don’t combined their conductances linearly (and add sub-linearly) is certainly

applicable here. The unfortunate result of this finding is that it is significantly more difficult than initially anticipated to estimate the penetration depth  $\delta$  of the PDMS discussed in subsection 5.2.3. Indeed if one were to assume such a linear scaling of the conductances and plotted the two conductances as a function of their thicknesses the penetration depth calculated would be negative, which makes no physical sense. The reason as to why this ratio presented in figure 5.14 is not constant is not known, however the average ratio is  $2.4 \pm 0.5$  where the uncertainty here is one standard deviation.

## 5.5 Conclusion

Using xurographic techniques a method for making patterns of GO has been developed. The patterns underwent shape and fidelity studies that indicated that under the right choice of parameters features down to  $\sim 200 \mu m$  can be realized. The RMS roughness of the films was found to be  $515 \pm 160 nm$ . Drying time was a significant parameter on the final form of the pattern, most importantly at the pattern's edge where a mould-GO artefact was formed under specific conditions. The edge artefact was found to be a vertically aligned wall of GO sheets which through multiple castings could be made thicker. The structure indicates that it is possible to have a densely packed vertically aligned film which is very promising for future applications of GO films in energy storage and separation sciences.

Polarized light microscopy studies showed that the patterns can have high degrees of order and that this ordering is related to how swiftly the patterns dried. Fingers of various widths indicated that wider fingers had, in general, lower degrees of order than thin fingers. Film left to dry outside of their moulds have very limited long range order compared to films left to dry inside their moulds. The surface tension driven flow that governs the spreading of the GO liquid crystals clearly undoes any of the benefit brought about by the initial shear alignment.

Surface charge governed conduction was demonstrated for sample devices produced using this technique. Surprisingly the conductance didn't plateau at low concentration, preferring instead to follow a  $1/4$  power law. The surface charge density at the transition between surface and bulk conduction is  $\sim 4.05 mC/m^2$ , although as mentioned this charge density varies a function of the concentration. This finding shows that GO is exhibiting intriguing new surface charge behaviour that warrants further study to understand the mechanisms behind this result, which will be addressed in chapter 7. In agreement with experimental findings on arrays of cylindrical nanopores [165] the two different thicknesses examined exhibited sub-linear scaling of their conductance. These findings demonstrate that fundamental experimentation can be performed on a simple system such as this and robust, repeatable results can be collected and compared from multiple devices.

While incorporation into a lab-on-a-chip device was not successful, this technique is still useful for producing macroscale, removable patterns of graphene oxide. These films could see potential use as interdigitated capacitors and applications as sensors.

## Chapter 6

# The inside out supercapacitor: induced charge storage in reduced graphene oxide

### 6.1 Introduction

This work was born out of observations that were made during the work described in chapter 4. In order to stabilize the graphene oxide in the devices, the material underwent mild reduction making reduced graphene oxide. While the principle of the rectification didn't change there was an unusual hysteresis observed in the measurements. From thorough investigation of the literature it was found that such a hysteresis was likely due to a polarization of the reduced graphene oxide under an applied potential much like how a capacitor functioned. The design was modified to include a separator which would enhance the hysteresis and many improvements in the reduction technique were made to create a material better suited to the application.

Interest in ionic circuit components and nanofluidic devices like ionic diodes [63,66] and ionic transistors [37,202] has been split into two distinct streams of application- scalable technologies focussed on desalination and energy harvesting and compact technologies focussed on sensing, DNA sequencing and implementing electronic like ionic circuits (also referred to as iontronics). Ionic circuits were recently reviewed by Chun [77], a review which highlights the potential applications of these systems and their use in interfacing man-made electronics with biological systems. Within this paradigm there has been significant focus on the active components which provide the switching and logic elements but little attention has been paid to the passive components. In this work we examine this issue and introduce an iontronic capacitor which could be implemented in these circuits. The following work was published in Physical Chemistry Chemical Physics in 2016.

CrossMark  
click for updates

Cite this: DOI: 10.1039/c6cp06463a

## The inside-out supercapacitor: induced charge storage in reduced graphene oxide†

 Samuel T. Martin,<sup>ab</sup> Abozar Akbari,<sup>a</sup> Parama Chakraborty Banerjee,<sup>a</sup> Adrian Neild<sup>b</sup> and Mainak Majumder<sup>\*a</sup>

Iontronic circuits are built using components which are analogous to those used in electronic circuits, however they involve the movement of ions in an electrolyte rather than electrons in a metal or semiconductor. Developments in these circuits' performance have led to applications in biological sensing, interfacing and drug delivery. While transistors, diodes and elementary logic circuits have been demonstrated for ionic circuits if more complex circuits are to be realized, the precedent set by electrical circuits suggests that a component which is analogous to an electrical capacitor is required. Herein, an ionic supercapacitor is reported, our experiments show that charge may be stored in a conductive porous reduced graphene oxide film that is contacted by two isolated aqueous solutions and that this concept extends to an arbitrary polarizable sample. Parametric studies indicate that the conductivity and porosity of this film play important roles in the resultant device's performance. This ionic capacitor has a specific capacitance of  $8.6 \text{ F cm}^{-3}$  at  $1 \text{ mV s}^{-1}$  and demonstrates the ability to filter and smooth signals in an electrolyte at a variety of low frequencies. The device has the same interfaces as a supercapacitor but their arrangement is changed, hence the name inside-out supercapacitor.

Received 20th September 2016,  
Accepted 4th November 2016

DOI: 10.1039/c6cp06463a

www.rsc.org/pccp

### Introduction

Iontronics<sup>1</sup> is the study of devices and components that operate somewhat analogously to electrical components like diodes and transistors to form ionic circuits.<sup>2</sup> Iontronics has potential applications in biosensing and the interfacing of man-made devices with biological systems.<sup>1,3</sup> Recently there has been an increase in the development of more complex ionic circuits. Full wave bridge rectifiers,<sup>4</sup> voltage multipliers<sup>5</sup> and ionic logic gates<sup>2,6</sup> have been implemented as largely on-chip compact demonstrations of coupled iontronic components. These works have allowed rectification of AC voltages in an electrolyte, the overcoming of the limitations of conventional DC ionic currents created at electrodes, accurate pumping of nanomolar concentrations of analyte and elementary computation. Although the field has extensively fabricated various types of iontronic components<sup>2,7–10</sup> using a variety of techniques and underlying mechanisms, the set of analogous components is incomplete. A cursory examination of even the most elementary electrical circuit designs for filters, amplifiers and control systems shows the need for a capacitor,

yet no ionic equivalent has been reported. This will be needed as the complexity of ionic circuitry grows,<sup>11</sup> particularly as we move from studying isolated circuit elements to coupled circuits.<sup>12</sup> This report proposes and demonstrates the capabilities of a graphene based ionic capacitor which serves as an ionic equivalent to a typical electric double layer capacitor or supercapacitor.

A conventional electric double layer occurs due to an equilibrium created between mobile charge within an electrolyte, thermal fluctuations and typically the surface charge at an interface.<sup>13,14</sup> An induced double layer is created when a potential field is applied to an electrolyte perturbing this equilibrium which then results in the formation of a steady state double layer structure at a polarizable interface, which is referred to as the work surface.<sup>15</sup> Induced double layers have been used in the literature to create electrokinetic effects resulting in net fluid motion even at AC potentials.<sup>16</sup> The induced double layer is typically bipolar and the work surface charges much like a capacitor. It should be mentioned that the work surface is isolated from any other electrical conductors and is contacted only by the electrolyte solution. In this work, we show that induced double layers can be used to store charge and thus energy at this interface. When the system is discharged the current is ionic rather than electrical and the result is an ionic capacitor.

The key components that make up a standard sandwich supercapacitor are a pair of electrically conducting plates coated with a high surface area porous carbon material

<sup>a</sup> Nanoscale Science and Engineering Laboratory (NSEL), Department of Mechanical and Aerospace Engineering, Monash University Clayton, VIC-3800, Australia. E-mail: [redacted]

<sup>b</sup> Laboratory for Microsystems (LMS), Department of Mechanical and Aerospace Engineering, Monash University Clayton, VIC-3800, Australia

† Electronic supplementary information (ESI) available. See DOI: 10.1039/c6cp06463a

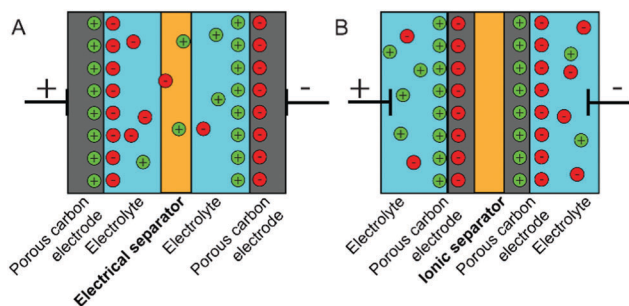


**Fig. 1** (A) A standard supercapacitor and its basic components, (B) the inside-out supercapacitor reverses the roles of the components so that the charge stored is accessible in an ionic circuit. The ionic separator is formed by curing PDMS within an RGO film rendering it impermeable to ions in the aqueous electrolyte.

(the electrodes), an electrolyte and a separator which is an ionic conductor and an electrical insulator preventing the two electrodes from contacting each other<sup>17</sup> as can be seen in Fig. 1A. The difference in this work is that we reverse the roles of the components and turn the design inside-out, our electrolyte becomes our pair of current collectors. Whilst, the porous carbon plays the role of the electrolyte. This means the device has virtually the same interfaces as a standard supercapacitor,<sup>18–20</sup> but has a separator which forbids ionic conduction rather than electrical conduction. This is introduced into our porous carbon to prevent an ionic short circuit (Fig. 1B) between our two current collectors.

The ionic capacitors in this work are made by reducing graphene oxide (GO) films to reduced graphene oxide (RGO) and incorporating these films in a design that turns the conventional supercapacitor inside-out (Fig. 1). To test this system a pair of electrodes are used to apply a potential to the electrolyte and thus polarize the electrolyte/RGO interfaces analogously to previous reports using induced charge electrokinetics.<sup>15,16</sup> In future ionic circuits ionic capacitors such as this could be embedded within the circuit and connected to neighbouring elements by fluidic interconnections. The imposed field then induces a pair of double layers, one at each interface between the work surface and an electrolyte reservoir.

The separator required here should be electrically conducting and ionically insulating which is done by taking a conductive RGO film and casting polydimethylsiloxane (PDMS) into a controlled section of the film, the PDMS then penetrates into the film isolating the two fluid reservoirs and creating regions in the film in which ionic conduction is blocked (see Fig. S1, ESI†). Control studies (Fig. S2, ESI†) show this penetration of PDMS into GO and the associated reduction in ionic conductance. These studies indicate that the separator reduces the ionic conductance of a GO sample by around 3 orders of magnitude.

In this report we demonstrate the generality of the concept of an ionic supercapacitor, examine the characteristics of the RGO film that affect the component's performance, present the results of a sample's electrochemical characterization in a similar manner to how one would characterize a conventional supercapacitor and finally, to show the capacitor's complete

analogy to its electrical counterpart, we demonstrate the capacitor's ability to smooth AC signals in an electrolyte.

## Fabrication and method

Graphene oxide (GO) was synthesized using Hummers' method (graphite used was Bay Carbon SP-1 grade 325 mesh graphite power) and concentrated into the nematic phase using the methods outlined in Akbari *et al.*<sup>21</sup> Briefly 5 g of potassium persulfate (Merck) and 5 g of phosphorus pentoxide (Sigma Aldrich) were dissolved in 15 mL of sulfuric acid heated to 90 °C, once dissolved 10 g of graphite were added to the mixture and this was allowed to stir at 80 °C for 4 hours. This pre-oxidized material was removed, washed until neutral and then dried. 230 mL of sulfuric acid (Univar 98%) was then placed in an ice bath along with the dried pre-oxidized graphite. 30 g of potassium permanganate (Sigma Aldrich) was slowly added to the mixture, after which the reaction was held at 35 °C for 2 hours. After this step the reaction was diluted to a volume of 2 L with deionized water and 25 mL of hydrogen peroxide solution (Merck 30%) was added to quench the reaction. The graphite oxide was then washed with 1.7 L of 10% hydrochloric acid solution (Univar 32%) and then a solution of sodium bicarbonate (Sigma Aldrich) was added to neutralize the graphite oxide suspension. This was then washed three more times with deionized water to remove the sodium bicarbonate. Samples from this suspension were diluted again 1:2 with deionized water, sonicated for half an hour and centrifuged. This process is repeated a number of times to produce a sufficient quantity of graphene oxide suspension. Concentration was performed using super absorbent polymers to remove water from the suspension, leaving the GO in place. This procedure needed to be repeated a few times in order to concentrate the suspension to the concentration used in these experiments, which was  $\sim 30 \text{ mg mL}^{-1}$ .

The device fabrication is outlined in Fig. 2. The GO was shear cast using a doctor blade into a vinyl mould adhered to a glass slide (Sail Brand cat. No. 7101). The resultant film is permeable<sup>21</sup> to solvents such as water and highly ordered due to the shear alignment of the graphene oxide sheets. The vinyl moulds for casting were cut using a Roland SV-8 vinyl cutter and the vinyl used was Metamark series 7 vinyl (in white). Films produced using this method were reduced in hydrazine hydrate vapour (80% Merck) at 60 °C for 4 hours to make reduced graphene oxide (RGO).<sup>22</sup> Data on how film conductivity varied with hydrazine hydrate volume is provided in the Fig. S3 (ESI†). SEM images of the pristine GO and hydrazine exposed samples can be found in Fig. S4 (ESI†). After reduction the samples were washed in a 1:1 mixture of ethanol/deionized water. Resultant film thicknesses were estimated using a Bruker Contour GT-I optical profilometer. Conductivities of the reduced films were measured using a Jandal 4-point probe station. After this stage of characterization a vinyl seal was placed on the film sample. Polydimethylsiloxane (PDMS) (Sylgard 184 Dow Corning) was cast into a slot in the seal and allowed to cure over 24 hours. After this, the electrolyte reservoirs were bonded onto the

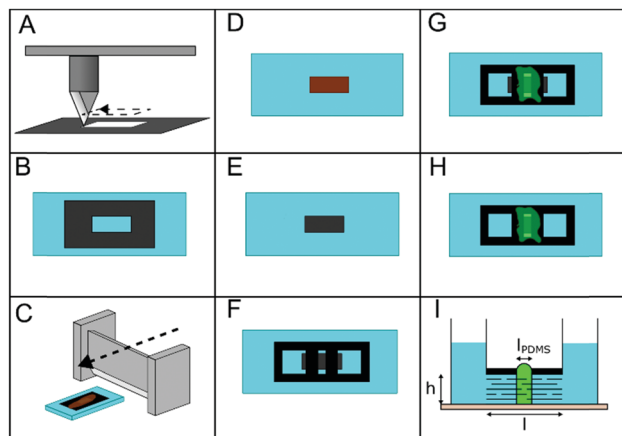


**Fig. 2** Fabrication process and model (A) a vinyl mould is cut using a plotter cutter (a rectangle 6 mm  $\times$  20 mm), (B) the mould is adhered to a glass slide, (C) a volume of nematic phase GO is placed on the mould and sheared using a doctor blade, (D) the vinyl mould is removed leaving the GO in place, (E) the GO is reduced to RGO using hydrazine vapour, (F) a vinyl seal is adhered to the top of the film, (G) PDMS is cast into the central slot and allowed to cure, (H) the film ends extending out of the seal are removed with a scalpel, the resultant shape is 6 mm  $\times$  14 mm, (I) the geometry of the devices used in these experiments, illustrating the layered RGO structure immersed in electrolyte and infiltrated by the PDMS ionic separator (sample  $h$  height is on the order of microns, length  $l$  is a constant 14 mm and the PDMS blockage length  $l_{\text{PDMS}}$  is 2 mm).

device using epoxy. Then excess film extending beyond the vinyl seal was removed using a scalpel. The final lateral dimensions of the films were 14 mm  $\times$  6 mm, with the 6 mm ends exposed to the electrolyte.

Electrochemical studies were performed in 1 M  $\text{Na}_2\text{SO}_4$  using a Biologic VSP potentiostat and a two electrode setup, where two Ag/AgCl electrodes (BASi Pty. Ltd) were used as the working and the counter electrode, one was placed in each reservoir to polarize the RGO films. Cyclic voltammetry (CV) was performed using a voltage window of [0, +1] V vs. Ag/AgCl. For each device the open circuit potential (OCP) was measured for 1 hour before experimentation began and electrochemical impedance spectroscopy (EIS) was performed before and after cyclic voltammetry tests. In each case the Nyquist plots before and after the CV were similar. For each scan rate the 5th cycle was considered for further analysis. Current densities (and other densities) are relative to the volume of the RGO film (6 mm wide, 14 mm long and thickness  $\sim 1 \mu\text{m}$ ), so the thickness was measured using an optical profilometer for each sample. Throughout these experiments the separator thickness was 2 mm. The method of calculating<sup>23</sup> the specific capacitance, power density and areal capacitance is given in the ESI.†

## Results

Firstly, to demonstrate the generality of the principle of the inside-out supercapacitor, a control experiment was built using gold sputtered onto a glass slide. Reservoirs were patterned on top of slide and filled with 1 M  $\text{Na}_2\text{SO}_4$  electrolyte. The findings demonstrate capacitive behaviour and double-layer charge

storage as can be seen in Fig. S5 (ESI†). Further investigation was conducted using RGO due to the ease at which its conductivity can be tuned and its high specific surface area.<sup>18</sup> To investigate the role of conductivity and work surface thickness in this design, two different studies were performed.

### Effect of conductivity

In a conventional supercapacitor conductivity plays a significant role in performance, particularly its effect on power.<sup>24,25</sup> Films of similar thickness were cast and reduced in various quantities of hydrazine to produce RGO films of varying conductivity. The thickness of each film sample was measured at multiple points using an optical profilometer (typically these films had thicknesses of  $\sim 1 \mu\text{m}$ ), the conductivity was also measured, using a 4-point probe. Once characterized, the films were fabricated into capacitors (schematically depicted in Fig. 2I). Data was collected from 31 different devices using two different, but similar, fabrication methods. In this way the efficacy of the fabrication methods could be verified, a discussion of this is included in the ESI.† The results of these experiments (Fig. 3) agree with expectations from conventional supercapacitors reports;<sup>24</sup> namely that lower scan rates give larger values of capacitance than higher scan rates. In addition, the data clearly shows that an increase in conductivity improves the capacitance of the device. The sudden increase in specific capacitance at low conductivities at 1  $\text{mV s}^{-1}$  and 10  $\text{mV s}^{-1}$  in Fig. 3A can be attributed to the presence of faradaic reactions in these devices,<sup>26</sup> as the films at these conductivities are not completely reduced, they contain oxygen functional groups that can undergo irreversible redox reactions. At higher conductivities the films are sufficiently reduced, so there is no discernible presence of such faradaic reactions in the cyclic voltammograms (Fig. S6, ESI†). Power density is inversely proportional to the resistance of a given electrochemical system, hence, the power density increases with conductivity.

### Effect of film thickness

So while the conductivity can be varied in the film it is known that hydrazine also swells GO film structures as gas evolves during the reduction process.<sup>27,28</sup> For this reason films of varying thickness were produced by casting GO multiple times on the vinyl mould and then the films were reduced in identical

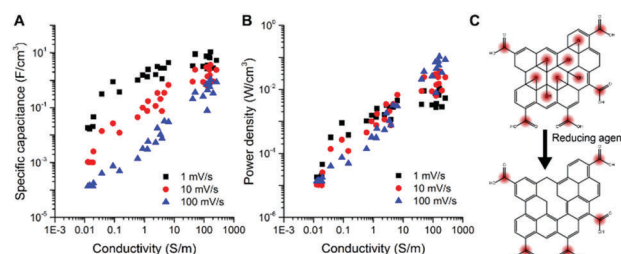


**Fig. 3** (A) Specific capacitance is plotted here as a function of the conductivity of the RGO film for various scan rates, (B) power density is plotted in a similar manner to specific capacitance, (C) GO is covered in oxygen functionalities which disrupt the  $\text{sp}^2$  bonded graphitic plane reducing conductivity, by reducing the sample the graphitic network is partially restored radically increasing conductivity and reducing oxygen content.

**Table 1** Profilometry data on samples made by casting GO multiple times over the same mould, the samples were then reduced, had their heights measured again and had their conductivity measured. Uncertainties here are one SD of measurements performed multiple times on multiple samples

	1 casting	2 castings	4 castings
GO thickness ( $\mu\text{m}$ )	$1.6 \pm 0.2$	$3.3 \pm 0.3$	$6.4 \pm 0.5$
RGO thickness ( $\mu\text{m}$ )	$1.0 \pm 0.2$	$2.3 \pm 0.3$	$5.3 \pm 0.4$
RGO conductivity ( $\text{S m}^{-1}$ )	$2850 \pm 220$	$1470 \pm 260$	$450 \pm 20$

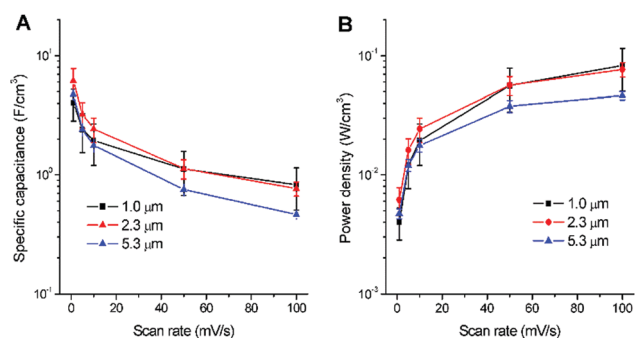


**Fig. 4** (A) The specific capacitance as a function of the scan rate is plotted for samples of varying average thickness, (B) power density here is plotted in a similar manner to the specific capacitance. Error bars here are one SD from measurements made on multiple samples.

hydrazine hydrate vapour conditions. While samples with 1, 2 and 4 castings of GO shrank during reduction, the degree of shrinkage decreased as the thickness increased (Table 1) and a negative trend of conductivity with sample thickness was observed. During reduction it is hypothesized that the evolved gas is more completely trapped in the  $6.4 \mu\text{m}$  GO films than thinner samples. Indeed, it has been previously reported that hydrazine vapour reduction of graphene oxide creates low density foam like structures with high porosity.<sup>28</sup> The optimal balance between conductivity and expansion due to gas evolution appears to be for  $2.3 \mu\text{m}$  thick RGO samples (Fig. 4), they have slightly lower power than the  $1 \mu\text{m}$  samples at high scan rates, however the enhancement in their porosity allows more ions to access more of the pores in the material leading to superior specific capacitance and power at lower scan rates.

### Electrochemical characterization

To evaluate the performance of a typical device cyclic voltammetry (CV), electrochemical impedance spectroscopy (EIS) and galvanostatic charge–discharge measurements were conducted on  $1 \mu\text{m}$  thick samples. The shape of the cyclic voltammograms in Fig. 5A indicate typical double-layer charge storage behaviour as they take a rectangular shape. A control device was cycled 100 times at  $1 \text{ mV s}^{-1}$  to illustrate the absence of faradaic reactions which could contribute to the measured capacitance (Fig. S6, ESI<sup>†</sup>). The decline of capacitance at high scan rates is attributed to the resistance of the work surface (which is  $14 \text{ mm}$  long) and the long ion path length in the electrolyte that adds further to the resistance. The Nyquist plots in Fig. 5B agrees with this hypothesis – the equivalent series resistance (ESR) is large

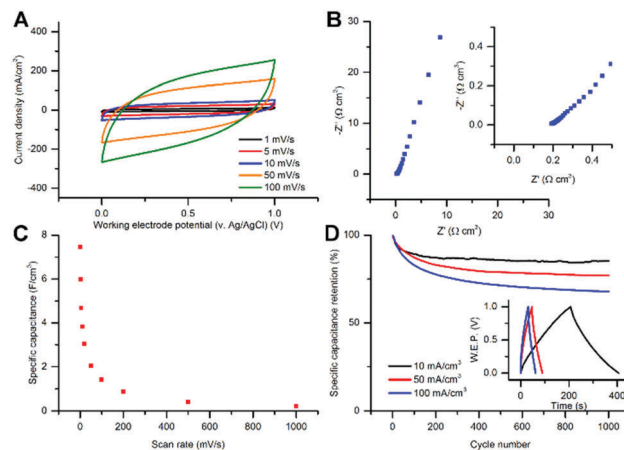


**Fig. 5** (A) Cyclic voltammograms at various scan rates indicate the classic double layer shape (5th cycle is displayed in each case), (B) a Nyquist plot with a low frequency phase angle of  $\sim 72^\circ$ , inset provides displays the high frequency data and the equivalent series resistance value, (C) specific capacitance plotted against scan rate, (D) specific capacitance retention over 1000 cycles for 3 current densities, inset contains a cycle of each of these tests. This study was performed on samples of thickness  $1.0 \mu\text{m}$ .

(over  $2 \text{ k}\Omega$ , which when normalized is  $0.19 \Omega \text{ cm}^{-3}$ ) compared to  $\sim 1 \Omega$  in more conventional, optimized designs.<sup>18,19</sup> The phase angle at low frequencies eventually plateaus to  $\sim 72^\circ$  (Fig. S7, ESI<sup>†</sup>). While this ESR is high, within the context of ionic circuitry, sensor systems,<sup>29</sup> membrane based ionic transistors,<sup>6</sup> conical nanopore logic gates<sup>30</sup> and polyelectrolyte based diode circuits<sup>2</sup> reported impedances are on the order of  $10^5$ – $10^8 \Omega$ . Thus in this context, the ESR of this system is actually quite small<sup>2,6</sup> compared to resistive elements with which it would potentially be coupled.

As can be seen in Fig. 5C, the capacitance is high at lower scan rates and decreases steadily with increasing scan rates. This trend is not surprising if one considers the high resistance of this system. The trend is also common to supercapacitors and is often observed as the curves of a particular system in a Ragone plot.<sup>19,23,31</sup> The increase in resistance  $R$  affects the charging time and the time constant  $\tau$ , so the higher ESR observed here, understandably, results in this trend being observed at slower scan rates.

Galvanostatic charge/discharge plots in the inset of Fig. 5D show a typical triangular shape with an IR drop, which is the characteristic shape of the charge/discharge plots for any supercapacitor. Specific capacitance retention is shown in Fig. 5D. The specific capacitance retention at a constant current density of  $10 \text{ mA cm}^{-3}$  was  $\sim 80\%$ . The loss of 20% in the specific capacitance over 1000 cycles is not surprising considering the high resistance of the system, which is in agreement with the EIS and CV measurements. The specific capacitance retention for higher current densities ( $50 \text{ mA cm}^{-3}$  and  $100 \text{ mA cm}^{-3}$ ) were lower than that at  $10 \text{ mA cm}^{-3}$ , which can be attributed to the losses corresponding to the larger iR drop (inset in Fig. 5D) in the system at higher current densities. The induced nature of the system results in an initial decrease in capacitance which stabilizes as cycling continues. Studies performed on the same

sample found that for cyclic voltammetry with a scan rate of  $1 \text{ mV s}^{-1}$  the specific capacitance was found to be  $2.8 \text{ F cm}^{-3}$  and for galvanostatic charge/discharge measurements at a constant current density of  $10 \text{ mA cm}^{-3}$  the specific capacitance measured was  $4.31 \text{ F cm}^{-3}$ .

## Discussion

Firstly, we examine the performance of the inside-out supercapacitor as an energy storage system, then we consider it in the context of iontronic circuitry.

While the device design has a long work surface (corresponding to a pair of 6 mm thick electrodes and a 2 mm thick separator) compared to standard designs the cross sectional area exposed to the bulk electrolyte has two interesting properties – it's quite small (around  $6000 \mu\text{m}^2$ ) and is made up of a large proportion of exposed graphene sheet edges. The resultant areal capacitance is enormous, the highest value measured in this study was  $5.9 \text{ F cm}^{-2}$  (accounting for both exposed areas of the work surface), which came from a  $2.3 \mu\text{m}$  sample. Certainly the length of the work surface plays a significant role in this large figure, as this means the electrodes are far thicker than conventional designs, but this value still lies above reported values for pseudocapacitive systems.<sup>32,33</sup> Studies performed on pyrolytic

graphite,<sup>34,35</sup> carbon nanotubes<sup>36</sup> and more recently single layer graphene<sup>37</sup> indicate that the edge plane of the carbon structure has faster kinetics and importantly for this study – stores more charge. In the case of the monolayer of graphene<sup>37</sup> the edge plane showed 4 orders of magnitude higher specific capacitance than the basal plane. While there have been vertically aligned graphene electrodes,<sup>20,38</sup> they have been fabricated by CVD and lack the dense packing of the exposed RGO film edges in this work. There have also been works which have used a similar design to produce standard supercapacitors taking advantage of alignment of the graphene sheets in a similar manner<sup>39,40</sup> but the calculated areal capacitances given are not relative to the thickness of the graphene (as both systems were very thin,  $t < 20 \text{ nm}$ ) and rather give a measure of the area on the substrate taken up by the active material. Considering the cross section of the film as the area of consideration highlights the massive potential of a densely packed vertically aligned graphene electrode in energy storage.

Turning our attention, now, to the iontronic use of the system, it is noteworthy that, in a recent review<sup>1</sup> Chun *et al.* drew attention to the advantages of iontronics in the area of biosensing and biological information processing. The field's attention has always been drawn towards the performance and characterization of the active elements (diodes and transistor like elements) however if more complex circuits<sup>4-6,10,12</sup> are to be designed and realized the need for capacitive components to store charge and filter signals is necessary. Electrical capacitors are frequently used in conjunction with active components (such as transistor and diodes) and integrated circuits to improve the quality of their response and enable closer to ideal behaviour.<sup>11</sup> As applications look to produce more complex time varying signals such as transient switching from ionic logic circuits<sup>6</sup> there is need to take a leaf from an electrical circuit designer's book and begin to utilize passive components (such as ionic resistors and capacitors) to improve performance.

While the focus of this report has been to study the component's performance in the manner of a conventional supercapacitor this component has a unique role to play in the field of iontronics. An ionic capacitor would have immediate application in rectification of AC signals<sup>4</sup> and in voltage multiplication in an electrolyte<sup>5</sup> in combination with ionic diodes. To demonstrate this system's capabilities an (electronic) bridge rectifier was constructed attached to a  $1 \text{ M}\Omega$  resistor, a quantity in the range of the impedance of a nanofluidic circuit (Fig. 6). The unfiltered signal in Fig. 6 shows how the circuit behaves in the absence of the capacitor. When the ionic capacitor is placed across the load it smooths the signal at a variety of frequencies common to these circuits.<sup>4,5</sup> The results of this study are found in Table 2 and show that once smoothed the current signal has a significantly smaller deviation from the average and that at

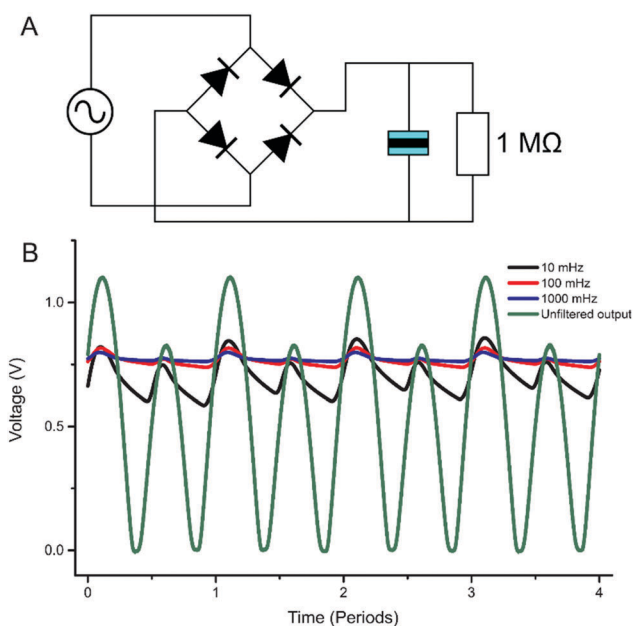


**Fig. 6** (A) Bridge rectifier circuit using electrical diodes and an electrical resistor in parallel with an inside-out supercapacitor, (B) the output signals as measured on a potentiostat for a variety of frequencies and the unfiltered signal (the signal in the absence of the inside-out supercapacitor).

**Table 2** Performance of the capacitor in smoothing an AC signal. The unfiltered data is collected from the circuit without the capacitor in place. Uncertainties here are one SD

	Unfiltered output	10 mHz	100 mHz	1000 mHz
Average output voltage (V)	$0.53 \pm 0.34$	$0.70 \pm 0.07$	$0.77 \pm 0.02$	$0.77 \pm 0.01$

higher frequencies the average voltage output across the load is higher which is due to reduced discharge from the capacitor. Whilst supercapacitors rarely perform this role of filtering and smoothing in electronics due to their poor high frequency response compared to electrolytic and dielectric based capacitors,<sup>11,17</sup> as the response times of iontronic components so far remains comparatively very slow to electronics,<sup>4,6</sup> it seems that ionic supercapacitors will be able to fulfil this role. As the concept behind the component examined here is simple and robust it is reasonable to think that, capacitors based on this concept made from porous carbons or conductive polymers,<sup>8,41</sup> could be integrated into fully-fledged ionic circuits.

## Conclusions

We have reported a new supercapacitor analogue for ionic circuits. The device's performance was studied and had a specific capacitance of 8.3 F cm<sup>-3</sup> and a large areal capacitance of 5.9 F cm<sup>-2</sup> in 1 M Na<sub>2</sub>SO<sub>4</sub> (at a scan rate of 1 mV s<sup>-1</sup>). Studies on the thickness of the film used indicate that a 2.3 μm thick film yielded the highest specific capacitance and had virtually the same power density as the more conductive 1.0 μm thick films. The electrochemical data indicates that the energy is stored in a pair of induced double layers at either exposed end of the work surface, in perfect analogy to a conventional supercapacitor. The inside-out supercapacitor has immediate application in the ionic rectification and voltage divider circuits that have recently been reported and highlights the importance of passive components in improving the output of ionic circuits. This work unveils an unexplored component in the growing field of ionic circuits.

## Acknowledgements

S. T. Martin conceived the project, performed the experiments and co-wrote the article, A. Akbari synthesized the GO and prepared the GO liquid crystals, P. Banerjee assisted with the electrochemistry, performed experiments and co-wrote the article, A. Neild and M. Majumder co-wrote the article. The authors acknowledge use of facilities within the Monash Centre for Electron Microscopy and funding from the Australian Research Council through the ARC LP 140100959. This work was performed in part at the Melbourne Centre for Nanofabrication (MCN) in the Victorian Node of the Australian National Fabrication Facility (ANFF). S. T. Martin and A. Akbari acknowledge the support of the Monash Centre for Atomically Thin Materials (MCATM). S. T. Martin wishes to thank P. Sheath and D. Lobo for their assistance with the SEM images.

## Notes and references

- H. Chun and T. D. Chung, *Annu. Rev. Anal. Chem.*, 2015, **8**, 441–462.
- J. H. Han, K. B. Kim, H. C. Kim and T. D. Chung, *Angew. Chem.*, 2009, **121**, 3888–3891.
- A. Jonsson, Z. Song, D. Nilsson, B. A. Meyerson, D. T. Simon, B. Linderroth and M. Berggren, *Sci. Adv.*, 2015, **1**, e1500039.
- E. O. Gabriellsson, P. Janson, K. Tybrandt, D. T. Simon and M. Berggren, *Adv. Mater.*, 2014, **26**, 5143–5147.
- P. Ramirez, V. Gomez, C. Verdia-Baguena, S. Nasir, M. Ali, W. Ensinger and S. Mafe, *Phys. Chem. Chem. Phys.*, 2016, **18**, 3995–3999.
- K. Tybrandt, R. Forchheimer and M. Berggren, *Nat. Commun.*, 2012, **3**, 871.
- R. Karnik, R. Fan, M. Yue, D. Li, P. Yang and A. Majumdar, *Nano Lett.*, 2005, **5**, 943–948.
- K. Tybrandt, E. O. Gabriellsson and M. Berggren, *J. Am. Chem. Soc.*, 2011, **133**, 10141–10145.
- I. Vlasiouk, T. R. Kozel and Z. S. Siwy, *J. Am. Chem. Soc.*, 2009, **131**, 8211–8220.
- E. O. Gabriellsson, K. Tybrandt and M. Berggren, *Lab Chip*, 2012, **12**, 2507–2513.
- N. Kularatna, *Electronic circuit design: from concept to implementation*, CRC Press, 2008.
- P. Ramirez, V. Gomez, J. Cervera, S. Nasir, M. Ali, W. Ensinger, Z. Siwy and S. Mafe, *RSC Adv.*, 2016, 54742–54746.
- J. N. Israelachvili, *Intermolecular and surface forces*, revised 3rd edn, Academic press, 2011.
- L. Bocquet and E. Charlaix, *Chem. Soc. Rev.*, 2010, **39**, 1073–1095.
- T. M. Squires, *Lab Chip*, 2009, **9**, 2477–2483.
- M. Z. Bazant and T. M. Squires, *Curr. Opin. Colloid Interface Sci.*, 2010, **15**, 203–213.
- A. Yu, V. Chabot and J. Zhang, *Electrochemical supercapacitors for energy storage and delivery*, CRC Press, Boca Raton, FL, 2013.
- M. D. Stoller, S. Park, Y. Zhu, J. An and R. S. Ruoff, *Nano Lett.*, 2008, **8**, 3498–3502.
- M. F. El-Kady, V. Strong, S. Dubin and R. B. Kaner, *Science*, 2012, **335**, 1326–1330.
- J. R. Miller, R. Outlaw and B. Holloway, *Science*, 2010, **329**, 1637–1639.
- A. Akbari, P. Sheath, S. T. Martin, D. B. Shinde, M. Shaibani, P. C. Banerjee, R. Tkacz, D. Bhattacharyya and M. Majumder, *Nat. Commun.*, 2016, **7**, 10891.
- I. K. Moon, J. Lee, R. S. Ruoff and H. Lee, *Nat. Commun.*, 2010, **1**, 73.
- D. E. Lobo, P. C. Banerjee, C. D. Easton and M. Majumder, *Adv. Energy Mater.*, 2015, **5**, 1500665.
- J. Sánchez-González, F. Stoeckli and T. A. Centeno, *J. Electroanal. Chem.*, 2011, **657**, 176–180.
- P. J. Hall, M. Mirzaeian, S. I. Fletcher, F. B. Sillars, A. J. R. Rennie, G. O. Shitta-Bey, G. Wilson, A. Cruden and R. Carter, *Energy Environ. Sci.*, 2010, **3**, 1238.
- M. Pumera, *Electrochem. Commun.*, 2013, **36**, 14–18.
- S. Pei, J. Zhao, J. Du, W. Ren and H.-M. Cheng, *Carbon*, 2010, **48**, 4466–4474.
- Z. Niu, J. Chen, H. H. Hng, J. Ma and X. Chen, *Adv. Mater.*, 2012, **24**, 4144–4150.
- B. J. Sanghavi, W. Varhue, J. L. Chávez, C.-F. Chou and N. S. Swami, *Anal. Chem.*, 2014, **86**, 4120–4125.

- 30 M. Ali, S. Mafe, P. Ramirez, R. Neumann and W. Ensinger, *Langmuir*, 2009, **25**, 11993–11997.
- 31 D. Pech, M. Brunet, H. Durou, P. Huang, V. Mochalin, Y. Gogotsi, P.-L. Taberna and P. Simon, *Nat. Nanotechnol.*, 2010, **5**, 651–654.
- 32 A. Sumboja, C. Y. Foo, X. Wang and P. S. Lee, *Adv. Mater.*, 2013, **25**, 2809–2815.
- 33 T. Zhai, F. Wang, M. Yu, S. Xie, C. Liang, C. Li, F. Xiao, R. Tang, Q. Wu and X. Lu, *Nanoscale*, 2013, **5**, 6790–6796.
- 34 J.-P. Randin and E. Yeager, *J. Electrochem. Soc.*, 1971, **118**, 711–714.
- 35 C. E. Banks and R. G. Compton, *Analyst*, 2006, **131**, 15–21.
- 36 C. E. Banks and R. G. Compton, *Analyst*, 2005, **130**, 1232–1239.
- 37 W. Yuan, Y. Zhou, Y. Li, C. Li, H. Peng, J. Zhang, Z. Liu, L. Dai and G. Shi, *Sci. Rep.*, 2013, **3**, 2248.
- 38 X. Xiao, P. Liu, J. S. Wang, M. Verbrugge and M. P. Balogh, *Electrochem. Commun.*, 2011, **13**, 209–212.
- 39 Z. Niu, L. Zhang, L. Liu, B. Zhu, H. Dong and X. Chen, *Adv. Mater.*, 2013, **25**, 4035–4042.
- 40 J. J. Yoo, K. Balakrishnan, J. Huang, V. Meunier, B. G. Sumpter, A. Srivastava, M. Conway, A. L. Reddy, J. Yu, R. Vajtai and P. M. Ajayan, *Nano Lett.*, 2011, **11**, 1423–1427.
- 41 A. Malti, J. Edberg, H. Granberg, Z. U. Khan, J. W. Andreasen, X. Liu, D. Zhao, H. Zhang, Y. Yao, J. W. Brill, I. Engquist, M. Fahlman, L. Wågberg, X. Crispin and M. Berggren, *Adv. Sci.*, 2016, **3**, DOI: 10.1002/advs.201500305.

## Chapter 7

# The nanofluidics of shear aligned graphene oxide membranes

### 7.1 Introduction

Shear aligned membranes (SAM), as discussed previously in chapter 3, are formed by shearing a nematic liquid crystal of graphene oxide across a substrate. Development of this membrane was pioneered in a recent work by Akbari et al. [125]. In this chapter samples of these membranes have their nanofluidic properties examined. The majority of this work was performed at the Ecole Normale Supérieure in France working with the MicroMEGAS research group.

Despite interest in GO's (graphene oxide) water transport properties [19,88,188,203,204], there has been limited publication of 2D systems' nanofluidic properties. Investigations of this layered structure are of increasing importance as presently little work is aimed at understanding this structure and results drawn from crude models [131] often leading to superlative results that are misleading [205], in this case Nair's [131] approximation leads a large estimated path length within the membrane resulting in a large value (4-5 orders of magnitude above the bulk value) for the diffusion of coefficient of water within the GO membrane. Simulations and analysis by Yoshida [19] indicate suggest that additional capillary forces driving Nair's flow are absent in the analysis in [131]. Further and more systematic study of this geometry has disproved the "defect-free" assumption made by numerous authors [130,131,205] when interpreting their data [132]. When investigating 2D structures like layered GO films there are two approaches taken by experimentalists shown in figure 7.1. The planar case, where net transport is in the plane of the sheets, usually involves encasing a film sample within an impermeable matrix (like polydimethylsiloxane) and opening the film ends with a scalpel (figure 7.1a). Work using this technique was pioneered by Raidongia [35,181] and allows experimenters a far simpler set of nanofluidic channels to investigate than the other case. Due to the design of this experiment and the macroscopically large length of the film used, pressure tests have not been feasible. Additionally whilst this geometry is analytically simpler, more ionically conductive [113] and potentially enormously porous in comparison to the other case no technique exists yet for producing thin, large areas of this configuration as discussed in chapter 5. The second

case represents films formed under any number of techniques (shear-alignment on a porous substrate [125], vacuum filtration [2, 131] etc.) where the forcing is applied perpendicular to the plane of the film (figure 7.1b).

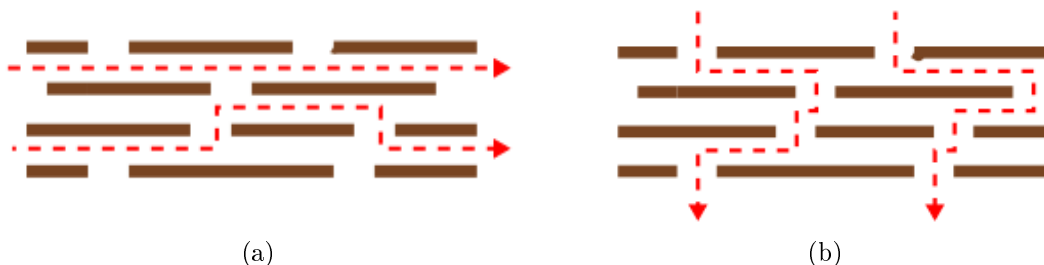


Figure 7.1: Two different experimental setups for investigating 2D nanochannels. a) The 'planar' case typically has the ion transport parallel to the substrate supporting the 2D film structure. b) The transverse/u-tube type experiment has the disadvantage of having the 2D sheets perpendicular to the direction of transport.

In addition to this challenging anisotropic geometry there are more elusive effects suggested by findings in the literature that require further study in order to understand what is happening at GO's interface with water. Secchi [173] found that for carbon nanotubes the ionic conductance scaled with the concentration to the power of one third  $G \propto C^{\frac{1}{3}}$  which is explained by the author as the adsorption of hydroxyl ions onto the graphitic surface. However no such scaling is reported in Raidongia's [35], Miansari's [143] or Guo's [2] works on GO and reduced GO. Reasoning behind why, until now, no unusual behaviour and constant surface charge density has been reported is discussed in section 7.4 and will compare findings from this chapter and chapter 5 with the literature. Particularly in the case of Guo's experiments on a chemically reduced graphene oxide membrane one might expect some agreement between results for carbon nanotubes and relatively graphitic carbon. Additionally the reported surface charge value for Raidongia's work is an incredibly low  $0.77 \text{ mC/m}^2$  which is below that of silica [44], however in light of experimental studies on GO performed in chapter 5 this value can be revised to  $\sim 4.05 \text{ mC/m}^2$  at the point of transition to bulk conduction. Under typical conditions surface charge densities of  $10 - 100 \text{ mC/m}^2$  are quite normal [30, 37, 45]. It is surprising that despite the presence of functional groups and the availability of graphitic regions the surface charge density is so small. One possible explanation of the small value of the surface charge density is that the interstitial gap size is prohibitive to hydrated ions [6], Secchi's work did not extend to carbon nanotubes of sizes less than  $3.5 \text{ nm}$  which is well above the hydrated radius of chlorine, potassium and sodium. This explanation is somewhat in disagreement with findings by Chmiola [206], who found that carbon based pores smaller than the hydration radius could not only store charge in a supercapacitor but also resulted in a dramatic enhancement in the stored charge.

A report by Duan [161] studying the transport of cations in silicon dioxide nanochannels models the observed behaviour by assuming that the surface charge is derived purely from the equilibrium of the silanol functional groups on the surface of the channel, whose ionization state is dependent on the pH. By shifting the equilibrium of the reaction one

can effect the surface charge at the interface. In fact this model was used earlier by van der Heyden [44] but Duan extends the modelling to consider the confinement of the channel to be a way of perturbing equilibrium state of the electric double layers. In the dilute state the surface charge is neutralized by the diffuse cloud of counter-ions forming the electric double layer near the interface. If two of these surfaces are brought closer to each other then the counter-ion concentration in the enclosed volume must rise, leading to the surface reaction equilibrium being pushed towards reducing the surface charge. This is reflected in Duan's model and provides a reasonable explanation as to why the surface charge on GO could be so low.

Studies by Konkena [4] highlight the interesting surface activity of GO as pH changes. Gudarzi [207] compares surface charge calculated from zeta potential measurements with Konkena's charge titration results and finds good agreement between the two data sets for a large spread of pHs. At pH 7 the surface charge of a colloidal suspension of GO was calculated to be around  $\sim 28 \text{ mC/m}^2$  and at very high pHs the surface charge was around  $\sim 37 \text{ mC/m}^2$ . This suggests that a confinement like effect as found in Duan's silanol model could be applied to GO to understand why the surface charge observed by Raidongia [35] and in chapter 5 was so low. Additionally Konkena was able to show a three step ionization of GO with pKa values of 4.3, 6.6 and 9.8. The lower two are suggested to be the ionization of carboxylic acid groups, the lower of which has a neighbouring hydroxyl group which stabilizes it, allowing the lower pKa. The highest pKa is suggested to be the ionization of phenolic hydroxyl groups. So any forthcoming model would likely need to consider the various number and pKas of these groups.

GO is a complex system to study as almost all of its features vary [117]. The amount, type and distribution of function groups, defects, sheet dimensions all have potentially different effects on the resultant property investigated [132]. In terms of conduction mechanisms, apart from bulk and surface conduction of ions, GO is a known proton conductor [208] and additionally films of hydrated graphene oxide have been used as a dielectric in capacitors [209]. One of the driving factors of these experiments was to see if there was an enhancement in the dielectric constant of water due to the confinement of the GO.

## 7.2 Experimental methods

### 7.2.1 Experimental setup for membrane studies at ENS

These experiments were conducted in a custom made cell which is depicted in figure 7.2. A porous polytetrafluoroethylene frit was used to support the flexible membrane and mesh electrode, this allowed streaming current measurements to be performed on the membrane without macroscopically deforming or stretching it. In these experiments the cell's electrodes were controlled using a Keithley 2400 source measurement unit and the pressure was controlled using a Fluigent MFCS-EZ pressure based flow controller. Cross sections of the membrane were performed by shattering it in liquid nitrogen and imaging the cross sections on a Nova NanoSEM. The electrodes were Ag/AgCl and produced by immersing a silver wire into a solution of 10% sodium hypochlorite (Sigma Aldrich) for half an hour.

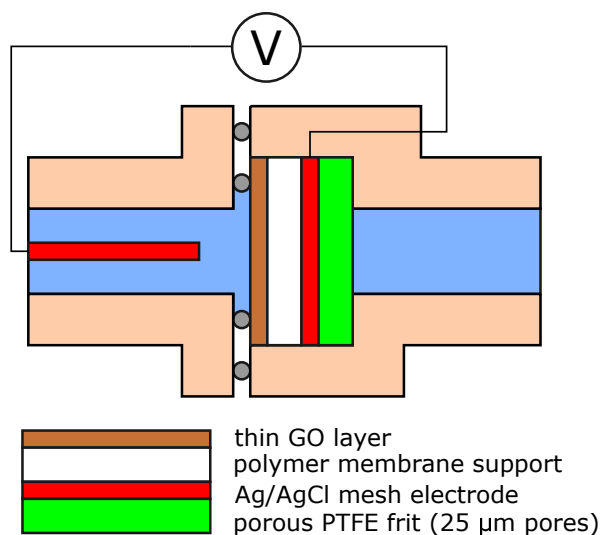


Figure 7.2: The ion current measurement cell design used in these experiments. The Ag/AgCl electrodes are depicted in red, one was a mesh electrode placed in close contact with the membrane's porous support, the other was placed near the GO surface in the electrolyte.

For current voltage (I/V) measurements the system typically had its open circuit potential monitored for a period of time to ensure stability and minimal concentration differences between the two reservoirs. Then a stepped potential was applied, varying typically between -5 mV and 5 mV. Once stepped the potential is held constant allowing the response of the system to relax leading to data similar to that shown in figure 7.3. This total stepped saw-tooth response was allowed to settle over multiple cycles until the signal had stabilized (which might take a couple of hours). This data was then collected and analyzed. From each relaxation curve the median of the last three data points was taken as the current value for the given applied potential. This set of data is what makes up a typical I/V curve.

The procedure for measuring a streaming current was to flow the electrolyte of relevant concentration through the cell at the lowest pressure (typically 500 mbar) for an hour. This was to allow the transient effect of concentration polarization to diminish so the flux

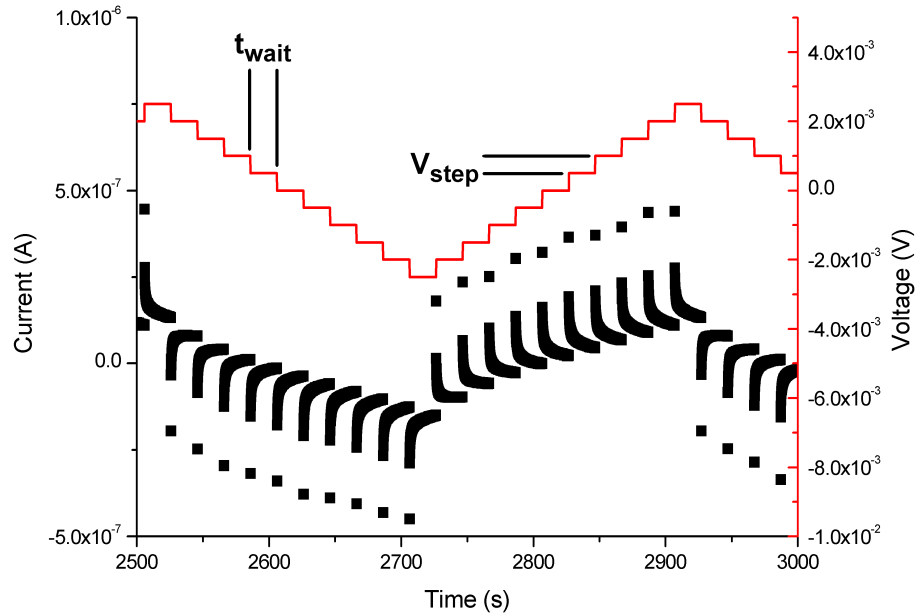


Figure 7.3: A data sample from a typical experiment. The current data is depicted in black and relaxes from an initially high value to a more stable one over the course of 10s of seconds. The applied voltage is depicted in red with the two important parameters; the wait time  $t_{wait}$  and the voltage step size  $V_{step}$  depicted.

through the membrane sample remained relatively constant for a given applied pressure over the measurement time. After this pre-polarization the current was then measured for a given applied pressure. Each pressure value was held for around 2000 seconds allowing the current signal to stabilize. Once this time had elapsed the pressure was increased stepwise, repeating this measurement procedure until the maximum pump pressure was reached (2 bar).

Concentration difference measurements were performed by priming the cell and membrane at the lower concentration for 24 hours and then exchanging the electrolyte in one reservoir with the high concentration electrolyte. The reservoir chosen faced the porous support of the GO membrane as it was thought that the higher concentration electrolyte would have less difficult diffusing through the porous structure and maintaining the expected concentration difference across the membrane itself.

### 7.2.2 COMSOL modelling of GO at equilibrium

As well as being experimentally investigated GO was modelled using COMSOL Multiphysics to see if the surface charge density could be understood within the limits of the Poisson Nernst-Planck (PNP) equations. In order to model the surface charge density on GO a modified charge regulation model needs to be proposed as the present model used for silica doesn't have the complexity required. As mentioned in section 7.1, Konkena [4] proposed 3 different equilibrium reactions for the different functional groups on GO, which are summarized in table 7.1. In the COMSOL model of this system these reactions describe the number of ionized sites on the GO's surface for a given pH. It is assumed that these sites when ionized represent the only source of surface charge in this system (we ignore, for

Reaction	pKa	Distribution ratio
$\text{COOH}^* \rightleftharpoons \text{COO}^{*-} + \text{H}^+$	4.3	3.0
$\text{COOH} \rightleftharpoons \text{COO}^- + \text{H}^+$	6.6	7.4
$\text{OH} \rightleftharpoons \text{O}^- + \text{H}^+$	9.8	6.5

Table 7.1: The 3 equilibrium reactions proposed by Konkena [4] which form the basis for GO's surface charge. The \* denotes carboxyl groups stabilized by near by hydroxyl groups near the edge of the GO sheet.

instance, the adsorption of ions onto GO). Typically charge regulation models [44, 161] deal with the silanol equilibrium on the interface of silica, here however there are three different functional groups contributing to the surface charge. The fraction of ionization of a particular functional group is denoted as  $\alpha_i$  and is given by

$$\alpha_i = \frac{K_{d,i}}{K_{d,i} + [H^+]}, \quad (7.1)$$

where  $K_{d,i}$  is the dissociation constant and is derived from the pKa of that particular functional group. As Konkena provides not only the pKas but also the distribution of these functional groups we can then weigh each  $\alpha_i$  by the appropriate amount  $q_i$  to get the fraction of ionization of the GO's surface. This is multiplied by the surface charge density at total ionization  $\sigma_0$  (which is a fitting parameter here) to give the surface charge density  $\sigma$

$$\sigma = \sigma_0 \frac{\sum q_i \alpha_i}{\sum q_i}. \quad (7.2)$$

This defines the boundary condition for the Poisson equation at the GO-electrolyte interface, coupling it to the PNP equations.

The 2D model is a pair of GO sheets separated by 15 mM KCl electrolyte shown in figure 7.4. Details of the boundary conditions and various parameters are provided in tables 7.2 and 7.3. No perturbation is applied and thus the system is studied in equilibrium. While Konkena's data is relatively comprehensive, it is not stated in the manuscript if there was a background electrolyte used (as at moderate pHs the ionic strength can be very low). Recent work by Gudarzi [207] used zeta potential measurements in a 15 mM KCl background electrolyte to calculate the surface charge of GO using the Grahame equation. Additionally the author compares the work to Konkena's charge titration measurements finding a decent match if one assume the specific surface area of GO to be 1800 m<sup>2</sup>/g. Assuming that Konkena's work is performed using a similar background electrolyte the model can be solved and compared to existing experimental results.

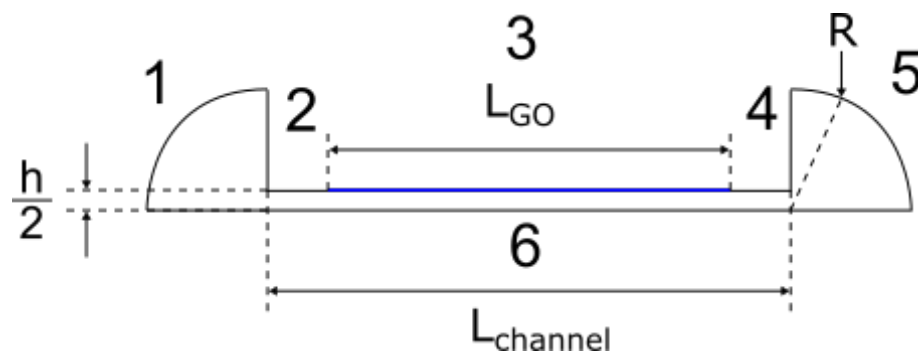


Figure 7.4: A schematic of the COMSOL model with parameters and boundaries marked.

Boundary	Equation	Condition
1	Poisson	Applied potential (0 V)
2, 4, 6	Poisson	Insulating
3	Poisson	Surface charge density (charge regulated)
5	Poisson	Ground
1, 5	Nernst-Planck	Concentration = $C_{inf}$
2, 3, 5	Nernst-Planck	No flux
6	Nernst-Planck	Planar symmetry

Table 7.2: The boundary conditions for the PNP equations solved using the COMSOL model described in this section.

Parameter	Value
$h$	1.4 or 200 nm
$L_{channel}$	1000 nm
$L_{GO}$	750 nm
$R$	150 nm
$C_{inf}(K^+)$	15 mM
$C_{inf}(Cl^-)$	15 mM
$C_{inf}(H^+)$ and $C_{inf}(OH^-)$	pH dependent

Table 7.3: The values of various parameters used in the COMSOL modelling performed here.

## 7.3 Results

### 7.3.1 Experimental results

Studies were performed at pH 10 and pH 4 representing, roughly speaking, the two extremes of the surface charge of GO- highly charged at pH 10 and poorly charged at pH 4. Increasing the pH beyond pH 10 runs the risk of reducing the GO in the alkaline conditions [210]. As the SAM is quite thin it's an important initial experiment to show that the majority of the impedance is due to the GO and not the bulk resistance. Concentration conductance plots clearly demonstrate that the dominant behaviour of the measurement is due to the GO's nanochannels. The shape of the curve (figure 7.5) at pH 10 closely matches a constant surface charge material. Unfortunately the membrane sample fouled with continued use and gave anomalously low conductances at high concentrations at pH 4. The inset in figure 7.5 shows the low concentration regime of the sample for both pHs.

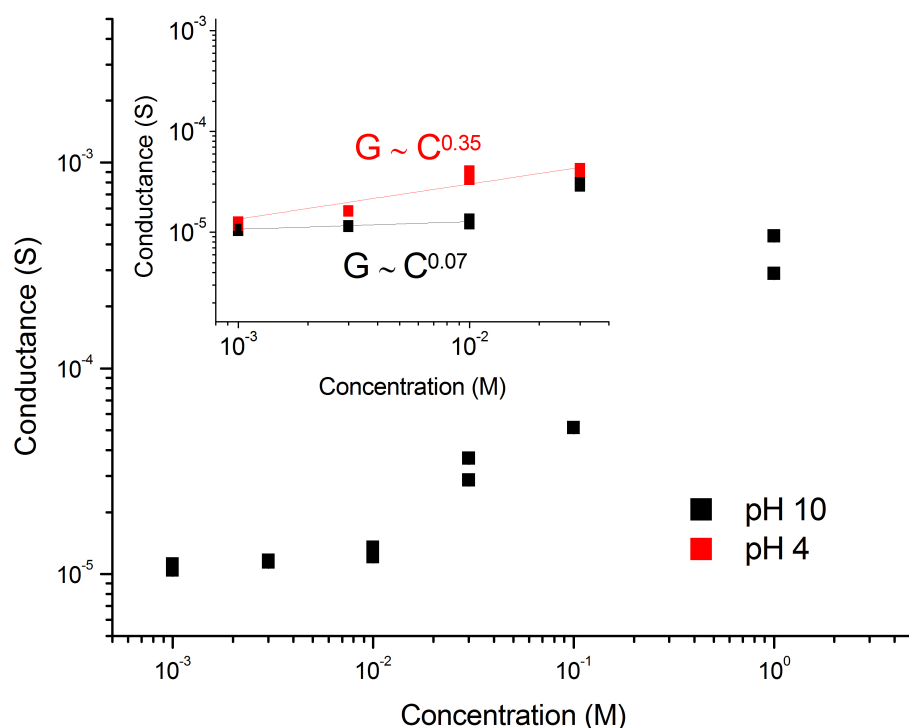


Figure 7.5: The conductance is plotted against the concentration for the two pHs considered.

The conductance plateau for pH 10 (figure 7.5) appears to be well defined and changes from surface dominated conduction to bulk conduction at around  $10\text{ mM}$ . Assuming this to be a Dukhin number of 1 and the interstitial height between GO sheets to be  $1.4\text{ nm}$  [35], the surface charge is approximately  $1.35\text{ mC/m}^2$  which is in quite good agreement with Raidongia's corrected value of  $4.05\text{ mC/m}^2$  and the estimate from chapter 5. Differences in surface charge density here can be attributed to the fact that the GO batches were different. Variation in oxidation levels can lead to different distributions of functional groups on the GO sheets. In all cases however, these surface charge density values remain lower than the expected values from colloidal zeta potential measurements.

As for the pH 4 data it is worth noting that it is at least as conductive as the pH 10 case which is a counter-intuitive result in the low concentration limit where one expects a geometrically similar system with higher surface charges to conduct far better! In the low concentration limit the data scales with  $G \propto C^{0.35}$  which suggests a kind of pH dependent shift in the surface charge density. It is quite likely that this unexpectedly high conductivity can be attributed to proton conduction in the film which is a known charge transport mechanism in GO [208]. The pH 10 findings agree with claims of constant surface charge density reported by Raidongia [35] and Guo [2], with only a weak scaling with concentration and are in strong contrast to measurements made using CNTs reported by Secchi [173] and the observation of power law like behaviour in chapter 5.

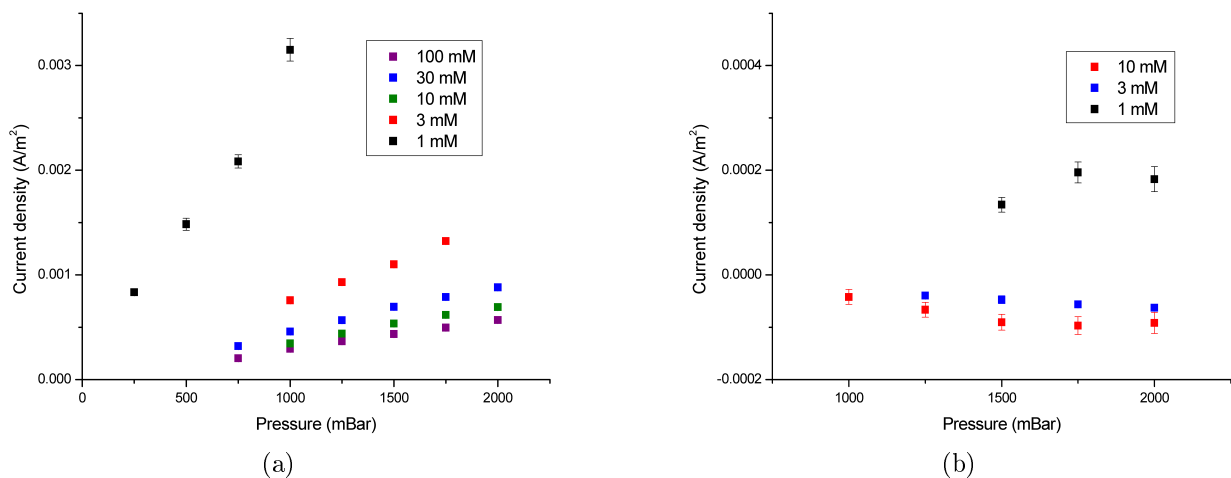


Figure 7.6: Streaming current densities at various applied pressures and concentrations for a) pH 10 and b) pH 4.

Both streaming current plots have the same trend that as concentration increases the streaming current decreases. This agrees with trends observed by others [44,211,212]. Streaming currents have been described in the literature to be proportional to the zeta potential of a system (in addition to some geometric factors). Zeta potentials [16] in the Debye-Hückel limit scale with  $\frac{1}{\sqrt{c_\infty}}$  like the Debye length. This power law like trend is not observed here suggesting a more complex relation between the streaming current and the zeta potential or the zeta potential and the electrolyte concentration. The reason that the streaming current reversed at pH 4 in figure 7.6 is probably due to that fact that the GO is near its isoelectric point and very little charge is present at the interface. It is also worth noting that in both cases these currents are very small, the membrane area is  $\sim 44.2 \text{ mm}^2$  so even the largest current measured at pH 10 is around  $150 \text{ nA}$  and the currents at pH 4 are all less than  $10 \text{ nA}$ .

Conductance was calculated by taking the line of best fit of the I/V data and taking the gradient of this line as the ionic conductance, as illustrated in figure 7.7. Frequently, as the applied potentials were very small, there was an offset in the data which is due to diffusive currents and concentration imbalances. As can be seen in figure 7.7 there is an obvious hysteresis in this system even at these small potentials. This was hypothesized to be due to the anticipated high dielectric constant of water in the GO. In order to determine

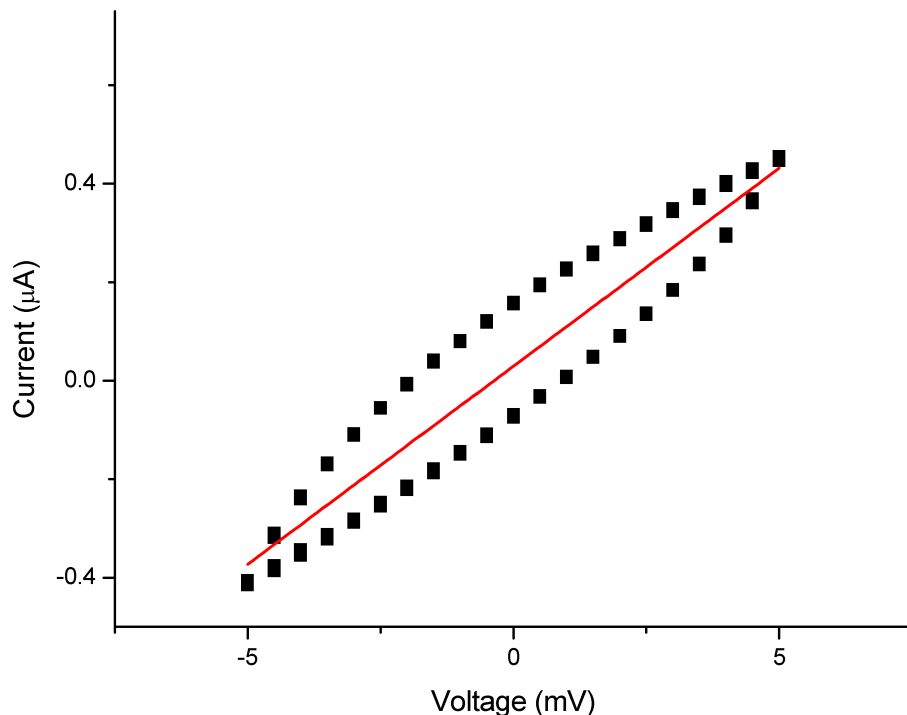


Figure 7.7: I/V curves for GO generally have an unusual hysteresis. The data is for pH 4 with a concentration of 10 mM of KCl.

the ionic conductance of the membrane and to obviate this additional effect, large wait times (in excess of 20 seconds) were used to 'discharge' this capacitive effect. Variances in wait time were also studied. The effect of wait time is characterized in figure 7.8, where it can be seen that the hysteresis is indeed decreasing for larger wait times but the channel's conductance is also unexpectedly decreasing as well.

More systematic studies of this behaviour calculated a capacitance based off this hysteresis which was performed in an identical way to how one does cyclic voltammetry. So

$$C = \frac{1}{2\nu\Delta V} \oint i(V)dV \quad (7.3)$$

where  $\nu$  is the scan rate (here that's simply  $V_{step}/t_{wait}$ ),  $\Delta V$  is the voltage range and all other symbols have their usual meanings. It was found that this capacitance increases with  $t_{wait}$  and that the conductance through the channel falls as  $t_{wait}$  increases, which is shown in figure 7.9. These experiments were also conducted with a 5% ethanol electrolyte to see if it might disturb the water-GO interaction. The results show that the ethanol had only a limited effect.

Taking the defined capacitance in equation 7.3 and applying it to the concentration - conductance I/V data gave an interesting relationship between the conductance of the channel and the capacitance measured. In both cases the capacitance was found to be roughly proportional to the conductance of the channel (figure 7.10). This is a particularly surprising result given the initial hypothesis that the hysteresis effect might be attributable to a high water-GO relative permittivity. The nature of this hysteresis will be expanded upon in the next section.

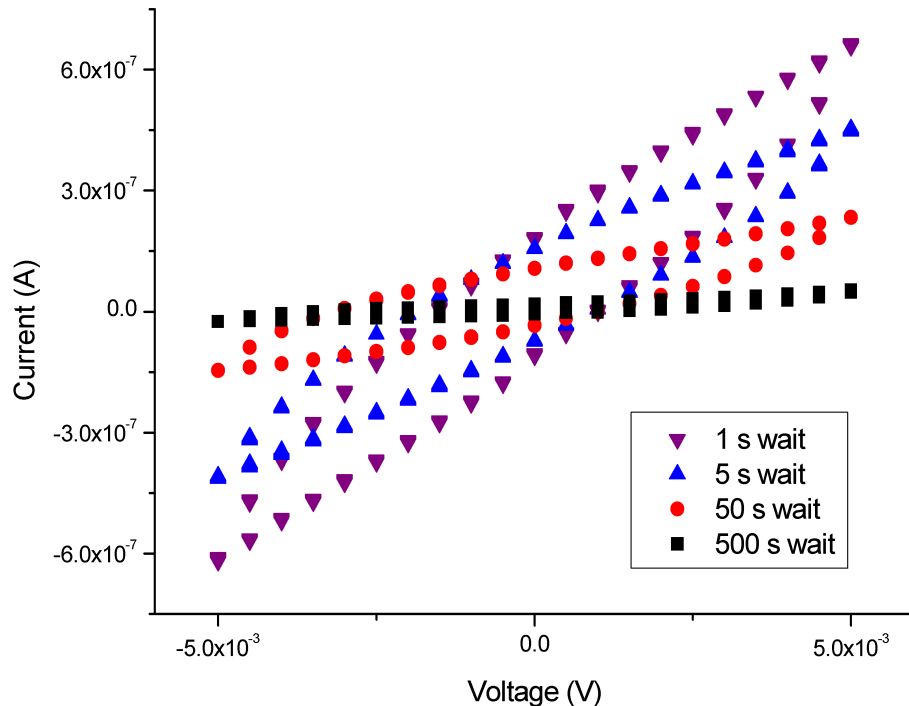


Figure 7.8: Increasing the wait time did cause the hysteresis to reduce however the conductance of the membrane also decreased.

The streaming current work was expanded upon by considering the hysteresis effect observed in the I/V data as a kind of capacitance. In that sense the streaming current  $i_{stream}$  would be given by

$$i_{stream} = G_{stream}\Delta P + C\frac{dV_{stream}}{dt}, \quad (7.4)$$

where  $G_{stream}$  is the streaming conductance,  $\Delta P$  is applied pressure difference,  $C$  is the system's capacitance and  $\frac{dV_{stream}}{dt}$  is the time derivative of the streaming potential. Since the streaming potential is proportional to the applied pressure, an oscillating pressure leads to an oscillating streaming potential. The advantage of technique over conventional attempts to generate power from streaming currents would be that the applied pressure need not be large, it need only rapidly oscillate. This was tested in an experiment, figure 7.11, and allowed transient current values in excess of the typical constant pressure values. This was tested for a sample using a 10 mM KCl electrolyte at pH 4. Comparing the peak current value of 25 nA to the constant value of 4 nA at 1500 mbar suggests that a system like this might work. However the fact that the measured capacitance in this system is proportional to the current (figure 7.10) means that the simple equation suggested above becomes somewhat complicated. This equation also implicitly assumes that the capacitive current can be superimposed with the standard streaming current (perhaps it could as a perturbation).

After confirming such a miniscule surface charge density, the expectation for a large osmotic current was unlikely. Siria [30] found for the case of boron nitride nanotubes that the osmotic current was approximately

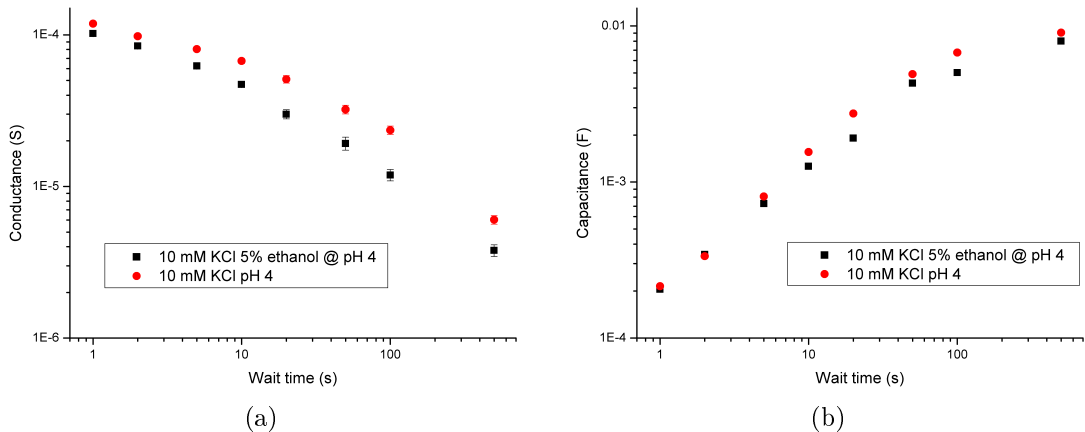


Figure 7.9: The conductance (a) and the capacitance (b) of the GO membrane at various scan rates for an aqueous electrolyte and a 5% ethanol electrolyte.

$$i_{osm} \propto 2\pi R \Sigma V_{DO} \quad (7.5)$$

where  $R$  is the radius of the nanotube,  $\Sigma$  is the surface charge density and  $V_{DO}$  is the diffusio-osmotic potential across the nanotube. Since the surface charge density is so low, this system isn't of great interest to power generation from concentration differences. What is somewhat surprising is the similarity in the currents observed in figure 7.12. A small I/V perturbation is applied on top of the diffusion current so a steady state conductance can be easily obtained. The concentration difference in both cases was a ratio of 1 : 1000. In the inset of figure 7.12 one can even observe the conductivity of the membrane increasing as time passes, noticeable particularly by the changing size of the initial current transients. While large initial transient in the diffusion current is large (around  $10 \mu A$  compared to the steady state of  $\sim 100 nA$ ) and swift to settle, no further investigation was conducted here.

### 7.3.2 Simulation results

Solving the COMSOL model described in subsection 7.2.2 requires a few steps. Firstly it's necessary to consider the GO sheets relatively independent of one another. Overlapping potentials and concentration enhancement could lead to changes in the surface equilibrium (and thus the surface charge density) of the GO. Initially the GO sheets were placed  $200 nm$  apart and in a  $15 mM$  KCl electrolyte, the Debye length is  $\sim 2.5 nm$  so the GO sheets are certainly distant enough from one another that their potentials are screened from one another, as can be seen in figure 7.13a. For a maximal surface charge of  $\sim 55 mC/m^2$  the Gouy-Chapman length is  $\sim 0.6 nm$  so the mesh size is kept below this. Since the concentration of  $H^+$  is enhanced at a particular surface due to the negative surface charge of GO, the surface pKas needed to be calculated from the bulk pKas experimentally found by Konkana [4]. This is performed by setting the pH to the appropriate pKa and then using Konkana's surface charge titration data to defined a constant surface charge boundary condition. The potentials calculated by the model match the anticipated potentials given

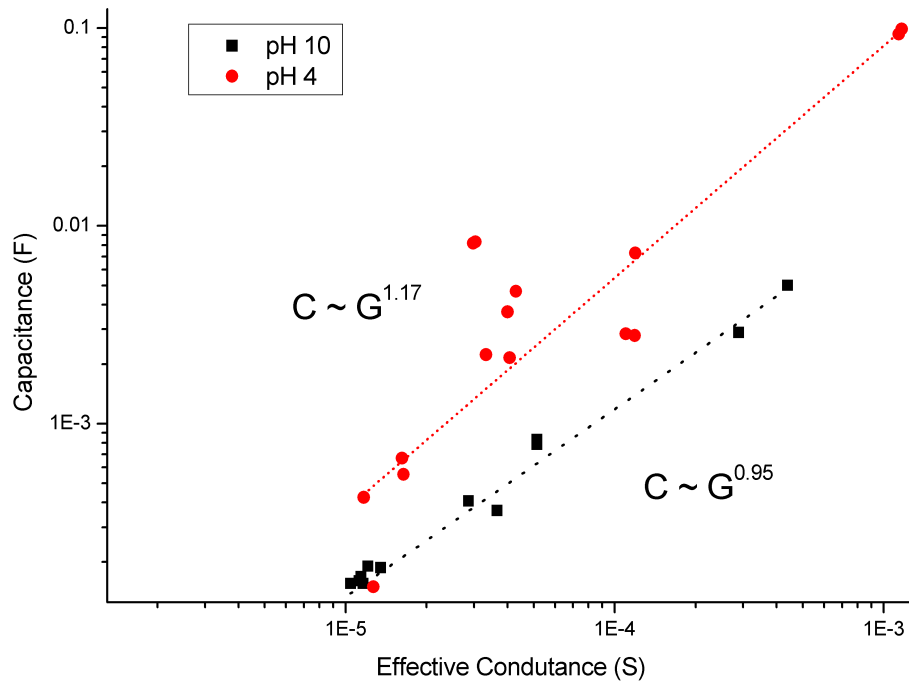


Figure 7.10: It was found for both cases that the conductance of the GO membrane was proportional to its calculated capacitance.

by the Grahame equation for surface charges given in Konkena's charge titration data [4,207]. The Grahame equation is

$$\sigma = \sqrt{8I_C\epsilon\epsilon_0RT} \sinh\left(\frac{F\psi_0}{2RT}\right), \quad (7.6)$$

where  $I_C$  is the ionic strength and  $\psi_0$  is the surface potential. The pH as a function of distance from the channel's centreline is plotted in figure 7.14. The surface contact values of pH were then used in the next step of the model to fit  $\sigma_0$  (which was found to be  $\sim \sigma_0 = -55 \text{ mC/m}^2$ ). Once the surface pKas were found it was then possible to decrease the interstitial distance and allow the sheets' potentials to overlap. These simulations were run using the charge regulation model proposed in the subsection 7.2.2 and the data is summarized in figure 7.15. Additionally data from Gudarzi [207] and Konkena [4] are plotted as well as the equilibrium equations themselves uncoupled from the PNP model (for  $\sigma_0 = -55 \text{ mC/m}^2$ ). While the agreement with Konkena's experimental data is excellent the anticipated confinement effect is not strongly observed.

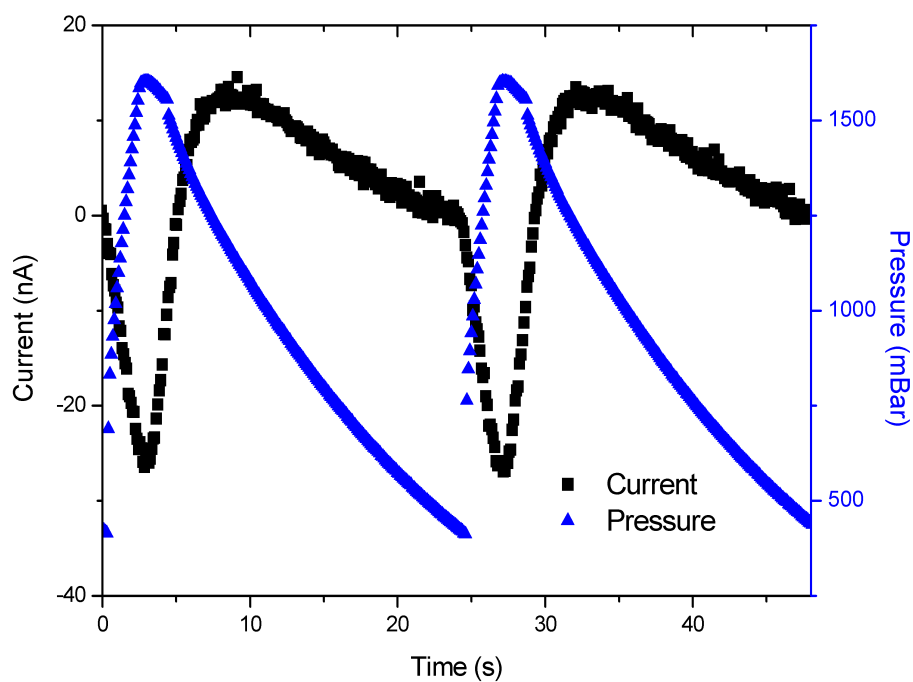


Figure 7.11: An oscillating pressure signal applied to the membrane results in an oscillating streaming current.

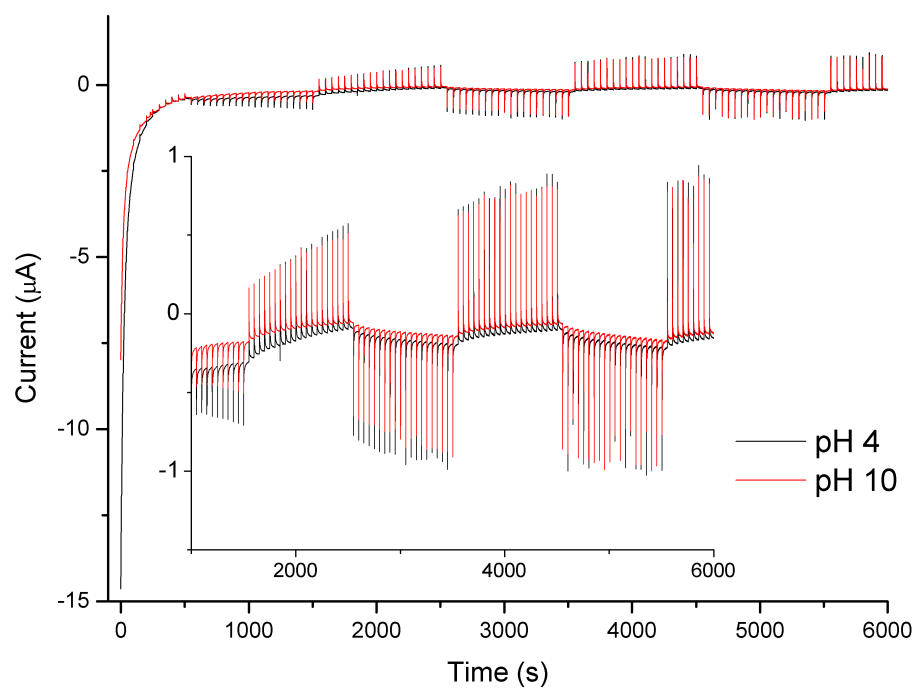


Figure 7.12: Concentration gradient driven currents for pH 10 and 4 under a concentration ratio of 1000. A small I/V is applied to help measure the conductance of the GO nanochannels.

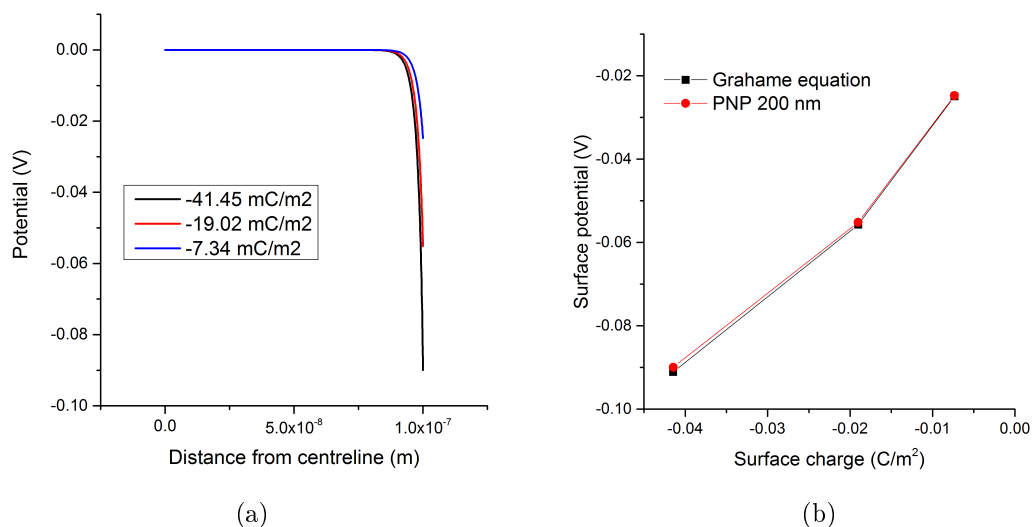


Figure 7.13: a) The potentials for 3 different surface charges on GO at  $pH_i = pK_{a_i}$ , b) the surface potentials calculated using the model match the expected surface potentials calculated from the Grahame equation.

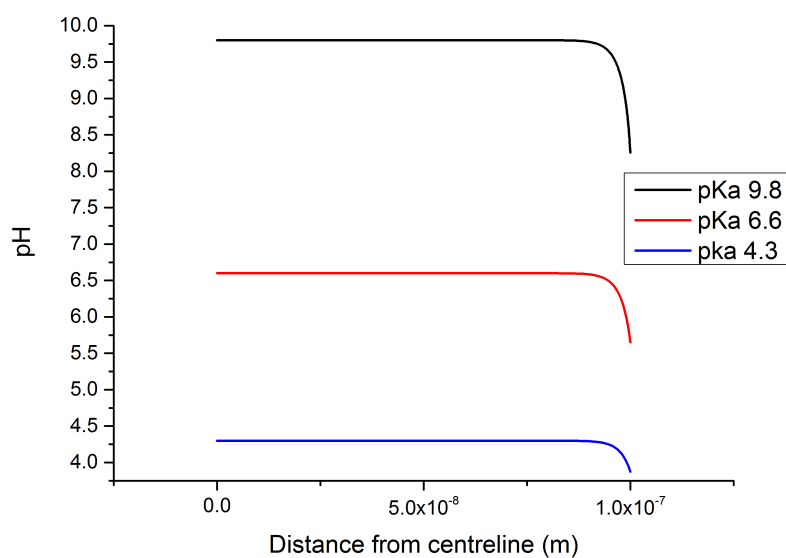


Figure 7.14: The pH as a function of the distance from the centreline between the two GO sheets. The GO sheets are separated by 200 nm in a 15 mM background electrolyte.

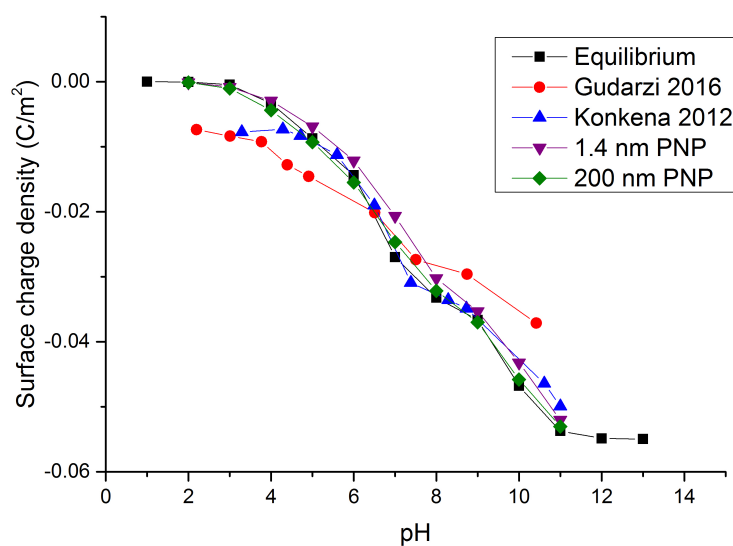


Figure 7.15: The surface charge density for GO is plotted here against pH. Equilibrium data are calculated using the equilibrium equations with no coupling to any model/geometry, Gudarzi's data are calculated from zeta potential measurements in 15 *mM* KCl background electrolyte, Konkena's data are calculated using charge titration results and by assuming a GO surface area of 1800 *m*<sup>2</sup>/*g*, the full PNP model was also solved for two interstitial distances; 1.4 *nm* and 200 *nm*.

## 7.4 Discussion

The discussion here is ordered as follows- firstly the difficulties of measuring concentration-conductance plateaus are described, a comparison between the streaming conductance results of the SAM and a similar work [2] is made, then the simulation results are compared to the experimental data collected and finally the origin of the hysteresis observed in I/V measurements (such as 7.7) is examined.

Concentration-conductance plateaus can be quite misleading depending on how the experiment is conducted. For instance Karnik [37] and Duan [161] explore concentrations down to  $10^{-7} M$ , whose conductances one naively expects to scale with the concentration listed. While Stein's [36] work, which introduced the concept to the literature, referred to the idea of nanochannel conductance independent of concentration in the dilute limit, it is more importantly conductance independent of electrolyte conductivity, which in his equations is given by a dilute monovalent electrolyte. There are at least three additional effects and complications which make very low concentrations like these experimentally challenging to accurately probe in the context of a conductance - concentration plot. Importantly the higher mobility of the hydronium and hydroxide ions means that in low concentrations these two ions contribute significantly to bulk electrolyte conductivity. As the dissociation constant of water is  $10^{-14}$ , at  $10^{-7} M$  of salt (for instance KCl or NaCl) the concentration of hydronium and hydroxide is equal to the concentration of salt. The second point is mentioned in the supplementary information in Duan's report [161], the carbon dioxide in the air will form an equilibrium reaction with the water forming carbonic acid, which will then dissociate into carbonate, bicarbonate and hydronium ions. The equilibrium of this reaction is around pH 5 (understandably this is environmentally dependent). Most authors report measuring their systems over a number of hours and thus this effect certainly plays a role in open systems (and likely in closed systems). Finally most authors use Ag/AgCl electrodes to apply potentials to their device and place them quite close to the channel system in order to increase the resultant electric field. While AgCl is quite insoluble in water the solubility product is  $1.8 \times 10^{-10}$  [213] which whilst low does mean that in chloride concentrations of  $10^{-5} M$  the  $Ag^+$  concentration will rise to  $1.8 \times 10^{-5} M$ . These three factors mean that exceptional consideration would need to be conducted to probe the dilute regions of nanofluidic systems or the reality maybe in many cases that reported plateaus are simply due to experimental error rather than a true change in electrolyte conductivity.

The streaming currents shown in figure 7.6 are very small. The highest achieved was for 1 mM of KCl at pH 10 and had a performance of  $3 mA/m^2/bar$ , which is much less than Guo's [2] result for a graphene hydrogel membrane of  $\sim 168 mA/m^2/bar$ . What is striking about this result is that whilst the GO membrane studied here is  $\sim 100 - 200 nm$  thick, Guo's hydrogel membrane is a significantly thicker  $\sim 100 \mu m$ . Indeed examining the ionic conductances measured and normalizing them we see that Guo's membrane is significantly more ionically conductive than a shear aligned GO membrane (figure 7.16). Due to Guo's experimental setup the hydrogel membrane was not strong enough to withstand pressures greater than 10 kPa. Additionally the hydrogel structure is still greatly affected by colloidal

forces, measurably changing its thickness in response to changes in concentration. So whilst the result is significantly better than GO, it does pose the question as to whether it would extend to larger pressures and real world applications, such as micro-power generation.

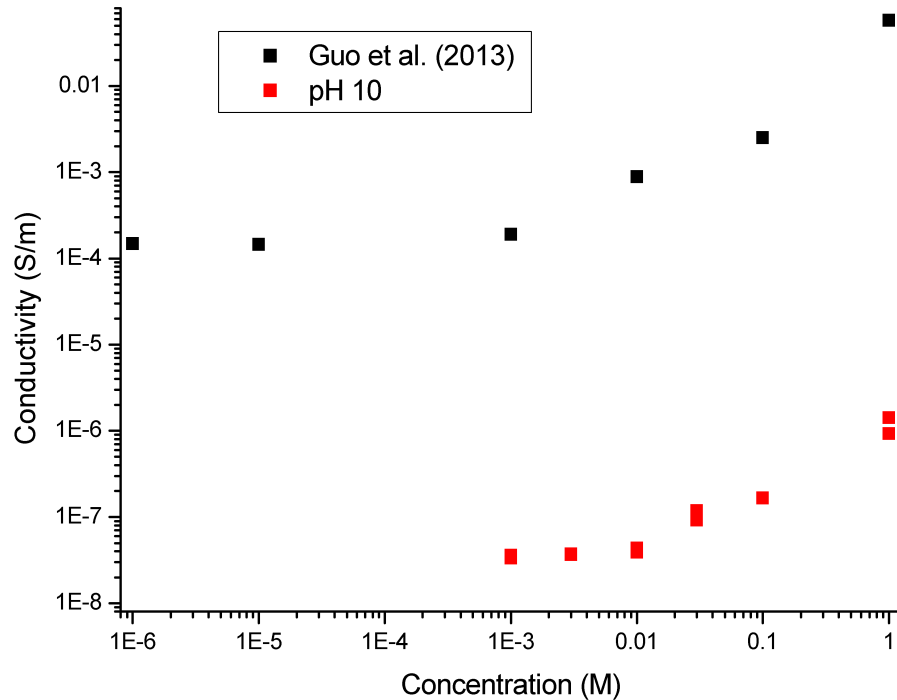


Figure 7.16: The ionic conductivities of the pH 10 data and Guo’s [2] are compared. The graphene hydrogel membrane is significantly more conductive than the GO.

Differences in performance can be attributed to a number of factors- the structure of the hydrogel membrane is more disordered (it gives no signal in X-ray diffraction [2]) and the interstitial space is much larger, varying from 11 *nm* to 8 *nm* depending on the concentration. This is quite different to the SAM case where the peak in the X-ray diffraction is noticeably sharper than the peaks given by films formed using vacuum filtration [125]. While no hydrated SAM X-ray diffraction has been performed yet the result given in Raidongia [35] for a vacuum filtration film provides a likely estimate of the interstitial space of 1.4 *nm*. The difference in interstitial height here is critical as not only does it increase the hydraulic resistance of any particular rectangular channel by a factor of  $\sim 1000$  as  $R_h \propto h^3$  but it also affects the surface charge density of the material as highlighted by the differences between nanofluidic [35] (chapter 5) and colloidal findings [4,207]. The more structured ordering of the GO SAM is no doubt detrimental to its ionic conductivity compared to the hydrogel membrane, where defects and changes in the direction of the alignment could mean shorter path lengths for ions. Finally the experimental methodology is quite different. Guo’s approach applied a pressure on and off for 30 *s* pulses with no mention of effects like concentration polarization, nor is any data for more than 1000 *s* presented, making unbiased comparison between the two sets of measurements difficult. However, in comparison to larger, similar nanochannels SAM has worse streaming conductivity and ionic conductivity. It should be mentioned here that the entire volume of material used was considered when normalizing the current value rather than attempting

to estimate the volume of nanochannels within these materials as the structure here is quite complex.

In contrast to the zeta potential measurements made by Gudarzi [207] both Guo [2] and the work performed here observe a change in sign in the streaming current at low pH. At pH 4 (figure 7.6) by varying the concentration the sign of the surface potential changes resulting in a change in sign of the streaming current. This could be unexpected in GO however the current measured is very low which suggests only a very small positive zeta potential and one can attribute this to differences in the synthesis process between this GO and that studied by Gudarzi. Guo's pH 3 results are anticipated from zeta potential measurements in the literature as graphene hydrogels reduced in hydrazine have nitrogen doped onto them resulting in some positively charged functionalities at low pH [104].

The surface charge results in figure 7.15 are quite surprising. There is almost no effect of confinement on the surface charge density using this model. This points to additional mechanisms such as those mentioned by Bocquet [6] as to why the surface charge density of GO in a compact film is so low ( $\sim 1.35 \text{ mC/m}^2$  at pH 10) compared to measurements performed on a colloidal suspension ( $\sim 37 \text{ mC/m}^2$ ). What adds further to this mystery is that ions permeate through GO membranes, with claims that their diffusion is in fact enhanced [130], one might anticipate that partial shedding or distortion of the hydration shell might lead to a reduced diffusivity. Additionally it is worth also noting that at low pH the charge regulation model fails to describe the experimental data again. This is explained by Gudarzi [207] as surface charge contributed by sulfur present as a contaminate functional group in the GO.

An important factor in the absence of this confinement effect is the background electrolyte. The ionic strengths in these simulations go to a maximum of  $25 \text{ mol/m}^3$ ,  $15 \text{ mol/m}^3$  of which is contributed by the KCl electrolyte. The majority of surface charge present on GO is screened by the more abundant  $\text{K}^+$  ions. In cases where the KCl concentration is low the regulation effect is stronger as the surface concentration of  $\text{H}^+$  is higher, as can be seen in figure 7.17. Even at pH 10 as the concentration of KCl decreases the  $\text{H}^+$  ions are able to reduce the surface charge of GO, however it still isn't enough to explain the differences observed in colloidal and film measurements.

It is important here to highlight the role concentration play in comparing the simulation results with the experimental ones. The transitioning concentration from surface to bulk conduction was found to be  $\sim 10 \text{ mM}$  in this chapter and  $\sim 30 \text{ mM}$  in chapter 5 however Gudarzi's and Konkana's results were performed and assumed to be performed, respectively, at  $15 \text{ mM}$ . From figure 7.17 the simulation data suggests that at the pHs considered this concentration difference between the two sets of experimental data again will not account for the large difference in the surface charge densities.

The role of bulk concentration does however explain the changes in the power laws observed in the I/V plots in 7.5 and the results found in chapter 5. In figure 7.17 the surface charge densities for a range of pHs and concentrations are plotted. The resulting curves are fitted to power laws whose exponents agree well with the surface charge governed results measured using ion current measurements. A comparison of the results found from

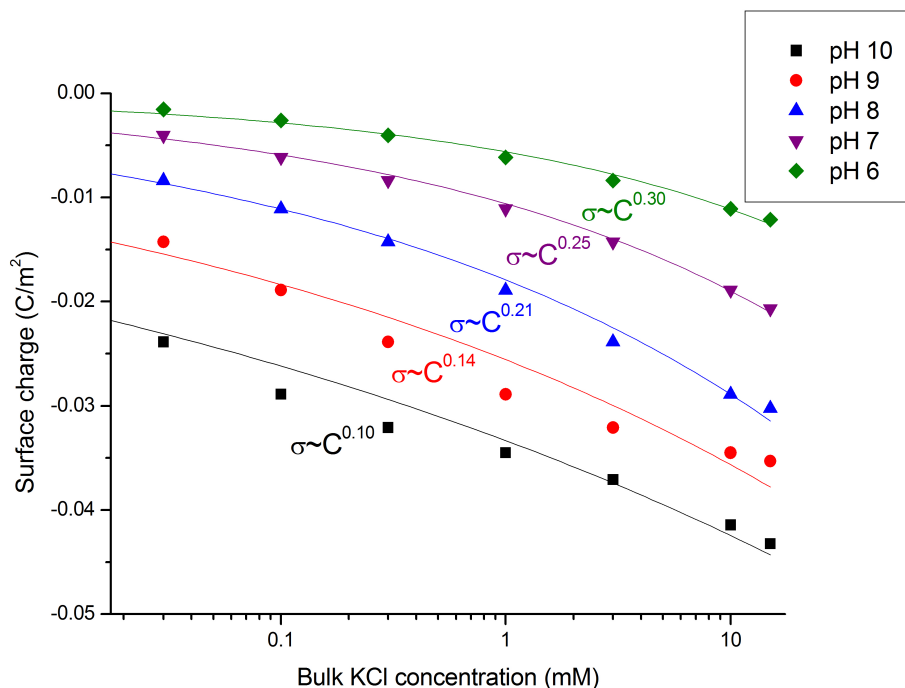


Figure 7.17: The bulk concentration of KCl was modified showing the effect of  $H^+$  on the surface charge density for a range of pHs.

experiments and simulations is tabulated in table 7.4. The agreement of the exponents suggests that the power law behaviour in the surface conduction regime is due to this charge regulation effect. This finding shows that GO's complex surface behaviour can be understood, at least partially, within the context of the PNP equations. Concentration dependent surface charge variation, particularly around pH 7, will have important effects in the results from pressure driven separations.

Work in  $2\text{ nm}$  nanochannels by Duan [161] can provide some insight into this irregularity between colloidal measurements and nanofluidic estimates of the surface charge density. Duan's work in silica is easy to compare to colloidal studies as the material is so commonly used. For a transition concentration of  $\sim 100\text{ mM}$  the estimate of Duan's surface charge density based off the Dukhin length is  $\sim 19.3\text{ mC/m}^2$  for both KCl and

Experiment	pH	Experimental power law exponent	$R^2$	Simulation exponent
2.1 $\mu\text{m}$ planar devices in chapter 5	6	0.25	0.99	0.30
7.1 $\mu\text{m}$ planar devices in chapter 5	6	0.32	0.98	0.30
Shear aligned membrane	4	0.35	0.85	$\sim 0.4^*$
Shear aligned membrane	10	0.07	0.68	0.10

Table 7.4: A comparison of power law exponents measured experimentally and those calculated using the charge regulated COMSOL model described here. The \* is a result extrapolated from the simulation data.

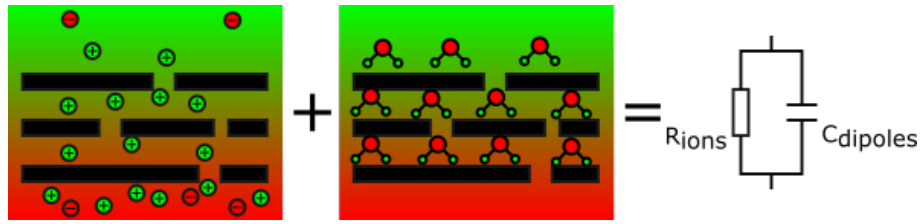


Figure 7.18: The motivating picture for the hysteresis observed in GO. There are two mechanism - resistive like ionic conduction and capacitive behaviour due to an expected large dielectric constant of water.

NaCl. Simulations performed in the same work suggest that for  $100\text{ mM}$  of KCl the surface charge is  $26.4\text{ mC}/\text{m}^2$ . In the case of the charge at total ionization Duan assumes this to be  $-1.28\text{ C}/\text{m}^2$ . A review by Kirby [214] provides the zeta potential of silica at pH of 5.8 with an electrolyte concentration of  $100\text{ mM}$  KCl as  $-21\text{ mV}$  which when put in the Grahame equation gives a surface charge of  $15.75\text{ mC}/\text{m}^2$ . So in Duan's case the colloidal zeta potential measurement and the nanofluidic estimate agree rather well. This suggests that GO's surface charge density's mismatch may be limited to GO itself or systems like it with heterogeneous charge distributions (which was not considered in the modelling here).

Now to address the underlying observations within these experiments- the nature of the hysteresis observed in the I/V measurements characterized in figure 7.7 which is related to the discharge of the current signal (figure 7.3) and the experimental method used to investigate the GO. An initial motivation for these experiments was a potentially large value of the dielectric constant of water in the vicinity of GO. The model proposed here to describe this behaviour is characterized by two simple features summarized in figure 7.18. In this sense the two effects would operate in parallel leading to essentially a leaky capacitor. One can quickly ascertain whether this model is realistic by taking values of resistance and capacitance calculated from the I/V plots and assigning them to resistors and capacitors in equivalent circuits to give approximate values to these elements and then compare them to the experimental data. While this won't provide a quantitative match to the experimental data, it should indicate whether the model is somewhat describing the correct behaviour. Using SPICE (Simulation Program with Integrated Circuit Emphasis) one can simulate these circuits for a variety of input signals. In figure 7.19 the data plotted are for a stepped potential, identical to the experimental data, collected for the proposed parallel and a series circuits. Neither simple circuit is able to correctly describe the behaviour observed in the experimental data however it is clear that the parallel circuit differs significantly from the experimental data. This illustrates that the hysteresis measured cannot be so simply described and that a more complex mechanism is at play.

Work on ion selective membranes [3, 215, 216] suggests a more likely reason for this hysteresis is concentration polarization. Moya's [216] work on chronoamperometric response in a cation selective membrane (standard CMX Neosepta) has many similar features. Chronoamperometry applies a single step potential change and observes the current response. The experiment is performed in the under-limiting current range like the experiments performed here and Moya models the behaviour using a 1D PNP model which is

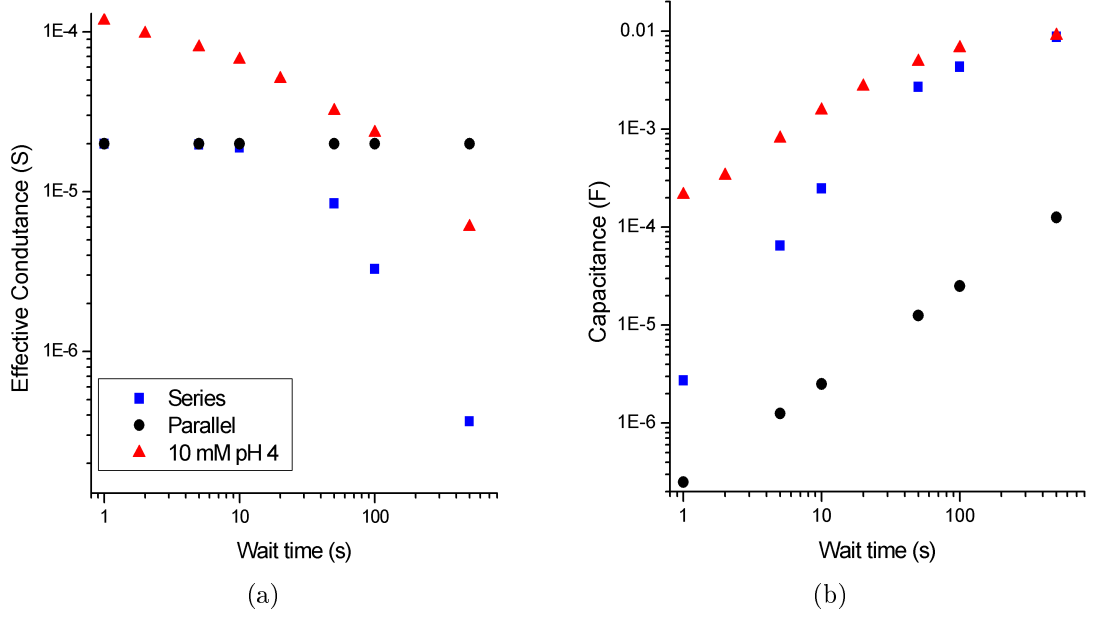


Figure 7.19: A comparison of SPICE simulation data with experimentally collected data from a GO membrane for a) conductance and b) capacitance as a function of the wait time. The value of  $R$  is  $50\text{ k}\Omega$  and the value of  $C$  is  $5\text{ mF}$ . The potential applied in all cases was the same.

solved numerically. The works [3,216] describe a membrane where there is a bulk in either reservoir (which is stirred), diffuse boundary layers close to the membrane, an infinitely thin electric double layer on the membrane's surface and the membrane itself (see figure 7.20). In particular the membrane system, in steady state when a constant current is applied, can be described by 3 separate resistances [3]-

$$R_{tot} = R_{dif} + R_{ohm} + R_{cond} \quad (7.7)$$

where

$$R_{dif} = \frac{RT}{F\bar{i}} 2t_2 \left[ \frac{\Phi^I}{1 - \Phi^I} + \frac{\Phi^{II}}{1 + \Phi^{II}} \right], \quad (7.8)$$

$$R_{ohm} = \frac{RT}{F\bar{i}} \frac{2t_1 t_2}{T_1 - t_1} \ln \frac{1 + \Phi^{II}}{1 - \Phi^I} + R_{s+mb} \quad (7.9)$$

and

$$R_{cond} = \frac{RT}{F\bar{i}} \frac{2t_1 t_2}{T_1 - t_1} \left( \frac{\Phi^I}{1 - \Phi^I} + \frac{\Phi^{II}}{1 + \Phi^{II}} - \ln \frac{1 + \Phi^{II}}{1 - \Phi^I} \right), \quad (7.10)$$

where  $t_i = \frac{D_i}{D_i + D_j}$  for  $i \neq j$ ,  $\bar{i}$  is the DC steady current,  $\Phi^n = \frac{\bar{i}}{i_{lim}^n}$  is the normalized current density for the  $n^{th}$  diffuse boundary layer,  $i_{lim}^n$  is the limiting current density in that boundary layer and  $T_n$  is the transport number of the  $n^{th}$  ion in the membrane. What is particularly important here are the additional resistance contributions from  $R_{dif}$  which is due to diffusion and  $R_{cond}$  which is due to the variation in conductivity in the diffuse boundary layer. Since the membrane in this instance is defined only by a few assumptions - that its flux is given by

$$j_n = T_n \frac{i}{z_n F} \quad (7.11)$$

and that the transport number does vary with applied current and is 1 for the counter-ion and 0 for the co-ion, this theory would most certainly apply to membranes made from GO. In these equations Moya only solves the PNP equations with no coupling to Navier-Stokes and finds excellent agreement with the experiments performed. Additionally Moya finds a steady state current for the membrane investigated by setting  $i(t_{wait} = 300 s) = i_{steadystate}$ . For GO (figure 7.19) it is pretty clear even at 500 s the conductance has not stabilized, it indeed appears to be diverging. When the data is extracted (figure 7.21) it shows no strong indication of a steady state forming. In figure 7.21 the sample has already been cycled many times and starts from  $t = 0$  on the plot not in equilibrium. One of the reasons for this instability in the current is that the diffuse boundary layer hasn't grown enough yet. As this layer grows the conductance will shift from purely the membrane resistance, the naively anticipated results, to the sum of the 3 resistances described above. In most systems the diffuse boundary layer will grow until its boundary is stabilized by convective mixing, so larger wait times may in fact be necessary. The sharp nature of the curves in figure 7.21 are, however, quite different to those found in Moya's results and may indeed be indicative of this enhance dielectric constant. Untangling the effect of the concentration polarization of the diffuse boundary layers from this far swifter spike would require the use of other electrochemical techniques like impedance spectroscopy. Indeed given the tiny perturbation values explored here, it is somewhat surprising that this effect is so extreme.

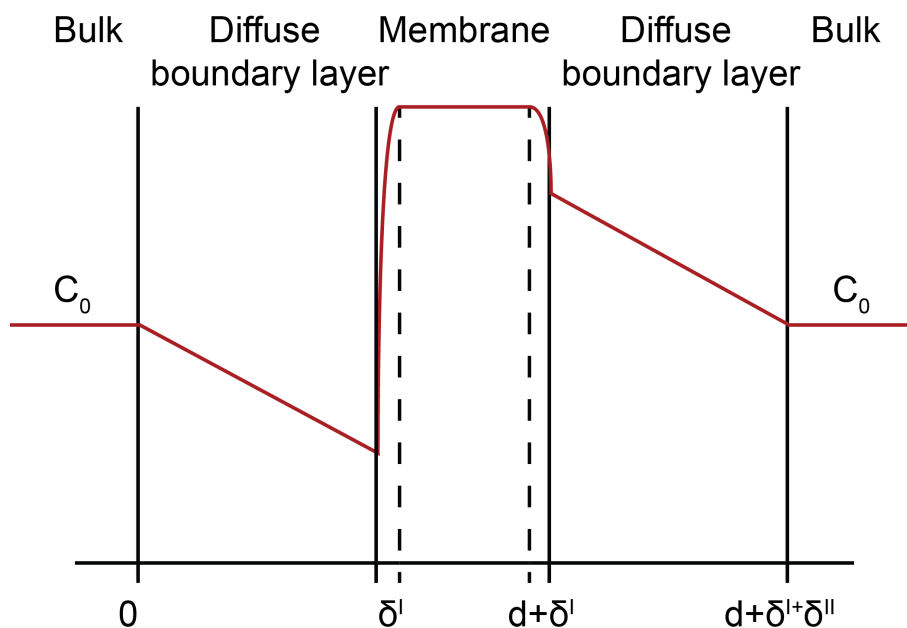


Figure 7.20: This figure is a recreation of figure 1 in [3], it describes a membrane with infinitely thin electric double layers and diffuse boundary layers of thickness  $\delta^I$  and  $\delta^{II}$ .

What is interesting is when one compares the results for a planar style device from chapter 5 with the membrane result (figure 7.22). While the membrane passes more current ( $\sim 10 \mu S$  for the membrane,  $\sim 2.8 \mu S$  for the planar device) the cross section of the planar device is significantly smaller and more porous. Taken as bulk conductivities the planar device roughly  $6.87 \times 10^7$  times more conductive than the membrane. This figure uses the measured height of  $2.1 \mu m$ , width of  $6 mm$  and length of  $14 mm$  for the planar

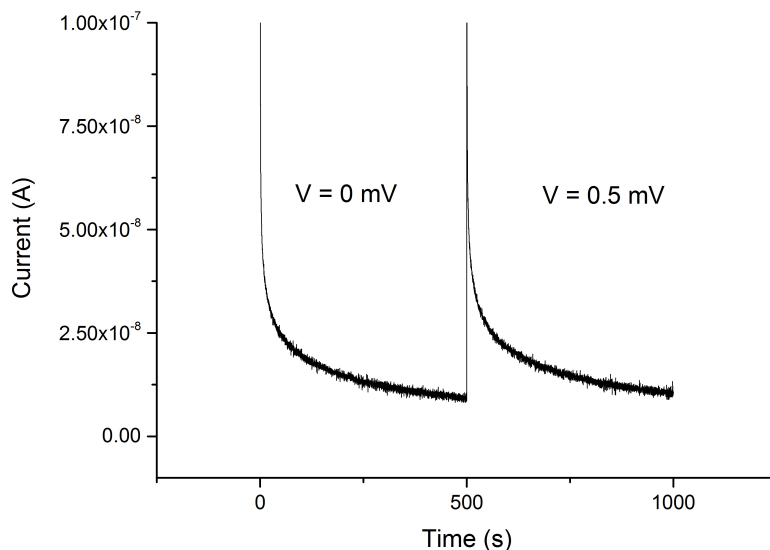


Figure 7.21: This data is a snippet of data collected from a GO membrane at a concentration of  $10\text{ mM}$  at pH 4. At this point in the experiment the membrane is already perturbed from equilibrium.

device. The membrane has a thickness of  $\sim 200\text{ nm}$  as measured using a cross section on a scanning electron microscope and an exposed area of  $44.2\text{ mm}^2$ . This figure doesn't account for the solution and electrode resistance in either case. The two samples were measured in an identical manner (ie. a stepped potential) with a wait time of  $20\text{ s}$ . So while the membrane is significantly less conductive than the planar device it also is exhibiting stronger concentration polarization. This figure, due to this curious difference between the two geometries, therefore does not accurately reflect the difference between the two membrane resistances. It's fairly obvious when one looks at the two data sets that the current signal is quite different, the planar case showing only small changes in resistance over the wait time whereas the membrane sample changes far more significantly which is certainly affecting its conductance. This could indeed be related to the effective pore area of each membrane, one might expect given this experimental result that the current density around the pores in the membranes is significantly higher than in the planar device.

For a given current, assuming a continuously porous structure in both cases the current density should be around  $\sim 3500$  times larger in the planar device (from the ratio of the two areas). However it's clear from figure 7.1 that the porosity of the two geometries is going to be closely linked with the ratio of the sheet length to the interlayer spacing. While work by Nair [131] has lead many authors to believe that the porosity of the GO film's surface is  $\sim d_{\text{interlayer}}/L_{\text{sheet}}$ , Cheng [132] found the role of defect sites to be critical when matching experimental diffusion data with 2D modelling. Naively with  $L_{\text{sheet}} \sim 900\text{ nm}$  and  $d_{\text{interlayer}} \sim 1.4\text{ nm}$  reduces the membrane's area by a factor of  $\sim 643$ . The porosity for the planar device can be estimated to be  $\frac{d_{\text{interlayer}} - 0.35\text{ nm}}{d_{\text{interlayer}}}$  where the  $0.35\text{ nm}$  figure comes from the extension of the electron clouds off the surface of the planes of GO [131].

Even with the conservative estimation of the porosity of the membrane for the areas studied the planar design is still has fewer channels exposed to the reservoirs, so it doesn't account for the suggested higher current density in the pores of the membrane. Further investigation here will be necessary to account for the enormous anisotropy in conductivity and the what the connection is between the structure and phenomena like concentration polarization. It is also worth pointing out that whilst the polarization behaviour is quite different between the two geometries both sets of experimental data I/V can be partially explained by charge regulation, however both geometries estimate the surface charge to be much lower than colloidal measurements.

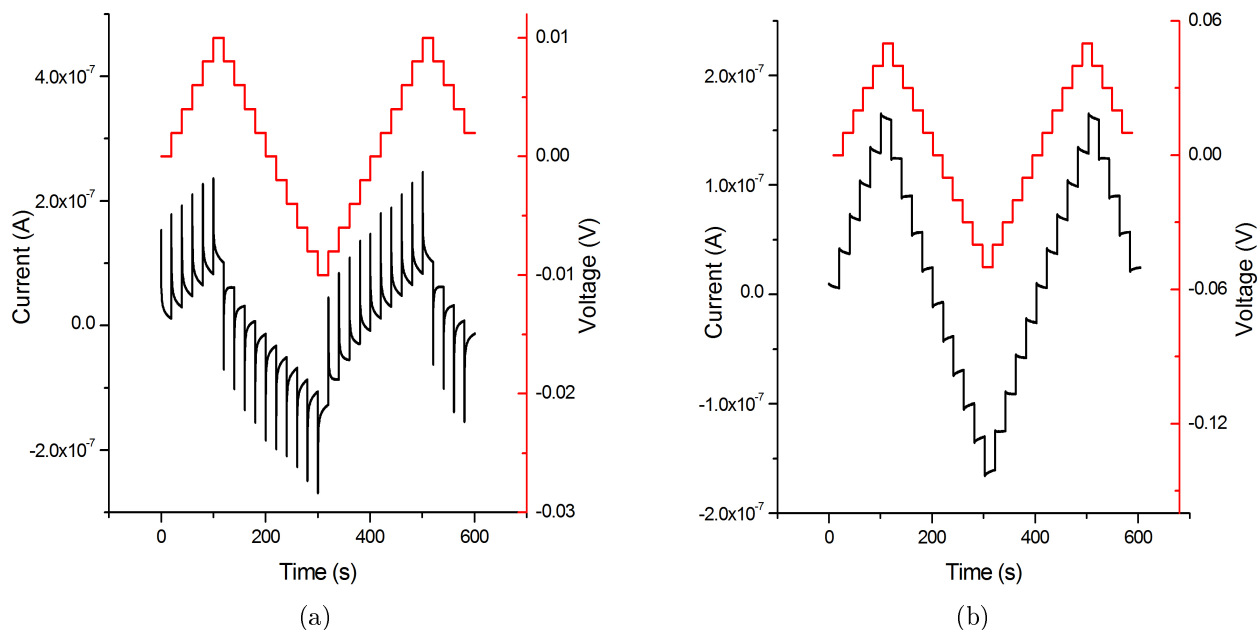


Figure 7.22: A comparison of the I/V data of the two different geometries illustrated in figure 7.1. a) The current-time and voltage-time data for a GO SAM membrane with a concentration of  $1 \text{ mM}$  KCl with a pH of 10, b) The current-time and voltage-time data for a planar device described in chapter 5 at a concentration of  $1 \text{ mM}$  with a pH of  $\sim 6$ .

## 7.5 Conclusion

This chapter has made significant progress in understanding the aqueous interfacial behaviour of GO. With further improvements to theory it may be possible, for instance, to account for the proton conduction of GO when measuring a conductance concentration curve. Studies on membranes (and indeed nanochannels, Sistas's results [3] are very general) stating a particular conductance should be taken with a certain caution, as clearly the manner of measurement plays a significant role in that figure, particularly in the dilute regime. In order to measure a membrane's conductance more accurately faster scan rates (or here shorter wait times) will result in reduced concentration polarization and a more accurate measurement of the membrane's resistance, however this particular figure is not relevant to real-world applications (such as electrodialysis) where DC potentials are applied. Understanding why GO membranes exhibit such a strong polarization effect compared to the planar equivalent is very important for future research as GO is something of a template for future 2D materials work. It may indeed be possible that this particular structure is unfriendly towards constant forcing which has important implications in areas like osmotic power generation and desalination.

The charge regulation model here was highly successful in explaining the power-law behaviour of the GO I/V data at various pHs. It seems, however, that charge regulation alone does not explain the differences observed between the colloidal zeta potential and charge titration experiments and those performed in GO nanochannels and membranes. In this case the compact form of the membrane seems to be affecting the surface charge density measured which is an important and significant result as GO is frequently used in nanofiltration research as a potential commercial membrane. Whether this property is linked to the inhomogeneity of the surface charge density on GO or is purely a property of the confined structure is a question of significant importance, as again, future 2D material-based membranes may also be affected.

As the concentration polarization effect seems to be enhanced in the membrane form, there could be interest for particular applications that use concentration polarization such as creating concentrated plugs of analyte for downstream analysis in lab-on-a-chip systems [180]. Further studies of the diffuse boundary layers and the intriguing depletion zone could bring potential applications to the foreground [59].

## Chapter 8

# Conclusion

### 8.1 Outcomes from this work

A new form of rectifier was produced and studied. By introducing a geometric asymmetry to a GO (graphene oxide) film, an imbalance at the film-electrolyte junction lead to rectification of ions. The film, embedded in PDMS (polydimethylsiloxane), formed a prototype for future investigation into confined ion transport. This work was published in APL-Materials in 2014.

Forming patterns of GO films on a substrate will be of great utility to future work, allowing the development of circuit-like systems for more complex applications. A method was developed to take nematic phase GO and shear it over a mould to leave a pattern of shear-aligned GO in place. The method was characterized and investigated using binary image analysis, profilometry, electron microscopy and polarized light imaging. It was found that patterns of critical dimension  $\sim 200 \mu m$  could be formed and be fabricated into nanofluidic elements for further investigation. These planar films were investigated using ion currents measurements which revealed concentration dependence in the surface charge of GO in the surface conduction regime.

An iontronic capacitor was developed using planar films of RGO (reduced graphene oxide). Iontronics until this point has solely investigated switch like elements such as ionic diodes and transistors and there are frequent comments made as to the performance of such systems [77]. Typically electronics designers couple passive elements to their active ones to improve performance, if iontronics is to progress a similar method could be adopted. In order to demonstrate this the iontronic capacitor was used to smooth the output from a bridge rectifier. Future iontronic circuit designs can take inspiration from the concept discussed in this work and take advantage of the massive number of exposed RGO edges leading to very high capacitances. This work was published in PCCP (Physical Chemistry Chemical Physics) in 2016.

A comparison of electrical and streaming current measurements was performed for GO shear aligned membranes. While the streaming currents depended on the surface charge of the material, higher currents were generated at higher pHs as expected, electrical measurements were unexpectedly conductive at low pH. This enhancement in conduction

is understood to be the conduction of protons through the confined water and functional groups of the material.

Investigation into the difference between colloidal zeta potential measurements of the surface charge density of GO compared to values estimated using nanofluidics found that a model based on charge regulation and the effect of confinement was insufficient to explain the difference in the results. The model was highly successful in explaining the concentration dependence of the surface charge in the surface conduction regime however. This study is very important as 2D layered materials become more common and are one of the easier ways of producing large area membranes [125] and thus scaling interesting nanoscopic effects.

Hysteresis observed in I/V measurements is explained in terms of varying resistance of the transiently growing diffuse boundary layers of the shear aligned GO membrane. The diffuse boundary layer concentration polarization is an important phenomenon not only in electrical measurements but also in separations and will become increasingly important as GO membranes begin to become commercialized and enter industrial applications. Differences in transport were examined for the two opposing geometries of GO used in this thesis- planar style with transport parallel to the sheets and membrane style with transport perpendicular to them. For ion conductivity the planar geometry was found to be  $6.87 \times 10^7$  more conductive. This clearly shows that researchers should very seriously consider methods for fabricating dense vertically aligned films of GO.

## 8.2 Future outlook

Nanofluidics is an intriguing area to study as it can address challenges at radically different scales. Highly promising work with solid state nanopores is allowing researchers to monitor single molecule transport [217], concentration polarization is allowing researchers to desalinate water without membrane fouling [59] and new nanofabrication techniques are offering promise in the development of new membranes for osmotic power generation [30,166]. Graphene has potential roles to play in all these problems.

GO patterning is becoming increasingly popular in the energy storage community. Typically various scanning probe techniques are used to pattern a conductive RGO pattern on a GO substrate. The natural extension of the work performed in chapter 5 is to pattern using gravure style printing. This would allow large patterned areas to be produced in an industrially scalable manner. Unfortunately a printing system such as this cannot achieve the same feature size as some scanning probe technologies but it would enable researchers to demonstrate the benefits of micro supercapacitor energy storage in real world applications.

What is the direction of iontronics? While the likelihood of a full-blown iontronic computer is unlikely, there is scope for cleverly designed circuits for a number of applications. For instance when interfacing biological matter with an electrode there are inherently problems as concentrations fluctuate, pH changes and the electrode slowly releases material in to the aqueous environment. In this situation interfacing and sensing the changes in the electric field may be better performed by an iontronic system shielding the biological matter from the electrode. With advances in cybernetics such as robotic eyes and limbs there is an ever increasing need to make these system safer and able to remain and function in the body for longer. GO in the end may prove to be too confined for many applications in iontronics. Conical nanopore systems that can anchor nanoparticles and proteins within the pore will lead to interesting in-situ sensing applications that could be easily coupled with other components. However increasing the suite of iontronic components available enables researchers to improve the design of their systems and explore other applications of iontronics.

The planar iontronic circuits is the most common design in the literature. Most diode designs require elaborate nanometric clean-room fabrication or the integration of a membrane with conical nanopores which is a complex task. Using patterns of self-assembled nanochannels certainly has an attractive advantage over these systems. While in this case the material was GO, other authors have used vermiculite [181] and other 2D materials are expected to form similar structures in film form [142]. There is even evidence that materials can be patterned into film structures like this using a sacrificial templating technique [129]. The techniques developed here extend naturally to these structures and will help future research in making highly confined 2D systems increasingly accessible to researchers.

The work performed in chapter 7 plays an important role in the scalability of nanofluidics as 2D materials become increasingly popular. Exfoliated and restacked 2D materials allow researchers to produced large area membranes with intriguing nanometric characteristics for the transistion to real world applications. GO is the forerunner in what

could become a new paradigm of membranes so understanding how confinement and the membrane structure play roles in the physics of the membrane will be quite important for a number of applications. An open question from this work for osmotic power generation would be; is there any advantage in going to greater confinement? The two most prominent studies [30,166] both use 2D materials in various conformations but, in principle these materials can be fabricated into layered membranes. With its unexpectedly low surface charge in film form GO is not of interest to this application but the two confinement and geometry related effects examined in chapter 7- the surface charge density and concentration polarization may also occur in similarly structured systems.

# Bibliography

- [1] Je-Luen Li, Jaehun Chun, Ned S Wingreen, Roberto Car, Ilhan A Aksay, and Dudley A Saville. Use of dielectric functions in the theory of dispersion forces. *Physical Review B*, 71(23):235412, 2005.
- [2] Wei Guo, Chi Cheng, Yanzhe Wu, Yanan Jiang, Jun Gao, Dan Li, and Lei Jiang. Bio-inspired two-dimensional nanofluidic generators based on a layered graphene hydrogel membrane. *Advanced Materials*, 25(42):6064–6068, 2013.
- [3] Philippe Sistat, Anton Kozmai, Natalia Pismenskaya, Christian Larchet, Gerald Pourcelly, and Victor Nikonenko. Low-frequency impedance of an ion-exchange membrane system. *Electrochimica Acta*, 53(22):6380–6390, 2008.
- [4] Bharathi Konkana and Sukumaran Vasudevan. Understanding aqueous dispersibility of graphene oxide and reduced graphene oxide through p k a measurements. *The journal of physical chemistry letters*, 3(7):867–872, 2012.
- [5] Jan CT Eijkel and Albert Van Den Berg. Nanofluidics: what is it and what can we expect from it? *Microfluidics and Nanofluidics*, 1(3):249–267, 2005.
- [6] Lydéric Bocquet and Elisabeth Charlaix. Nanofluidics, from bulk to interfaces. *Chemical Society Reviews*, 39(3):1073–1095, 2010.
- [7] Qiaosheng Pu, Jongsin Yun, Henryk Temkin, and Shaorong Liu. Ion-enrichment and ion-depletion effect of nanochannel structures. *Nano letters*, 4(6):1099–1103, 2004.
- [8] Hirofumi Daiguji, Peidong Yang, and Arun Majumdar. Ion transport in nanofluidic channels. *Nano Letters*, 4(1):137–142, 2004.
- [9] Frederick George Donnan. The theory of membrane equilibria. *Chemical Reviews*, 1(1):73–90, 1924.
- [10] Stephanie A Gajar and Michael W Geis. An ionic liquid-channel field-effect transistor. *Journal of the Electrochemical Society*, 139(10):2833–2840, 1992.
- [11] NV Churaev, VD Sobolev, and AN Somov. Slippage of liquids over lyophobic solid surfaces. *Journal of Colloid and Interface Science*, 97(2):574–581, 1984.
- [12] DM Tolstoi. Mercury sliding on glass. In *Dokl. Akad. Nauk SSSR*, volume 85, pages 1329–1335, 1952.

- [13] Uri Raviv and Jacob Klein. Fluidity of bound hydration layers. *Science*, 297(5586):1540–1543, 2002.
- [14] Mehdi Neek-Amal, Francois M Peeters, Irina V Grigorieva, and Andre K Geim. Commensurability effects in viscosity of nanoconfined water. *ACS nano*, 10(3):3685–3692, 2016.
- [15] Ivan Vlassiouk, Sergei Smirnov, and Zuzanna Siwy. Nanofluidic ionic diodes. comparison of analytical and numerical solutions. *Acs Nano*, 2(8):1589–1602, 2008.
- [16] Brian J. Kirby. *Micro- and Nanoscale Fluid Mechanics*. Cambridge, Cambridge, 1 edition, 2010.
- [17] A Terrence Conlisk. *Essentials of micro-and nanofluidics: with applications to the biological and chemical sciences*. Cambridge University Press, 2012.
- [18] Reto B Schoch, Jongyoon Han, and Philippe Renaud. Transport phenomena in nanofluidics. *Reviews of modern physics*, 80(3):839, 2008.
- [19] Hiroaki Yoshida and Lydéric Bocquet. Labyrinthine water flow across multilayer graphene-based membranes: molecular dynamics versus continuum predictions. *arXiv preprint arXiv:1605.09259*, 2016.
- [20] Pierre-Gilles de Gennes. On fluid/wall slippage. *Langmuir*, 18(9):3413–3414, 2002.
- [21] Mainak Majumder, Nitin Chopra, Rodney Andrews, and Bruce J Hinds. Nanoscale hydrodynamics: enhanced flow in carbon nanotubes. *Nature*, 438(7064):44–44, 2005.
- [22] Jason K Holt, Hyung Gyu Park, Yinmin Wang, Michael Stadermann, Alexander B Artyukhin, Costas P Grigoropoulos, Aleksandr Noy, and Olgica Bakajin. Fast mass transport through sub-2-nanometer carbon nanotubes. *Science*, 312(5776):1034–1037, 2006.
- [23] Bruce J Hinds, Nitin Chopra, Terry Rantell, Rodney Andrews, Vasilis Gavalas, and Leonidas G Bachas. Aligned multiwalled carbon nanotube membranes. *Science*, 303(5654):62–65, 2004.
- [24] Eleonora Secchi, Sophie Marbach, Antoine Niguès, Derek Stein, Alessandro Siria, and Lydéric Bocquet. Massive radius-dependent flow slippage in carbon nanotubes. *Nature*, 537(7619):210–213, 2016.
- [25] CI Bouzigues, Paul Tabeling, and L Bocquet. Nanofluidics in the debye layer at hydrophilic and hydrophobic surfaces. *Physical Review Letters*, 101(11):114503, 2008.
- [26] Christian Sendner, Dominik Horinek, Lydéric Bocquet, and Roland R Netz. Interfacial water at hydrophobic and hydrophilic surfaces: Slip, viscosity, and diffusion. *Langmuir*, 25(18):10768–10781, 2009.

- [27] Armand Ajdari and Lydéric Bocquet. Giant amplification of interfacially driven transport by hydrodynamic slip: Diffusio-osmosis and beyond. *Physical review letters*, 96(18):186102, 2006.
- [28] John L Anderson and Dennis C Prieve. Diffusiophoresis caused by gradients of strongly adsorbing solutes. *Langmuir*, 7(2):403–406, 1991.
- [29] John L Anderson. Colloid transport by interfacial forces. *Annual review of fluid mechanics*, 21(1):61–99, 1989.
- [30] Alessandro Siria, Philippe Poncharal, Anne-Laure Biance, Rémy Fulcrand, Xavier Blase, Stephen T Purcell, and Lydéric Bocquet. Giant osmotic energy conversion measured in a single transmembrane boron nitride nanotube. *Nature*, 494(7438):455–458, 2013.
- [31] Jan Lyklema. *Solid-Liquid Interfaces*, volume 2 of *Fundamentals of interface and colloid science*. Academic Press, London, 1 edition, 1995.
- [32] SS Dukhin. Non-equilibrium electric surface phenomena. *Advances in Colloid and Interface Science*, 44:1–134, 1993.
- [33] Martin Z Bazant and Todd M Squires. Induced-charge electrokinetic phenomena: theory and microfluidic applications. *Physical Review Letters*, 92(6):066101, 2004.
- [34] Jacob N Israelachvili. *Intermolecular and surface forces: revised third edition*. Academic press, 2011.
- [35] Kalyan Raidongia and Jiaying Huang. Nanofluidic ion transport through reconstructed layered materials. *Journal of the American Chemical Society*, 134(40):16528–16531, 2012.
- [36] Derek Stein, Maarten Kruithof, and Cees Dekker. Surface-charge-governed ion transport in nanofluidic channels. *Physical Review Letters*, 93(3):035901, 2004.
- [37] Rohit Karnik, Rong Fan, Min Yue, Deyu Li, Peidong Yang, and Arun Majumdar. Electrostatic control of ions and molecules in nanofluidic transistors. *Nano letters*, 5(5):943–948, 2005.
- [38] Weihua Guan, Rong Fan, and Mark A Reed. Field-effect reconfigurable nanofluidic ionic diodes. *Nature communications*, 2:506, 2011.
- [39] Reto B Schoch and Philippe Renaud. Ion transport through nanoslits dominated by the effective surface charge. *Applied Physics Letters*, 86(25):253111, 2005.
- [40] Adrien Plecis, Reto B Schoch, and Philippe Renaud. Ionic transport phenomena in nanofluidics: experimental and theoretical study of the exclusion-enrichment effect on a chip. *Nano Letters*, 5(6):1147–1155, 2005.

- 
- [41] Charles R Martin, M Nishizawa, K Jirage, M Kang, and Sang Bok Lee. Controlling ion-transport selectivity in gold nanotubule membranes. *Advanced Materials*, 13(18):1351–1362, 2001.
- [42] Ivan Vlassioux, Sergei Smirnov, and Zuzanna Siwy. Ionic selectivity of single nanochannels. *Nano letters*, 8(7):1978–1985, 2008.
- [43] Todd M Squires and Stephen R Quake. Microfluidics: Fluid physics at the nanoliter scale. *Reviews of modern physics*, 77(3):977, 2005.
- [44] Frank HJ van der Heyden, Derek Stein, and Cees Dekker. Streaming currents in a single nanofluidic channel. *Physical review letters*, 95(11):116104, 2005.
- [45] Frank HJ van der Heyden, Douwe Jan Bonthuis, Derek Stein, Christine Meyer, and Cees Dekker. Power generation by pressure-driven transport of ions in nanofluidic channels. *Nano letters*, 7(4):1022–1025, 2007.
- [46] W Sparreboom, A Van Den Berg, and JCT Eijkel. Principles and applications of nanofluidic transport. *Nature nanotechnology*, 4(11):713–720, 2009.
- [47] Sumita Pennathur, Jan CT Eijkel, and Albert Van Den Berg. Energy conversion in microsystems: is there a role for micro/nanofluidics? *Lab on a Chip*, 7(10):1234–1237, 2007.
- [48] JG Wijmans, S Nakao, JWA Van Den Berg, FR Troelstra, and CA Smolders. Hydrodynamic resistance of concentration polarization boundary layers in ultrafiltration. *Journal of Membrane Science*, 22(1):117–135, 1985.
- [49] GB Van den Berg and CA Smolders. Flux decline in ultrafiltration processes. *Desalination*, 77:101–133, 1990.
- [50] SS Sablani, MFA Goosen, R Al-Belushi, and M Wilf. Concentration polarization in ultrafiltration and reverse osmosis: a critical review. *Desalination*, 141(3):269–289, 2001.
- [51] KS Spiegler. Polarization at ion exchange membrane-solution interfaces. *Desalination*, 9(4):367–385, 1971.
- [52] JJ Krol, M Wessling, and H Strathmann. Concentration polarization with monopolar ion exchange membranes: current–voltage curves and water dissociation. *Journal of Membrane Science*, 162(1):145–154, 1999.
- [53] Isaak Rubinstein and Boris Zaltzman. Electro-osmotically induced convection at a permselective membrane. *Physical Review E*, 62(2):2238, 2000.
- [54] Thomas A Zangle, Ali Mani, and Juan G Santiago. Theory and experiments of concentration polarization and ion focusing at microchannel and nanochannel interfaces. *Chemical Society Reviews*, 39(3):1014–1035, 2010.

- [55] Sun Min Kim, Mark A Burns, and Ernest F Hasselbrink. Electrokinetic protein pre-concentration using a simple glass/poly (dimethylsiloxane) microfluidic chip. *Analytical Chemistry*, 78(14):4779–4785, 2006.
- [56] Sung Jae Kim, Ying-Chih Wang, Jeong Hoon Lee, Hongchul Jang, and Jongyoon Han. Concentration polarization and nonlinear electrokinetic flow near a nanofluidic channel. *Physical review letters*, 99(4):044501, 2007.
- [57] Ying-Chih Wang, Anna L Stevens, and Jongyoon Han. Million-fold preconcentration of proteins and peptides by nanofluidic filter. *Analytical chemistry*, 77(14):4293–4299, 2005.
- [58] Biswajit Sarkar, Srimanta Pal, Timir Baran Ghosh, Sirshendu De, and Sunando DasGupta. A study of electric field enhanced ultrafiltration of synthetic fruit juice and optical quantification of gel deposition. *Journal of Membrane Science*, 311(1):112–120, 2008.
- [59] Sung Jae Kim, Sung Hee Ko, Kwan Hyoung Kang, and Jongyoon Han. Direct seawater desalination by ion concentration polarization. *Nature Nanotechnology*, 5(4):297–301, 2010.
- [60] ST Martin, Adrian Neild, and Mainak Majumder. Graphene-based ion rectifier using macroscale geometric asymmetry. *APL Materials*, 2(9):092803, 2014.
- [61] Zuzanna S Siwy. Ion-current rectification in nanopores and nanotubes with broken symmetry. *Advanced Functional Materials*, 16(6):735–746, 2006.
- [62] Clara B Picallo, Simon Gravelle, Laurent Joly, Elisabeth Charlaix, and Lydéric Bocquet. Nanofluidic osmotic diodes: Theory and molecular dynamics simulations. *Physical review letters*, 111(24):244501, 2013.
- [63] Li-Jing Cheng and L Jay Guo. Nanofluidic diodes. *Chemical Society Reviews*, 39(3):923–938, 2010.
- [64] Li-Jing Cheng and L Jay Guo. Rectified ion transport through concentration gradient in homogeneous silica nanochannels. *Nano letters*, 7(10):3165–3171, 2007.
- [65] Hirofumi Daiguji, Yukiko Oka, and Katsuhiko Shirono. Nanofluidic diode and bipolar transistor. *Nano Letters*, 5(11):2274–2280, 2005.
- [66] Rohit Karnik, Chuanhua Duan, Kenneth Castelino, Hirofumi Daiguji, and Arun Majumdar. Rectification of ionic current in a nanofluidic diode. *Nano letters*, 7(3):547–551, 2007.
- [67] Klas Tybrandt, Karin C Larsson, Agneta Richter-Dahlfors, and Magnus Berggren. Ion bipolar junction transistors. *Proceedings of the National Academy of Sciences*, 107(22):9929–9932, 2010.

- [68] Erik O Gabrielsson, Klas Tybrandt, and Magnus Berggren. Ion diode logics for ph control. *Lab on a Chip*, 12(14):2507–2513, 2012.
- [69] Ji-Hyung Han, Kwang Bok Kim, Hee Chan Kim, and Taek Dong Chung. Ionic circuits based on polyelectrolyte diodes on a microchip. *Angewandte Chemie International Edition*, 48(21):3830–3833, 2009.
- [70] Z Siwy, Y Gu, HA Spohr, D Baur, A Wolf-Reber, R Spohr, P Apel, and YE Korchev. Rectification and voltage gating of ion currents in a nanofabricated pore. *EPL (Europhysics Letters)*, 60(3):349, 2002.
- [71] Ji Wu, Karen Gerstandt, Hongbo Zhang, Jie Liu, and Bruce J Hinds. Electrophoretically induced aqueous flow through single-walled carbon nanotube membranes. *Nature nanotechnology*, 7(2):133–139, 2012.
- [72] Klas Tybrandt, Robert Forchheimer, and Magnus Berggren. Logic gates based on ion transistors. *Nature communications*, 3:871, 2012.
- [73] Ivan Vlasiouk, Thomas R Kozel, and Zuzanna S Siwy. Biosensing with nanofluidic diodes. *Journal of the American Chemical Society*, 131(23):8211–8220, 2009.
- [74] Ivan Vlasiouk and Zuzanna S Siwy. Nanofluidic diode. *Nano letters*, 7(3):552–556, 2007.
- [75] Erik O Gabrielsson, Per Janson, Klas Tybrandt, Daniel T Simon, and Magnus Berggren. A four-diode full-wave ionic current rectifier based on bipolar membranes: Overcoming the limit of electrode capacity. *Advanced Materials*, 26(30):5143–5147, 2014.
- [76] P Ramirez, V Gomez, C Verdia-Baguena, S Nasir, M Ali, W Ensinger, and S Mafe. Designing voltage multipliers with nanofluidic diodes immersed in aqueous salt solutions. *Physical Chemistry Chemical Physics*, 18(5):3995–3999, 2016.
- [77] Honggu Chun and Taek Dong Chung. Iontronics. *Annual Review of Analytical Chemistry*, 8:441–462, 2015.
- [78] AC Lau, DN Furlong, TW Healy, and F Grieser. The electrokinetic properties of carbon black and graphitized carbon black aqueous colloids. *Colloids and surfaces*, 18(1):93–104, 1986.
- [79] MV López-Ramón, C Moreno-Castilla, J Rivera-Utrilla, and R Hidalgo-Alvarez. Activated carbons from a subbituminous coal: pore texture and electrokinetic properties. *Carbon*, 31(5):815–819, 1993.
- [80] Sumio Iijima and Toshinari Ichihashi. Single-shell carbon nanotubes of 1-nm diameter. *Nature*, 363(6430):603–605, 1993.
- [81] PM Ajayan, TW Ebbesen, T Ichihashi, S Iijima, Ks Tanigaki, and H Hiura. Opening carbon nanotubes with oxygen and implications for filling. *Nature*, 362(6420):522–525, 1993.

- 
- [82] PM Ajayan and S Iijima. Capillarity-induced filling of carbon nanotubes. *Nature*, 361(6410):333–334, 1993.
- [83] Sumio Iijima et al. Helical microtubules of graphitic carbon. *nature*, 354(6348):56–58, 1991.
- [84] Gerhard Hummer, Jayendran C Rasaiah, and Jerzy P Noworyta. Water conduction through the hydrophobic channel of a carbon nanotube. *Nature*, 414(6860):188–190, 2001.
- [85] Lyderic Bocquet and Patrick Tabeling. Physics and technological aspects of nanofluidics. *Lab on a Chip*, 14(17):3143–3158, 2014.
- [86] John A Thomas and Alan JH McGaughey. Reassessing fast water transport through carbon nanotubes. *Nano letters*, 8(9):2788–2793, 2008.
- [87] Sony Joseph and NR Aluru. Why are carbon nanotubes fast transporters of water? *Nano letters*, 8(2):452–458, 2008.
- [88] Kerstin Falk, Felix Sedlmeier, Laurent Joly, Roland R Netz, and Lydéric Bocquet. Molecular origin of fast water transport in carbon nanotube membranes: superlubricity versus curvature dependent friction. *Nano letters*, 10(10):4067–4073, 2010.
- [89] M Whitby and N Quirke. Fluid flow in carbon nanotubes and nanopipes. *Nature Nanotechnology*, 2(2):87–94, 2007.
- [90] Aleksandr Noy, Hyung Gyu Park, Francesco Fornasiero, Jason K Holt, Costas P Grigoropoulos, and Olgica Bakajin. Nanofluidics in carbon nanotubes. *Nano Today*, 2(6):22–29, 2007.
- [91] Mainak Majumder, Nitin Chopra, and Bruce J Hinds. Mass transport through carbon nanotube membranes in three different regimes: ionic diffusion and gas and liquid flow. *ACS nano*, 5(5):3867–3877, 2011.
- [92] Sridhar Kumar Kannam, BD Todd, Jesper Schmidt Hansen, and Peter J Daivis. How fast does water flow in carbon nanotubes? *The Journal of chemical physics*, 138(9):094701, 2013.
- [93] B Radha, A Esfandiar, FC Wang, AP Rooney, K Gopinadhan, A Keerthi, A Mishchenko, A Janardanan, P Blake, L Fumagalli, et al. Molecular transport through capillaries made with atomic-scale precision. *Nature*, 538(7624):222–225, 2016.
- [94] KS Novoselov, D Jiang, F Schedin, TJ Booth, VV Khotkevich, SV Morozov, and AK Geim. Two-dimensional atomic crystals. *Proceedings of the National Academy of Sciences of the United States of America*, 102(30):10451–10453, 2005.
- [95] Andre K Geim and Konstantin S Novoselov. The rise of graphene. *Nature materials*, 6(3):183–191, 2007.

- [96] Changgu Lee, Xiaoding Wei, Jeffrey W Kysar, and James Hone. Measurement of the elastic properties and intrinsic strength of monolayer graphene. *science*, 321(5887):385–388, 2008.
- [97] Meryl D Stoller, Sungjin Park, Yanwu Zhu, Jinho An, and Rodney S Ruoff. Graphene-based ultracapacitors. *Nano letters*, 8(10):3498–3502, 2008.
- [98] Alexander A Balandin, Suchismita Ghosh, Wenzhong Bao, Irene Calizo, Desalegne Teweldebrhan, Feng Miao, and Chun Ning Lau. Superior thermal conductivity of single-layer graphene. *Nano letters*, 8(3):902–907, 2008.
- [99] KS Novoselov, Andre K Geim, SV Morozov, D Jiang, MI Katsnelson, IV Grigorieva, SV Dubonos, and AA Firsov. Two-dimensional gas of massless dirac fermions in graphene. *nature*, 438(7065):197–200, 2005.
- [100] Andre Konstantin Geim. Graphene: status and prospects. *science*, 324(5934):1530–1534, 2009.
- [101] Andre K Geim and Philip Kim. Carbon wonderland. *Scientific American*, 298(4):90–97, 2008.
- [102] William S Hummers Jr and Richard E Offeman. Preparation of graphitic oxide. *Journal of the American Chemical Society*, 80(6):1339–1339, 1958.
- [103] Sasha Stankovich, Dmitriy A Dikin, Geoffrey HB Dommett, Kevin M Kohlhaas, Eric J Zimney, Eric A Stach, Richard D Piner, SonBinh T Nguyen, and Rodney S Ruoff. Graphene-based composite materials. *nature*, 442(7100):282–286, 2006.
- [104] Dan Li, Marc B Mueller, Scott Gilje, Richard B Kaner, and Gordon G Wallace. Processable aqueous dispersions of graphene nanosheets. *Nature nanotechnology*, 3(2):101–105, 2008.
- [105] T Ramanathan, AA Abdala, S Stankovich, DA Dikin, M Herrera-Alonso, RD Piner, DH Adamson, HC Schniepp, X Chen, RS Ruoff, et al. Functionalized graphene sheets for polymer nanocomposites. *Nature nanotechnology*, 3(6):327–331, 2008.
- [106] Yuxi Xu, Wenjing Hong, Hua Bai, Chun Li, and Gaoquan Shi. Strong and ductile poly (vinyl alcohol)/graphene oxide composite films with a layered structure. *Carbon*, 47(15):3538–3543, 2009.
- [107] Donglin Han, Lifeng Yan, Wufeng Chen, and Wan Li. Preparation of chitosan/graphene oxide composite film with enhanced mechanical strength in the wet state. *Carbohydrate Polymers*, 83(2):653–658, 2011.
- [108] Sukang Bae, Hyeongkeun Kim, Youngbin Lee, Xiangfan Xu, Jae-Sung Park, Yi Zheng, Jayakumar Balakrishnan, Tian Lei, Hye Ri Kim, Young Il Song, et al. Roll-to-roll production of 30-inch graphene films for transparent electrodes. *Nature nanotechnology*, 5(8):574–578, 2010.

- 
- [109] Goki Eda, Giovanni Fanchini, and Manish Chhowalla. Large-area ultrathin films of reduced graphene oxide as a transparent and flexible electronic material. *Nature nanotechnology*, 3(5):270–274, 2008.
- [110] Héctor A Becerril, Jie Mao, Zunfeng Liu, Randall M Stoltenberg, Zhenan Bao, and Yongsheng Chen. Evaluation of solution-processed reduced graphene oxide films as transparent conductors. *ACS nano*, 2(3):463–470, 2008.
- [111] Maher F El-Kady and Richard B Kaner. Scalable fabrication of high-power graphene micro-supercapacitors for flexible and on-chip energy storage. *Nature communications*, 4:1475, 2013.
- [112] Derrek E Lobo, Parama Chakraborty Banerjee, Christopher D Easton, and Mainak Majumder. Micro-supercapacitors: Miniaturized supercapacitors: Focused ion beam reduced graphene oxide supercapacitors with enhanced performance metrics. *Advanced Energy Materials*, 5(19), 2015.
- [113] Wei Gao, Neelam Singh, Li Song, Zheng Liu, Arava Leela Mohana Reddy, Lijie Ci, Robert Vajtai, Qing Zhang, Bingqing Wei, and Pulickel M Ajayan. Direct laser writing of micro-supercapacitors on hydrated graphite oxide films. *Nature Nanotechnology*, 6(8):496–500, 2011.
- [114] Cecilia Mattevi, Hokwon Kim, and Manish Chhowalla. A review of chemical vapour deposition of graphene on copper. *Journal of Materials Chemistry*, 21(10):3324–3334, 2011.
- [115] Matthew J Allen, Vincent C Tung, and Richard B Kaner. Honeycomb carbon: a review of graphene. *Chemical reviews*, 110(1):132–145, 2009.
- [116] Keith R Paton, Eswaraiah Varrla, Claudia Backes, Ronan J Smith, Umar Khan, Arlene O’Neill, Conor Boland, Mustafa Lotya, Oana M Istrate, Paul King, et al. Scalable production of large quantities of defect-free few-layer graphene by shear exfoliation in liquids. *Nature materials*, 13(6):624–630, 2014.
- [117] Daniel R Dreyer, Sungjin Park, Christopher W Bielawski, and Rodney S Ruoff. The chemistry of graphene oxide. *Chemical Society Reviews*, 39(1):228–240, 2010.
- [118] Anton Lerf, Heyong He, Michael Forster, and Jacek Klinowski. Structure of graphite oxide revisited. *The Journal of Physical Chemistry B*, 102(23):4477–4482, 1998.
- [119] Jaemyung Kim, Laura J Cote, Franklin Kim, Wa Yuan, Kenneth R Shull, and Jiaying Huang. Graphene oxide sheets at interfaces. *Journal of the American Chemical Society*, 132(23):8180–8186, 2010.
- [120] Sungjin Park, Jinho An, Inhwa Jung, Richard D Piner, Sung Jin An, Xuesong Li, Aruna Velamakanni, and Rodney S Ruoff. Colloidal suspensions of highly reduced graphene oxide in a wide variety of organic solvents. *Nano letters*, 9(4):1593–1597, 2009.

- [121] Natnael Behabtu, Jay R Lomeda, Micah J Green, Amanda L Higginbotham, Alexander Sinitskii, Dmitry V Kosynkin, Dmitri Tsentelovich, A Nicholas G Parra-Vasquez, Judith Schmidt, Ellina Kesselman, et al. Spontaneous high-concentration dispersions and liquid crystals of graphene. *Nature nanotechnology*, 5(6):406–411, 2010.
- [122] Cristina Gómez-Navarro, R Thomas Weitz, Alexander M Bittner, Matteo Scolari, Alf Mews, Marko Burghard, and Klaus Kern. Electronic transport properties of individual chemically reduced graphene oxide sheets. *Nano letters*, 7(11):3499–3503, 2007.
- [123] Xuan Wang, Linjie Zhi, and Klaus Müllen. Transparent, conductive graphene electrodes for dye-sensitized solar cells. *Nano letters*, 8(1):323–327, 2008.
- [124] Dmitriy A Dikin, Sasha Stankovich, Eric J Zimney, Richard D Piner, Geoffrey HB Dommett, Guennadi Evmenenko, SonBinh T Nguyen, and Rodney S Ruoff. Preparation and characterization of graphene oxide paper. *Nature*, 448(7152):457–460, 2007.
- [125] Abozar Akbari, Phillip Sheath, Samuel T Martin, Dhanraj B Shinde, Mahdokht Shaibani, Parama Chakraborty Banerjee, Rachel Tkacz, Dibakar Bhattacharyya, and Mainak Majumder. Large-area graphene-based nanofiltration membranes by shear alignment of discotic nematic liquid crystals of graphene oxide. *Nature communications*, 7, 2016. doi: 10.1038/ncomms10891.
- [126] Rachel Tkacz, Rudolf Oldenbourg, Alex Fulcher, Morteza Miansari, and Mainak Majumder. Capillary-force-assisted self-assembly (cas) of highly ordered and anisotropic graphene-based thin films. *The Journal of Physical Chemistry C*, 118(1):259–267, 2013.
- [127] Scott Gilje, Song Han, Minsheng Wang, Kang L Wang, and Richard B Kaner. A chemical route to graphene for device applications. *Nano letters*, 7(11):3394–3398, 2007.
- [128] In Kyu Moon, Junghyun Lee, Rodney S Ruoff, and Hyoyoung Lee. Reduced graphene oxide by chemical graphitization. *Nature communications*, 1:73, 2010.
- [129] Che-Ning Yeh, Kalyan Raidongia, Jiaojing Shao, Quan-Hong Yang, and Jiaying Huang. On the origin of the stability of graphene oxide membranes in water. *Nature chemistry*, 7(2):166–170, 2015.
- [130] RK Joshi, P Carbone, FC Wang, VG Kravets, Y Su, IV Grigorieva, HA Wu, AK Geim, and RR Nair. Precise and ultrafast molecular sieving through graphene oxide membranes. *Science*, 343(6172):752–754, 2014.
- [131] RR Nair, HA Wu, PN Jayaram, IV Grigorieva, and AK Geim. Unimpeded permeation of water through helium-leak-tight graphene-based membranes. *Science*, 335(6067):442–444, 2012.

- [132] Chi Cheng, Gengping Jiang, Christopher J Garvey, Yuanyuan Wang, George P Simon, Jefferson Z Liu, and Dan Li. Ion transport in complex layered graphene-based membranes with tuneable interlayer spacing. *Science advances*, 2(2):e1501272, 2016.
- [133] Maher F El-Kady, Veronica Strong, Sergey Dubin, and Richard B Kaner. Laser scribing of high-performance and flexible graphene-based electrochemical capacitors. *Science*, 335(6074):1326–1330, 2012.
- [134] John R Miller, RA Outlaw, and BC Holloway. Graphene double-layer capacitor with ac line-filtering performance. *Science*, 329(5999):1637–1639, 2010.
- [135] Chenguang Liu, Zhenning Yu, David Neff, Aruna Zhamu, and Bor Z Jang. Graphene-based supercapacitor with an ultrahigh energy density. *Nano letters*, 10(12):4863–4868, 2010.
- [136] Yan Wang, Zhiqiang Shi, Yi Huang, Yanfeng Ma, Chengyang Wang, Mingming Chen, and Yongsheng Chen. Supercapacitor devices based on graphene materials. *The Journal of Physical Chemistry C*, 113(30):13103–13107, 2009.
- [137] Ji Eun Kim, Tae Hee Han, Sun Hwa Lee, Ju Young Kim, Chi Won Ahn, Je Moon Yun, and Sang Ouk Kim. Graphene oxide liquid crystals. *Angewandte Chemie International Edition*, 50(13):3043–3047, 2011.
- [138] Zhen Xu and Chao Gao. Aqueous liquid crystals of graphene oxide. *ACS nano*, 5(4):2908–2915, 2011.
- [139] Rekha Narayan, Ji Eun Kim, Ju Young Kim, Kyung Eun Lee, and Sang Ouk Kim. Graphene oxide liquid crystals: Discovery, evolution and applications. *Advanced Materials*, 28(16):3045–3068, 2016.
- [140] Horst Stegemeyer. *Liquid Crystals*, volume 3 of *Topics in physical chemistry*. Springer Verlag, New York, 1 edition, 1994.
- [141] Rachel Tkacz. *Graphene-based assemblies from colloidal suspensions*. PhD thesis, Monash University, Clayton, Australia, 2015.
- [142] Andrew R Koltonow and Jiaxing Huang. Two-dimensional nanofluidics. *Science*, 351(6280):1395–1396, 2016.
- [143] Morteza Miansari, James R Friend, Parama Banerjee, Mainak Majumder, and Leslie Y Yeo. Graphene-based planar nanofluidic rectifiers. *The Journal of Physical Chemistry C*, 118(38):21856–21865, 2014.
- [144] Nina I Kovtyukhova, Patricia J Ollivier, Benjamin R Martin, Thomas E Mallouk, Sergey A Chizhik, Eugenia V Buzaneva, and Alexandr D Gorchinskiy. Layer-by-layer assembly of ultrathin composite films from micron-sized graphite oxide sheets and polycations. *Chemistry of Materials*, 11(3):771–778, 1999.

- 
- [145] Daniel A Bartholomeusz, Ronald W Boutté, and Joseph D Andrade. Xurography: rapid prototyping of microstructures using a cutting plotter. *Journal of Microelectromechanical Systems*, 14(6):1364–1374, 2005.
- [146] Po Ki Yuen and Vasiliy N Goral. Low-cost rapid prototyping of flexible microfluidic devices using a desktop digital craft cutter. *Lab on a Chip*, 10(3):384–387, 2010.
- [147] Steffen Cosson, Luc G Aeberli, Nathalie Brandenberg, and Matthias P Lutolf. Ultra-rapid prototyping of flexible, multi-layered microfluidic devices via razor writing. *Lab on a Chip*, 15(1):72–76, 2015.
- [148] Richard P Feynman. There’s plenty of room at the bottom. *Engineering and science*, 23(5):22–36, 1960.
- [149] Weilie Zhou and Zhong Lin Wang. *Scanning microscopy for nanotechnology: techniques and applications*. Springer science & business media, 2007.
- [150] DG Chetwynd, Xianping Liu, and ST Smith. Signal fidelity and tracking force in stylus profilometry. *International Journal of Machine Tools and Manufacture*, 32(1):239–245, 1992.
- [151] Takao Abe, Edgar F Steigmeier, Walter Hagleitner, and Allan J Pidduck. Microroughness measurements on polished silicon wafers. *Japanese journal of applied physics*, 31(3R):721, 1992.
- [152] FM Smits. Measurement of sheet resistivities with the four-point probe. *Bell System Technical Journal*, 37(3):711–718, 1958.
- [153] Haldor Topsoe. Geometric factors in four point resistivity measurement, may 1968. Available online: <http://four-point-probes.com/haldor-topsoe-geometric-factors-in-four-point-resistivity-measurement/#hal>, accessed 24/08/2016.
- [154] Rachel Tkacz, Rudolf Oldenbourg, Shalin B Mehta, Morteza Miansari, Amitabh Verma, and Mainak Majumder. ph dependent isotropic to nematic phase transitions in graphene oxide dispersions reveal droplet liquid crystalline phases. *Chemical communications*, 50(50):6668–6671, 2014.
- [155] Rudolf Oldenbourg. *Polarization microscopy with the LC-PolScope*, 2003. Available online: <https://darchive.mblwhoilibrary.org/bitstream/handle/1912/6277/OldenbourgLC-PolScopeLabManual2005.pdf?sequence=1&isAllowed=y>, accessed 24/08/2016.
- [156] R Oldenbourg and G Mei. New polarized light microscope with precision universal compensator. *Journal of microscopy*, 180(2):140–147, 1995.
- [157] Mahdokht Shaibani, Abozar Akbari, Phillip Sheath, Christopher D Easton, Parama Chakraborty Banerjee, Kristina Konstas, Armaghan Fakhfour, Marzieh Barghamadi, Mustafa M Musameh, Adam S Best, et al. Suppressed polysulfide crossover in li-s batteries through a high-flux graphene oxide membrane supported on a sulfur cathode. *ACS nano*, 10(8):7768–7779, 2016.

- 
- [158] Parama Chakraborty Banerjee, Derrek E Lobo, Rick Middag, Woo Kan Ng, Mahdokht E Shaibani, and Mainak Majumder. Electrochemical capacitance of ni-doped metal organic framework and reduced graphene oxide composites: more than the sum of its parts. *ACS applied materials & interfaces*, 7(6):3655–3664, 2015.
- [159] Yuyan Shao, Jun Wang, Hong Wu, Jun Liu, Ilhan A Aksay, and Yuehe Lin. Graphene based electrochemical sensors and biosensors: a review. *Electroanalysis*, 22(10):1027–1036, 2010.
- [160] Digby Macdonald. *Transient techniques in electrochemistry*. Springer Science & Business Media, 2012.
- [161] Chuanhua Duan and Arun Majumdar. Anomalous ion transport in 2-nm hydrophilic nanochannels. *Nature nanotechnology*, 5(12):848–852, 2010.
- [162] Sung Jae Kim and Jongyoon Han. Self-sealed vertical polymeric nanoporous-junctions for high-throughput nanofluidic applications. *Analytical chemistry*, 80(9):3507–3511, 2008.
- [163] Z Siwy and A Fuliński. Fabrication of a synthetic nanopore ion pump. *Physical Review Letters*, 89(19):198103, 2002.
- [164] Javier Cervera, Patricio Ramirez, Salvador Mafe, and Pieter Stroeve. Asymmetric nanopore rectification for ion pumping, electrical power generation, and information processing applications. *Electrochimica Acta*, 56(12):4504–4511, 2011.
- [165] A Gadaleta, C Sempere, S Gravelle, A Siria, R Fulcrand, C Ybert, and L Bocquet. Sub-additive ionic transport across arrays of solid-state nanopores. *Physics of Fluids (1994-present)*, 26(1):012005, 2014.
- [166] Jiandong Feng, Michael Graf, Ke Liu, Dmitry Ovchinnikov, Dumitru Dumcenco, Mohammad Heiranian, Vishal Nandigana, Narayana R Aluru, Andras Kis, and Aleksandra Radenovic. Single-layer mos2 nanopores as nanopower generators. *Nature*, 536(7615):197–200, 2016.
- [167] Zhen Xu and Chao Gao. Graphene chiral liquid crystals and macroscopic assembled fibres. *Nature communications*, 2:571, 2011.
- [168] Rouhollah Jalili, Seyed Hamed Aboutalebi, Dorna Esrafilzadeh, Roderick L Shepherd, Jun Chen, Sima Aminorroaya-Yamini, Konstantin Konstantinov, Andrew I Minett, Joselito M Razal, and Gordon G Wallace. Scalable one-step wet-spinning of graphene fibers and yarns from liquid crystalline dispersions of graphene oxide: towards multifunctional textiles. *Advanced Functional Materials*, 23(43):5345–5354, 2013.
- [169] Kiana Aran, Lawrence A Sasso, Neal Kamdar, and Jeffrey D Zahn. Irreversible, direct bonding of nanoporous polymer membranes to pdms or glass microdevices. *Lab on a Chip*, 10(5):548–552, 2010.

- 
- [170] J De Jong, RGH Lammertink, and M Wessling. Membranes and microfluidics: a review. *Lab on a Chip*, 6(9):1125–1139, 2006.
- [171] Hsih Yin Tan, Weng Keong Loke, and Nam-Trung Nguyen. A reliable method for bonding polydimethylsiloxane (pdms) to polymethylmethacrylate (pmma) and its application in micropumps. *Sensors and Actuators B: Chemical*, 151(1):133–139, 2010.
- [172] Chang Young Lee, Wonjoon Choi, Jae-Hee Han, and Michael S Strano. Coherence resonance in a single-walled carbon nanotube ion channel. *Science*, 329(5997):1320–1324, 2010.
- [173] Eleonora Secchi, Antoine Niguès, Laetitia Jubin, Alessandro Siria, and Lydéric Bocquet. Scaling behavior for ionic transport and its fluctuations in individual carbon nanotubes. *Physical review letters*, 116(15):154501, 2016.
- [174] Nadanai Laohakunakorn, Benjamin Gollnick, Fernando Moreno-Herrero, Dirk GAL Aarts, Roel PA Dullens, Sandip Ghosal, and Ulrich F Keyser. A landau–squire nanojet. *Nano letters*, 13(11):5141–5146, 2013.
- [175] Chang Wei, Allen J Bard, and Stephen W Feldberg. Current rectification at quartz nanopipet electrodes. *Analytical Chemistry*, 69(22):4627–4633, 1997.
- [176] Yaqin Fu, Hideo Tokuhisa, and Lane A Baker. Nanopore dna sensors based on dendrimer-modified nanopipettes. *Chemical Communications*, (32):4877–4879, 2009.
- [177] LI Segerink and JCT Eijkel. Nanofluidics in point of care applications. *Lab on a Chip*, 14(17):3201–3205, 2014.
- [178] Ulrich F Keyser, Bernard N Koeleman, Stijn Van Dorp, Diego Krapf, Ralph MM Smeets, Serge G Lemay, Nynke H Dekker, and Cees Dekker. Direct force measurements on dna in a solid-state nanopore. *Nature Physics*, 2(7):473–477, 2006.
- [179] Samir M Iqbal, Demir Akin, and Rashid Bashir. Solid-state nanopore channels with dna selectivity. *Nature nanotechnology*, 2(4):243–248, 2007.
- [180] Sung Jae Kim, Yong-Ak Song, and Jongyoon Han. Nanofluidic concentration devices for biomolecules utilizing ion concentration polarization: theory, fabrication, and applications. *Chemical Society Reviews*, 39(3):912–922, 2010.
- [181] Jiao-Jing Shao, Kalyan Raidongia, Andrew R Koltonow, and Jiaying Huang. Self-assembled two-dimensional nanofluidic proton channels with high thermal stability. *Nature communications*, 6, 2015. doi: 10.1038/ncomms10891.
- [182] Jun Yin, Xuemei Li, Jin Yu, Zhuhua Zhang, Jianxin Zhou, and Wanlin Guo. Generating electricity by moving a droplet of ionic liquid along graphene. *Nature nanotechnology*, 9(5):378–383, 2014.

- [183] Keun Soo Kim, Yue Zhao, Houk Jang, Sang Yoon Lee, Jong Min Kim, Kwang S Kim, Jong-Hyun Ahn, Philip Kim, Jae-Young Choi, and Byung Hee Hong. Large-scale pattern growth of graphene films for stretchable transparent electrodes. *Nature*, 457(7230):706–710, 2009.
- [184] Xiaogan Liang, Zengli Fu, and Stephen Y Chou. Graphene transistors fabricated via transfer-printing in device active-areas on large wafer. *Nano Letters*, 7(12):3840–3844, 2007.
- [185] Jinming Cai, Pascal Ruffieux, Rached Jaafar, Marco Bieri, Thomas Braun, Stephan Blankenburg, Matthias Muoth, Ari P Seitsonen, Moussa Saleh, Xinliang Feng, et al. Atomically precise bottom-up fabrication of graphene nanoribbons. *Nature*, 466(7305):470–473, 2010.
- [186] Qiyuan He, Herry Gunadi Sudibya, Zongyou Yin, Shixin Wu, Hai Li, Freddy Boey, Wei Huang, Peng Chen, and Hua Zhang. Centimeter-long and large-scale micro-patterns of reduced graphene oxide films: fabrication and sensing applications. *Acs Nano*, 4(6):3201–3208, 2010.
- [187] Zhen Xu and Chao Gao. Aqueous liquid crystals of graphene oxide. *ACS nano*, 5(4):2908–2915, 2011.
- [188] Sumedh P Surwade, Sergei N Smirnov, Ivan V Vlassiuk, Raymond R Unocic, Gabriel M Veith, Sheng Dai, and Shannon M Mahurin. Water desalination using nanoporous single-layer graphene. *Nature nanotechnology*, 10(5):459–464, 2015.
- [189] Lisa J Wang, Maher F El-Kady, Sergey Dubin, Jee Youn Hwang, Yuanlong Shao, Kristofer Marsh, Brian McVerry, Matthew D Kowal, Mir F Mousavi, and Richard B Kaner. Flash converted graphene for ultra-high power supercapacitors. *Advanced Energy Materials*, 5(18), 2015. doi: 10.1002/aenm.201500786.
- [190] Yuxin Liu, Xiaochen Dong, and Peng Chen. Biological and chemical sensors based on graphene materials. *Chemical Society Reviews*, 41(6):2283–2307, 2012.
- [191] M Bulut Coskun, Abozar Akbari, Daniel TH Lai, Adrian Neild, Mainak Majumder, and Tuncay Alan. Ultrasensitive strain sensor produced by direct patterning of liquid crystals of graphene oxide on a flexible substrate. *ACS applied materials & interfaces*, 8(34):22501–22505, 2016.
- [192] Suguru Suzuki, Kenji Itoh, Masako Ohgaki, Masaya Ohtani, and Masakuni Ozawa. Preparation of sintered filter for ion exchange by a doctor blade method with aqueous slurries of needlelike hydroxyapatite. *Ceramics international*, 25(3):287–291, 1999.
- [193] Hidenori Watanabe, Toshio Kimura, and Takashi Yamaguchi. Particle orientation during tape casting in the fabrication of grain-oriented bismuth titanate. *Journal of the American Ceramic Society*, 72(2):289–293, 1989.

- [194] Alfred IY Tok, Freddy YC Boey, and KA Khor. Tape casting of high dielectric ceramic composite substrates for microelectronics application. *Journal of Materials Processing Technology*, 89:508–512, 1999.
- [195] Hyun Jun Kim, Matthew John M Krane, Kevin P Trumble, and Keith J Bowman. Analytical fluid flow models for tape casting. *Journal of the American Ceramic Society*, 89(9):2769–2775, 2006.
- [196] Alfred IY Tok, Freddy YC Boey, and YC Lam. Non-newtonian fluid flow model for ceramic tape casting. *Materials Science and Engineering: A*, 280(2):282–288, 2000.
- [197] Morteza Miansari, James R Friend, and Leslie Y Yeo. Enhanced ion current rectification in 2d graphene-based nanofluidic devices. *Advanced Science*, 2(6), 2015. doi: 10.1002/advs.201500062.
- [198] Budhadipta Dan, Glen C Irvin, and Matteo Pasquali. Continuous and scalable fabrication of transparent conducting carbon nanotube films. *ACS nano*, 3(4):835–843, 2009.
- [199] Eugenio Hamm, Pedro Reis, Michael LeBlanc, Benoit Roman, and Enrique Cerda. Tearing as a test for mechanical characterization of thin adhesive films. *Nature materials*, 7(5):386–390, 2008.
- [200] Vineet Dua, Sumedh P Surwade, Srikanth Ammu, Srikanth Rao Agnihotra, Sujit Jain, Kyle E Roberts, Sungjin Park, Rodney S Ruoff, and Sanjeev K Manohar. All-organic vapor sensor using inkjet-printed reduced graphene oxide. *Angewandte Chemie*, 122(12):2200–2203, 2010.
- [201] Linh T Le, Matthew H Ervin, Hongwei Qiu, Brian E Fuchs, and Woo Y Lee. Graphene supercapacitor electrodes fabricated by inkjet printing and thermal reduction of graphene oxide. *Electrochemistry Communications*, 13(4):355–358, 2011.
- [202] Eric B Kalman, Ivan Vlassiuk, and Zuzanna S Siwy. Nanofluidic bipolar transistors. *Advanced Materials*, 20(2):293–297, 2008.
- [203] Hubiao Huang, Zhigong Song, Ning Wei, Li Shi, Yiyin Mao, Yulong Ying, Luwei Sun, Zhiping Xu, and Xinsheng Peng. Ultrafast viscous water flow through nanostrand-channelled graphene oxide membranes. *Nature communications*, 4, 2013. doi: 10.1038/ncomms3979.
- [204] David Cohen-Tanugi and Jeffrey C Grossman. Water desalination across nanoporous graphene. *Nano letters*, 12(7):3602–3608, 2012.
- [205] Pengzhan Sun, He Liu, Kunlin Wang, Minlin Zhong, Dehai Wu, and Hongwei Zhu. Ultrafast liquid water transport through graphene-based nanochannels measured by isotope labelling. *Chemical Communications*, 51(15):3251–3254, 2015.

- 
- [206] John Chmiola, G Yushin, Yury Gogotsi, Christele Portet, Patrice Simon, and Pierre-Louis Taberna. Anomalous increase in carbon capacitance at pore sizes less than 1 nanometer. *Science*, 313(5794):1760–1763, 2006.
- [207] Mohsen Moazzami Gudarzi. Colloidal stability of graphene oxide: aggregation in two dimensions. *Langmuir*, 32(20):5058–5068, 2016.
- [208] Mohammad Razaul Karim, Kazuto Hatakeyama, Takeshi Matsui, Hiroshi Takehira, Takaaki Taniguchi, Michio Koinuma, Yasumichi Matsumoto, Tomoyuki Akutagawa, Takayoshi Nakamura, Shin-ichiro Noro, et al. Graphene oxide nanosheet with high proton conductivity. *Journal of the American Chemical Society*, 135(22):8097–8100, 2013.
- [209] Da-Wei Wang, Aijun Du, Elena Taran, Gao Qing Max Lu, and Ian R Gentle. A water-dielectric capacitor using hydrated graphene oxide film. *Journal of Materials Chemistry*, 22(39):21085–21091, 2012.
- [210] Xiaobin Fan, Wenchao Peng, Yang Li, Xianyu Li, Shulan Wang, Guoliang Zhang, and Fengbao Zhang. Deoxygenation of exfoliated graphite oxide under alkaline conditions: a green route to graphene preparation. *Advanced Materials*, 20(23):4490–4493, 2008.
- [211] Song Xue, Li-Hsien Yeh, Yu Ma, and Shizhi Qian. Tunable streaming current in a ph-regulated nanochannel by a field effect transistor. *The Journal of Physical Chemistry C*, 118(12):6090–6099, 2014.
- [212] Chih-Chang Chang and Ruey-Jen Yang. A perspective on streaming current in silica nanofluidic channels: Poisson–boltzmann model versus poisson–nernst–planck model. *Journal of colloid and interface science*, 339(2):517–520, 2009.
- [213] Brian J Polk, Anna Stelzenmuller, Geraldine Mijares, William MacCrehan, and Michael Gaitan. Ag/agcl microelectrodes with improved stability for microfluidics. *Sensors and Actuators B: Chemical*, 114(1):239–247, 2006.
- [214] Brian J Kirby and Ernest F Hasselbrink. Zeta potential of microfluidic substrates: 1. theory, experimental techniques, and effects on separations. *Electrophoresis*, 25(2):187–202, 2004.
- [215] Philippe Sistat and Gérald Pourcelly. Chronopotentiometric response of an ion-exchange membrane in the underlimiting current-range. transport phenomena within the diffusion layers. *Journal of membrane science*, 123(1):121–131, 1997.
- [216] AA Moya and P Sistat. Chronoamperometric response of ion-exchange membrane systems. *Journal of membrane science*, 444:412–419, 2013.
- [217] Cees Dekker. Solid-state nanopores. *Nature nanotechnology*, 2(4):209–215, 2007.

# MicroTAS 2015 Conference paper

# THE INSIDE OUT SUPER-CAPACITOR: INDUCED CHARGE STORAGE ON GRAPHENE

S.T. Martin<sup>1\*</sup>, A. Neild<sup>1</sup> and M. Majumder<sup>1</sup>

<sup>1</sup>Monash University, AUSTRALIA

## ABSTRACT

A new kind of super-capacitor has been developed which uses ionic rather than electronic currents to charge and discharge it. The super-capacitor functions by inducing charge on a reduced graphene oxide (RGO) film which spans two electrolyte reservoirs. Typically such induced charge is used to create electrokinetic effects however unlike induced charge electrokinetic geometries the work surface in this geometry has its bipolar double layer split by an ionically insulating separator. This device represents the iontronic analogue of the electronic super-capacitor.

**KEYWORDS:** Ionic circuits, iontronics, induced charge electrokinetics, energy storage,

## INTRODUCTION

Iontronics is an emerging field interested in implementing ionic equivalents of electrical components. The field promises highly interesting information processing [1] and (bio-)chemical handling applications [2]. Most of the interest in the literature has been drawn towards the active components- the ion diode and transistor[1-4]. However even basic electronic circuits require capacitors throughout them to smooth signals and to store and deliver charge, this work presents the iontronic equivalent.

The devices are made using a viscous high concentration nematic phase graphene oxide solution which is deposited onto a glass slide. Once dried the film has a lamellar structure made up of thousands of nanochannels with a characteristic height of ~1nm. Films like this have been studied before using the nanochannel like capillaries to demonstrate nanofluidic properties [5].

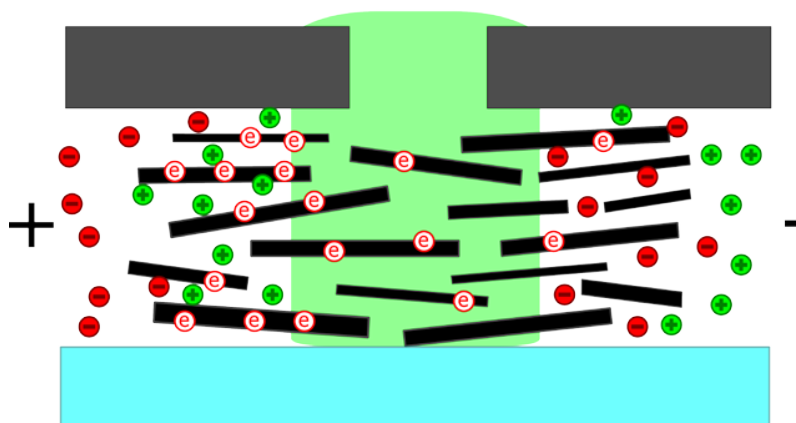


Figure 1: The ordered lamellar film structure (black) is sealed between vinyl (grey) and glass (blue). The ionic separator (green) prevents ions from traversing the film from one reservoir to another. Applied field in the electrolyte causes a build-up of charge at each end of the RGO film creating a pair of induced double layers either side of the separator which store the charge.

## THEORY

A traditional double layer occurs due to an equilibrium created by mobile charge within an electrolyte and the surface charge at an interface. In this work induced double layers are used to store charge at this interface. An induced double layer is created by an applied field in an electrolyte which induces the

double layer on a polarizable surface, referred to as the work surface [6]. The double layer induced is typically bipolar and the work surface charges much like a capacitor with an RC time constant. It should be mentioned that the work surface is isolated in the solution thus there is no way to have net charge transfer from it.

In this work it is proposed that by inserting an ionically insulating layer across the work surface an analogue to a super-capacitor is created (figure 1). The separator in this case is polydimethylsiloxane (PDMS) which overtime infiltrates into the RGO film and reduces its ionic conductivity without affecting its electrical conductivity.

## EXPERIMENTAL

The devices are made by doctor blading a concentrated (30mg/mL) dispersion of graphene oxide (GO) over a patterned vinyl mask. The vinyl mask is prepared from a large sheet using a plotter cutter. When the mask is removed the excess GO is taken with it leaving in place a patterned GO film (typically in the shape of a rectangle). The samples are then reduced in 80% hydrazine hydrate vapour at 60°C to produce reduced graphene oxide (RGO)[7]. A seal made of vinyl is then applied to the film and substrate leaving holes for the separator to be cast and the reservoirs to be placed over the ends of the film. A small quantity of polydimethylsiloxane (PDMS) is then cast over the separator slot and allowed to infiltrate into the film over 24 hours by which time it has set. The reservoirs are then bonded on with epoxy and filled with electrolyte which for this report is exclusively 1M Na<sub>2</sub>SO<sub>4</sub>. Pieces of film extending out beyond the seal are then removed mechanically with a blade to ensure that each device has a similar exposed surface area.

Electrochemical characterization is conducted on a Biologic VSP potentiostat using Ag/AgCl reference electrodes from BASi. The 4-point probe tests were conducted using a custom probe and an Agilent B2902A precision source measurement unit.

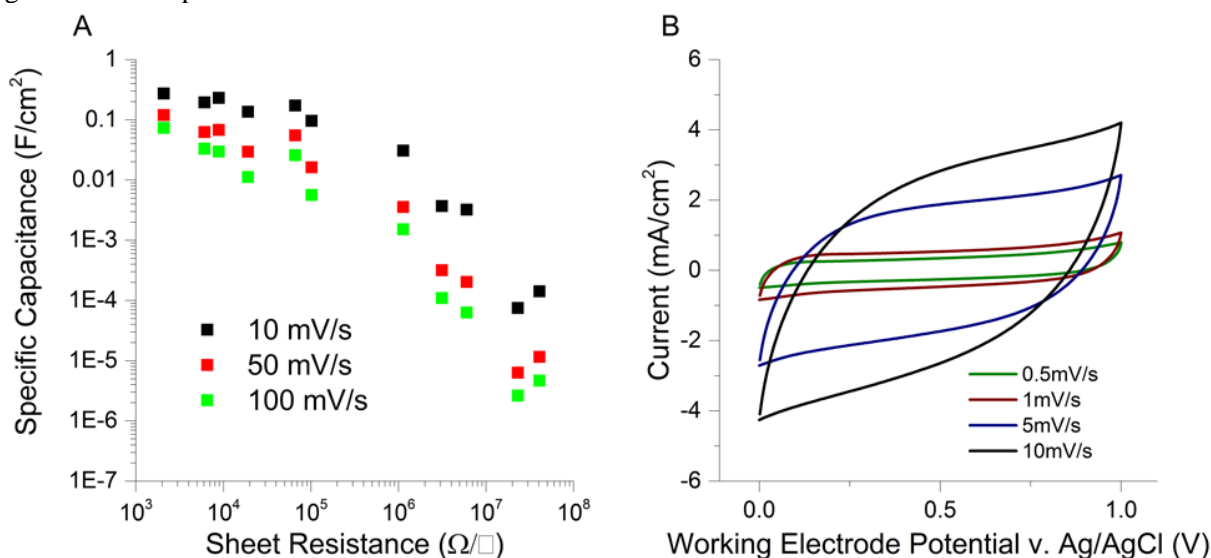


Figure 2: A) By reducing the RGO by different degrees and measuring its sheet resistance a clear trend between the measured sheet resistance and the devices' specific capacitance is observed at multiple scan rates. B) Cyclic voltammograms of the system show rectangular behavior only at low scan rates.

## RESULTS AND DISCUSSION

These devices were first studied by varying the degree of reduction and measuring the resultant sheet resistance using a 4-point probe. By varying the quantity of hydrazine used in the reduction process films with a variety of sheet resistances were produced. It was found that more conductive films have higher capacitances than films with higher sheet resistance as shown in figure 2A. This agrees with the

proposed mechanism that charge is being stored on the RGO by inducing a double layer on a polarizable material as a more conductive material will be more polarizable.

It was found that at conventional scan rates for super-capacitors this system behaved poorly however by reducing the scan rate the shape of the cyclic voltammograms improved (figure 2B). This slower nature agrees with previous reports of ionic systems compared to their electrical counterparts [2] and while it is related to the large difference between the mobilities of ions in a fluid and electrons in metallic conductors (a difference of  $\sim 8$  orders of magnitude) the presented design is also open to significant optimization. Using standard electrochemical analysis techniques (figure 2B) the device was found to have a capacitance of 8 F/g however due to the thin nature of the material it also resulted in an areal capacitance of 0.28 F/cm<sup>2</sup> at a scan rate of 10 mV/s. Power densities of 8mW/cm<sup>3</sup> and energy densities of 0.45 mWh/cm<sup>3</sup> (for a scan rate of 10 mV/s) put this device close to the performance of a thin film lithium ion battery, whilst the power density of this system is low for a super-capacitor the energy density is quite comparable to values reported in high impact journals [8].

## CONCLUSION

An iontronic capacitor has been developed using induced charge phenomena to store energy on a polarizable surface made of reduced graphene oxide. The device fits neatly into the expanding suite of iontronic components used to construct ionic circuits. The system is most closely related to a super-capacitor in its nature but much like other iontronic components displays slower response than equivalent electrical systems.

## ACKNOWLEDGEMENTS

S. T. Martin acknowledges the support of the Monash Centre for Atomically Thin Materials. The authors acknowledge A. Akbari for synthesizing the graphene oxide and P. Banerjee for her assistance with the electrochemical studies.

## REFERENCES

- [1] J. H. Han *et al.*, "Ionic circuits based on polyelectrolyte diodes on a microchip," *Angewandte Chemie*, vol. 121, no. 21, pp. 3888-3891, 2009.
- [2] E. O. Gabrielson *et al.*, "A four-diode full-wave ionic current rectifier based on bipolar membranes: overcoming the limit of electrode capacity," *Adv Mater*, vol. 26, no. 30, pp. 5143-7, Aug 13, 2014.
- [3] S. T. Martin, A. Neild, and M. Majumder, "Graphene-based ion rectifier using macroscale geometric asymmetry," *Apl Materials*, vol. 2, no. 9, pp. 092803, 2014.
- [4] H. Daiguji, "Ion transport in nanofluidic channels," *Chem Soc Rev*, vol. 39, no. 3, pp. 901-11, Mar, 2010.
- [5] K. Raidongia, and J. Huang, "Nanofluidic ion transport through reconstructed layered materials," *J Am Chem Soc*, vol. 134, no. 40, pp. 16528-31, Oct 10, 2012.
- [6] T. M. Squires, "Induced-charge electrokinetics: fundamental challenges and opportunities," *Lab on a Chip*, vol. 9, no. 17, pp. 2477-2483, 2009.
- [7] I. K. Moon *et al.*, "Reduced graphene oxide by chemical graphitization," *Nature communications*, vol. 1, pp. 73, 2010.
- [8] M. F. El-Kady *et al.*, "Laser scribing of high-performance and flexible graphene-based electrochemical capacitors," *Science*, vol. 335, no. 6074, pp. 1326-1330, 2012.

## CONTACT

\* Mr Samuel Martin : 

Electronic supporting information for  
PCCP publication the inside out  
supercapacitor: induced charge  
storage on reduced graphene oxide

## Electronic supporting information for the inside-out supercapacitor: induced charge storage in reduced graphene oxide

Samuel T. Martin<sup>a,b</sup>, Abozar Akbari<sup>a</sup>, Parama Chakraborty Banerjee<sup>a</sup>, Adrian Neild<sup>b</sup>, Mainak

Majumder<sup>a\*</sup>

### Table of Contents

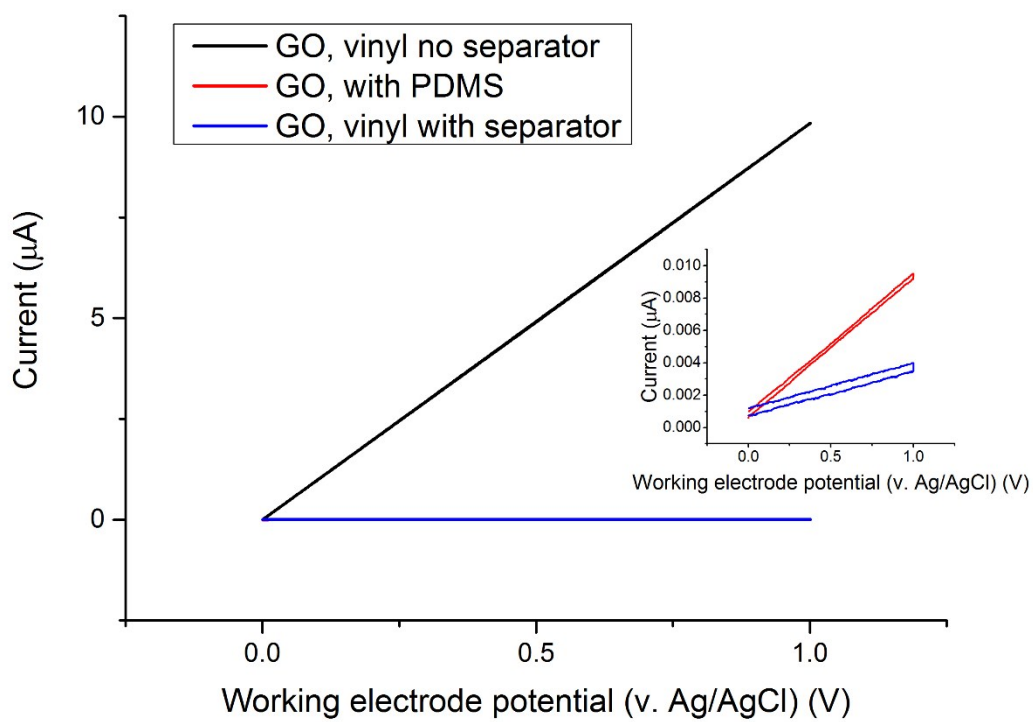
Role of the PDMS Separator .....	2
Varying the conductivity of reduced graphene oxide.....	5
Gold control inside out supercapacitor .....	7
Electrochemical calculations .....	8
Additional electrochemical characterization .....	10
Role of the vinyl seal.....	12

---

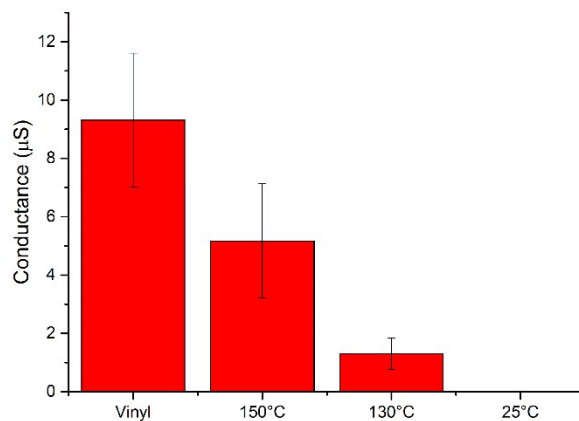
<sup>a</sup> *Nanoscale Science and Engineering Laboratory (NSEL), Department of Mechanical and Aerospace Engineering, Monash University Clayton, VIC-3800 Australia*

<sup>b</sup> *Laboratory for Microsystems (LMS), Department of Mechanical and Aerospace Engineering, Monash University Clayton, VIC-3800 Australia*

## Role of the PDMS Separator



*Supplementary figure 1- Cyclic voltammetry plot for 3 different graphene oxide (GO) based device designs. GO samples with no separator permit an unimpeded path for ion to travel through the interlayer spacing of the GO. GO devices where PDMS is used to penetrate into the microstructure of the film and block it exhibit radically reduced ionic conductance. These tests were performed at a scan rate of 1 mV/s in a 1M  $\text{Na}_2\text{SO}_4$  electrolyte.*



*Supplementary figure 2 - The conductance of a series of devices, sealed in different manners, one with a vinyl seal, three with PDMS seals cured at different temperatures (150 °C 130 °C and 25 °C) was monitored for 20 hours in 1 mM NaCl electrolyte. The 25 °C sample had an average conductance of 9 nS.*

PDMS cures more swiftly as temperature increases. GO devices were fabricated to test the effect of curing temperature on the resultant ionic conductance. The vinyl devices used in this control experiment have the same fabrication as described in figure 2 of the main text, except there is no slot present for PDMS to be cast into. This allows ions to move unimpeded parallel to the hydrophilic GO sheets from one reservoir to the other as described in Raidongia et al.<sup>1</sup> The PDMS based devices take a GO film on a glass substrate and buries the film in freshly prepared PDMS. This is then cured in the oven at various temperatures changing the diffusivity of the polymer, its curing time and its viscosity. Once cured the film is cut to length (14 mm) and reservoirs are attached using epoxy.

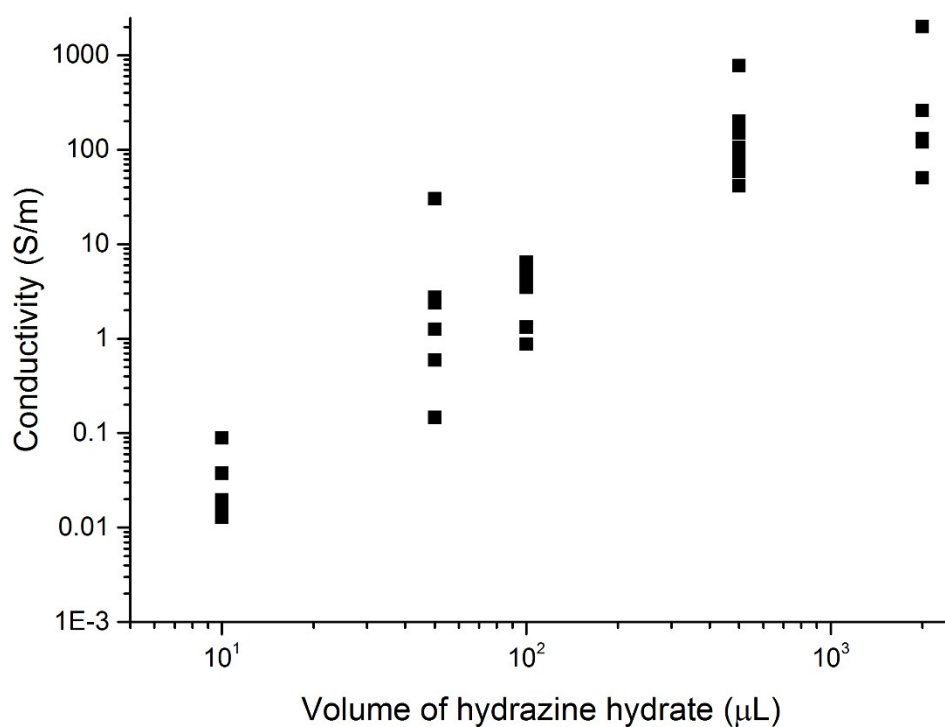
There's almost a 2-fold loss in conductance from the vinyl case to the PDMS cured at 150 °C, which is listed to cure in 5 minutes. From this there are two possible conclusions – the vinyl seal leaks or the PDMS penetrates rapidly into the film (these films are quite thin it should be mentioned, ~2 μm). If there is a leak it is uniform across all samples tested as the uncertainty doesn't really change between the PDMS case and the vinyl, which is somewhat unexpected in the case where the vinyl seal is leaking. When the temperature is decreased to 130 °C there is almost a 5-fold loss in

conductance from 150 °C despite only a 5 minute increase in curing time. This points to the fact that for these thin film the PDMS very rapidly penetrates and blocks the nanochannels of these devices.

The GO with PDMS device in Supplementary figure 1 was fabricated in the same manner as described in PDMS penetration testing section above. Once the pattern was formed 3 different designs were produced- those completely buried in PDMS, those with slots cut in the vinyl for PDMS penetration and devices with a vinyl seal and no PDMS. The PDMS was set over 24 hours allowing it to penetrate into the film.

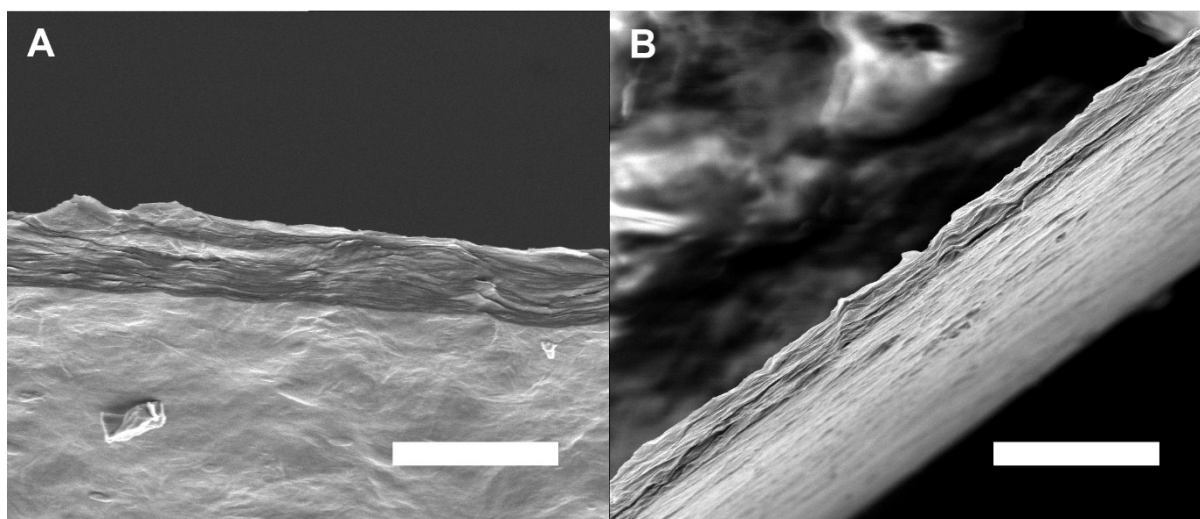
As can be seen in Supplementary figure 1, the device with no PDMS infiltration (one with a simple vinyl seal) has significantly higher ionic conductivity. The devices entirely buried in PDMS and one with a separator slot performed similarly with conductivities in the nS range. This suggests clearly that the separator is reducing ionic conduction in the material.

## Varying the conductivity of reduced graphene oxide



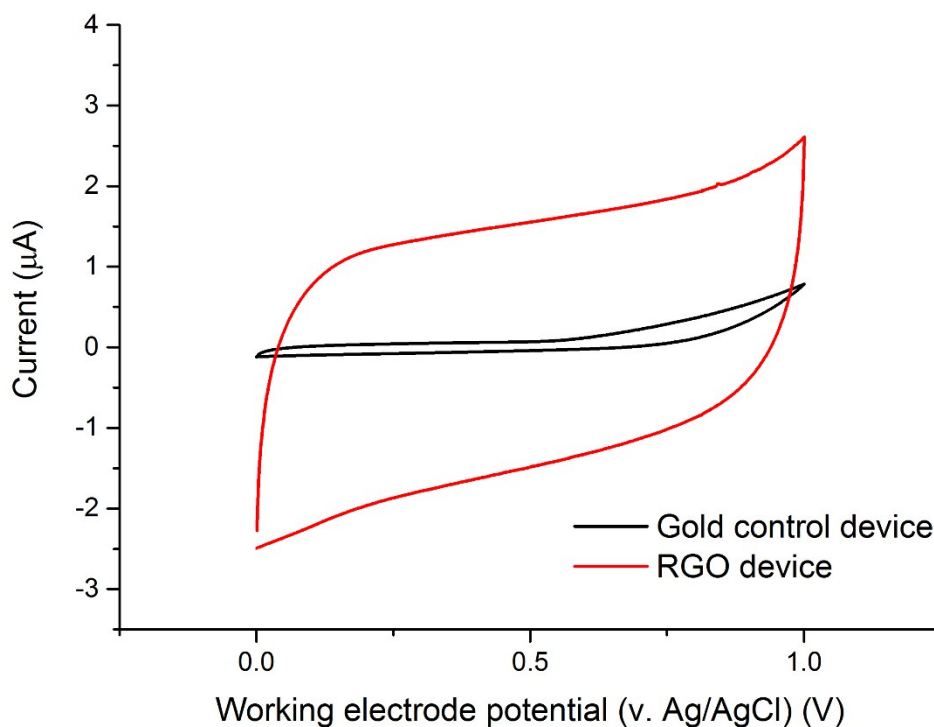
*Supplementary figure 3 – Various volumes of hydrazine were used to vary the level of reduction in the graphene oxide films. The conductivities here are calculated using the reduced sample's height measured using an optical profilometer.*

In order to vary the conductivity, samples were exposed to different quantities of hydrazine vapour as shown in Supplementary figure 3. The objective of this was to create a variety of samples with different conductivities to demonstrate that the resultant electrical properties were of key importance and not the exact quantity of reducing agent used.



*Supplementary figure 4 – a) a cross section of a graphene oxide film illustrating continuous film structure, b) a film sample exposed to 30  $\mu\text{L}$  of hydrazine hydrate, exfoliation has occurred due to the development of gas during reduction indicated by the presence of voids in the film structure. Scale bar in both figures is 10  $\mu\text{m}$ .*

## Gold control inside out supercapacitor



*Supplementary figure 5 – cyclic voltammograms of a typical RGO inside-out supercapacitor and a gold coated microscope slide with reservoirs adhered to its surface at a scan rate of 1 mV/s in 1M Na<sub>2</sub>SO<sub>4</sub> electrolyte.*

The gold device was prepared by sputtering a thin layer of gold onto a microscope slide. Reservoirs were then bonded onto the gold directly at two places on the slide and filled with electrolyte. The area of gold exposed to the electrolyte in each reservoir was 8 mm x 8 mm. The capacitance of the gold based device was small in comparison to the RGO device's. This is attributed to the difference in exposed specific surface area of the two materials. Both devices demonstrate induced double-layer charge storage and show the generality of the mechanism described here.

## Electrochemical calculations

The capacitance of a device was calculated using CV data at a given scan rate using, (calculations follow those used in Lobo et al.)<sup>2</sup>

$$C = \frac{1}{v\Delta\varphi} \int_0^1 i(\varphi) d\varphi, \text{ for } i > 0 \quad (1)$$

where  $\Delta\varphi$  is the applied potential window,  $v$  is the scan rate,  $i$  is the current and  $\varphi$  is the voltage.

This integral was calculated for the 5<sup>th</sup> cycle. To calculate the specific capacitance the capacitance value was divided by the volume of the work surface (6 mm × 14 mm × thickness).

Capacitance from GCPL data was calculated using

$$C = \frac{i}{-\frac{d\varphi}{dt}}, \quad (2)$$

where the derivative of  $\varphi$  is the gradient of the discharge curve.

Specific capacitance was calculated by

$$C_{sp} = \frac{C}{V}, \quad (3)$$

where  $V$  is the volume of the work surface. Power was calculated from the cyclic voltammetry data by

$$P = \int_0^1 i(\varphi) d\varphi, \text{ for } i > 0. \quad (4)$$

Power density was calculated using

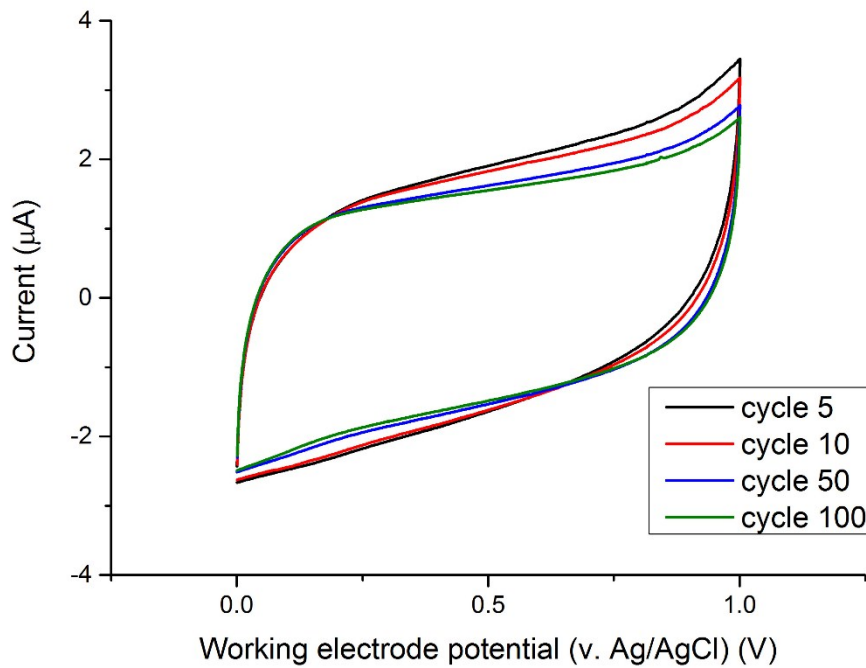
$$\rho = \frac{P}{V}. \quad (5)$$

Areal capacitance was calculated using

$$C_{Areal} = \frac{C}{2A_{int}}, \quad (6)$$

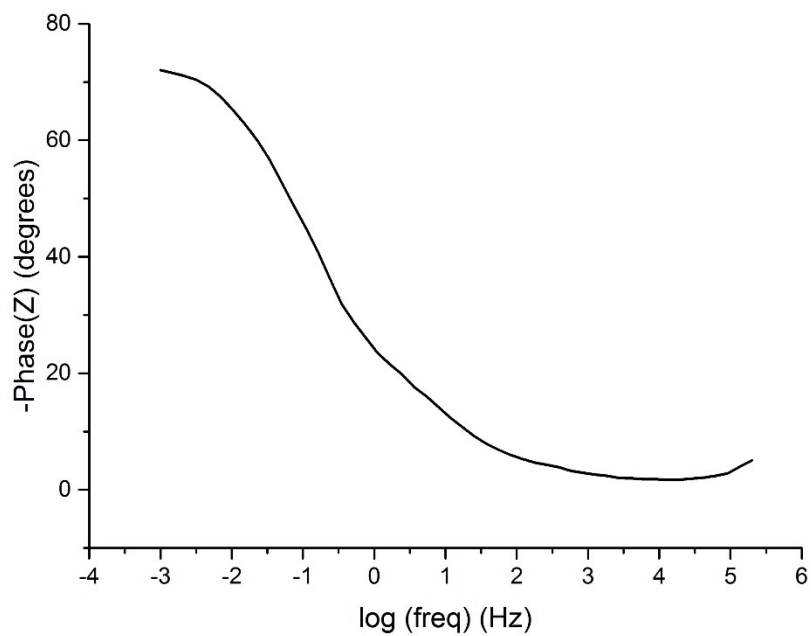
where  $A_{int}$  is the cross sectional area of the work surface.

## Additional electrochemical characterization

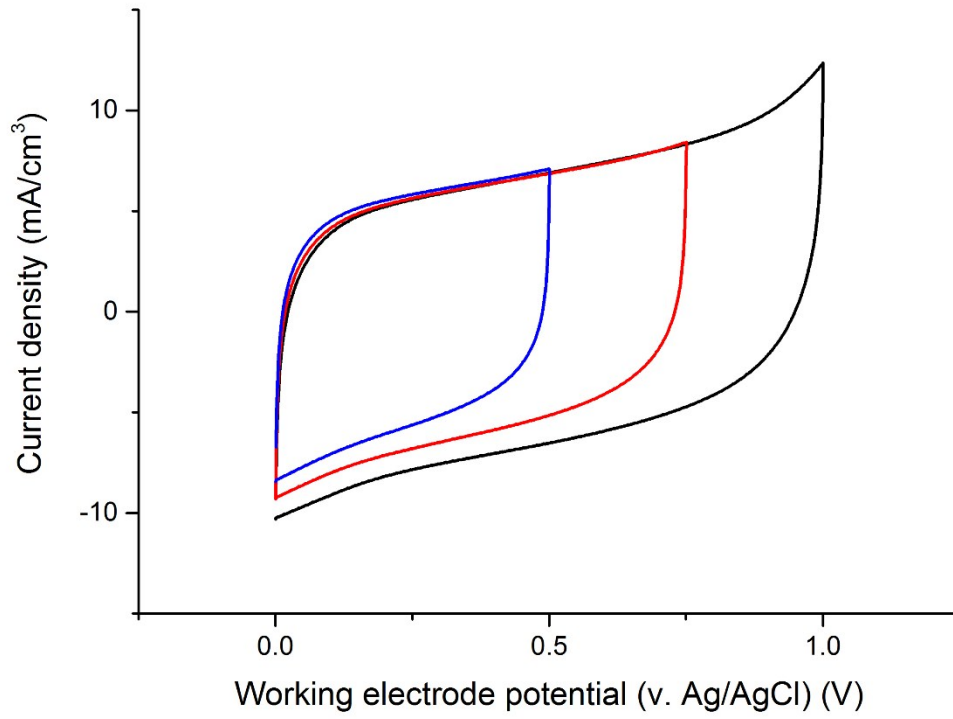


Supplementary figure 6 –Cyclic voltammograms for a 2.3 μm thick device scanned at 1 mV/s for 100 cycles in 1 M Na<sub>2</sub>SO<sub>4</sub>.

There is no significant change to the shape of the curve indicating the absence of faradaic reactions.



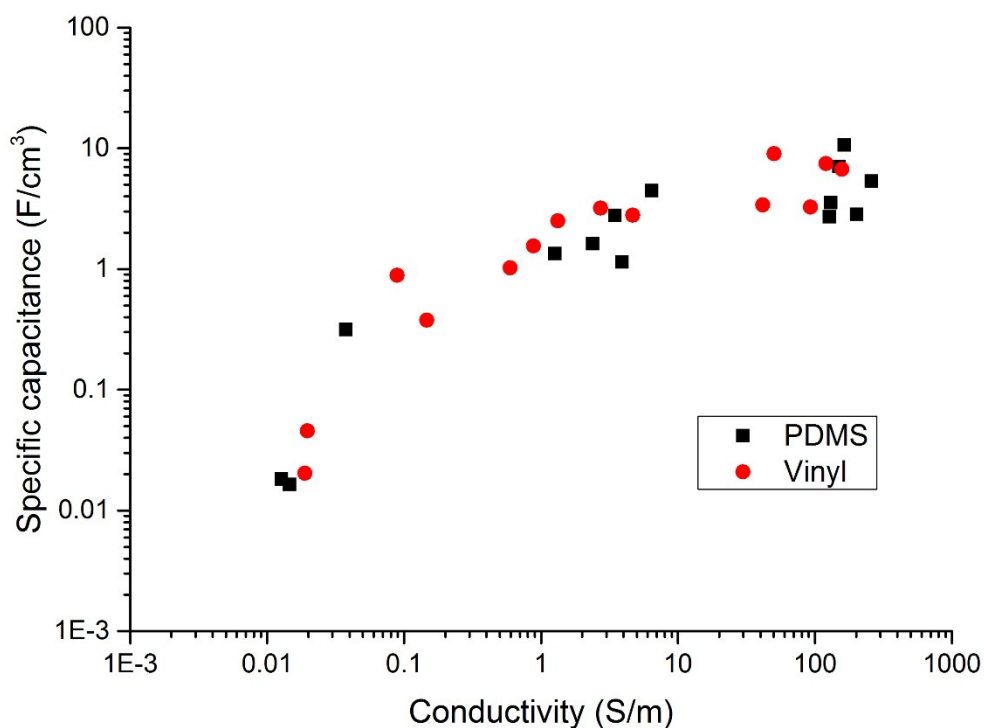
Supplementary figure 7 – A typical Bode phase plot for a 1 μm thick inside out supercapacitor.



Supplementary figure 8 – Cyclic voltammograms for a 1  $\mu\text{m}$  thick device cycled at several different voltage ranges, in all cases the scan rate was 1 mV/s in 1 M  $\text{Na}_2\text{SO}_4$  electrolyte.

## Role of the vinyl seal

Understandably the question must arise as to the efficacy of this vinyl seal in this concentrated salt solution. In this first experiment (Figure 3 and Supplementary figure 9) two different designs were used- a vinyl seal with a slot for the PDMS separator and a design that was purely PDMS with no vinyl. As it is known from previous experiments that PDMS will penetrate into GO and radically alter its ionic conductivity (Supplementary figure 1) this would suggest that no electrolyte penetrates into the RGO as the PDMS penetrates into the film and is given 24 hours at 25 °C to do so. According to Supplementary figure 1 this increases ionic resistance by around 3 orders of magnitude. It follows that if the electrolyte were to wet the entire vinyl covered film volume and/or form a thin wetting layer between the vinyl and the RGO then the vinyl case would have significantly more exposed area (as the current area exposed is  $\sim 6000 \mu\text{m}^2$ ) and thus higher capacitance. It is arguable that the vinyl design slightly outperforms the PDMS one (Supplementary figure 9) which we attribute to the PDMS preventing electrolyte entering the porous work surface at the exposed ends which one might expect given the results in Supplementary figure 1 and not as a result of the vinyl seal exposing more area than proposed. However it is quite clear that regardless of the method the performance depends far more strongly on the conductivity of the work surface than the exact nature of the separator and device design.



Supplementary figure 9 – Specific capacitances at a scan rate of 1 mV/s in a 1M Na<sub>2</sub>SO<sub>4</sub> electrolyte for the two different device fabrications – one with a vinyl seal and PDMS separator and one entirely coated in PDMS.

## References

1. Raidongia K, Huang J. Nanofluidic Ion Transport through Reconstructed Layered Materials. *J Am Chem Soc* **134**, 16528-16531 (2012).
2. Lobo DE, Banerjee PC, Easton CD, Majumder M. Miniaturized Supercapacitors: Focused Ion Beam Reduced Graphene Oxide Supercapacitors with Enhanced Performance Metrics. *Advanced Energy Materials* **5**, (2015).